

Dissertation zur Erlangung des Doktorgrades
der Fakultät für Chemie und Pharmazie
der Ludwig-Maximilians-Universität München

**Photoinitiated processes in functionally
diverse organic molecules elucidated by
theoretical methods**

Matthias Karl Hellmuth Roos

aus

München, Deutschland

2018

Erklärung:

Diese Dissertation wurde im Sinne von §7 der Promotionsordnung vom 28. November 2011 von Frau Prof. Dr. Regina de Vivie-Riedle betreut.

Eidesstattliche Versicherung:

Diese Dissertation wurde eigenständig und ohne unerlaubte Hilfe erarbeitet.

München, den 18.10.2018
Matthias K. Roos

Dissertation eingereicht am: 18.10.2018
1. Gutachterin: Prof. Dr. Regina de Vivie-Riedle
2. Gutachter: Prof. Dr. Christian Ochsenfeld
Tag der mündlichen Prüfung: 14.11.2018

Contents

Abstract	v
List of publications	vii
Introduction	1
1. Wilson G-matrix method for quantum dynamics in reduced coordinates	3
1.1. Design of a dimensionality reduced, quasi-relaxed coordinate system . . .	4
1.2. Some remarks on Eckart conditions	17
2. Light-induced bond cleavage in diphenylmethyl compounds	19
2.1. Reaction mechanisms for two different leaving groups in direct comparison	20
2.2. Simulation of experimental signals from reduced dimensionality wave packet dynamics	37
2.3. The effect of a higher homologue on the reaction dynamics	46
3. Photophysics of elongated π systems in organic molecules	57
3.1. Ultrafast relaxation from 1L_a to 1L_b in pyrene	57
3.2. Identification of the absorbing species in a cyanine dye-DNA construct .	69
4. Chemical stability of two standard electrolytes used in lithium-ion batteries towards singlet oxygen	79
5. Summary and outlook	95
A. The ONIOM method and its implementation	99
B. Supporting information for chapter 4	107
List of abbreviations	121
Bibliography	123
Danksagung	135

Abstract

In this thesis reaction mechanisms of organic compounds with applications in different areas, such as kinetic studies, labeling, and battery electrolytes, are investigated with theoretical methods from quantum chemistry, quantum dynamics, and molecular dynamics. The variety of the investigated molecules ranges from polycyclic hydrocarbons, dyes, electrolytes to precursors of reactive species. The work was performed either in close collaboration with experimentalists or based on experimental results and in this way allows an in-depth look at the occurring chemistry.

In the first part the concept of adapted reactive coordinates for reduced dimensional quantum dynamics is presented necessary for the studies in the following part. It relies on the Wilson G-matrix method as formulation of the kinetic part of the Hamiltonian and allows to include the relaxation of background coordinates besides the identified main reactive coordinates without optimizations for each grid point. The concept is shown for a photodissociation involving complex structural changes and the G-matrix elements and their influence on the dynamics are discussed.

In the second part the photoinitiated bond cleavage reaction for diphenylmethyl chloride and diphenylmethyl bromide is studied. Based on the reactive coordinate system presented before, quantum dynamical simulations enlighten the path of the wave packet, which passes through two consecutive conical intersections—a three-state and a two-state one—as decisive elements for the product splitting. In the case of chlorine, the experimental signal is modeled from the simulated data to further prove the mechanism. For the bromine case, additionally non-adiabatic mixed quantum-classical dynamics is used to clarify the role of vibrations during the bond cleavage, which are responsible for small amplitude oscillations of the experimental signals. Throughout this part the “our own n -layered integrated molecular orbital and molecular mechanics” (ONIOM) method is used to reduce the involved computational cost.

The third part is dedicated to the photophysics of elongated π systems in organic molecules discussing two examples. The first one is the polycyclic hydrocarbon pyrene, the second one covalently linked constructs of DNA and the dye Cyanine 3. For pyrene, the ultrafast transition from the photo-accessible S_2 state to the fluorescent S_1 is simulated for the first time using two complementary dynamical methods. It is shown that both methods yield comparable results and demonstrate the strong coupling between the two states. The constructs in the second example are investigated experimentally and theoretically. Simulated spectra for a model system help attributing an occurring blue-shift to dimerization. Circular dichroism measurements and molecular dynamics simulations further characterize the formed dimers.

The last part comprises a joint experimental and theoretical study concerning the chemical stability of two electrolytes commonly used in lithium-ion batteries towards singlet oxygen. It is shown that singlet oxygen is reactive towards the electrolyte ethylene carbonate. *Ab initio* calculations suggest a concerted double hydrogen abstraction by the singlet oxygen as mechanism, which is not possible for the second electrolyte dimethyl carbonate. It is an example for the unusual reaction of an alkyl group with singlet oxygen and yields hydrogen peroxide. Ground state mixed quantum-classical dynamics verify the further decay of the reaction intermediate vinylene carbonate to carbon dioxide, which is found experimentally. The theoretically predicted

intermediate formation of hydrogen peroxide is detected colorimetrically proving the reaction mechanism and its detrimental effect is investigated experimentally.

List of publications

This thesis is based on the following 7 publications listed in chronological order. They are reprinted in the chapters 1 (**2**), 2 (**1, 4, 6**), 3 (**3, 5**), 4 (**7**).

- 1** S. Thallmair, M. K. Roos, and R. de Vivie-Riedle
Molecular features in complex environment: Cooperative team players during excited state bond cleavage.
Struct. Dyn. **3**, 043205 (2016).
Contributions by M. K. Roos: performing all calculations in Sec. II. and their analysis, writing of Sec. II.
- 2** S. Thallmair, M. K. Roos, and R. de Vivie-Riedle
Design of specially adapted reactive coordinates to economically compute potential and kinetic energy operators including geometry relaxation.
J. Chem. Phys. **144**, 234104 (2016).
Contributions by M. K. Roos: developing, implementing and testing the presented concepts and procedures.
- 3** F. Nicoli, M. K. Roos, E. A. Hemmig, M. Di Antonio, R. de Vivie-Riedle, and T. Liedl
Proximity-Induced H-Aggregation of Cyanine Dyes on DNA-Duplexes.
J. Phys. Chem. A **120**, 9941–9947 (2016).
Contributions by M. K. Roos: performing all theoretical calculations and their analysis, writing of the theoretical part.
- 4** E. Riedle, M. K. Roos, S. Thallmair, C. F. Sailer, N. Krebs, B. P. Fingerhut, and R. de Vivie-Riedle
Ultrafast photochemistry with two product channels: wavepacket motion through two distinct conical intersections.
Chem. Phys. Lett. **683**, 128–134 (2017).
Contributions by M. K. Roos: performing all theoretical calculations and their analysis.
- 5** M. K. Roos, S. Reiter, and R. de Vivie-Riedle
Ultrafast relaxation from 1L_a to 1L_b in pyrene: a theoretical study.
Chem. Phys. (2018), DOI: 10.1016/j.chemphys.2018.08.002.
Contributions by M. K. Roos: supervising and/or performing all calculations and their analysis, writing.
- 6** F. Schüppel, M. K. Roos, and R. de Vivie-Riedle
Ultrafast non-adiabatic dynamics of excited diphenylmethyl bromide elucidated by quantum dynamics and semi-classical on-the-fly dynamics.
Phys. Chem. Chem. Phys. **20**, 22753–22761 (2018).
Contributions by M. K. Roos: supervising all calculations, analysis, and writing.

- 7** A. T. S. Freiberg, M. K. Roos, J. Wandt, R. de Vivie-Riedle, H. A. Gasteiger
Singlet Oxygen Reactivity with Carbonate Solvents used for Li-Ion Battery Electrolytes.
Submitted to *J. Phys. Chem. A* (2018).
Contributions by M. K. Roos: performing all theoretical calculations and their analysis, writing.

Additional publication:

- 8** S. Thallmair, M. Kowalewski, J. P. P. Zauleck, M. K. Roos, and R. de Vivie-Riedle
Quantum dynamics of a photochemical bond cleavage influenced by the solvent environment: A dynamic continuum approach
J. Phys. Chem. Lett. **5**, 3480–3485 (2014).

Introduction

Studying the dynamics of chemical reactions is an important and growing research area connecting the fields of chemistry, physics, and biology [1]. The scope of this area is going beyond the question of what products emerge from the reaction. It aims to understand in detail how the reaction occurs and why the specific products are built. The macroscopic world is left behind and a look deep down at the microscopic world is made to gain an understanding of the processes at a molecular level.

To experimentally resolve such processes, laser pulses of the same duration as the occurring dynamics are required. Advances of laser technology in the 1980s made it possible to reach the femtosecond regime necessary for the dynamics of chemical bonds and, hence, the area of femtochemistry was born. Its pioneer Ahmed H. Zewail was awarded the Nobel Prize in Chemistry “for his studies of the transition states of chemical reactions using femtosecond spectroscopy” in 1999 [2–6]. The most widespread technique of choice for such studies is transient absorption spectroscopy [7]. Its pump-probe pulse sequence allows to follow the temporal evolution of reactants, intermediates, and products by its respective spectroscopic signature.

Dynamical simulation methods are an ideal complement for such an experimental technique [8–10]. While the experiment observes the molecule from the outside, theory gives direct access to chemical structures and its fluctuations in time. For spatially very extended systems molecular mechanics (MM) is a capable option, which completely leaves out the electrons and models the atoms as round spheres connected by springs [11]. The dynamics of these classical spheres can be described using Newton’s equations of motion and is called molecular dynamics (MD). Unfortunately, this kind of model is not able to account for changes in the bonding structure.

Thus, to describe a true chemical reaction, quantum chemistry (QC) methods are essential. Hierarchically speaking they are the foundation the advanced dynamical methods are based on. Two families of methods—density- or wave function-based—are available, also represented in the Nobel Prize in Chemistry in 1998 for Walter Kohn (“for his development of the density-functional theory”) [12] and John A. Pople (“for his development of computational methods in quantum chemistry”) [13]. The QC methods provide potential energy surfaces (PESs) and non-adiabatic couplings, which can be used by the dynamical methods to go beyond the Born-Oppenheimer approximation [14]. Reactions with transitions between different electronic states can be modeled in this way.

The points, where these transitions between electronic states can occur and, thus, a radiation-less transfer of population, are called conical intersections (CoIns) [15–22], named after their characteristic double-cone form of the potential. Reactions through CoIns occur ultrafast and are known to be important in several aspects of life, like for DNA photostability [23] or the process of vision [24].

A major part of this thesis is concerned with such reactions. An established method to describe them is quantum dynamics (QD) [25]. While highly accurate QD requires pre-knowledge of the PESs, it is afflicted with the curse of dimensionality and therefore only feasible in reduced subspaces. In chapter 1 the Wilson G-matrix method [26–29] is introduced, enabling the usage of arbitrary coordinates in QD. Based on this, the concept of adapted reactive coordinates (aRCs) is presented, a coordinate

system developed for the description of the photoinitiated bond cleavage of diphenylmethyl compounds. It offers a convenient way to include the relaxation of background coordinates in reduced dimensionality QD without optimizations for each grid point. The shape of the G-matrix elements and their influence on the dynamics is discussed in detail.

This coordinate system is put to use in chapter 2, where the initial bond cleavage reactions of diphenylmethyl chloride ($\text{Ph}_2\text{CH}-\text{Cl}$) and diphenylmethyl bromide ($\text{Ph}_2\text{CH}-\text{Br}$) are simulated. Contrary to previous simulations [30] both product channels, the homolytic and the heterolytic one, are included, featuring three-state and two-state CoIns. For the first time, a three-state CoIn seam is included in a QD propagation. A comparison with experimental observables in the case of $\text{Ph}_2\text{CH}-\text{Cl}$ and with a second dynamical method—non-adiabatic mixed quantum-classical dynamics (MQCD) [31]—in the case of $\text{Ph}_2\text{CH}-\text{Br}$ complete the overall picture of this ultrafast reaction. To reduce the computational cost the multi-scale method “our own n -layered integrated molecular orbital and molecular mechanics” (ONIOM) [32–37] is used for all QC calculations. Even more versatile than quantum mechanics/molecular mechanics (QM/MM) [38–44], it allows the combination of different QC methods in an extrapolative manner. Details about ONIOM and its implementation as part of this thesis can be found in appendix A.

Chapter 3 is dedicated to the photophysics of elongated π systems in organic molecules used for labeling in spectroscopic measurements. It is subdivided in two sections. In the first section, the polycyclic hydrocarbon pyrene is investigated. It is an experimentally well studied molecule [45–51]. However, the ultrafast relaxation from the initially populated 1L_a state to the fluorescent 1L_b is not yet understood. Using both QD and MQCD this transfer through a CoIn is simulated for the first time.

The second section of chapter 3 is concerned with the characterization of dimers built from dye molecules Cyanine 3 (Cy3). The dyes are covalently linked to DNA strands which act as a scaffold. Simulated spectra help to interpret the experimental signals. The dynamics of the dimers on the DNA strand is further captured by MD simulations.

The last chapter of this thesis is dedicated to the chemical reactivity of two standard electrolytes used in lithium-ion batteries towards singlet oxygen. In a rigorous way, this joint experimental-theoretical investigation elucidates the emerging reaction and its mechanism, which leads to poor cycling behavior for some electrolytes. Ground state MQCD is used here in an explorative manner starting from a critical transition state (TS) to identify all products energetically in reach.

Chapter 1.

Wilson G-matrix method for quantum dynamics in reduced coordinates

Dynamical simulations of chemical reactions are a suitable tool to elucidate the microscopic mechanisms governing our macroscopic world [8, 10]. Two main branches of methods were developed to simulate the dynamics: On the one hand, there are mixed quantum-classical dynamics (MQCD) methods [52, 53] treating the electrons at a quantum level, the nuclear motion at a classical level. Prominent examples for this branch are *trajectory surface hopping* [31] and *multiple spawning* [54]. On the other hand, there are full quantum methods [55] treating both electrons and nuclei at a quantum level. Unfortunately these methods are only feasible in reduced dimensionality. While *multi-configuration time-dependent Hartree (MCTDH)* [56–58] can include relatively many dimensions, this is only possible by approximating the wave function with a Hartree product of single particle functions. With this nature it does not sufficiently describe the dynamics far from the Franck-Condon (FC) region, e.g. for a bond cleavage, as it does not include the complete topographic information of the PESs along the selected degrees of freedom. The state-of-the-art method to describe such and other processes is to numerically solve the time-dependent Schrödinger equation by wave packet propagation. This method is based on a pseudo-spectral representation like a grid [59, 60] to propagate on. The operator which is applied on the wave function in each time step is the Hamiltonian \hat{H} . It consists of the kinetic energy \hat{T} and potential energy operator \hat{V} :

$$\hat{H} = \hat{T} + \hat{V}. \quad (1.1)$$

For QD in reduced dimensionality a formulation of the Hamiltonian in this coordinate system is necessary. While for \hat{V} as a multiplicative operator this task is trivial, the challenge is in \hat{T} .

The Wilson G-matrix method was first introduced by Podolsky [26] and formalized by Wilson [27] as an ansatz of the kinetic energy operator \hat{T}_q in M arbitrary internal coordinates q :

$$\hat{T}_q = -\frac{\hbar^2}{2} \sum_{r=1}^M \sum_{s=1}^M j^{-1/2} \frac{\partial}{\partial q_r} \left[j G_{rs} \frac{\partial}{\partial q_s} j^{-1/2} \right], \quad (1.2)$$

with j the determinant of the Jacobian matrix \mathbf{J} responsible for the coordinate transformation with the elements:

$$J_{ri} = \frac{\partial x_i}{\partial q_r}. \quad (1.3)$$

The matrix elements G_{rs} of the G-matrix are given by:

$$G_{rs} = \sum_{i=1}^{3N} \frac{1}{m_i} \frac{\partial q_r}{\partial x_i} \frac{\partial q_s}{\partial x_i}. \quad (1.4)$$

The derivatives contained in this matrix perform the effective coordinate transformation and are paired with the inverse masses. As these both parts of the G-matrix do not change during the QD propagation, the matrix elements can be calculated beforehand. Note that the G-matrix—containing derivatives with respect to two internal coordinates—introduces off-diagonal terms and in this way a kinetic coupling between the coordinates.

In general, the G-matrix and also the Jacobian determinant j are position-dependent. Only for the special case of linear coordinates both are constant for all positions. As the position dependency of j can be assumed to be negligible compared to the derivatives in the G-matrix [29], the kinetic energy of eq. 1.2 can be written in a simpler form [28]:

$$\hat{T}_q \simeq -\frac{\hbar^2}{2} \sum_{r=1}^M \sum_{s=1}^M \frac{\partial}{\partial q_r} \left[G_{rs} \frac{\partial}{\partial q_s} \right]. \quad (1.5)$$

Recently, an assessment of the hereby potentially included error was undertaken and possible ways of recuperation were shown [61].

The usage of the Wilson G-matrix method is demonstrated in the following section. Based on this, a quasi-relaxed coordinate system is built for a real chemical test case, the photodissociation of diphenylmethyltriphenylphosphonium ion ($\text{Ph}_2\text{CH}-\text{PPh}_3^+$) and the influence of the G-matrix on the dynamics is shown. Further details about the course of the photodissociation and a comparison with another leaving group can be found in section 2.1 of chapter 2. The second section of this chapter contains details about algorithms for adhering the Eckart conditions necessary for the calculation of the G-matrix. In chapter 2, further applications of the G-matrix are described based on the coordinate system explained in the following section. In section 3.1 of chapter 3 the Wilson G-matrix method is also applied, using linear coordinates.

1.1. Design of a dimensionality reduced, quasi-relaxed coordinate system

For a successful QD description of a reaction, it is key to have beforehand knowledge about the system like minima, CoIns or the minimum energy path (MEP). Based on that knowledge, it is the task to identify the reactive internal coordinates that describe the reaction at hand as best as possible. Some approaches exist to guide and quantify this process [62–65], in this thesis the coordinates are found by thorough reaction analysis. As in the QD each dimension drastically increases the simulation time, two or three dimensions are the limit.

In the article “Design of specially adapted reactive coordinates to economically compute potential and kinetic energy operators including geometry relaxation” published in *The Journal of Chemical Physics* a quasi-relaxed coordinate system for the description of the photodissociation of $\text{Ph}_2\text{CH}-\text{PPh}_3^+$ (for details see chapter 2) is presented [66]. The concept of adapted reactive coordinates (aRCs) is introduced. For that, two principal reactive coordinates are found first. Along the MEP major changes of other non-reactive coordinates are identified and the respective coordinates expressed as a function of the aRC. In this way, relaxation is included in the coordinate system without optimization at every geometry point. After defining the coordinate system and the algorithm for the construction of quasi-relaxed geometries, the G-matrix and its elements are discussed in detail and comparative QD calculations are shown.

The key points of the article are:

- Two reactive coordinates are chosen. The first one is the length r of the bond cleaved here, the second one an angle ϕ defined to reach the CoIn known as decisive for the product formation [67]. Analyzing the MEP, further major structural changes are identified, namely the bond distances and angles to the central carbon atom, the pyramidalization of the central carbon atom, and the positioning of the phenyl rings. Fitting functions are used to bring these coordinates in dependence of r . It is especially important to include the relaxation in the diphenylmethyl cation moiety as it accounts for 85% of the relaxation energy. As the relaxation coordinates are not linearly independent, it is essential to adhere to the presented protocol for the reconstruction of quasi-relaxed geometries.
- To economically describe the excitation of $\text{Ph}_2\text{CH}-\text{PPh}_3^+$ with complete active space self consistent field (CASSCF), the ONIOM method is successfully employed using the constraint low-level state (CLS) approximation [36] with density functional theory (DFT) as low-level method. A program of our own design was written to efficiently calculate and combine the energies of CASSCF calculated with MOLPRO [68] and of DFT calculated with GAUSSIAN [69] for the complete grid. It is described in appendix A.
- The Wilson G-matrix formalism and a convenient way of calculating the matrix elements are introduced. At first, the inverse G-matrix is built in adherence to the Eckart conditions (see section 1.2 below). In a detailed analysis, the shape of the G-matrix elements is traced back to the used fitting functions built into the aRCs. Note that the changes along the bond cleavage coordinate r are much more pronounced.
- The influence of the background relaxation in the G-matrix becomes apparent in two QD calculations on the same PES. In both cases, one with, one without the dynamic continuum ansatz [70], the background relaxation leads to distinctively more movement in the ϕ direction, drastically reducing the time necessary to reach the CoIn in the first case.

Hereafter, the article “Design of specially adapted reactive coordinates to economically compute potential and kinetic energy operators including geometry relaxation” published in *The Journal of Chemical Physics* is reprinted with permission from *J. Chem. Phys.* **144**, 234104 (2016). Copyright 2016 AIP Publishing.



Design of specially adapted reactive coordinates to economically compute potential and kinetic energy operators including geometry relaxation

Sebastian Thallmair,^{1,2} Matthias K. Roos,¹ and Regina de Vivie-Riedle^{1,a)}

¹Department Chemie, Ludwig-Maximilians-Universität München, D-81377 München, Germany

²Lehrstuhl für BioMolekulare Optik, Ludwig-Maximilians-Universität München, D-80538 München, Germany

(Received 15 March 2016; accepted 27 May 2016; published online 17 June 2016)

Quantum dynamics simulations require prior knowledge of the potential energy surface as well as the kinetic energy operator. Typically, they are evaluated in a low-dimensional subspace of the full configuration space of the molecule as its dimensionality increases proportional to the number of atoms. This entails the challenge to find the most suitable subspace. We present an approach to design specially adapted reactive coordinates spanning this subspace. In addition to the essential geometric changes, these coordinates take into account the relaxation of the non-reactive coordinates without the necessity of performing geometry optimizations at each grid point. The method is demonstrated for an ultrafast photoinduced bond cleavage in a commonly used organic precursor for the generation of electrophiles. The potential energy surfaces for the reaction as well as the Wilson G-matrix as part of the kinetic energy operator are shown for a complex chemical reaction, both including the relaxation of the non-reactive coordinates on equal footing. A microscopic interpretation of the shape of the G-matrix elements allows to analyze the impact of the non-reactive coordinates on the kinetic energy operator. Additionally, we compare quantum dynamics simulations with and without the relaxation of the non-reactive coordinates included in the kinetic energy operator to demonstrate its influence. *Published by AIP Publishing.* [<http://dx.doi.org/10.1063/1.4953667>]

I. INTRODUCTION

Quantum dynamics (QD) simulations are the most accurate way to describe reactive molecular processes. The quantum mechanical character of the nuclei is preserved in addition to the one of the electrons. Important features like vibrational or electronic transitions induced by a laser pulse,^{1–4} non-adiabatic processes mediated by conical intersections (CoIns),^{3,5,6} or coherent control studies^{2,7,8} can be straightforwardly described. Linked to the high accuracy is the high computational cost making a full-dimensional treatment already for medium sized molecules very demanding. In the case of absorption spectra, internal conversion, autocorrelation functions, and hydrogen transfer, the multi-configuration time-dependent Hartree (MCTDH) method proved to be an efficient way to include comparatively many dimensions.^{9–11} Semi-classical on-the-fly trajectories enable to consider all degrees of freedom; however, the nuclei are treated classically.¹²

In general, the number of internal degrees of freedom is $(3N - 6)$ for non-linear and $(3N - 5)$ for linear molecules, where N is the number of atoms. Thus, a quantum dynamical treatment of reactions with a larger number of atoms can only be achieved, if their dimensionality — i.e., the number of considered coordinates — is reduced. To perform this reduction, the decisive regions of the molecular configuration space — i.e., critical points like the minima of reactant and product, the transition state, as well as the minimum energy path (MEP) — have to be known beforehand. On this basis, reactive internal coordinates can be constructed which are

then used for the QD simulations. The challenge is to find the few best possible reactive internal coordinates, as in the majority of cases only up to three coordinates are utilized.

In the 1980s, Miller *et al.* portrayed the idea of a reaction path Hamiltonian.^{13,14} It is based on the intrinsic reaction coordinate of a chemical reaction which is one coordinate of the system. The remaining coordinates are orthogonal and obtained by diagonalizing the Hessian matrix.¹³ A related approach has been applied recently for QD simulations of a S_N2 reaction.¹⁵ Polyspherical coordinates are another prominent type of coordinates.^{16–18} They are, for example, used for ring opening reactions of furan¹⁹ and benzopyran,³ molecular collisions,²⁰ or bond cleavage processes.²¹ The coordinates for the ring opening reaction of 1,3-cyclohexadiene were derived in a different way: by a thorough analysis of relevant geometries in the excited state (minima, intermediate structures, and CoIns), three reactive coordinates have been set up.^{7,22} Normal modes constitute another prominent kind of coordinates because they entail a trivial formulation of the kinetic energy operator. They have been used, for example, to study the control of Na_3 ²³ or the photoelectron spectrum of the pentatetraene cation.²⁴

Here, we present an approach to design adapted reactive coordinates (aRCs) based on the MEP which include structural relaxation. The first step is to determine the most important reactive internal coordinates. Second, the major structural relaxations along the MEP are identified. Third, these structural relaxations of the non-reactive coordinates are recorded along the reactive internal coordinates chosen in step one. This opens a way to include the relaxation into the final aRCs. The aRCs are set up in line with the adiabatic-constraint

^{a)}Electronic mail: regina.de_vivie@cup.uni-muenchen.de

approach,¹⁷ which implies that the relaxation of the non-active coordinates takes place adiabatically with the molecular deformation. When the aRCs are defined, the next step is to calculate the potential energy surface (PES) with standard quantum chemistry. To derive an expression for the kinetic energy operator, we apply the Wilson G-matrix formalism.^{25,26} Finally, we discuss QD simulations considering the aRCs and the simple reactive internal coordinates in the kinetic energy operator, respectively. They illustrate the impact of the relaxation of the non-reactive coordinates contained in the kinetic energy operator on the simulated dynamics.

The article is structured as follows: Sec. II briefly introduces the chosen test case of a photoinduced ultrafast bond cleavage. The strategy to design the aRCs is given in Sec. III. Based thereon, we present the PESs for the reaction in Sec. IV. The matrix elements of the Wilson G-matrix are given in Sec. V together with a brief introduction to the Wilson G-matrix formalism for the kinetic energy operator. Moreover, we will discuss how the relaxation of the non-reactive coordinates is reflected in the shape of the G-matrix elements. Sec. VI compares QD simulations employing different kinetic energy operators before the results are summarized in Sec. VII.

II. THE BOND CLEAVAGE OF $\text{Ph}_2\text{CH-PPH}_3^+$ IONS AS TEST CASE

The strategy of our approach will be presented for the bond cleavage of diphenylmethyltriphenylphosphonium ions ($\text{Ph}_2\text{CH-PPH}_3^+$) involving many structural changes along the reaction path. Quaternary phosphonium ions are well-suited to generate carbocations after photoexcitation as short-lived reactive intermediates.^{27,28} The underlying reaction mechanism for the bond cleavage of this complex class of molecules has been unclear until recently and needed theoretical investigations.^{6,29,30} To explain the reaction outcome on an ultrafast time scale, population transfer through a CoIn has to be considered. State-of-the-art quantum chemical and quantum dynamical calculations could clarify the reaction mechanism.

To solve the time-dependent Schrödinger equation, the potential energy operator \hat{V} as well as the kinetic energy operator \hat{T} are necessary,

$$i\hbar \frac{\partial}{\partial t} \Psi(x,t) = \hat{H}_x \Psi(x,t) \\ = (\hat{T}_x + \hat{V}_x) \Psi(x,t). \quad (1)$$

Eq. (1) is generally set up in Cartesian coordinates $\{x\}$ with the Hamiltonian \hat{H}_x being the sum of \hat{T}_x and \hat{V}_x . To perform the QD calculations using the aRCs derived in Sec. III, the Schrödinger equation has to be transformed into internal coordinates $\{q\}$.^{31,32} The transformation of the multiplicative operator \hat{V}_x into \hat{V}_q is trivial. This is not the case for the kinetic part \hat{T}_x of the Hamiltonian

$$\hat{T}_x = -\frac{\hbar^2}{2} \sum_{i=1}^{3N} \frac{1}{m_i} \frac{\partial^2}{\partial x_i^2} \quad (2)$$

with the masses m_i and the total number of atoms N . Especially, if the chosen internal coordinates include angles,

the transformation is challenging because they describe a non-linear motion. In this work, we use the G-matrix formalism^{25,26,31} which is briefly introduced in Sec. V A.

In order to clarify the mechanism of the bond cleavage, we decided to perform QD simulations in reduced dimensionality.^{6,29} To achieve an as accurate as possible description of the PES, it is often not sufficient to solely select the major and most apparent structural changes (like bond cleavage and formation) as reactive coordinates. Especially when complex chemical reactions are considered, structural relaxations of the non-reactive coordinates are often associated therewith. One popular example is the change of hybridization of an atom but also bond length adjustments are omnipresent. As these relaxations adiabatically follow the major structural changes, we will refer to them as background relaxations from hereon. They give rise to a decisive energetic stabilization. As a result, their consideration is crucial for an adequate description of the reaction dynamics. The straightforward way to include the background relaxations is to perform partial optimizations at each point in the low dimensional space to obtain a relaxed structure. However, this can be computationally very demanding especially if highly correlated quantum chemical methods are applied. In the following, we present a computationally much more economic approach to receive approximately relaxed structures with the help of aRCs.

III. DESIGN OF ADAPTED REACTIVE COORDINATES

The bond cleavage of $\text{Ph}_2\text{CH-PPH}_3^+$ is described by two reactive internal coordinates. One is the C1-P distance r (see Fig. 1). The second one is the angle ϕ which leads to the S_1/S_0 CoIn being decisive for the branching into the product channels.³³ To optimally define this second reactive internal coordinate, a dummy atom X is used. It lies in the plain spanned by the three C atoms of the allyl moiety (C1, C2 and C3 in Fig. 1) in such a way that the vector pointing from X to the P atom is orthogonal to the allyl plain at

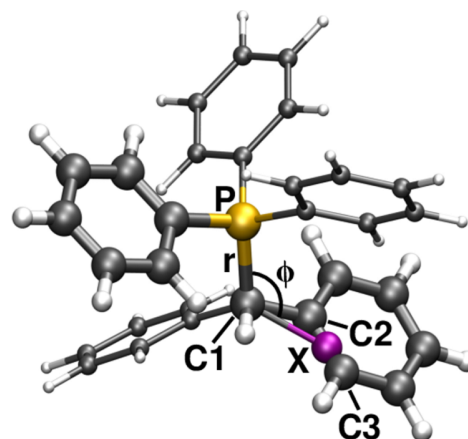


FIG. 1. Optimized structure of $\text{Ph}_2\text{CH-PPH}_3^+$ in its electronic ground state with the dummy atom X and the two chosen coordinates for the QD simulations: the C1-P distance r and the P-C1-X angle ϕ . For the ONIOM calculations (for details see Sec. IV), the thicker drawn phenyl rings constitute the high-level system while the thinner drawn phenyl rings are only contained in the low-level system.

the CoIn. As, by definition, normal modes are only valid in the vicinity of stationary points on the PES, a chemical reaction including bond formation or cleavage far from the Franck-Condon region as considered here cannot be described by a few normal modes.

A. Identification of the major contributions to the relaxation energy

The two reactive internal coordinates r and ϕ only describe the most apparent structural changes during the bond cleavage including the passage through the CoIn. Especially along r important background relaxations take place, primarily in the diphenylmethyl (Ph_2CH) moiety. The major contribution stems from the sp^3 to sp^2 rehybridization at the central methyl carbon atom C1 and the bond length changes associated therewith. Fig. 2(a) illustrates the structural changes of the Ph_2CH moiety (red: unrelaxed, cyan: relaxed). To describe the PES including these background relaxations, first, the energetic stabilization and the structural differences associated with the relaxation are analyzed. Next, the crucial contributions are included into the corresponding coordinates to improve the description of the PES (Sec. III B).

To quantify the overall relaxation energy for the C1–P bond cleavage of $\text{Ph}_2\text{CH–PPh}_3^+$, we follow the process in the ground state.³³ The energy difference between the unrelaxed and the relaxed structures at $r = \infty$ gives the relaxation energy. Its total amount is 1.97 eV at the density functional theory (DFT) level of theory (functional B3LYP/basis set 6-31G(d)). Therefrom 15% (0.30 eV) stem from the relaxation of the leaving group (LG) PPh_3 while the diphenylmethyl cation Ph_2CH^+ accounts for 85% (1.68 eV). The root-mean-square deviation (RMSD)³⁴ between the unrelaxed and the relaxed structures is 0.46 Å for PPh_3 and 0.72 Å for Ph_2CH^+ . At first glance, the small difference in the RMSD values seems to be astonishing compared to the significantly larger difference in the relaxation energies. But a closer look at the nature of the structural changes in both fragments explains these observations. The geometry relaxation of PPh_3 entails rotations of the phenyl rings (see Fig. 2(b)) which result in a relatively small energetic stabilization. In contrast thereto, the most important geometry change in Ph_2CH^+ is the sp^3 to sp^2 rehybridization, which is accompanied by a much larger energetic stabilization.

B. Description of the background relaxation depending on the reactive internal coordinates

As the geometric changes of Ph_2CH^+ are more important for the relaxation energy than the ones of PPh_3 , the focus

lies on Ph_2CH^+ . In good approximation, the relaxation is independent of the angle ϕ and we concentrate solely on the r direction. Along this MEP in the S_0 state, all non-reactive internal coordinates have been analyzed. The changes of the most strongly varying ones were fitted in dependence of r to be able to reconstruct the molecular geometry including background relaxation at any point of the two-dimensional coordinate space $\{r, \phi\}$. First, we discuss the structural changes connected with the sp^3 to sp^2 rehybridization in Ph_2CH^+ .

- The height d_{py} of the C1 pyramid (see inlay of Fig. 4) built by the central methyl carbon atom C1 at the top, the two linked carbon atoms C2 and C8, as well as the H atom (for the atom numbering see Fig. 3) changes during the bond cleavage. It decreases with starting sp^2 hybridization of C1 and its change along r is fitted with a sigmoid function,

$$d_{\text{py}}(r) = a \left(\frac{1}{1 + \exp(-b(r - r_0))} - 1 \right). \quad (3)$$

- The distance between C1 and its attached atoms shortens due to the higher s orbital character in the sp^2 orbitals compared to the sp^3 orbitals. The C1–C2 and C1–C8 bond length modifications are also fitted with a sigmoid function,

$$d_{\text{C1-C2/8}}(r) = c \frac{1}{1 + \exp(-d(r - r_0))} - e. \quad (4)$$

The C1–H distance change was neglected as it varies at most by 0.015 Å.

- The change of the angles α with C1 as central atom (α_{C2C1H} , α_{C2C1C8} , and α_{HC1C8}) is also fitted with the sigmoid function given in Eq. (4).
- In addition, the relative orientation between the two planes of the phenyl rings changes. This change is not symmetric as the LG breaks the symmetry of the Ph_2CH moiety. To model this reorientation, first, the position of the left phenyl ring (Fig. 3) is referenced with respect to the C1 pyramid. Therefore, the angle $\alpha_{\text{ph-C1C8}}$ between the normal vector of the C3C5C7 plane defining the left phenyl ring and the C1–C8 bond has to be fitted analogously to Eq. (4). Next, the relative orientation of both phenyl rings is adapted via the angle between the normal vectors of the planes C3C5C7 (left phenyl ring) and C8C10C12 (right phenyl ring) using the following fit function:

$$\alpha_{\text{ph-ph}}(r) = f \exp(-gr) + \alpha_{\text{ph-ph}}^{\infty}. \quad (5)$$

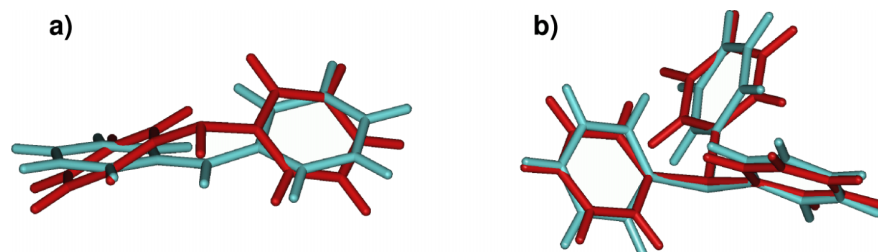


FIG. 2. Unrelaxed (red) and relaxed (cyan) geometry of (a) the diphenylmethyl cation (Ph_2CH^+) and (b) the PPh_3 moiety. The change in hybridization from sp^3 to sp^2 at the central C1 atom of the Ph_2CH^+ can be easily recognized whereas the major differences concerning PPh_3 are rotations of the phenyl rings.

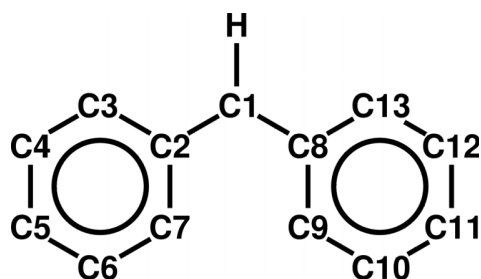


FIG. 3. Structural formula of the Ph_2CH moiety illustrating the numbering of the carbon atoms. The view is taken from the position of the P atom of the PPh_3 LG. For the sake of clarity, the aromatic hydrogen atoms are omitted.

Here, the angle $\alpha_{\text{ph-ph}}^\infty$ is set to the value of the optimized Ph_2CH^+ without further being fitted.

To define the position of the PPh_3 LG three coordinates are necessary. Two of them are the reactive internal coordinates r and ϕ . The third coordinate — the dihedral angle β_{LG} — is defined between P, C1, X, and C3. Its change along the MEP

TABLE I. Fitted parameters of the fit functions given in Eqs. (3)–(6) to describe the relaxation of the carbon backbone of the Ph_2CH moiety and the dihedral angle β_{LG} of the PPh_3 LG along the MEP for the bond cleavage in the ground state. The last column specifies the relative error of the fitted parameters.

Coordinate	Fit function	Fit parameters	Relative error
d_{py}	Equation (3)	$a = (-0.649 \pm 0.005) \text{ \AA}$	0.007
		$b = (2.15 \pm 0.02) \text{ \AA}^{-1}$	0.010
		$r_0 = (2.280 \pm 0.009) \text{ \AA}$	0.004
$d_{\text{C1-C2}}$	Equation (4)	$c = (-0.168 \pm 0.003) \text{ \AA}$	0.02
		$d = (2.07 \pm 0.05) \text{ \AA}^{-1}$	0.02
		$r_0 = (2.17 \pm 0.02) \text{ \AA}$	0.008
$d_{\text{C1-C8}}$	Equation (4)	$c = (-0.192 \pm 0.003) \text{ \AA}$	0.02
		$d = (2.17 \pm 0.04) \text{ \AA}^{-1}$	0.02
		$r_0 = (2.09 \pm 0.02) \text{ \AA}$	0.008
α_{C2C1H}	Equation (4)	$c = (12.4 \pm 0.6)^\circ$	0.05
		$d = (3.6 \pm 0.3) \text{ \AA}^{-1}$	0.07
		$r_0 = (2.06 \pm 0.03) \text{ \AA}$	0.014
α_{C2C1C8}	Equation (4)	$e = (102.3 \pm 0.5)^\circ$	0.005
		$c = (33 \pm 1.4)^\circ$	0.04
		$d = (2.16 \pm 0.08) \text{ \AA}^{-1}$	0.04
α_{HC1C8}	Equation (4)	$r_0 = (1.88 \pm 0.04) \text{ \AA}$	0.02
		$e = (98 \pm 1.4)^\circ$	0.014
		$c = (12.6 \pm 0.7)^\circ$	0.05
$\alpha_{\text{ph-C1C8}}$	Equation (4)	$d = (3.6 \pm 0.3) \text{ \AA}^{-1}$	0.08
		$r_0 = (2.05 \pm 0.03) \text{ \AA}$	0.02
		$e = (102.0 \pm 0.6)^\circ$	0.006
$\alpha_{\text{ph-ph}}$	Equation (4)	$c = (-80 \pm 3)^\circ$	0.04
		$d = (1.83 \pm 0.08) \text{ \AA}^{-1}$	0.05
		$r_0 = (2.14 \pm 0.05) \text{ \AA}$	0.02
β_{LG}	Equation (5)	$e = (94 \pm 3)^\circ$	0.03
		$f = (3.8 \pm 0.2) \cdot 10^{20}$	0.06
		$g = (1.24 \pm 0.03) \text{ \AA}^{-1}$	0.03
β_{LG}	Equation (6)	$h = (-16.7 \pm 1.1) \text{ \AA}^{-1}$	0.07
		$r_0 = (3.45 \pm 0.08) \text{ \AA}$	0.02

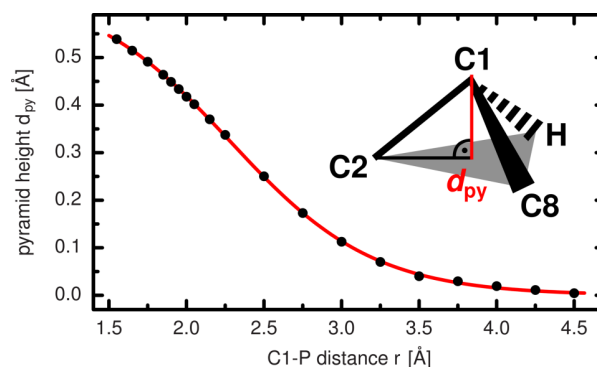


FIG. 4. Change of the height d_{py} (black circles) of the C1 pyramid defined by the atoms C1, C2, C8 and H (inlay) along the ground state MEP for the bond cleavage in $\text{Ph}_2\text{CH} - \text{PPh}_3^+$. The red line depicts the fit function (Eq. (3)) using the parameters listed in Table I.

is fitted with the function

$$\beta_{\text{LG}}(r) = \ln \left(\frac{\exp(-h(r - r_0))}{1 + \exp(-h(r - r_0))} \right) + \beta_{\text{LG}}^{\text{CoIn}}. \quad (6)$$

$\beta_{\text{LG}}^{\text{CoIn}}$ is chosen in a way to optimally reach the geometry of the CoIn in the two-dimensional space.

Table I provides an overview of the fitted parameters. All relative errors lie well below 10% (see last column of Table I). Fig. 4 shows how d_{py} (black circles) changes along the MEP together with the fitted function (red line; Eq. (3)). The larger r , the lower is the height d_{py} , reflecting the rehybridization from sp^3 to sp^2 . Around $r = 4.0\text{--}4.5 \text{ \AA}$, the methyl C1 atom is almost fully planarized. In the optimized Ph_2CH^+ fragment, d_{py} takes a value of $5 \cdot 10^{-5} \text{ \AA}$.

The selection of the reactive internal coordinates r and ϕ reduces the full dimensional configuration space and the PESs become a function of $V(r, \phi; n = \text{const})$ with n being the non-reactive coordinates. With the fitted non-reactive coordinates, which describe the background relaxation along r at hand, the relaxed structure of the Ph_2CH moiety can be reconstructed at any point of the two-dimensional coordinate space $\{r, \phi\}$. The configuration space is still two-dimensional, but now it contains the background relaxation and the PESs are a function of $V(r, \phi; n(r))$. The combination of the reactive internal coordinates with the fitted non-reactive ones forms the adapted reactive coordinates aRCs.

In general, the behavior of the non-reactive coordinates n which describes the background relaxation may depend on all selected reactive internal coordinates. There are three different scenarios possible which increase the complexity of the employed fit functions and thus of the fitting procedure. In the first case, the complete relaxation depends only on one reactive internal coordinate and the fit functions are only one-dimensional. In scenario two which encompasses an increased complexity, the relaxation depends on multiple reactive internal coordinates but no coupling occurs. Consequently, one-dimensional fit functions are still sufficient but the dependencies of the non-reactive coordinates on all reactive internal coordinates have to be evaluated. In the present example, this would lead to PESs depending on $V(r, \phi; n(r), n'(\phi))$. The most complex scenario occurs when the behavior of the non-reactive coordinates can only

be described by two-dimensional fit functions due to their intricate linkage with the reactive internal coordinates. The PESs are then a function of $V(r, \phi; n(r, \phi))$. Our example belongs to the first scenario but in principle the approach to generate aRCs is applicable to all three scenarios.

The fitted non-reactive coordinates are not linearly independent; thus, the order in which they are adjusted is important to guarantee a proper reconstruction. One example is d_{py} (Fig. 4, inlay). It is easier to adjust the bond lengths $d_{\text{C1-C2}}$ and $d_{\text{C1-C8}}$ before the adjustment of d_{py} . A reversed order will change d_{py} again, unless an additional constraint is introduced. The protocol of the reconstruction is visualized in Fig. 5. After loading the S_0 minimum geometry, the chosen C1–P distance r determines the adjustment of the background relaxation. First, the distances between the methyl C1 atom and both phenyl rings $d_{\text{C1-C2}}$ and $d_{\text{C1-C8}}$ are adjusted, followed by the height d_{py} . Then the angles α_{C2C1H} , α_{C2C1C8} , and α_{HC1C8} are adapted. Thereby it is sufficient to match only two of the three angles, i.e., α_{C2C1H} and α_{HC1C8} in the present case. Here, an iterative procedure with the normal vector of the C2–C8–H plain as rotational axis and C1 in the origin is applied. Otherwise, the rotation would affect the pyramidalization. The next step is to match the relative orientation of both

phenyl rings which is realized via $\alpha_{\text{ph-C1C8}}$ and $\alpha_{\text{ph-ph}}$. Again, an iterative procedure is used. To adjust $\alpha_{\text{ph-C1C8}}$ the left phenyl ring in Fig. 3 is rotated with C1C2 as rotational axis. In the case of $\alpha_{\text{ph-ph}}$, the right phenyl ring is rotated around the C1C8 axis. Before finally the PPh₃ moiety can be positioned according to r , ϕ , and β_{LG} , the RMSD between the relaxed and the loaded Ph₂CH moiety has to be minimized.³⁴ This corresponds to fulfill the Eckart conditions.

The relaxation energy covered by the reconstructed Ph₂CH moiety is 1.56 eV which is 93% of the 1.68 eV obtained from the optimization. The RMSD between the reconstructed and the optimized Ph₂CH is 0.087 Å which means that the initial RMSD is reduced by 88%. Although 12% of the initial RMSD remains, only 7% of the initial relaxation energy is not covered. This implies that the energetically most important backbone motions are included in the aRCs. The covered fraction of the total relaxation energy of both fragments is still 79% due to the fact that the geometry of the PPh₃ LG is not adapted.

IV. POTENTIAL ENERGY OPERATOR IN ADAPTED REACTIVE COORDINATES

The specially designed aRCs satisfactorily include background relaxation and efficiently describe relaxed geometries in the multidimensional configuration space. They open a way to economically compute PESs with approximately relaxed structures via single point calculations. Regardless of the chosen level of theory for the quantum chemical calculations, the computational time is significantly reduced as no partial optimizations are required. Here, we apply the procedure to the PESs for the ground state S_0 and the first excited state S_1 . Due to the complexity of the system also in the electronic structure, the PESs are evaluated at the “our own n-layered integrated molecular orbital and molecular mechanics” (ONIOM) level of theory using the constraint low-level state approximation.^{35–38} The molecular structures were constructed following the procedure displayed in Fig. 5 and single point calculations were performed. The high-level system phenylmethylphenylphosphonium ion (PhCH₂–PH₂Ph⁺) contains the thicker drawn phenyl rings in Fig. 1. It was calculated at the CASSCF(10,10) level of theory using the program package Molpro.³⁹ The thinner drawn phenyl rings were only part of the low-level system and replaced by H atoms in the high-level system. The low-level system was calculated at the DFT (M06-2X⁴⁰) level of theory using Gaussian09.⁴¹ The setup of the high-level system as well as the active space of the complete active space self consistent field (CASSCF) calculations has been carefully tested beforehand.³³ Throughout all calculations the basis set 6-31G(d) was used.

The resulting PESs for S_0 and S_1 are depicted in Fig. 6. The minimum of the ground state is located at $r = 1.9$ Å and $\phi = 125^\circ$ (see Fig. 6(a)). The first excited state exhibits a local minimum next to the Franck-Condon point recognizable in Fig. 6(b). A small barrier separates this minimum from the dissociative area of the S_1 PES. A large gradient mainly in r direction leads to a gain of potential energy of about 2.0 eV during the dissociation process.

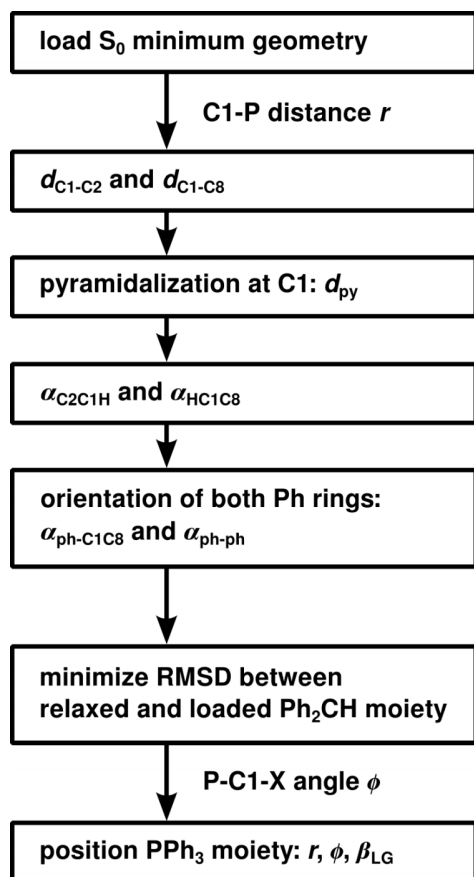


FIG. 5. Flowchart for the construction of the relaxed Ph₂CH–PPh₃⁺ geometry at any point of the two-dimensional coordinate space $\{r, \phi\}$. After loading the S_0 minimum geometry, the carbon backbone of the Ph₂CH moiety is relaxed using the parameters given in Table I. Finally, the PPh₃ moiety is positioned after minimization of the RMSD between the relaxed and the loaded Ph₂CH fragment.

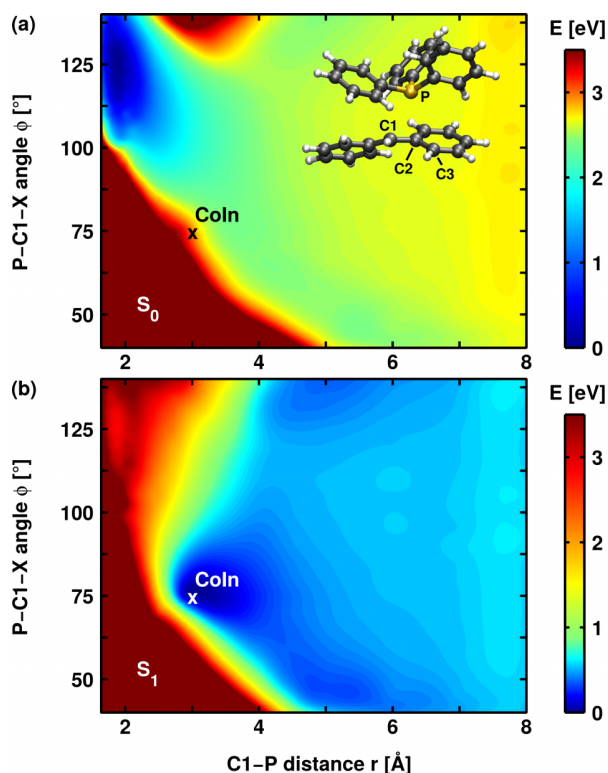


FIG. 6. Molecular PESs of $\text{Ph}_2\text{CH-PPh}_3^+$ calculated at the ONIOM level of theory. The data were interpolated to the spatial grid used for the QD simulations presented in Sec. VI. (a) The ground state potential S_0 has its minimum at $r = 1.9 \text{ \AA}$ and $\phi = 125^\circ$. The inset displays the structure of the S_1/S_0 CoIn of the full system $\text{Ph}_2\text{CH-PPh}_3^+$. (b) The excited state potential S_1 shows a local minimum in the Franck-Condon region. Its global minimum lies next to the S_1/S_0 CoIn at $r = 2.9 \text{ \AA}$ and $\phi = 75^\circ$. Note that the minimum of each surface is set to zero separately.

The global minimum of the S_1 surface lies in the vicinity of a S_1/S_0 CoIn. Its presence within the PES confirms the success of the reactive coordinate choice because the angular coordinate ϕ was chosen in a way that the CoIn is included in the two-dimensional coordinate space. The CoIn is located at $r = 2.9 \text{ \AA}$ and $\phi = 75^\circ$, the point of minimal energy difference ($\Delta E = 0.085 \text{ eV}$) between S_1 and S_0 at the ONIOM level of theory. The structure of the marked S_1/S_0 CoIn is presented in the inset of Fig. 6(a) and is similar to the S_1/S_0 CoIn optimized for the high-level system $\text{PhCH}_2\text{-PPh}_2^+$.³³

Without the background relaxation, the energy gain during the bond cleavage in the S_1 state would be reduced by about 75% (1.56 eV). Thus the gradient would decrease significantly and the dynamics of the bond cleavage would be considerably slower. Also it is not guaranteed that the CoIn would be energetically reachable from the Franck-Condon region.

V. KINETIC ENERGY OPERATOR IN ADAPTED REACTIVE COORDINATES

A. The Wilson G-matrix formalism

The G-matrix formalism introduced by B. Podolsky opens a way to reformulate the kinetic energy operator \hat{T}_x (Eq. (2))

in arbitrary internal coordinates.^{25,26,31} The coordinate transformation can be formulated with the help of the matrix elements $(J^{-1})_{ri}$ of the inverse of the Jacobian matrix \mathbf{J} ,

$$q_r = \sum_{i=1}^{3N} (J^{-1})_{ri} x_i \quad \text{with} \quad (J^{-1})_{ri} = \frac{\partial q_r}{\partial x_i}. \quad (7)$$

Using the Jacobian determinant $j = \det |\mathbf{J}|$ the kinetic energy operator \hat{T}_q can be formulated in internal coordinates,^{26,31} in our case aRCs,

$$\hat{T}_q = -\frac{\hbar^2}{2} \sum_{r=1}^{3N} \sum_{s=1}^{3N} j^{-\frac{1}{2}} \frac{\partial}{\partial q_r} \left[j G_{rs} \frac{\partial}{\partial q_s} j^{-\frac{1}{2}} \right]. \quad (8)$$

The elements G_{rs} of the G-matrix are calculated according to

$$G_{rs} = \sum_{i=1}^{3N} \frac{1}{m_i} \frac{\partial q_r}{\partial x_i} \frac{\partial q_s}{\partial x_i}. \quad (9)$$

In principle, the Jacobian determinant j as well as the G-matrix \mathbf{G} is position-dependent. Assuming that the change of j with respect to $\{q\}$ is negligible compared to the position dependence of \mathbf{G} , Eq. (8) can be simplified,⁴²

$$\hat{T}_q \approx -\frac{\hbar^2}{2} \sum_{r=1}^{3N} \sum_{s=1}^{3N} \frac{\partial}{\partial q_r} \left[G_{rs} \frac{\partial}{\partial q_s} \right]. \quad (10)$$

In practice, if the matrix elements $(J^{-1})_{ri}$ are unknown, \mathbf{G} is usually calculated via its inverse \mathbf{G}^{-1} , which has the following elements:⁴²

$$(G^{-1})_{rs} = \sum_{i=1}^{3N} m_i \frac{\partial x_i}{\partial q_r} \frac{\partial x_i}{\partial q_s}. \quad (11)$$

To yield the inverse elements, the partial derivatives are reversed, which makes them much easier to be calculated compared to the normal G-matrix elements G_{rs} . Especially in the case of reduced dimensionality, it is now possible to use the finite differences method. The molecular system can be displaced slightly along the aRCs and the actual atomic positions can be written in Cartesian coordinates. After fulfilling the Eckart conditions⁴³ which provide for the three rotational and three translational degrees of freedom being separated from the internal coordinates, the elements of \mathbf{G}^{-1} can be calculated.⁴² To fulfill the Eckart conditions, a method proposed by A. Y. Dymarsky and K.N. Kudin is used.^{34,44,45} Subsequent inversion of \mathbf{G}^{-1} yields the desired G-matrix \mathbf{G} . In the case of linear coordinates q_i , the G-matrix is position independent whereas it becomes position dependent for non-linear q_i . The latter is true here. As the coordinates do not change during the QD simulations, the elements of the G-matrix can be calculated and analyzed beforehand (cf. Secs. V B and V C). The diagonal elements of the G-matrix can be interpreted as the effective inverse reduced mass which may change along the coordinate. Due to the multiplication with $\left(\frac{\partial q_r}{\partial x_i}\right)^2$ in Eq. (9), the position dependence encodes information about the actual mass which moves along the internal coordinate. The off-diagonal elements contain information about the kinetic coupling between the coordinates.

So far, the G-matrix is formulated for the complete $(3N - 6)$ dimensional internal coordinate space plus the

rotational and translational degrees of freedom. If a reduced number of reactive internal coordinates is used — as it is often the case — the matrix \mathbf{G} can be blocked leading to the following structure:⁴⁶

$$\mathbf{G} = \begin{pmatrix} \mathbf{G}_{\text{active}} & \mathbf{G}_{\text{coupling}} \\ \mathbf{G}_{\text{coupling}} & \mathbf{G}_{\text{inactive}} \end{pmatrix}, \quad (12)$$

with $\mathbf{G}_{\text{active}}$ being the block of the considered active coordinates, $\mathbf{G}_{\text{inactive}}$ the one with the not considered inactive coordinates, and the coupling block $\mathbf{G}_{\text{coupling}}$. Assuming no coupling between the active and inactive coordinates, it is sufficient to calculate the inverse of $\mathbf{G}_{\text{active}}$, as the diagonal blocks of the matrix can be inverted separately. In the present work, we use this assumption and take into account only the active coordinates, i.e., the aRCs.

Finally, let us take a look on the requirements for the G-matrix method. The first two are that the internal coordinates $\{q\}$ are linearly independent³¹ and that the coordinate transformation is bijective.⁴⁷ The common set of $(3N - 6)$ internal coordinates, which is used to specify a molecular geometry in the Z-matrix format, namely, distances, angles, and dihedral angles, is usually chosen in a way that they are linearly independent. In case of $\{q\}$ containing linear combinations of these distances, angles, or dihedral angles, like in the aRCs, they have to be constructed as linearly independent. The second requirement is ensured by fulfillment of the Eckart conditions. A third requirement of more technical nature is a smooth behavior of the atomic motion along the internal coordinates $\{q\}$. This is in general the case as long as reactive internal coordinates are used without taking into account background relaxations of the non-reactive coordinates. However, for a better description of the investigated process, relaxed PESs obtained via optimizations are often more appropriate. This leads to more intricate atomic movements. As the optimizations are performed independently, no correlations between the resulting structures exist. This can lead to sudden changes of the displacement vectors connecting neighboring optimized structures and immediately problems arise during the calculation of the G-matrix because the derivatives in Eq. (11) are not continuous any more. A conceivable scenario could be the sudden change of a dihedral angle during a relaxed scan of an angular coordinate. One way to omit these problems is to use the aRCs described in Sec. III. They allow to include the background relaxation into the potential as well as the kinetic energy operator on equal footing.

B. Shape of the G-matrix elements

The G-matrix is evaluated for the two aRCs r and ϕ for the bond cleavage of $\text{Ph}_2\text{CH} - \text{PPh}_3^+$. Fig. 7 illustrates the shape of the three matrix elements G_{rr} , $G_{r\phi}$ and $G_{\phi\phi}$. The off-diagonal elements $G_{r\phi}$ and $G_{\phi r}$ are identical as \mathbf{G} is symmetric. As expected, G_{rr} and $G_{\phi\phi}$ have a positive sign (cf. Eq. (9)). In contrast, the coupling element $G_{r\phi}$ is mostly negative along the evaluated two-dimensional coordinate space $\{r, \phi\}$.

In the range of $1.7 \text{ \AA} \leq r \leq 4 \text{ \AA}$, the matrix element G_{rr} shown in (a) reveals three maxima which become

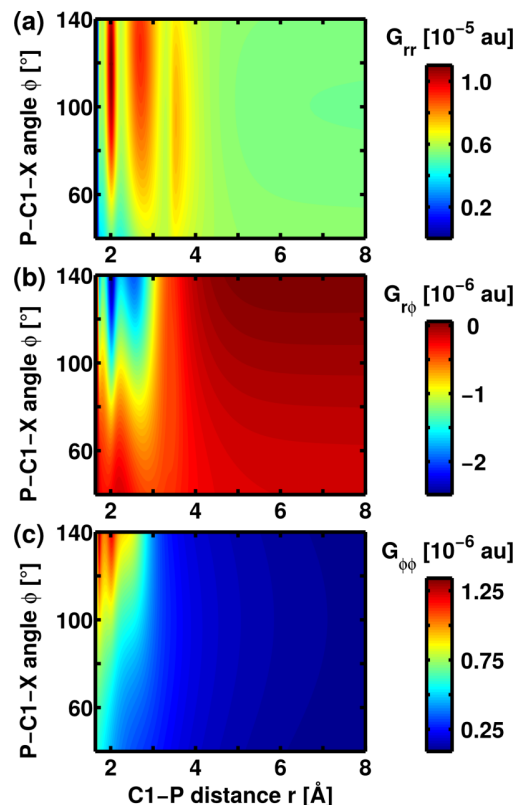


FIG. 7. G-matrix elements for the two-dimensional coordinate space $\{r, \phi\}$. The first diagonal element G_{rr} is depicted in (a), the off-diagonal element $G_{r\phi}$ in (b), and the second diagonal element $G_{\phi\phi}$ in (c). As the matrix is symmetric, both off-diagonal elements $G_{r\phi}$ and $G_{\phi r}$ are identical.

more pronounced with increasing P-C1-X angle ϕ . The first maximum is the highest and the second one has the broadest shape. For $r > 4 \text{ \AA}$ G_{rr} becomes constant.

The off-diagonal element $G_{r\phi}$ specifies the kinetic coupling between r and ϕ (see Fig. 7(b)). Its absolute value is smaller by about a factor of five compared to G_{rr} . In the area of $2 \text{ \AA} \leq r \leq 4 \text{ \AA}$, two minima occur which again become more pronounced for larger ϕ values. For $r > 4 \text{ \AA}$, $G_{r\phi}$ approaches zero ($|G_{r\phi}| < 10^{-7}$ a.u.) meaning that the kinetic coupling decreases significantly.

The second diagonal element $G_{\phi\phi}$ shown in Fig. 7(c) is smaller by about a factor of 10 compared to G_{rr} . For $r < 3 \text{ \AA}$, it is faintly structured showing two maxima for $\phi > 100^\circ$. For $r > 4 \text{ \AA}$, the matrix element $G_{\phi\phi}$ levels off below 10^{-7} a.u.

C. Relation between background relaxation and shape of the G-matrix elements

To analyze how the shape of the G-matrix elements along the two-dimensional coordinate space $\{r, \phi\}$ is linked to the background relaxation, we switch off parts of the relaxation process. By skipping the corresponding steps during the reconstruction shown in Fig. 5, we obtain the respective G-matrices and can analyze their changes. Thereto, we divided the reconstruction of Ph_2CH into three parts: the first part is rehybridization of C1 including the adaption of $d_{\text{C1-C2}}$, $d_{\text{C1-C8}}$, d_{py} , α_{C2C1H} , and α_{HC1C8} . The second one contains the relative

orientation of both phenyl rings by adapting $\alpha_{\text{ph-C1C8}}$ and $\alpha_{\text{ph-ph}}$ and the third part is the adjustment of β_{LG} , the third coordinate of the PPh_3^+ LG.

Fig. 8 depicts the G-matrix elements G_{rr} (a), $G_{r\phi}$ (b), and $G_{\phi\phi}$ (c) along the C1–P distance r for a fixed value of $\phi = 125^\circ$ including different parts of the background relaxation: no relaxation (green dashed-dotted line), relaxation around C1 (blue shortly dashed line), relaxation around C1 and relative orientation of both phenyl rings (black dotted line), adaption of β_{LG} (orange dashed line), and complete relaxation (red solid line). The first point attracting attention is that for all three matrix elements, the modulations in the range up to $r = 4 \text{ \AA}$ disappear without the relaxation. Thus they are a signature of the background relaxation and only occur for shorter C1–P distances. For larger distances, the relaxation is completed (see, e.g., Fig. 4).

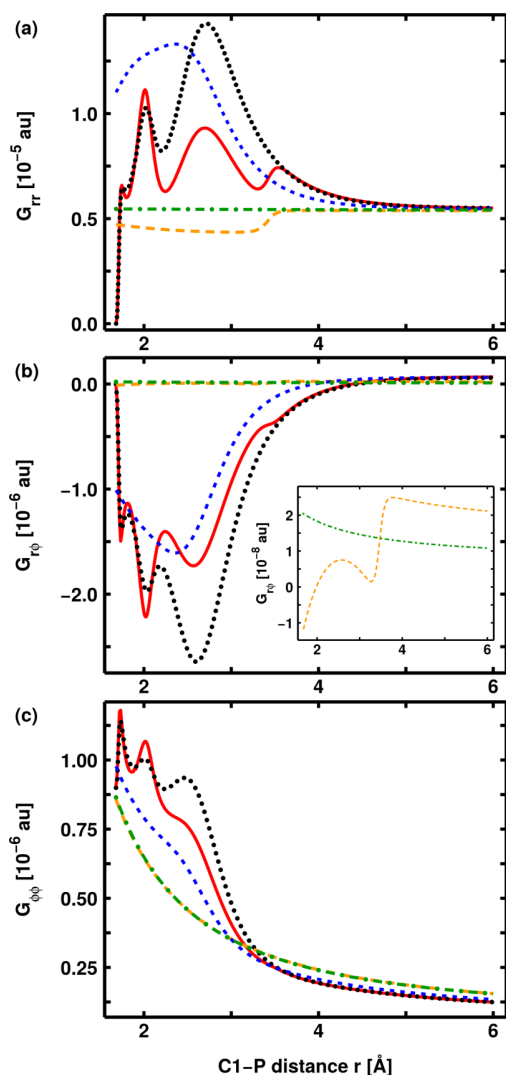


FIG. 8. G-matrix elements G_{rr} (a), $G_{r\phi}$ (b), and $G_{\phi\phi}$ (c) depicted along the C1–P distance r for a fixed value of $\phi = 125^\circ$. The curves illustrate the influence of the different parts of the background relaxation on the G-matrix elements: no relaxation (green dashed-dotted line), relaxation around C1 (blue shortly dashed line), relaxation around C1 and relative orientation of both phenyl rings (black dotted line), adaption of β_{LG} (orange dashed line), and full relaxation (red solid line).

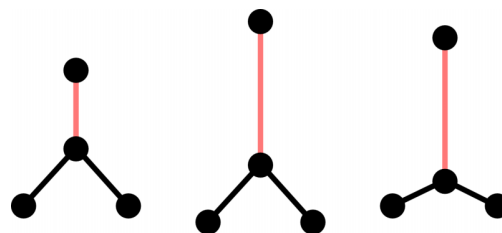


FIG. 9. Schematic illustration of the influence of the background relaxation on the net atomic movements. Starting from the initial structure (left) the red bond is elongated by the same amount for the structures in the middle and on the right side, respectively. In addition, the Eckart conditions are fulfilled. Without any relaxation (middle), the whole triatomic fragment moves, whereas with the relaxation (right) the lower two atoms of the triatomic fragment keep their position.

The diagonal element G_{rr} (Fig. 8(a)) without any relaxation (green dashed-dotted line) is constant as expected, since in this case r is a linear coordinate. Relaxation around C1 leads to an increase of G_{rr} by a maximum factor of more than two with one pronounced maximum at $r = 2.5 \text{ \AA}$ (blue shortly dashed line). Fig. 9 schematically illustrates the scenario. Starting from the initial structure (left), the red bond is elongated by the same amount for the two other structures always fulfilling the Eckart conditions. Without any relaxation (middle), the whole triatomic fragment moves, with relaxation (right) only the central atom of the triatomic fragment moves while the lower two atoms keep their position. This results in different masses for the motion of the triatomic fragment. In the case of no relaxation, the whole mass of the triatomic fragment has to be taken into account while with relaxation only the mass of the central atom is relevant. Accordingly, the G-matrix elements containing the inverse reduced mass are larger with relaxation than without (cf. Eq. (9)). The maximum of G_{rr} is reached for the turning point of the sigmoid function for d_{py} (see Fig. 4). For further elongation of the red bond, the entire triatomic fragment starts to move also in the case with relaxation and as a consequence the G-matrix element decreases again.

Relaxation of the relative orientation of both phenyl rings in addition to the C1 rehybridization (black dotted line) introduces more structure. Now two maxima appear at about 2.0 \AA and 2.8 \AA . This reflects the complexity of the motion during the reorientation of the phenyl rings and the C1 rehybridization. For $r < 1.7 \text{ \AA}$ G_{rr} drops to a value of less than 10^{-7} a.u. If only the dihedral angle β_{LG} of the PPh_3^+ LG is taken into account (orange dashed line), a slight decrease of G_{rr} is observed compared to the case without any relaxation as an additional motion occurs. Finally, considering the full relaxation (red solid line), the three pronounced maxima for $r < 4 \text{ \AA}$ already identified in Fig. 7(a) reappear. The one located at $r = 3.5 \text{ \AA}$ can be traced back to β_{LG} , while the other two at $r = 2.7 \text{ \AA}$ and $r = 2.0 \text{ \AA}$ occur due to the phenyl ring orientation. Altogether, the order of magnitude of G_{rr} is maintained if the background relaxation is taken into account.

Without any relaxation, the off-diagonal element $G_{r\phi}$ (Fig. 8(b)) is smaller by more than two orders of magnitude. Inclusion of the relaxation around C1 results in negative values with a minimum at 2.5 \AA whose absolute value is

almost enlarged by a factor of 100. Again, an additional consideration of the phenyl ring orientation introduces more structure. Here, three local minima occur; the positions of the two outermost are comparable to the maxima of G_{rr} . If only the dihedral angle β_{LG} is adapted, $G_{r\phi}$ stays almost unchanged compared to no relaxation. The inlay of Fig. 8(b) shows that there are still slight changes which are about two orders of magnitude smaller than for the other background motions. Taking all relaxation processes into account leads to a $G_{r\phi}$ exhibiting three local minima. The overall decrease occurs due to the C1 rehybridization while its modulations can be traced back to the adjustment of the phenyl ring orientation. The position of the small shoulder at $r = 3.5$ Å corresponds to the step caused by β_{LG} (cf. inlay Fig. 8(a)). The consideration of all background motions increases the absolute value of the off-diagonal element $G_{r\phi}$ by a factor of more than 120. Thus, it affects the kinetic coupling term much more than the diagonal element G_{rr} .

Fig. 8(c) depicts the second diagonal element $G_{\phi\phi}$. Without any relaxation, it exhibits an r dependence as ϕ is a non-linear coordinate. Including the relaxation around C1 introduces only moderate changes, especially, in comparison to the other two elements. Further adaption of the phenyl ring orientation introduces the three maxima, which appear at similar positions as the three minima of $G_{r\phi}$. The almost negligible changes of $G_{\phi\phi}$ if β_{LG} is adapted are in the same range as for the off-diagonal element $G_{r\phi}$. The entire background relaxation leads to two local maxima at $r = 1.7$ Å and $r = 2.0$ Å as well as a shoulder at $r = 2.5$ Å. Its effect on the magnitude of $G_{\phi\phi}$ is less important compared to the one on G_{rr} , which might be due to the relaxation being completely included in the r coordinate.

VI. QUANTUM DYNAMICS WITH AND WITHOUT ADAPTED REACTIVE COORDINATES INCLUDED IN THE KINETIC ENERGY OPERATOR

In this section, we apply the Wilson G-matrix taking into account the complete background relaxation in QD simulations for the excited state bond cleavage of $\text{Ph}_2\text{CH}-\text{PPh}_3^+$ ions. In addition, we compare the results with simulations where no relaxation has been taken into account for the G-matrix. The mechanism of the bond cleavage has only recently been clarified.^{6,29,30} For the generation of the experimentally observed Ph_2CH^+ ,²⁷ the system relaxes to the S_0 state through the S_1/S_0 CoIn (cf. Fig. 6).³³ With the help of QD simulations employing the here described potential and kinetic energy operators, we could show that only the dynamic effect of the solvent environment enables the wave packet to reach the CoIn. The simulated emergence of Ph_2CH^+ within roughly 400 fs^{6,29} is in good agreement with the experimentally observed initial rise of the Ph_2CH^+ absorption signal.²⁷

To demonstrate the impact of the relaxation in the G-matrix on the wave packet dynamics more clearly, we first discuss the excited state bond cleavage in the gas phase without the dynamic effect of the solvent. In addition, we present simulations where the solvent is taken into account applying our recently developed dynamic continuum ansatz.⁶

The QD simulations have been performed using a homemade program numerically solving the time-dependent Schrödinger equation on a regular space grid employing the Chebychev propagation scheme.⁴⁸ The grid size was $r \in [1.65 \text{ Å}, 8.00 \text{ Å}]$ and $\phi \in [40^\circ, 140^\circ]$ for the normal simulation with 2048×1024 grid points in r and ϕ , respectively. When the dynamic continuum ansatz was applied, the range of the r coordinate was reduced to $r \in [1.65 \text{ Å}, 6.00 \text{ Å}]$ using 1024×512 grid points. The time step was 200 a.u. for the normal simulation and 2 a.u. for the simulation with the dynamic continuum ansatz, respectively. The eigenfunction of the vibrational ground state in S_0 was calculated via propagation in imaginary time.⁴⁹

Fig. 10 shows the S_1 potential together with exemplary snapshots of the wave packet simulated without (a) and with (b) the dynamic continuum ansatz. The white isolines depict snapshots from the simulation with no background relaxation taken into account in the G-matrix; the black isolines show snapshots from the simulation including the background relaxation. First, we focus on the simulations in the gas phase (Fig. 10(a)). Two snapshots of each QD propagation are shown: one at 145 fs (solid isolines) and one at 290 fs (dashed isolines) after starting the wave packet in the Franck-Condon region. The difference between both simulations is clearly

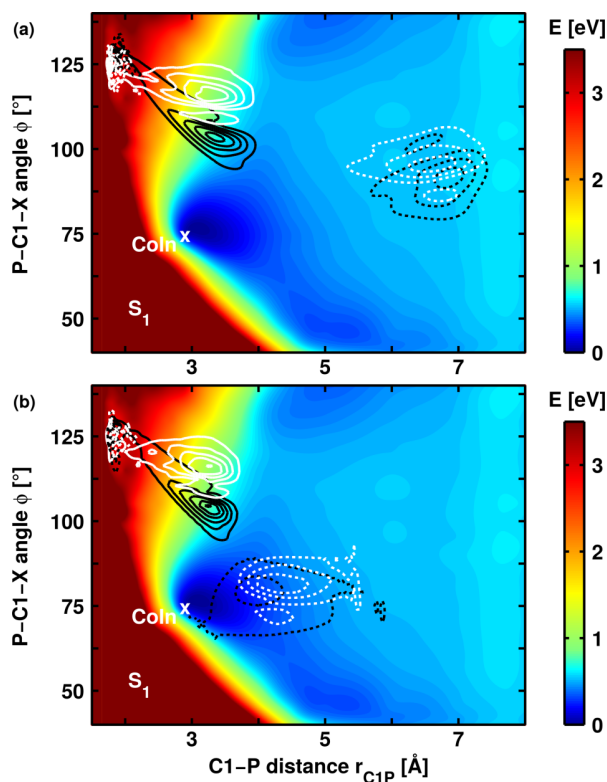


FIG. 10. PES of the S_1 state together with exemplary snapshots of the wave packet simulated (a) without and (b) with the dynamic continuum ansatz. The white isolines depict snapshots from the simulation without background relaxation considered in the G-matrix; the black isolines show snapshots from the simulation including the background relaxation. (a) The snapshots were taken 145 fs (solid isolines) and 290 fs (dashed isolines) after the wave packet has started in the Franck-Condon region. (b) The snapshots were taken 145 fs (solid isolines) and 375 fs (dashed isolines) after the wave packet has started.

visible. In the case of the G-matrix without relaxation (white), the wave packet moves less in ϕ direction. It follows more strictly the gradient of the PES which is mainly oriented toward increasing r behind the barrier in the Franck-Condon region. As the absolute value of the off-diagonal element $G_{r\phi}$ which describes the coupling between both coordinates is smaller without relaxation (cf. Fig. 8(b)), less kinetic energy is transferred from r to ϕ . Thus, the motion of the wave packet is more restricted to the r direction. Nevertheless, in both cases, the wave packet misses the CoIn.

The same difference between both simulations occurs if the dynamic effect of the solvent is taken into account (Fig. 10(b)). The snapshots are taken 145 fs (solid isolines) and 375 fs (dashed isolines) after starting the propagation in the Franck-Condon region. Again the white wave packet moves less in ϕ compared to the black one. But here, the wave packet is decelerated due to the solvent cage and follows the small gradient along decreasing ϕ . Thus, it reaches the CoIn where it can relax to the S_0 state. As a large angular motion is necessary to reach the CoIn, both G-matrices lead to different propagation times to reach the vicinity of the CoIn. This can be seen in the second snapshot (dashed isolines). To estimate the time when the first Ph_2CH^+ cations are generated, we integrated the probability density $\Psi^* \cdot \Psi$ in the area around the CoIn $r \in [2.68 \text{ \AA}, 3.12 \text{ \AA}]$ and $\phi \in [70^\circ, 80^\circ]$ and chose 1.0% as lower threshold. In the case of the G-matrix including the background relaxation, this value is reached for the first time after 390 fs whereas it takes 680 fs without relaxation. These results show that scenarios exist for which it is important to take into account the background relaxation also in the kinetic energy operator, e.g., via the G-matrix formalism.

VII. SUMMARY

We presented a new strategy to design adapted reactive coordinates (aRCs) using the ultrafast bond cleavage of $\text{Ph}_2\text{CH}-\text{PPh}_3^+$ as an example.^{27,28} In order to perform QD simulations in reduced dimensionality,^{6,29} reactive coordinates including background relaxation are developed. First, the most important reactive internal coordinates for the description of the reaction — two in our case — are identified. Second, the major changes of the non-reactive coordinates during the relaxation are extracted. In our example, this is the sp^3 to sp^2 rehybridization of the methyl carbon atom C1 linking the two phenyl rings which almost exclusively takes place along one coordinate, namely, the C1-P distance r . With this information at hand, the changes of the non-reactive coordinates along the reactive internal coordinates can be fitted based on the MEP in the third step. The subsequent combination of the reactive internal coordinates with the fitted non-reactive ones yields the aRCs. On their basis, relaxed molecular geometries can be included in the dynamics without explicit energy optimization.

Two key advantages come along with our strategy to deduce aRCs. First, the necessary computing time to obtain an approximately relaxed PES can be drastically reduced. Due to the ability to construct approximately relaxed molecular geometries, only single point calculations are required instead of optimizations for each point. Second, the corresponding kinetic energy operator is realizable via the

G-matrix formalism. Thereby, the background relaxation can be included into the potential as well as the kinetic energy operator on equal footing. The aRCs prevent the occurrence of unphysical artifacts in the G-matrix. In addition, they enable a detailed analysis of the shape of the G-matrix elements. Its changes reflect how the background relaxation influences the kinetic energy operator in reduced dimensions.

We demonstrated the impact of the background relaxation within the kinetic energy operator on QD simulations by a comparison of simulations using the aRCs or the reactive internal coordinates in the G-matrix. The results clearly illustrate the importance to take into account the relaxation of the non-reactive coordinates as in the example of $\text{Ph}_2\text{CH}-\text{PPh}_3^+$, the propagation time until the CoIn is reached differs by 74% (280 fs).

Our new approach opens a valuable way to economically compute multi-dimensional potential and kinetic energy operators including background relaxation on equal footing when required for QD simulations. Moreover, we showed that considering the background relaxation in the kinetic energy operator changes the results of QD simulations. In our example, we observed quantitative changes, in different scenarios even qualitative changes may emerge.

ACKNOWLEDGMENTS

Financial support by the Deutsche Forschungsgemeinschaft through the SFB749 and the excellence cluster Munich-Centre for Advanced Photonics (MAP) is acknowledged. We thank Julius Zauleck for fruitful discussions.

- ¹C. Gollub, M. Kowalewski, S. Thallmair, and R. de Vivie-Riedle, *Phys. Chem. Chem. Phys.* **12**, 15780 (2010).
- ²P. von den Hoff, S. Thallmair, M. Kowalewski, R. Siemering, and R. de Vivie-Riedle, *Phys. Chem. Chem. Phys.* **14**, 14460 (2012).
- ³M. Saab, L. J. Doriol, B. Lasorne, S. Guérin, and F. Gatti, *Chem. Phys.* **442**, 93 (2014).
- ⁴D. Keefer, S. Thallmair, J. P. P. Zauleck, and R. de Vivie-Riedle, *J. Phys. B: At., Mol. Opt. Phys.* **48**, 234003 (2015).
- ⁵A. Hofmann and R. de Vivie-Riedle, *Chem. Phys. Lett.* **346**, 299 (2001).
- ⁶S. Thallmair, M. Kowalewski, J. P. P. Zauleck, M. K. Roos, and R. de Vivie-Riedle, *J. Phys. Chem. Lett.* **5**, 3480 (2014).
- ⁷D. Geppert, L. Seyfarth, and R. de Vivie-Riedle, *Appl. Phys. B: Lasers Opt.* **79**, 987 (2004).
- ⁸S. Thallmair, R. Siemering, P. Kölle, M. Kling, M. Wollenhaupt, T. Baumert, and R. de Vivie-Riedle, in *Molecular Quantum Dynamics—From Theory to Applications*, edited by F. Gatti (Springer-Verlag, 2014), pp. 213–248.
- ⁹M. Beck, A. Jäckle, G. Worth, and H.-D. Meyer, *Phys. Rep.* **324**, 1 (2000).
- ¹⁰*Multidimensional Quantum Dynamics: MCTDH Theory and Applications*, edited by H.-D. Meyer, G. A. Worth, and F. Gatti (Wiley-VCH Verlag GmbH & Co. KGaA, Weinheim, Germany, 2009).
- ¹¹H.-D. Meyer, *WIREs: Comput. Mol. Sci.* **2**, 351 (2012).
- ¹²M. Barbatti, *WIREs: Comput. Mol. Sci.* **1**, 620 (2011).
- ¹³W. H. Miller, N. C. Handy, and J. E. Adams, *J. Chem. Phys.* **72**, 99 (1980).
- ¹⁴E. Kraka, *WIREs: Comput. Mol. Sci.* **1**, 531 (2011).
- ¹⁵M. Kowalewski, J. Mikosch, R. Wester, and R. de Vivie-Riedle, *J. Phys. Chem. A* **118**, 4661 (2014).
- ¹⁶C. Iung and F. Gatti, *Int. J. Quantum Chem.* **106**, 130 (2006).
- ¹⁷F. Gatti and C. Iung, *Phys. Rep.* **484**, 1 (2009).
- ¹⁸L. Joubert-Doriol, B. Lasorne, F. Gatti, M. Schröder, O. Vendrell, and H.-D. Meyer, *Comput. Theor. Chem.* **990**, 75 (2012).
- ¹⁹E. V. Gromov, A. B. Trofimov, F. Gatti, and H. Köppel, *J. Chem. Phys.* **133**, 164309 (2010).
- ²⁰D. Geppert, A. Hofmann, and R. de Vivie-Riedle, *J. Chem. Phys.* **119**, 5901 (2003).

- ²¹B. P. Fingerhut, D. Geppert, and R. de Vivie-Riedle, *Chem. Phys.* **343**, 329 (2008).
- ²²A. Hofmann and R. de Vivie-Riedle, *J. Chem. Phys.* **112**, 5054 (2000).
- ²³B. Reischl, R. de Vivie-Riedle, S. Rutz, and E. Schreiber, *J. Chem. Phys.* **104**, 8857 (1996).
- ²⁴A. Markmann, G. A. Worth, S. Mahapatra, H.-D. Meyer, H. Köppel, and L. S. Cederbaum, *J. Chem. Phys.* **123**, 204310 (2005).
- ²⁵B. Podolsky, *Phys. Rev.* **32**, 812 (1928).
- ²⁶E. B. Wilson, Jr., J. C. Decius, and P. C. Cross, *Molecular Vibrations* (McGraw-Hill, New York, 1955).
- ²⁷J. Ammer, C. F. Sailer, E. Riedle, and H. Mayr, *J. Am. Chem. Soc.* **134**, 11481 (2012).
- ²⁸J. Ammer and H. Mayr, *J. Phys. Org. Chem.* **26**, 956 (2013).
- ²⁹S. Thallmair, J. P. P. Zauleck, and R. de Vivie-Riedle, *J. Chem. Theory Comput.* **11**, 1987 (2015).
- ³⁰S. Thallmair, M. K. Roos, and R. de Vivie-Riedle, *Struct. Dyn.* **3**, 043205 (2016).
- ³¹L. J. Schaad and J. Hu, *J. Mol. Struct.: THEOCHEM* **185**, 203 (1989).
- ³²D. J. Tannor, *Introduction to Quantum Mechanics: A Time-Dependent Perspective* (University Science Books, Sausalito, California, USA, 2007).
- ³³S. Thallmair, B. P. Fingerhut, and R. de Vivie-Riedle, *J. Phys. Chem. A* **117**, 10626 (2013).
- ³⁴E. A. Coutias, C. Seok, and K. A. Dill, *J. Comput. Chem.* **25**, 1849 (2004).
- ³⁵M. Svensson, S. Humbel, R. D. J. Froese, T. Matsubara, S. Sieber, and K. Morokuma, *J. Phys. Chem.* **100**, 19357 (1996).
- ³⁶M. J. Bearpark, S. M. Larkin, and T. Vreven, *J. Phys. Chem. A* **112**, 7286 (2008).
- ³⁷B. P. Fingerhut, S. Oesterling, K. Haiser, K. Heil, A. Glas, W. J. Schreier, W. Zinth, T. Carell, and R. de Vivie-Riedle, *J. Chem. Phys.* **136**, 204307 (2012).
- ³⁸L. W. Chung, W. M. C. Sameera, R. Ramozzi, A. J. Page, M. Hatanaka, G. P. Petrova, T. V. Harris, X. Li, Z. Ke, F. Liu, H.-B. Li, L. Ding, and K. Morokuma, *Chem. Rev.* **115**, 5678 (2015).
- ³⁹H.-J. Werner, P. J. Knowles, G. Knizia, F. R. Manby, M. Schütz *et al.*, version 2012.1, a package of *ab initio* programs, 2012, see <http://www.molpro.net>.
- ⁴⁰Y. Zhao and D. Truhlar, *Theor. Chem. Acc.* **120**, 215 (2008).
- ⁴¹M. J. Frisch, G. W. Trucks, H. B. Schlegel, G. E. Scuseria, M. A. Robb, J. R. Cheeseman, G. Scalmani, V. Barone, B. Mennucci, G. A. Petersson, H. Nakatsuji, M. Caricato, X. Li, H. P. Hratchian, A. F. Izmaylov, J. Bloino, G. Zheng, J. L. Sonnenberg, M. Hada, M. Ehara, K. Toyota, R. Fukuda, J. Hasegawa, M. Ishida, T. Nakajima, Y. Honda, O. Kitao, H. Nakai, T. Vreven, J. J. A. Montgomery, J. E. Peralta, F. Ogliaro, M. Bearpark, J. J. Heyd, E. Brothers, K. N. Kudin, V. N. Staroverov, T. Keith, R. Kobayashi, J. Normand, K. Raghavachari, A. Rendell, J. C. Burant, S. S. Iyengar, J. Tomasi, M. Cossi, N. Rega, J. M. Millam, M. Klene, J. E. Knox, J. B. Cross, V. Bakken, C. Adamo, J. Jaramillo, R. Gomperts, R. E. Stratmann, O. Yazyev, A. J. Austin, R. Cammi, C. Pomelli, J. W. Ochterski, R. L. Martin, K. Morokuma, V. G. Zakrzewski, G. A. Voth, P. Salvador, J. J. Dannenberg, S. Dapprich, A. D. Daniels, O. Farkas, J. B. Foresman, J. V. Ortiz, J. Cioslowski, and D. J. Fox, 09, Revision D.01, Inc., Wallingford, CT, 2013.
- ⁴²V. Alexandrov, D. M. A. Smith, H. Rostkowska, M. J. Nowak, L. Adamowicz, and W. McCarthy, *J. Chem. Phys.* **108**, 9685 (1998).
- ⁴³C. Eckart, *Phys. Rev.* **47**, 552 (1935).
- ⁴⁴A. Y. Dymarsky and K. N. Kudin, *J. Chem. Phys.* **122**, 124103 (2005).
- ⁴⁵K. N. Kudin and A. Y. Dymarsky, *J. Chem. Phys.* **122**, 224105 (2005).
- ⁴⁶J. E. Hadder and J. H. Frederick, *J. Chem. Phys.* **97**, 3500 (1992).
- ⁴⁷M. Kowalewski, "Quantendynamik isolierter molekularer Systeme," Ph.D. thesis, Ludwig-Maximilians-Universität München, 2012.
- ⁴⁸H. Tal-Ezer and R. Kosloff, *J. Chem. Phys.* **81**, 3967 (1984).
- ⁴⁹R. Kosloff and H. Tal-Ezer, *Chem. Phys. Lett.* **127**, 223 (1986).

1.2. Some remarks on Eckart conditions

In the previous section, the Eckart conditions [71] were necessary for the generation of the G matrix *via* its inverse as they offer a way to reliably add the missing translational and rotational degrees of freedom to the $3N - 6$ ($3N - 5$ for linear molecules) internal motions. But as these conditions are also relevant for further applications, multiple algorithms are reported in the literature [72–79] to satisfy the second condition (see below). In this section, a very brief overview is given and the codebase is discussed in detail.

The two Eckart conditions are the translational (eq. 1.6) and rotational (eq. 1.7) condition:

$$\sum_{a=1}^N m_a \mathbf{r}_a = 0, \quad (1.6)$$

$$\sum_{a=1}^N m_a (\mathbf{r}_a \times \mathbf{R}_a) = 0. \quad (1.7)$$

Here, N is the number of atoms, m_a the mass of atom a , and \mathbf{r}_a and \mathbf{R}_a are the Cartesian coordinates of the atom a in the structure to be rotated and the ones of the reference structure, respectively. The first condition requires the center of mass to be located at the origin and its adherence is trivial as it is a simple linear shift. For the second condition a rotation conducted by matrix \mathbf{T} is necessary as already pointed out by Eckart [71]. The algorithms differ in regard of finding this rotation matrix \mathbf{T} . A good overview can be found in Ref. [80]. All methods are based on a proper assignment of the atoms of one structure to the corresponding ones on the other structure.

Overall, two methods are described to adhere to the Eckart conditions. The first one is based on building the correlation matrix \mathbf{A} :

$$A_{ij} = \sum_{a=1}^N m_a r_{ia} R_{ja} \quad (1.8)$$

and symmetrizing it to yield \mathbf{T} [72, 73, 77]. This method is especially found in the rotation-vibration spectroscopy community [80], where the application is essential to separate rotational and vibrational modes.

The second method consists of the minimization of the mass-weighted root-mean-square deviation (RMSD), a problem equivalent to the Eckart conditions [80–82] and found in crystallography and bioinformatics [75, 76, 79]:

$$\min_{T \in SO(3)} \sum_{a=1}^N m_a |\mathbf{R}_a - (\mathbf{T} \cdot \mathbf{r}_a)|^2. \quad (1.9)$$

The implementation used for the work in this thesis is based on Ref. [78] and uses quaternions to find the matrix \mathbf{T} , an ansatz deemed universal due to no special cases [82]. It is kind of a cross-over algorithm as at first the correlation matrix \mathbf{A} (Eq. 1.8) is built, but not symmetrized. From its matrix elements the four-dimensional matrix \mathbf{F} can be constructed:

$$\mathbf{F} = \begin{pmatrix} A_{11} + A_{22} + A_{33} & A_{23} - A_{32} & A_{31} - A_{13} & A_{12} - A_{21} \\ A_{23} - A_{32} & A_{11} - A_{22} - A_{33} & A_{12} + A_{21} & A_{13} + A_{31} \\ A_{31} - A_{13} & A_{12} + A_{21} & -A_{11} + A_{22} - A_{33} & A_{23} + A_{32} \\ A_{12} - A_{21} & A_{13} + A_{31} & A_{23} + A_{32} & -A_{11} - A_{22} + A_{33} \end{pmatrix}. \quad (1.10)$$

The eigenvector $\mathbf{q}_1 = (q_0, q_1, q_2, q_3)$ associated with the largest eigenvalue λ_1 of matrix \mathbf{F} is then used to get the rotation matrix \mathbf{T} [78, 80, 83]:

$$\mathbf{T} = \begin{pmatrix} q_0^2 + q_1^2 - q_2^2 - q_3^2 & 2(q_1q_2 - q_0q_3) & 2(q_1q_3 + q_0q_2) \\ 2(q_1q_2 + q_0q_3) & q_0^2 - q_1^2 + q_2^2 - q_3^2 & 2(q_2q_3 - q_0q_1) \\ 2(q_1q_3 - q_0q_2) & 2(q_2q_3 + q_0q_1) & q_0^2 - q_1^2 - q_2^2 + q_3^2 \end{pmatrix}. \quad (1.11)$$

The vector \mathbf{q}_1 is a quaternion, a generalization of a complex number. It can be considered as consisting of a scalar number and a three-dimensional vector: $\mathbf{q} = (q_0, \underline{\mathbf{q}})$ with $\underline{\mathbf{q}} = (q_1, q_2, q_3)$. It can be interpreted as a rotation around the axis $\underline{\mathbf{q}}$ by the angle q_0 .

If the geometry to be rotated is mirrored compared to the reference structure, the eigenvalue λ_1 will not give the best fit. Instead the minimal eigenvalue λ_4 can be the right choice. Such cases are discussed in Ref. [78].

Chapter 2.

Light-induced bond cleavage in diphenylmethyl compounds

Triggering precursor molecules with light is a standard procedure in organic chemistry to generate reactive species *in situ* [84–89]. Undergoing either homolytic or heterolytic bond cleavage upon irradiation carbocations or carboradicals result, which can react with nearby molecules and in this way form new bonds. One important class of precursor molecules are diphenylmethyl compounds $\text{Ph}_2\text{CH-X}$ with different leaving groups X (see fig. 2.1). This class is the basis of a scale of reactivity for nucleophiles, developed in the last decades by Mayr and co-workers spanning 40 orders of magnitude [90–95]. The methodology of this extensive work is based on the reference electrophile diphenylmethyl cation (Ph_2CH^+) and its derivatives, which can be spectroscopically identified and distinguished from the precursor and the other possible photoproduct, diphenylmethyl radical ($\text{Ph}_2\text{CH}^\bullet$) [84]. As a consequence, it is possible to study the reaction mechanism in detail and gain a microscopic understanding of it. Here, especially the formation of the reactive species is of great interest, as the consecutive bimolecular reaction is mostly diffusion controlled [88]. First experimental contributions came from Peters and co-workers [87, 96–98], indicating a sub-picosecond time scale for the generation of the radical and ion pairs [87]. Employing transient absorption spectroscopy with time resolutions of a few tens of femtoseconds, Riedle and co-workers undertook further major efforts in recent years [89, 99–105]. For their investigation they chose three species $\text{Ph}_2\text{CH-X}$ showing different behavior in the kinetic experiments of Mayr and co-workers: the uncharged precursors $\text{Ph}_2\text{CH-Cl}$ and $\text{Ph}_2\text{CH-Br}$; and the charged and bulky precursor $\text{Ph}_2\text{CH-PPh}_3^+$.

From these kinetic experiments it is known that $\text{Ph}_2\text{CH-Cl}$ and $\text{Ph}_2\text{CH-Br}$ yield carbocations on the nanosecond time scale only in polar solvents like acetonitrile,

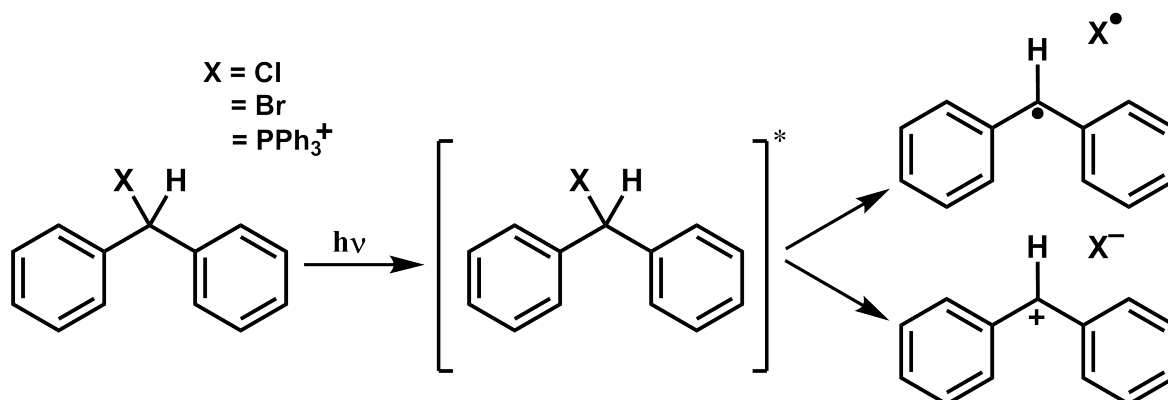


Figure 2.1.: Reaction scheme for the photodissociation of diphenylmethyl compounds with leaving group X.

while $\text{Ph}_2\text{CH}-\text{PPh}_3^+$ also does in apolar dichloromethane [88]. On the picosecond time scale accessible by transient absorption, all three species show significant amounts of carbocation in dichloromethane, which undergo geminate recombination for $\text{Ph}_2\text{CH}-\text{Cl}$ and $\text{Ph}_2\text{CH}-\text{Br}$. The apolar medium hinders the diffusional separation of the ion pair that can not escape the solvent cage [89]. This fact is of no concern for $\text{Ph}_2\text{CH}-\text{PPh}_3^+$, as both precursor and photoproduct are positively charged. Additionally, the cations in $\text{Ph}_2\text{CH}-\text{Cl}$ and $\text{Ph}_2\text{CH}-\text{Br}$ are primarily produced by electron transfer (ET) from the radicals measured in solution with a time constant of 22 ps and successfully modeled with a combined Marcus-Smoluchowski model [89].

On the even faster femtosecond time scale, the initial generation of the photoproducts before eventual ET can be followed. For $\text{Ph}_2\text{CH}-\text{PPh}_3^+$ together with a non-oxidizable counter-anion mainly carbocations are detectable [99, 100]. QD calculations incorporating the solvent in two different new ansatzes could prove that the carbocations in this case are directly produced [70, 106], for which a S_1/S_0 CoIn accessible only by solvent interaction is responsible. For $\text{Ph}_2\text{CH}-\text{Cl}$ initially the product distribution is heavily biased towards the radical pairs (95%) with only 5% ion pairs [89]. With a delay time of 76 fs, the radicals are built faster than the ion pairs (124 fs) [105, 107]. For $\text{Ph}_2\text{CH}-\text{Br}$ the radical pairs still dominate (70%) over the ion pairs (30%), but the ratio is more balanced [103, 104]. The delay times are slower, 100 fs for the radicals and 200 fs for the ion pairs. Furthermore, both measured signals for $\text{Ph}_2\text{CH}-\text{Br}$ show a small-amplitude oscillation deemed to be associated with a vibration of the carbon backbone [104].

In this thesis, the initial bond cleavage dynamics of $\text{Ph}_2\text{CH}-\text{Cl}$ and $\text{Ph}_2\text{CH}-\text{Br}$ is simulated with theoretical dynamical methods to elucidate the microscopic mechanism responsible for the different product distributions and delay times. This chapter is divided in three sections: In section 2.1 the QC and QD of $\text{Ph}_2\text{CH}-\text{Cl}$ is discussed in comparison with the results for $\text{Ph}_2\text{CH}-\text{PPh}_3^+$ published before [67, 70, 106, 108]. Based on the results from this section, the following section 2.2 models the experimental signals for $\text{Ph}_2\text{CH}-\text{Cl}$ and in this way directly links simulation and measurement to prove the reaction mechanism. In section 2.3 the results for $\text{Ph}_2\text{CH}-\text{Br}$ are presented with a special emphasis on vibrations during the bond cleavage. Therefore, besides QD also MQCD is used. For all calculations, the ONIOM method with the CLS approximation is employed (see appendix A) with CASSCF as high-level method. As the π -systems of the phenyl rings are uncoupled like in triarylmethyl derivatives [109, 110] and the orbitals of them therefore separable [30, 107], the model system only contains one phenyl ring. This reduces the computational cost significantly. All QD calculations in this chapter are based on the Wilson G-matrix method and the concept of adapted reactive coordinate (aRC) introduced in chapter 1.

2.1. Reaction mechanisms for two different leaving groups in direct comparison

As already mentioned in the introduction above, the photodissociation of $\text{Ph}_2\text{CH}-\text{Cl}$ was studied extensively in experiments [87, 89, 98, 101, 103, 105]. After the initial bond cleavage predominantly radical pairs are observed. A previous theoretical study identified a S_1/S_0 CoIn directly connecting the ion and radical pair channel [30]. In subsequent two-dimensional QD simulations the wave packet did not reach this CoIn, which implies heterolytic dissociation and contradicts the experiment. Therefore, the dissociation path is not yet known and the reaction not yet sufficiently understood.

In this paper “Molecular features in complex environment: Cooperative team players during excited state bond cleavage” published in *Structural Dynamics* the ultrafast photoinitiated bond cleavage of $\text{Ph}_2\text{CH}-\text{Cl}$ is simulated featuring both product channels [111]. Contrary to previous simulations [30], the lone pairs of the chlorine atom are included in the active space of the CASSCF calculations, which were shown to be important in QC calculations [107] and indeed are essential. The QC and QD of $\text{Ph}_2\text{CH}-\text{Cl}$ is compared with the results for $\text{Ph}_2\text{CH}-\text{PPh}_3^+$ [67, 70, 106], where the influence of the solvent is decisive.

The key statements of the article are:

- For $\text{Ph}_2\text{CH}-\text{Cl}$ the crucial influence of the chlorine lone pairs is demonstrated in a comparative calculation, voiding the S_1/S_0 CoIn previously deemed essential [30] for the reaction process. The lone pair states provide a direct connection between the initially populated $\pi\pi^*$ state and the homolytic product channel. Two new CoIns, a three-state and two-state one, are identified near the FC region, which are the decisive element for the product splitting.
- To include the three-state CoIn in a QD calculation, a transformation to a diabatic picture is adopted based on a molecular property, the dipole and transition dipole moment. It offers an adept way to drop the coupling between the lone pair states, which is irrelevant for the product distribution.
- Using the concept of aRCs previously introduced (see section 1.1 of chapter 1), two main reaction coordinates r and d_{py} are chosen to span the PESs. The coordinate r is the length of the bond cleaved here, d_{py} a measure for the pyramidalization of the central carbon atom. The three-state CoIn appears as a seam in this coordinate space. The QD simulation yields delay times in good agreement with the experiment and confirm the radical pair as main product. The motion of the wave packet is almost exclusively restricted to the r direction. The G-matrix elements used for the QD in this article are shown in fig. 2.2 on the following page. The coupling element (b) and the d_{py} element (c) are at least one order of magnitude smaller than the r element (a). Only the r element shows a distinct modulation along the r coordinate, while the other two elements solely have a prominent structure around $d_{py} = 0$.
- For $\text{Ph}_2\text{CH}-\text{PPh}_3^+$ one phenyl ring of the leaving group has to be additionally included in the active space to account for charge-transfer states. As coordinates again the bond length r is chosen and an angle ϕ to include a S_1/S_0 CoIn.
- In the QD the effect of the environment decelerates the wave packet, which then can reach the CoIn in a time window comparable to the rise of the experimental cation signal.

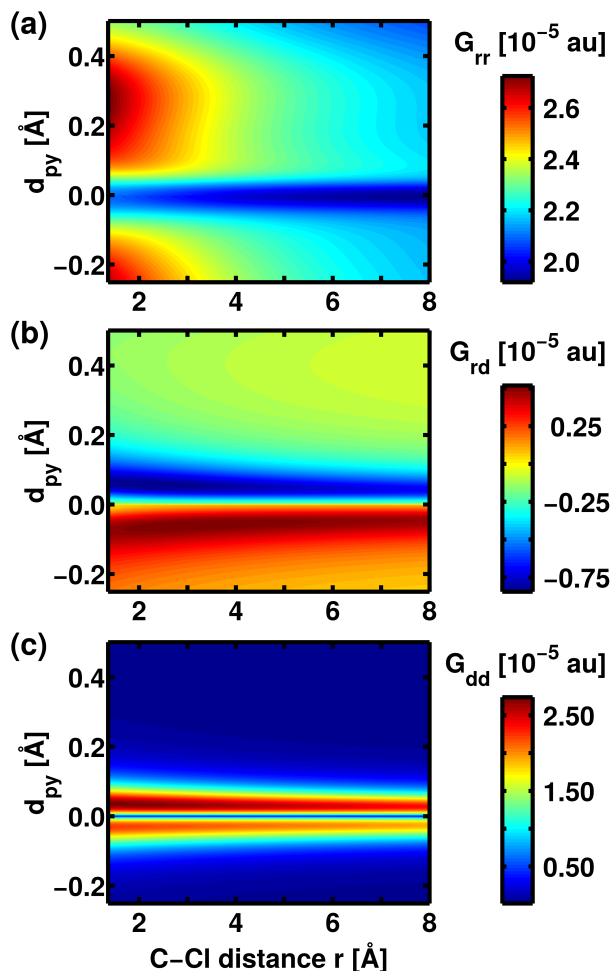


Figure 2.2.: G-matrix elements for $\text{Ph}_2\text{CH}-\text{Cl}$ in the two-dimensional coordinate space $\{r, d_{py}\}$, here partly shortened as $\{r, d\}$. The first diagonal element G_{rr} is depicted in **(a)**, the off-diagonal element G_{rd} in **(b)**, and the second diagonal element G_{dd} in **(c)**. As the matrix is symmetric, both off-diagonal elements G_{rd} and G_{dr} are identical.

By directly comparing the dynamics for two rather similar systems this paper illustrates that the seemingly simple change of the leaving group has huge consequences for the electronic structure and hence for the ensuing dynamics. It clearly shows that in the microscopic picture the leaving group has no minor part, but plays an elemental role.

The article “Molecular features in complex environment: Cooperative team players during excited state bond cleavage” was published in *Structural Dynamics* under a Creative Commons Attribution 3.0 Unported License (CC BY 3.0, URL: <https://creativecommons.org/licenses/by/3.0>). In the following it is reprinted unaltered from *Struct. Dyn.* **3**, 043205 (2016). The supporting information for this article is available under <https://doi.org/10.1063/1.4941600>.



Molecular features in complex environment: Cooperative team players during excited state bond cleavage

Sebastian Thallmair,^{1,2} Matthias K. Roos,¹ and Regina de Vivie-Riedle^{1,a)}

¹Department Chemie, Ludwig-Maximilians-Universität München, D-81377 München, Germany

²Lehrstuhl für BioMolekulare Optik, Ludwig-Maximilians-Universität München, D-80538 München, Germany

(Received 13 November 2015; accepted 22 December 2015; published online 11 February 2016)

Photoinduced bond cleavage is often employed for the generation of highly reactive carbocations in solution and to study their reactivity. Diphenylmethyl derivatives are prominent precursors in polar and moderately polar solvents like acetonitrile or dichloromethane. Depending on the leaving group, the photoinduced bond cleavage occurs on a femtosecond to picosecond time scale and typically leads to two distinguishable products, the desired diphenylmethyl cations (Ph_2CH^+) and as competing by-product the diphenylmethyl radicals ($\text{Ph}_2\text{CH}^\bullet$). Conical intersections are the chief suspects for such ultrafast branching processes. We show for two typical examples, the neutral diphenylmethylchloride ($\text{Ph}_2\text{CH}-\text{Cl}$) and the charged diphenylmethyltriphenylphosphonium ions ($\text{Ph}_2\text{CH}-\text{PPh}_3^+$) that the role of the conical intersections depends not only on the molecular features but also on the interplay with the environment. It turns out to differ significantly for both precursors. Our analysis is based on quantum chemical and quantum dynamical calculations. For comparison, we use ultrafast transient absorption measurements. In case of $\text{Ph}_2\text{CH}-\text{Cl}$, we can directly connect the observed signals to two early three-state and two-state conical intersections, both close to the Franck-Condon region. In case of the $\text{Ph}_2\text{CH}-\text{PPh}_3^+$, dynamic solvent effects are needed to activate a two-state conical intersection at larger distances along the reaction coordinate. © 2016 Author(s). All article content, except where otherwise noted, is licensed under a Creative Commons Attribution 3.0 Unported License. [<http://dx.doi.org/10.1063/1.4941600>]

I. INTRODUCTION

Photoinduced bond cleavage constitutes a common way to generate highly reactive species like carbocations *in situ*.^{1–6} In particular, in the case of diarylmethyl (Ar_2CH) compounds, the *in situ* generated carbocations are used to study their reactions with nucleophiles.^{6,7} Ph_2CH^+ and its various derivatives serve as reference electrophiles for one of the most extensive reactivity scales covering 40 orders of magnitude which is being developed by Mayr and co-workers.^{7–10} Different leaving groups (LGs) are used depending on the conditions under which the reactive species are generated.^{4–6} In the case of polar solvents like acetonitrile, $\text{Ph}_2\text{CH}-\text{Cl}$ is a suitable precursor. But for less polar solvents like dichloromethane or chloroform, the Ph_2CH^+ cation yield is extremely small on the nanosecond time scale.^{5,6} Using these solvents, $\text{Ph}_2\text{CH}-\text{PPh}_3^+$ constitutes a much better precursor for the Ph_2CH^+ generation.^{4,6} From a chemists point of view, this seems to be reasonable as the PPh_3^+ LG carries already a positive charge, and thus the generation of cations should be electrostatically preferred because no charge separation is necessary during bond cleavage.

Ultrafast broadband transient absorption measurements show that the Ph_2CH^+ generation differs for both LGs. In the case of Cl, initially homolytic bond cleavage occurs on the

^{a)}Electronic mail: regina.de_vivie@cup.uni-muenchen.de



hundreds of femtoseconds time scale followed by an electron transfer, which finally results in the ion pairs $\text{Ph}_2\text{CH}^+ + \text{Cl}^-$.⁵ The smaller driving force of the electron transfer in less polar solvents is the reason why the Cl LG is not suited for moderately polar solvents. In the case of PPh_3^+ , the measurements reveal a direct formation of Ph_2CH^+ for polar as well as moderately polar solvents.⁴ These observations already indicate that the underlying bond cleavage mechanisms might be different.

In the present work, we theoretically investigate the photoinduced bond cleavage of $\text{Ph}_2\text{CH}-\text{Cl}$ and $\text{Ph}_2\text{CH}-\text{PPh}_3^+$ (see Fig. 1) by means of state-of-the-art quantum chemical and quantum dynamical methods. We will discuss the individual molecular features introduced by the LG including two- and three-state conical intersections (CoIns) optimized at the complete active space self consistent field (CASSCF) level of theory. Three-state CoIns have already been shown to be important for photochemistry.^{11–13} To perform quantum dynamics (QD), we calculated potential energy surfaces (PESs) for both precursors in reduced dimensionality at the “our own *n*-layered integrated molecular orbital and molecular mechanics” (ONIOM) level of theory.^{14–17} In the case of $\text{Ph}_2\text{CH}-\text{Cl}$, the PESs have been diabaticized to describe the coupling through the three-state CoIn properly. For the first time to our knowledge, we present QD simulations including a three-state CoIn seam. Moreover in the case of $\text{Ph}_2\text{CH}-\text{PPh}_3^+$, the solvent environment comes into play during the bond cleavage and has a decisive influence on the reaction process.^{18,19}

The article is structured as follows: In Sec. II A, we discuss the quantum chemical results for $\text{Ph}_2\text{CH}-\text{Cl}$. Subsequently, the QD simulations are presented (Sec. II B). Then, the results for $\text{Ph}_2\text{CH}-\text{PPh}_3^+$ are compared therewith. Again they are split into a quantum chemical (Sec. III A) and a quantum dynamical part (Sec. III B). Finally, we conclude in Section IV.

II. BOND CLEAVAGE OF $\text{Ph}_2\text{CH}-\text{Cl}$

This section discusses the dissociation process of $\text{Ph}_2\text{CH}-\text{Cl}$ that has been extensively studied experimentally.^{1,5,20,21} The initial bond cleavage is found to be mainly homolytic on the sub-hundred femtosecond time scale, while a small heterolytic fraction is slightly delayed.²¹ In a previous theoretical study, a S_1/S_0 CoIn was identified connecting the heterolytic and

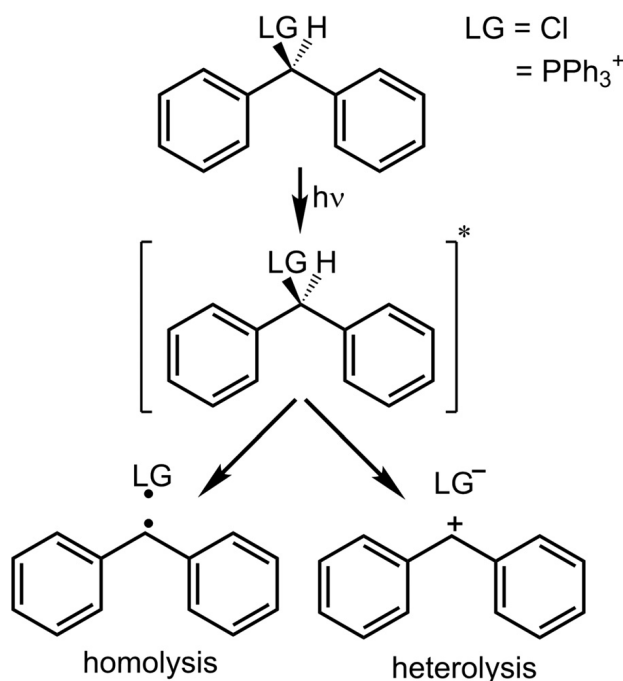


FIG. 1. Reaction scheme for the photoinduced bond cleavage of diphenylmethyl derivatives. Note that in the case of PPh_3^+ being the leaving group (LG), homolysis ($\text{Ph}_2\text{CH}^\bullet + \text{PPh}_3^+$) as well as heterolysis ($\text{Ph}_2\text{CH}^+ + \text{PPh}_3$) result in one positively charged and one neutral fragment.

homolytic product channel, but two-dimensional QD simulations revealed that the wave packet does not reach the CoIn.²² Thus, the exclusive product of the initial bond cleavage was—in contradiction to the experimental results—the ion pair of Ph_2CH^+ and Cl^- . In this previous study, the calculations have been performed at the CASSCF level of theory with an active space built up from all π -orbitals of one phenyl ring and the σ - and σ^* -orbitals of the carbon chlorine bond.²² Later, the importance of the Cl lone pairs has been shown by quantum chemical calculations.²¹

In the present work, we take both Cl lone pairs into account and employ an active space of 12 electrons in 10 orbitals, i.e., CASSCF(12,10). In addition, we use the ONIOM method.^{14–16} The angle between the phenyl moieties of $\text{Ph}_2\text{CH}-\text{Cl}$ at the Franck-Condon (FC) point is 77° , which is comparable to triarylmethyl derivatives for which it is reported in the literature that the π -systems of the phenyl rings are uncoupled.^{23,24} In previous CASSCF calculations for the whole molecule, it was demonstrated that the π - and π^* -orbitals of the phenyl rings can be separated.²² Furthermore, CASSCF calculations including the π -orbitals of both phenyl rings in the active space have shown that only one phenyl ring can interact with the σ^* -orbital of the C1-Cl bond.²¹ Therefore, it is possible that the high-level system treated at the CASSCF level of theory contains only one phenyl ring. This significantly reduces the computational cost. The second phenyl ring of the diphenylmethyl (Ph_2CH) moiety is replaced by a H atom in the high-level system and is solely included in the low-level system. It is evaluated at the UB3LYP level using Gaussian.²⁵ Fig. 2(a) displays the partitioning of the molecule with the thicker drawn part representing the high-level or model system. The constrained low-level state (CLS) approximation for ONIOM is used throughout the whole work.¹⁷ The basis set employed in all calculations is 6-31G(d).

A. Potential energy surfaces and the influence of the chlorine lone pairs

We optimized two CoIns for the model system which are shown in Figs. 2(b) and 2(c). A three-state CoIn could be located between the $\pi\pi^*$ S_1 state and both lone pair states exhibiting $n\pi^*$ character with the program package COLUMBUS^{26–29} (see Fig. 2(b)). The C1-Cl distance is 2.15 Å, the maximum energy gap between each pair of states is 0.017 eV. A second CoIn—this time a two-state CoIn—between the S_4 state of mixed $\pi\pi^*$ and $\pi\sigma^*$ character and the $\pi\pi^*$ state S_1 is located at a C1-Cl distance of 2.58 Å with the program package Molpro^{30–33} (see Fig. 2(c)). Here, the energy gap is 2.4×10^{-4} eV.

First, we calculated PESs along the dissociation coordinate, the C1-Cl distance r_{C1Cl} . Fig. 3 illustrates them in the diabatic representation as used in the QD calculations which will be discussed in Sec. II B. The bound S_0 state (black) correlates with the homolytic bond cleavage

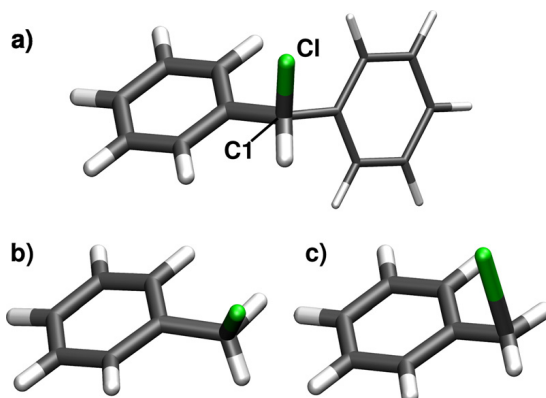


FIG. 2. (a) Optimized geometry of the S_0 minimum and visualization of the ONIOM partitioning for $\text{Ph}_2\text{CH}-\text{Cl}$: The thicker drawn part represents the high-level system treated with CASSCF(12,10). The second phenyl ring is only included in the low-level calculations with UB3LYP. (b) Optimized geometry of the three-state CoIn for the model system with a C1-Cl distance of 2.15 Å. (c) Optimized geometry of the two-state CoIn for the model system with a C1-Cl distance of 2.58 Å.

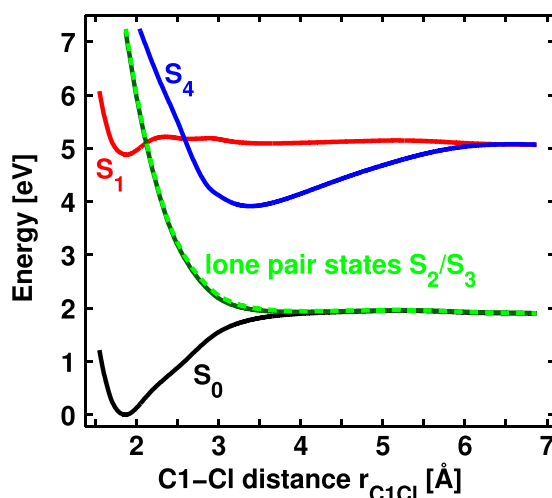


FIG. 3. Diabatic PESs of $\text{Ph}_2\text{CH-Cl}$ calculated at the ONIOM level of theory along the C1-Cl distance r_{C1Cl} . The S_0 state (black) and the lone pair states (green) form the homolytic product channel, the S_4 state (blue) forms the heterolytic product channel. The S_1 state (red) leads to excited radical pairs.

leading to radical pairs. The reaction starts with a π - π^* excitation to the S_1 state (red). The excitation energy is 4.88 eV (254 nm), which is in good agreement with the experimental value of 4.66 eV (266 nm).²⁰ At 2.12 Å, the lone pair states (green) cross the S_1 forming a three-state CoIn and are more and more stabilized with increasing C1-Cl distance, while their character changes from $n\pi^*$ to $n\sigma^*$. Finally, they become degenerate with the ground state S_0 . Therefore, the lone pair states constitute a direct connection between the optically accessed S_1 state and the homolytic product channel. After the three-state CoIn, the S_1 energy increases slightly to reach the S_4/S_1 CoIn at 2.60 Å. The S_4 state (blue) is identified as the heterolytic reaction channel for large C1-Cl distances. The S_1 state finally correlates with the first excited radical channel. Altogether, two consecutive CoIns are accountable for the product splitting, and the lone pair states are the key elements here.

To demonstrate the crucial influence of the Cl lone pairs, we performed CASSCF calculations without the Cl lone pairs being in the active space, i.e., CASSCF(8,8). At this level of theory, we optimized an additional S_1/S_0 CoIn for the model system which is the analog to the one identified previously,²² showing the Cl atom above an allylic subunit. We linearly interpolated the structure between the optimized S_1/S_0 CoIn and the S_0 minimum of the model system. Based on the obtained geometries, Fig. 4 compares the resulting PESs at the CASSCF(8,8) (dashed lines) and the CASSCF(12,10) level of theory (solid lines). Around the FC region, both methods yield similar results. But as soon as the lone pair states (green solid lines) cross the S_1 state (red solid line), the PESs begin to differ. In the case of CASSCF(8,8), the S_1/S_0 CoIn is clearly visible at $r_{\text{C1Cl}} = 3.11$ Å with an energy gap of 4.96×10^{-5} eV. In contrast thereto, the S_1/S_0 energy gap increases to 1.59 eV at the CASSCF(12,10) level of theory because the lone pair states intrude. Nevertheless, the character of S_0 and S_1 is remarkably similar. Obviously, the Cl lone pairs prevent the S_1/S_0 CoIn observed at the CASSCF(8,8) level of theory. Instead, they open up a completely new and direct connection between S_1 and S_0 already in the FC region, resulting in the formation of radical pairs.

B. Quantum dynamics in the presence of a three-state conical intersection

As a full dimensional quantum dynamical treatment is not feasible, we use a two-dimensional subspace to describe the reaction. The chosen coordinates are the C1-Cl distance and a coordinate accounting for the relaxation occurring in the carbon backbone during the bond cleavage. Most important is the hybridization of the central carbon atom C1 which changes from sp^3 to sp^2 . Thus, the C1 environment gets more and more planar during the reaction. We use the pyramidalization distance d_{py} to measure the distance of C1 above the plane

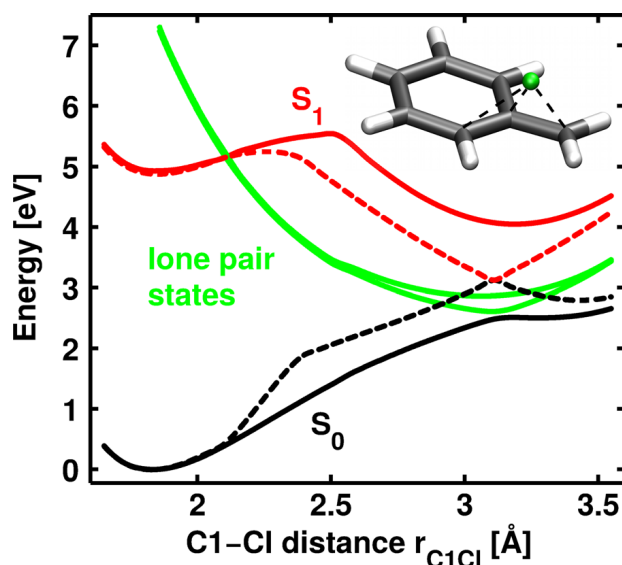


FIG. 4. PESs for the model system of $\text{Ph}_2\text{CH-Cl}$ using two different active spaces. The dashed lines show the results for the active space containing only the π -system and the C1-Cl bond (CASSCF(8,8)). The solid lines are obtained if the Cl lone pairs are additionally included in the active space (CASSCF(12,10)). The geometries are interpolated between the S_0 minimum and a S_1/S_0 CoIn located using CASSCF(8,8). This CoIn connects S_1 (red) and S_0 (black) at $r_{\text{C1Cl}} = 3.11$ Å. Its geometry is depicted in the right upper corner as inset. The lone pair states (green) which are shown as diabatic states separate S_1 and S_0 by 1.59 eV at the former CoIn.

formed by its three remaining neighboring atoms as coordinate. It includes additional relevant changes during re-hybridization like adaptations of bond lengths and ring positioning. As the lone pair states are rather independent of the carbon backbone relaxation, the three-state CoIn forms a seam along the pyramidalization distance d_{py} (see Fig. 5).

Since the quantum dynamical study should include population transfer between electronic states, the calculation of coupling elements is necessary. As the two lone pair states are always nearly degenerate, there will be significant coupling throughout the whole coordinate space that is not relevant for the product formation. To avoid this omnipresent coupling, we switch to the

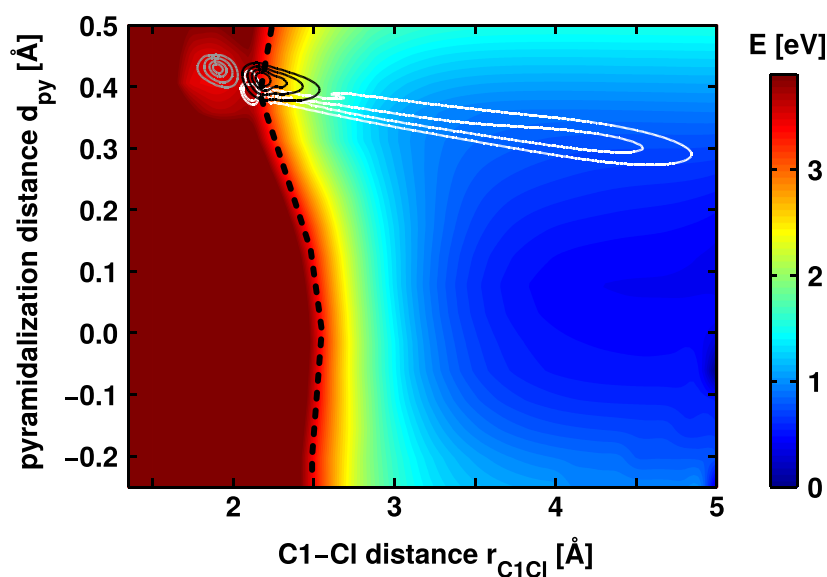


FIG. 5. PES of the adiabatic S_1 state of $\text{Ph}_2\text{CH-Cl}$ calculated at the ONIOM level of theory. Three wave packet snapshots taken from the diabatic propagation at different time points are also plotted. The first snapshot (gray isolines) is taken after 19 fs, the second (black isolines) after 36 fs, and the third (white isolines) after 82 fs. The three-state CoIn seam (black dashed line) is visible around the energy range of 3.3 eV (bright red).

diabatic picture where the electronic states maintain their specific character while passing a CoIn. In this picture, the coupling between the lone pair states can easily be set to zero. To transform the PESs, we solely employ *ab initio* molecular properties, namely, dipole μ_{ii}^{ad} and transition dipole moments μ_{ij}^{ad} forming the matrix μ^{ad} . The matrix elements are functions depending on the electronic structure and thus show the same behavior at the CoIn as the electronic energy. We will briefly discuss the procedure which is based on transformations for two-state CoIns.^{34–36} Due to the three-state CoIn, the matrix dimension is 3×3 .

Because the population transfer only occurs if two states come very close, it is useful to neglect the coupling far from the CoIn. Therefore, the off-diagonal terms μ_{ij}^{ad} between the states i and j are damped according to the following equation:³⁴

$$\tilde{\mu}_{ij}^{ad} = \mu_{ij}^{ad} \cdot e^{-f\Delta E_{ij}^2}. \quad (1)$$

Here, μ_{ij}^{ad} is multiplied by an exponential function depending on a damping factor f and the squared energy difference ΔE_{ij} . The damping factor f has to be chosen carefully with respect to a smooth behavior in the resulting PESs. In the present work, $f=500$ for the three-state CoIn and $f=5000$ to 10000 for the two-state CoIn. The modified matrix $\tilde{\mu}^{ad}$ is then diagonalized

$$\mu^{dia} = \mathbf{U}^\dagger \tilde{\mu}^{ad} \mathbf{U}, \quad (2)$$

and the resulting transformation matrix \mathbf{U} is applied to obtain the diabatic energies H_{ii}^{dia} and couplings H_{ij}^{dia} of the matrix \mathbf{H} (Eq. (3))

$$H_{ij}^{dia} = \sum_{k=1}^3 U_{ki} E_k U_{kj}. \quad (3)$$

E_k represents the adiabatic energies.

Fig. S1 in the supplementary material³⁷ shows the resulting two-dimensional diabatic PESs. The QD simulations were performed using the Chebychev propagation scheme³⁸ and the Wilson G-matrix formalism^{39–41} (for details, see supplementary material³⁷). The ground state vibrational eigenfunction was transferred to the S_1 PES and slightly shifted to a smaller C1-Cl distance and a higher pyramidalization distance d_{py} to account for the minimal barrier being not contained in the ONIOM PES. Fig. 5 depicts snapshots of the wave packet at three points in time. Although the propagation is performed in the diabatic presentation, the adiabatic S_1 PES is shown. This allows to place the three wave packets in the respective potential, which they experience during the propagation. The three-state CoIn seam (black dashed line) is very prominent in this representation. It is present for all values of d_{py} in the range of $r_{\text{C1Cl}}=2.1 \text{ \AA}$ to $r_{\text{C1Cl}}=2.5 \text{ \AA}$ at an energy of approximately 3.3 eV (bright red).

The first snapshot (gray isolines) is taken 19 fs after the propagation has been started and shows the wave packet at the S_1 minimum in the FC region. After 36 fs (black isolines), the wave packet has already coupled through the three-state CoIn seam and starts to follow the steep gradient of the lone pair state PES toward larger r_{C1Cl} . As there is also a small gradient in d_{py} toward planarization, the wave packet is slightly asymmetric in the direction of d_{py} . After 82 fs (white isolines), the wave packet is stretched from the three-state CoIn seam at $r_{\text{C1Cl}}=2.1 \text{ \AA}$ to $r_{\text{C1Cl}}=4.9 \text{ \AA}$ which results from the ongoing coupling through the three-state CoIn seam, while the first parts of the wave packet evolve very fast. It reaches a maximum C1-Cl distance of $r_{\text{C1Cl}}=5 \text{ \AA}$, which means that the bond cleavage is fully performed. But there still maintains a considerably large pyramidalization of $d_{py}=0.3 \text{ \AA}$. This observation is in agreement with experimental observations and on-the-fly simulations which reveal that the formation of the full absorption signal of the Ph_2CH^+ cation occurs with a time constant of 300 fs, which is attributed to planarization and solvation effects.⁴²

Fig. 6 illustrates the product formation obtained by the QD simulations. Therefore, the population of each state is collected at $r_{\text{C1Cl}}=4.0 \text{ \AA}$. It is clearly visible that the radical pairs are

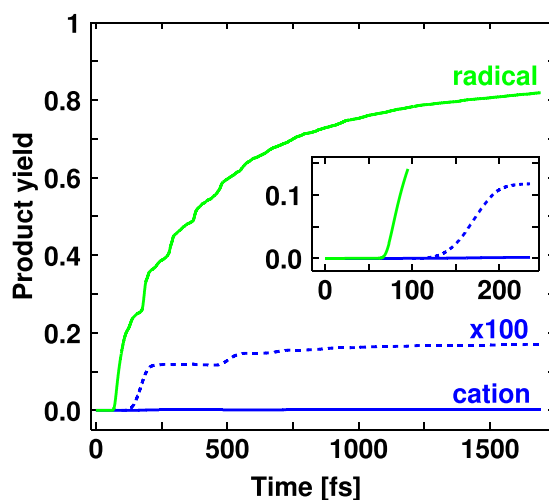


FIG. 6. Product yield progress for the propagation of $\text{Ph}_2\text{CH-Cl}$ up to 1700 fs. The ion pair yield is additionally plotted enlarged by the factor 100 with dashed lines. The inset especially depicts the onset of the rise of the product yield curves for the first 250 fs.

the main product of the initial bond cleavage. In the course of the propagation, 82% of the initial population reach the dissociation limit in the lone pair states or in the excited radical channel. At 67 fs, the radical yield starts to grow very rapidly as more and more parts of the wave packet couple through the three-state CoIn seam. This delay time is in very good agreement with the experimentally observed 76 fs.²¹ The delay time of 143 fs for the ion pairs is only slightly longer than the measured one of 124 fs (Ref. 21) and in excellent agreement with previous QD calculations where the lone pair states have not been considered.²² The simulated product yields deviate more from the experimental observations.⁵ The experimental radical yield of 40% is approximately half of the simulated yield of 82%. This may be attributed to recombination which is not considered in the simulation. On the other hand, the cation yield is underestimated with 0.2% here compared to 2% in the experiment. This might be due to the fact that the minimal barrier in the S_1 state before the S_4/S_1 CoIn is not included in the PES. Thus, the fraction of the wave packet reaching the S_4/S_1 CoIn is underestimated. All in all, it is possible to successfully model the initial bond cleavage of $\text{Ph}_2\text{CH-Cl}$ with radical pairs as the main product by the sequential passage through the CoIns in the FC region and to reproduce the observed delay times very well.

The subsequent processes—in particular, electron transfer, diffusional separation, and geminate recombination—can be treated with a combined Marcus-Smoluchowski model.⁵ Thereto, a pair of coupled differential equations can be set up and solved numerically (for details, see Ref. 5). The secondary processes typically take place on a time scale ranging from a few picoseconds up to several nanoseconds. They determine the chemically relevant cation yield which is available for subsequent, mostly bimolecular reactions.^{6–8,10}

III. BOND CLEAVAGE OF $\text{Ph}_2\text{CH-PPh}_3^+$

In this section, we will focus on the bond cleavage of $\text{Ph}_2\text{CH-PPh}_3^+$, which contains PPh_3^+ as LG in contrast to the previously investigated $\text{Ph}_2\text{CH-Cl}$. At first sight, the exchange of the LG introduces four major modifications: First, the PPh_3^+ moiety is considerably larger than the Cl atom. Second, it carries a positive charge. Third, the additional phenyl rings on the LG can be excited at a similar energy as the Ph_2CH moiety and thus are competing chromophores. And fourth, in contrast to the Cl, the P atom does not possess any lone pairs which have shown to be of great importance for the bond cleavage of $\text{Ph}_2\text{CH-Cl}$. Altogether, these changes coming along with the exchange of the Cl atom with the PPh_3^+ moiety already indicate changes of the key features during the bond cleavage.

A. Potential energy surfaces and a second chromophore carrying a positive charge

Initially, we take a look at the optical excitation process. As already mentioned, the phenyl rings of the PPh_3^+ moiety constitute additional chromophores, which absorb in the same spectral region as the phenyl rings of the Ph_2CH moiety. This results in an increased excited state manifold. The full system $\text{Ph}_2\text{CH} - \text{PPh}_3^+$ exhibits five locally excited states which are energetically quite close—two on the Ph_2CH moiety and three on the LG.⁴³ In addition, charge transfer excitations between both moieties are present. They are energetically well separated from the locally excited states and higher in energy.⁴³ Like in the case of $\text{Ph}_2\text{CH}-\text{Cl}$, the PESs for the QD calculations are evaluated at the ONIOM level of theory. The characteristics of $\text{Ph}_2\text{CH} - \text{PPh}_3^+$ in the FC region—in particular, the charge transfer states—already reveal that the high-level system has to contain not only one phenyl ring of the Ph_2CH moiety but also one of the PPh_3^+ moiety. Thus, the interplay between locally excited and charge transfer states can be described. Fig. 7(a) shows the ground state minimum structure of $\text{Ph}_2\text{CH} - \text{PPh}_3^+$. The thick part of the molecule is the high-level system phenylmethylphenylphosphonium ion ($\text{PhCH}_2-\text{PH}_2\text{Ph}^+$), while the thinner phenyl rings are only contained in the low-level system. The high-level system is calculated at the CASSCF(10,10) level of theory. The active space contains two π - and two π^* -orbitals of each phenyl ring as well as the σ - and σ^* -orbitals of the C1-P bond.⁴³ The low-level system is evaluated at the density functional theory (DFT) level of theory (functional M06-2X⁴⁴).

Fig. 8 illustrates the PES of the four lowest singlet states along the C1-P distance r_{C1P} for a constant P-C1-X angle $\phi = 125^\circ$ (see Fig. 7). A local $\pi-\pi^*$ excitation on PPh_3^+ leads to the S_1 state (red line), while the S_2 (blue line) is characterized by a local $\pi-\pi^*$ excitation on the Ph_2CH moiety. The S_3 state (orange line) has charge transfer character in the FC region. To observe bond cleavage experimentally, the system is excited to the locally excited states.⁴ The S_1 state opens the preferred reaction path compared to the S_2 as first it has the lower barrier, and second the S_2 population can immediately relax to the S_1 via a S_2/S_1 CoIn.⁴³ Therefore, we will focus on the S_1 state from now on. At a C1-P distance of $r_{\text{C1P}} = 2.1 \text{ \AA}$, the S_1 state exhibits a barrier of

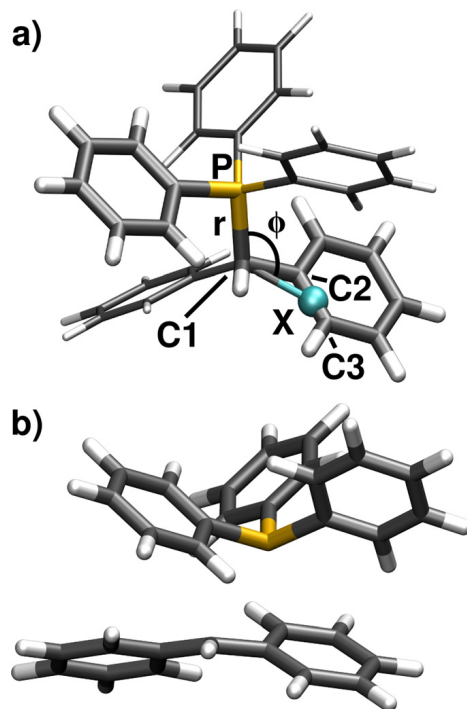


FIG. 7. (a) Ground state minimum geometry of $\text{Ph}_2\text{CH} - \text{PPh}_3^+$ optimized at the DFT level of theory (functional B3LYP). The thicker drawn part of the molecule constitutes the high-level system of the ONIOM calculations, while the thinner drawn phenyl rings are only contained in the low-level system. (b) Geometry of the S_1/S_0 CoIn of $\text{Ph}_2\text{CH} - \text{PPh}_3^+$ calculated at the ONIOM level of theory.

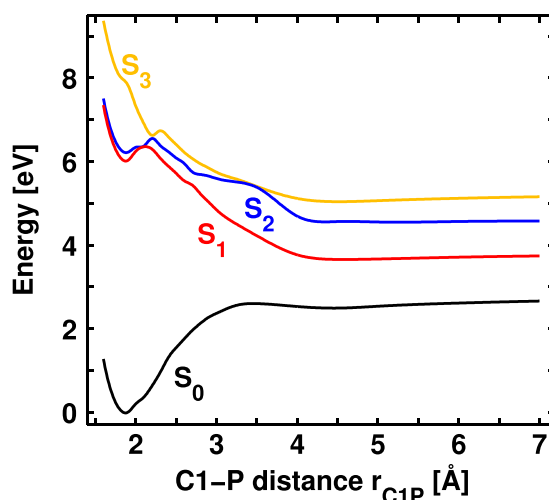


FIG. 8. Potential energy surface of the four lowest singlet states of $\text{Ph}_2\text{CH} - \text{PPh}_3^+$ along the C1-P distance r_{C1P} calculated at the ONIOM level of theory. The P-C1-X angle is kept constant at $\phi = 125^\circ$.

0.3 eV. Here, the S_1 character changes to $\pi\sigma^*$ followed by a change to a $\sigma\sigma^*$ character. This is in clear contrast to the excited state bond cleavage of $\text{Ph}_2\text{CH}-\text{Cl}$, where the Cl lone pairs induce the strong energetic stabilization of the adiabatic S_1 state after the three-state CoIn. In the dissociation limit, the ground state S_0 of $\text{Ph}_2\text{CH} - \text{PPh}_3^+$ has heterolytic character leading to $\text{Ph}_2\text{CH}^+ + \text{PPh}_3$, whereas the first and second excited state— S_1 and S_2 —have homolytic character. They result in the formation of radical pairs: diphenylmethyl radicals $\text{Ph}_2\text{CH}^\bullet + \text{PPh}_3^+$. This is the second major difference with respect to the Cl leaving group, where the S_0 has homolytic and the S_1 heterolytic character. The difference can be traced back to the initial positive charge of $\text{Ph}_2\text{CH} - \text{PPh}_3^+$, which leads to one positively charged and one neutral fragment in both (homolytic and heterolytic) dissociation channels. Thus, no charge separation occurs during the bond cleavage, which is the major reason for the destabilization of the heterolytic channel in $\text{Ph}_2\text{CH}-\text{Cl}$.

Due to the lack of lone pairs at the P atom, the three-state CoIn which is present in the FC region of $\text{Ph}_2\text{CH}-\text{Cl}$ disappears completely in $\text{Ph}_2\text{CH} - \text{PPh}_3^+$ as mentioned above. But at the same time, an energetically low lying two-state CoIn between S_1 and S_0 can be optimized in the high-level system $\text{PhCH}_2-\text{PH}_2\text{Ph}^+$, which is located at a larger C1-P distance.⁴³ The P atom is located above an allylic C_3 subunit containing C1, C2, and C3 showing a related geometry to the S_1/S_0 CoIn of $\text{Ph}_2\text{CH}-\text{Cl}$ calculated at the CASSCF(8,8) level of theory. For the full system $\text{Ph}_2\text{CH} - \text{PPh}_3^+$, this S_1/S_0 CoIn is depicted in Fig. 7(b). The C1-P distance is $r_{\text{C1P}} = 2.9 \text{ \AA}$; the P-C1-X angle is $\phi = 75^\circ$. The energy difference between S_1 and S_0 is 0.085 eV at the ONIOM level of theory. In the case of $\text{Ph}_2\text{CH}-\text{Cl}$, the CoIn was prevented by the Cl lone pairs (cf. Fig. 4). After the photoexcitation of $\text{Ph}_2\text{CH} - \text{PPh}_3^+$, the experimentally observed main products are Ph_2CH^+ and PPh_3 .⁴ Hence, the system has to relax to the ground state during the bond cleavage process because only there the Ph_2CH^+ are formed. The localized S_1/S_0 CoIn offers a fast way for the system to reach the S_0 .

In order to test the efficiency of the S_1/S_0 CoIn by QD simulations, like in $\text{Ph}_2\text{CH}-\text{Cl}$, a two-dimensional subspace is chosen in such a way that the CoIn can be described.^{18,19} Besides the C1-P distance r_{C1P} , an angular motion of the LG is necessary to reach the structure of the CoIn.⁴³ Thus, the P-C1-X angle ϕ shown in Fig. 7(a) is introduced as the second coordinate. The dummy atom X is placed in such a way in the allylic plane at the optimized CoIn of $\text{PhCH}_2-\text{PH}_2\text{Ph}^+$ that the angle ϕ optimally leads to the CoIn.⁴⁵ The relaxation of the carbon backbone of the Ph_2CH moiety which is the second coordinate in the case of $\text{Ph}_2\text{CH}-\text{Cl}$ is embedded into the r_{C1P} coordinate.⁴⁵ As a result, the CoIn shown in Fig. 7(b) is contained in the ONIOM PES.

Fig. 9 shows a one-dimensional representation of the minimum energy path (MEP) in the S_1 state in the two-dimensional subspace at the ONIOM level of theory. The first part on the

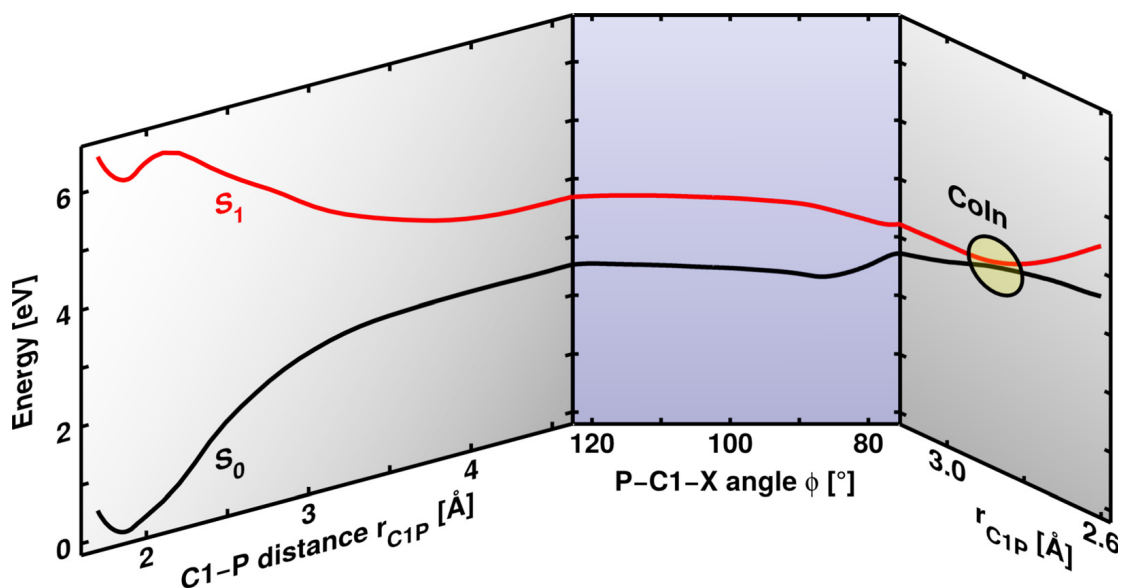


FIG. 9. Minimum energy path in the first excited state S_1 (red line) for the bond cleavage of $\text{Ph}_2\text{CH} - \text{PPH}_3^+$ in the two-dimensional coordinate space $\{r_{\text{C1P}}, \phi\}$. The ground state S_0 is depicted in black. The PES is displayed in three parts along the respective mainly changing coordinate. The first and the third part primarily involve changes in r_{C1P} , while in the second part the major motion is along ϕ .

left side starts in the FC region and is depicted depending on r_{C1P} . After crossing the barrier, the system moves mainly along r_{C1P} gaining about 2.6 eV of potential energy. Simultaneously, the energy of the ground state rises by 2.5 eV. In the second part (middle), where the primary motion is along ϕ , the energy of both electronic states remains almost constant. Only from $\phi = 90^\circ$ to $\phi = 76^\circ$, the S_1 energy lowers by approximately 0.36 eV. The last part of the MEP (right) is depicted again depending on r_{C1P} . A shortening of the C1-P distance to $r_{\text{C1P}} = 2.9 \text{ \AA}$ finally leads to the S_1/S_0 CoIn, where in principle the S_1 population can be transferred to the ground state to generate Ph_2CH^+ . The S_1 MEP emphasizes the fact that the system has to move considerably along ϕ . The key question is whether the motion from the FC region toward the CoIn is possible despite the large initial gradient along r_{C1P} .

B. Quantum dynamics influenced by the solvent cage

We could show that the molecular PES does not allow for the change of momentum from the r_{C1P} to the ϕ coordinate necessary to reach the CoIn.¹⁸ As the experiments are performed in solution, the solvent has to be considered in the simulation. In the case of $\text{Ph}_2\text{CH} - \text{PPH}_3^+$, both dissociation channels lead to one positively charged and one neutral fragment. Therefore, electrostatic solvent effects are insignificant.⁴³ Only dynamic solvent effects can come into play.^{18,19}

Thereby, the solvent cage prevents the free dissociation of the fragments and decelerates the motion along r_{C1P} . These dynamic solvent effects can be accounted for in QD calculations by means of an additional potential term \hat{V}_{solv} in the Hamiltonian \hat{H}_{tot} ,^{18,19}

$$\hat{H}_{\text{tot}} = \hat{T} + \hat{V}_{\text{mol}} + \hat{V}_{\text{solv}}, \quad (4)$$

with the kinetic energy operator \hat{T} and the molecular potential \hat{V}_{mol} . Recently, we developed two different approaches with increasing complexity to calculate the solvent potential \hat{V}_{solv} . The first method includes the solvent effects in a continuum-like fashion,¹⁸ the second treats the solvent environment explicitly.¹⁹ We will give a brief overview of both methods in the following.

In the dynamic continuum ansatz, Stokes' law is employed to calculate a decelerating force which acts on the wave packet. Thereto, the dynamic viscosity of the solvent η together with

the expectation value of velocity $\langle v(t) \rangle$ of the wave packet and an effective radius R_{eff} are needed

$$F_0(t) = -6\pi\eta R_{\text{eff}} \langle v(t) \rangle. \quad (5)$$

R_{eff} takes into account the different masses and radii of the generated fragments. To guarantee a deceleration of the wave packet only in an area where the solvent cavity is deformed, the actual decelerating force $F_{\text{dec}}(r, t)$ is obtained by multiplication of $F_0(t)$ with a sigmoid shape function. It was fitted to the course of the cavity surface area along the major bond cleavage coordinate r_{CIP} . Finally, an integration of $F_{\text{dec}}(r_{\text{CIP}}, t)$ over r_{CIP} yields the solvent potential V_{solv} ,

$$V_{\text{solv}}(r_{\text{CIP}}, t) = \int_0^{r_{\text{CIP}}} F_{\text{dec}}(r'_{\text{CIP}}, t) dr'_{\text{CIP}}. \quad (6)$$

In addition to the usual spatial dependence of a potential, $V_{\text{solv}}(r_{\text{CIP}}, t)$ is time-dependent. This is due to the time-dependence of the expectation value of velocity $\langle v(t) \rangle$ and describes the deceleration decrease with reducing velocity. For a more detailed description, see Ref. 18.

The second method, the QD/MD approach, combines QD calculations with molecular dynamics (MD) simulations of the solvent environment.¹⁹ Randomly selected snapshots from the MD trajectories give an averaged picture of the atomistic solvent surrounding of the reactant. The solvent potential V_{solv} is calculated for each snapshot individually. It contains the quantum chemically calculated interaction energy E_{sf} between each of the two fragments and each solvent molecule

$$V_{\text{solv}}(r_{\text{CIP}}, \phi) = \sum_{i=1}^{N_{\text{solv}}} \sum_{j=1}^{N_{\text{frag}}} E_{\text{sf}}(q_1^{ij}, q_2^{ij}, q_3^{ij}, \dots, q_6^{ij}), \quad (7)$$

with N_{frag} and N_{solv} being the number of fragments and solvent molecules, respectively. For each thus obtained V_{solv} , a QD simulation is conducted. The average of all wave packet propagations describes the effect of the solvent environment. More details to the QD/MD approach can be found in Ref. 19.

Here, we want to focus on the results obtained with the dynamic continuum ansatz. Acetonitrile is used as solvent with its dynamic viscosity of $\eta = 0.343$ mPas at 25 °C. But first of all, let us take a look at the bond cleavage process in the molecular potential without taking the solvent into account. Fig. 10(a) shows the S_1 PES together with snapshots from different QD simulations. The snapshots depicted by the dark gray and the black isolines are obtained by a QD simulation using only the molecular potential. They are taken 170 fs (dark gray) and 290 fs (black) after the wave packet started in the FC region. Obviously, the wave packet misses the CoIn as the initial gain of momentum in the r_{CIP} direction is too large to be compensated by the comparably small gradient toward the CoIn. Thus, the system dissociates in the first excited state, and radical pairs are generated.¹⁸ This is in clear contrast to the experimental observations in solution where Ph_2CH^+ cations are the main product.⁴

Fig. 10(a) displays two additional wave packet snapshots obtained from a propagation with the dynamic continuum ansatz. The snapshots are taken at 290 fs (white isolines) and 390 fs (light gray isolines) after starting in the FC region. The white isolines show the wave packet after the same propagation time as the black isolines for the QD simulation without the solvent potential. It is clearly visible that the motion along r_{CIP} is decelerated due to the solvent surrounding. Thus, the wave packet can experience the small gradient toward the CoIn and approaches it after approximately 390 fs. Here, the S_1 population can relax to the ground state where finally the formation of the experimentally observed Ph_2CH^+ cations takes place. Fig. 10(b) shows the rise of the Ph_2CH^+ cation population in the ground state after transfer through the S_1/S_0 CoIn calculated in the adiabatic picture.¹⁸ The population rise between 400 and 500 fs compares well with the experimentally observed initial rise of the cation absorption signal.⁴

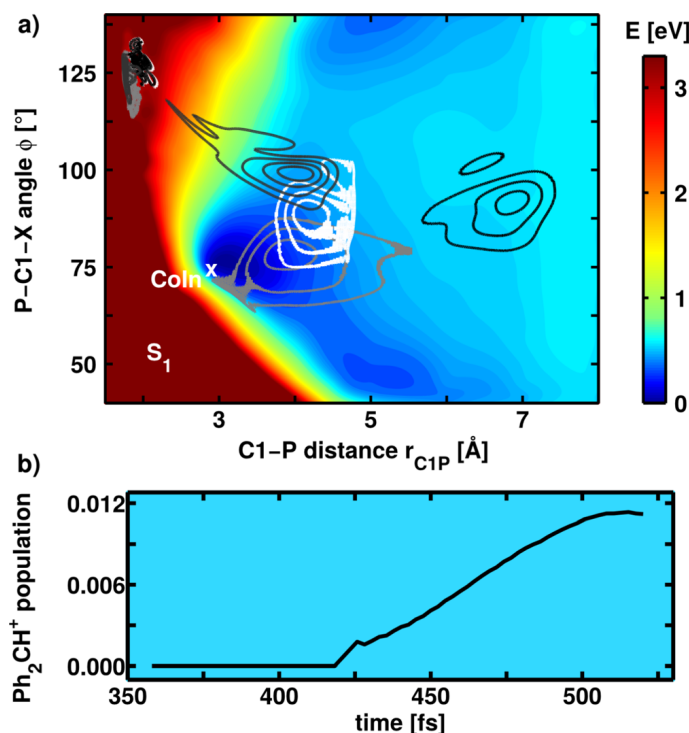


FIG. 10. (a) Potential energy surface of the S_1 state of $\text{Ph}_2\text{CH} - \text{PPh}_3^+$ calculated at the ONIOM level of theory. The S_0 minimum is located at $r_{\text{C1P}} = 1.87 \text{ \AA}$ and $\phi = 125^\circ$. In addition, snapshots from two different wave packet propagations are shown: The dark gray and black isolines depict wave packets from a normal propagation taken at 170 fs (dark gray) and 290 fs (black) after starting in the FC region. The white and light gray isolines display wave packets from a QD simulation with the dynamic continuum ansatz. They are taken at 290 fs (white) and 390 fs (light gray) after starting in the FC region. (b) Population of the S_0 state which evolves toward larger r_{C1P} values after coupling through the CoIn finally leading to Ph_2CH^+ cation generation.

IV. SUMMARY

We theoretically investigated the initial bond cleavage process in two Ph_2CH derivatives, namely, $\text{Ph}_2\text{CH}-\text{Cl}$ and $\text{Ph}_2\text{CH} - \text{PPh}_3^+$. By means of quantum chemical calculations, we first identified the individual molecular features of both precursors, which are clearly depending on the LG. Based on the knowledge of the important stationary points, we calculated PESs at the ONIOM level of theory and performed two-dimensional QD simulations.

The lowest excited state of both molecules is characterized by a local $\pi-\pi^*$ excitation on one phenyl ring. In the case of $\text{Ph}_2\text{CH}-\text{Cl}$, it is located on the Ph_2CH moiety; in the case of $\text{Ph}_2\text{CH} - \text{PPh}_3^+$ on the LG. These local $\pi\pi^*$ S_1 states initiate the bond cleavage. We showed that for $\text{Ph}_2\text{CH}-\text{Cl}$ the Cl lone pairs have a decisive impact on the molecular features in the FC region. Two successive CoIns determine the product formation at a very early stage of the bond cleavage. The first CoIn is a three-state CoIn which includes the lone pair states and opens the homolytic reaction channel, resulting in the formation of $\text{Ph}_2\text{CH}^\bullet + \text{Cl}^\bullet$. The second CoIn—this time a two-state CoIn—occurs at a slightly elongated C1-Cl distance and leads to the heterolytic channel with $\text{Ph}_2\text{CH}^+ + \text{Cl}^-$. QD simulations on the diabatic PESs reveal an extremely fast and efficient formation of $\text{Ph}_2\text{CH}^\bullet + \text{Cl}^\bullet$ within 67 fs. This delay time is in very good agreement with the observed 76 fs.²¹ The ion pair formation takes place on a slightly longer time scale of 143 fs compared to the experimental value of 124 fs and is like in the experiment the minor product channel. Our QD simulation shows the key role of the three-state CoIn seam during the photoinduced bond cleavage of $\text{Ph}_2\text{CH}-\text{Cl}$ and compares well with the experiment.

Changing the LG to PPh_3^+ results in significantly different molecular features. As the LG does not possess any lone pairs, the corresponding states being decisive in $\text{Ph}_2\text{CH}-\text{Cl}$ do not exist. Instead, we localized a two-state CoIn at longer C1-P distance far beyond the FC-region

which connects both reaction channels. QD simulations for the isolated molecule show that the wave packet misses the CoIn and dissociates in the S_1 state which has homolytic character. Thus, radical pairs are generated which is in contrast to the experimentally observed formation of Ph_2CH^+ cations.⁴ Only if the dynamic solvent effects are taken into account which lead to a deceleration of the wave packet during dissociation, the molecular system can follow the slight gradient toward the CoIn and reaches it after approximately 390 fs. Here, the S_1 population can relax to the ground state which has heterolytic character in the dissociation limit. The simulated onset of the Ph_2CH^+ population is in accordance with the initial rise of the Ph_2CH^+ absorption signal in the experiment.⁴

In a simplistic concept of photoinduced bond cleavage, the LG has just the function to leave the precursor and form a fragment, which is as stable as possible in the desired product channel. Our results impressively demonstrate that changing the LG may introduce far more extensive changes of the molecular features which set the stage for the bond cleavage process. In the presented cases of $\text{Ph}_2\text{CH}-\text{Cl}$ and $\text{Ph}_2\text{CH}-\text{PPh}_3^+$, the LG controls the position of the CoIns which decide the branching for the product formation. Furthermore, the delay time until the products are formed also depends on the spatial and energetic position of the CoIns. In addition, the LG influences the environmental impact on the reaction. In the case of $\text{Ph}_2\text{CH}-\text{PPh}_3^+$, the solvent cage decelerates the wave packet on the sub-picosecond time scale, and only thus enables a coupling through the CoIn to form the Ph_2CH^+ cations. The influence of the solvent environment occurs on a longer time scale for $\text{Ph}_2\text{CH}-\text{Cl}$. Here, an electron transfer subsequent to the initial bond cleavage described in the present work leads to Ph_2CH^+ generation. This electron transfer is strongly depending on the polarity of the solvent. Changing the LG of Ph_2CH derivatives from neutral to charged does not only modify the stability of the isolated fragments after bond cleavage, it also alters the molecular response and reaction outcome on the femtosecond time scale. Thus, a minor chemical change leads to a substantial change in the femtochemistry of the system.

ACKNOWLEDGMENTS

Financial support by the Deutsche Forschungsgemeinschaft through the SFB749 and the excellence cluster Munich-Centre for Advanced Photonics (MAP) is acknowledged. We thank Benjamin Fingerhut, Eberhard Riedle, Christian Sailer, Herbert Mayr, and Johannes Ammer for fruitful discussions.

- ¹J. Bartl, S. Steenken, H. Mayr, and R. A. McClelland, *J. Am. Chem. Soc.* **112**, 6918 (1990).
- ²P. K. Das, *Chem. Rev.* **93**, 119–144 (1993).
- ³R. A. McClelland, *Tetrahedron* **52**, 6823–6858 (1996).
- ⁴J. Ammer, C. F. Sailer, E. Riedle, and H. Mayr, *J. Am. Chem. Soc.* **134**, 11481–11494 (2012).
- ⁵C. F. Sailer, S. Thallmair, B. P. Fingerhut, C. Nolte, J. Ammer, H. Mayr, I. Pugliesi, R. de Vivie-Riedle, and E. Riedle, *ChemPhysChem* **14**, 1423 (2013).
- ⁶J. Ammer and H. Mayr, *J. Phys. Org. Chem.* **26**, 956–969 (2013).
- ⁷H. Mayr, *Tetrahedron* **71**, 5095–5111 (2015).
- ⁸H. Mayr and M. Patz, *Angew. Chem., Int. Ed.* **33**, 938–957 (1994).
- ⁹H. Mayr, T. Bug, M. F. Gotta, N. Hering, B. Irrgang, B. Janker, B. Kempf, R. Loos, A. R. Ofial, G. Remennikov, and H. Schimmel, *J. Am. Chem. Soc.* **123**, 9500–9512 (2001).
- ¹⁰H. Mayr, J. Ammer, M. Baidya, B. Maji, T. A. Nigst, A. R. Ofial, and T. Singer, *J. Am. Chem. Soc.* **137**, 2580–2599 (2015).
- ¹¹J. D. Coe, M. T. Ong, B. G. Levine, and T. J. Martínez, *J. Phys. Chem. A* **112**, 12559 (2008).
- ¹²J. González-Vázquez and L. González, *ChemPhysChem* **11**, 3617–3624 (2010).
- ¹³P. Krause and S. Matsika, *J. Chem. Phys.* **136**, 034110 (2012).
- ¹⁴M. Svensson, S. Humbel, R. D. J. Froese, T. Matsubara, S. Sieber, and K. Morokuma, *J. Phys. Chem.* **100**, 19357–19363 (1996).
- ¹⁵S. Dapprich, I. Komáromi, K. Byun, K. Morokuma, and M. J. Frisch, *J. Mol. Struct.: THEOCHEM* **461–462**, 1–21 (1999).
- ¹⁶T. Vreven and K. Morokuma, *J. Chem. Phys.* **113**, 2969 (2000).
- ¹⁷M. J. Bearpark, S. M. Larkin, and T. Vreven, *J. Phys. Chem. A* **112**, 7286 (2008).
- ¹⁸S. Thallmair, M. Kowalewski, J. P. P. Zaulack, M. K. Roos, and R. de Vivie-Riedle, *J. Phys. Chem. Lett.* **5**, 3480–3485 (2014).
- ¹⁹S. Thallmair, J. P. P. Zaulack, and R. de Vivie-Riedle, *J. Chem. Theory Comput.* **11**, 1987–1995 (2015).
- ²⁰K. S. Peters, *Chem. Rev.* **107**, 859 (2007).
- ²¹C. F. Sailer, N. Krebs, B. P. Fingerhut, R. de Vivie-Riedle, and E. Riedle, *EPJ Web Conf.* **41**, 05042 (2013).

- ²²B. P. Fingerhut, D. Geppert, and R. de Vivie-Riedle, *Chem. Phys.* **343**, 329 (2008).
- ²³L. E. Manring and K. S. Peters, *J. Phys. Chem.* **88**, 3516–3520 (1984).
- ²⁴T. Bizjak, J. Karpiuk, S. Lochbrunner, and E. Riedle, *J. Phys. Chem. A* **108**, 10763–10769 (2004).
- ²⁵M. J. Frisch, G. W. Trucks, H. B. Schlegel, G. E. Scuseria, M. A. Robb, J. R. Cheeseman, G. Scalmani, V. Barone, B. Mennucci, G. A. Petersson, H. Nakatsuji, M. Caricato, X. Li, H. P. Hratchian, A. F. Izmaylov, J. Bloino, G. Zheng, J. L. Sonnenberg, M. Hada, M. Ehara, K. Toyota, R. Fukuda, J. Hasegawa, M. Ishida, T. Nakajima, Y. Honda, O. Kitao, H. Nakai, T. Vreven, J. A. Montgomery, Jr., J. E. Peralta, F. Ogliaro, M. Bearpark, J. J. Heyd, E. Brothers, K. N. Kudin, V. N. Staroverov, R. Kobayashi, J. Normand, K. Raghavachari, A. Rendell, J. C. Burant, S. S. Iyengar, J. Tomasi, M. Cossi, N. Rega, J. M. Millam, M. Klene, J. E. Knox, J. B. Cross, V. Bakken, C. Adamo, J. Jaramillo, R. Gomperts, R. E. Stratmann, O. Yazyev, A. J. Austin, R. Cammi, C. Pomelli, J. W. Ochterski, R. L. Martin, K. Morokuma, V. G. Zakrzewski, G. A. Voth, P. Salvador, J. J. Dannenberg, S. Dapprich, A. D. Daniels, Ö. Farkas, J. B. Foresman, J. V. Ortiz, J. Cioslowski, and D. J. Fox, “Gaussian 09, Revision D.01, Gaussian, Inc., Wallingford CT, 2009” (2009).
- ²⁶H. Lischka, R. Shepard, I. Shavitt, R. M. Pitzer, M. Dallos, T. Müller, P. G. Szalay, F. B. Brown, R. Ahlrichs, H. J. Böhm, A. Chang, D. C. Comeau, R. Gdanitz, H. Dachsel, C. Ehrhardt, M. Ernzerhof, P. Höchtl, S. Irle, G. Kedziora, T. Kovar, V. Parasuk, M. J. M. Pepper, P. Scharf, H. Schiffer, M. Schindler, M. Schüler, M. Seth, E. A. Stahlberg, J.-G. Zhao, S. Yabushita, Z. Zhang, M. Barbatti, S. Matsika, M. Schuurmann, D. R. Yarkony, S. R. Brozell, E. V. Beck, J.-P. Blaudeau, M. Ruckebauer, B. Sellner, F. Plasser, and J. J. Szymczak, “COLUMBUS, an ab initio electronic structure program, release 7.0” (2013).
- ²⁷M. R. Manaa and D. R. Yarkony, *J. Chem. Phys.* **99**, 5251 (1993).
- ²⁸S. Matsika and D. R. Yarkony, *J. Chem. Phys.* **117**, 6907 (2002).
- ²⁹M. Dallos, H. Lischka, R. Shepard, D. R. Yarkony, and P. G. Szalay, *J. Chem. Phys.* **120**, 7330 (2004).
- ³⁰H.-J. Werner, P. J. Knowles, G. Knizia, F. R. Manby, M. Schütz, P. Celani, T. Korona, R. Lindh, A. Mitrushenkov, G. Rauhut, K. R. Shamasundar, T. B. Adler, R. D. Amos, A. Bernhardsson, A. Berning, D. L. Cooper, M. J. O. Deegan, A. J. Dobbyn, F. Eckert, E. Goll, C. Hampel, A. Hesselmann, G. Hetzer, T. Hrenar, G. Jansen, C. Köppl, Y. Liu, A. W. Lloyd, R. A. Mata, A. J. May, S. J. McNicholas, W. Meyer, M. E. Mura, A. Nicklass, D. P. O’Neill, P. Palmieri, D. Peng, K. Pflüger, R. Pitzer, M. Reiher, T. Shiozaki, H. Stoll, A. J. Stone, R. Tarroni, T. Thorsteinsson, and M. Wang, “MOLPRO, version 2012.1, a package of ab initio programs” (2012).
- ³¹M. J. Bearpark, M. A. Robb, and H. B. Schlegel, *Chem. Phys. Lett.* **223**, 269–274 (1994).
- ³²F. Eckert, P. Pulay, and H.-J. Werner, *J. Comput. Chem.* **18**, 1473–1483 (1997).
- ³³F. Sicilia, L. Blancafort, M. J. Bearpark, and M. A. Robb, *J. Chem. Theory Comput.* **4**, 257–266 (2008).
- ³⁴H.-J. Werner and W. Meyer, *J. Chem. Phys.* **74**, 5802 (1981).
- ³⁵A. J. Dobbyn and P. J. Knowles, *Mol. Phys.* **91**, 1107 (1997).
- ³⁶E. S. Kryachko and D. R. Yarkony, *Int. J. Quantum Chem.* **76**, 235 (2000).
- ³⁷See supplementary material at <http://dx.doi.org/10.1063/1.4941600> for the two-dimensional diabatic PES of diphenylmethylchloride (Fig. S1), details of the QD simulations, and optimized geometries.
- ³⁸H. Tal-Ezer and R. Kosloff, *J. Chem. Phys.* **81**, 3967 (1984).
- ³⁹B. Podolsky, *Phys. Rev.* **32**, 812 (1928).
- ⁴⁰E. B. Wilson, Jr., J. C. Decius, and P. C. Cross, *Molecular Vibrations: The Theory of Infrared and Raman Vibrational Spectra* (Dover Publications, New York, 1980).
- ⁴¹L. Schaad and J. Hu, *J. Mol. Struct.: THEOCHEM* **185**, 203 (1989).
- ⁴²B. P. Fingerhut, C. F. Sailer, J. Ammer, E. Riedle, and R. de Vivie-Riedle, *J. Phys. Chem. A* **116**, 11064–11074 (2012).
- ⁴³S. Thallmair, B. P. Fingerhut, and R. de Vivie-Riedle, *J. Phys. Chem. A* **117**, 10626–10633 (2013).
- ⁴⁴Y. Zhao and D. Truhlar, *Theor. Chem. Acc.* **120**, 215–241 (2008).
- ⁴⁵S. Thallmair, M. K. Roos, and R. de Vivie-Riedle, “The design of specially adapted reactive coordinates to economically compute potential and kinetic energy operators including geometry relaxation” (unpublished).

2.2. Simulation of experimental signals from reduced dimensionality wave packet dynamics

To prove that a reaction mechanism is indeed responsible for the signals observed in the experiment, it is necessary to model these signals using the theoretical data. The comparison then makes it evident if the model is correct or if further factors of influence have to be considered. Based on the QD description of the bond cleavage of $\text{Ph}_2\text{CH}-\text{Cl}$ described in the section above, such a comparison between experiment and simulation is done in this section. Before, two reaction channels were identified leading to the radical pair and the ion pair, whereby a three-state CoIn is decisive for the primary product splitting and a two-state CoIn responsible for the ion pair yield. Now the question remains if the further motion of the wave packets on the respective PES supports the generation of a signal similar to the experiment.

In this paper “Ultrafast photochemistry with two product channels: wavepacket motion through two distinct conical intersections” published by *Chemical Physics Letters*, both experimental and theoretical results are reported [104]. This side-by-side presentation shows first the experimental conditions necessary for the high temporal resolution, which in the second step have to be taken into account while analyzing the wave packet. In this way, the width of the probe pulse and the temporal resolution are directly transferred into the equations for the simulated signal. Essential for the strong transient absorption of the photoproducts compared to the precursor $\text{Ph}_2\text{CH}-\text{Cl}$ is the fact that after the bond cleavage the carbon backbone planarizes. This leads to a drastic change in intensity of the transient absorption, while the signals simultaneously undergo a strong shift as shown in fig. 6 of this paper. Therefore, only almost planar photoproducts are detectable by the probe pulses.

The key points of the article are:

- A transient absorption setup is described to reach a temporal resolution of exceptional 40 fs. In this experiment, a 270 nm pump pulse is used to excite the molecule and a probe pulse at either 327 nm or 435 nm to follow the two possible reaction products. Special measures are taken to determine the delay between these two pulses with high precision (4 fs).
- The resulting transient absorption signals for $\text{Ph}_2\text{CH}-\text{Cl}$ are shown. Correcting the raw data by two-photon solvent contributions, the pure molecular signal results with a delay time of 76 fs for the radical pair and 124 fs for the ion pair. The product distribution strongly favors the radical pair. Results for a fluorinated species are identical within the experimental error.
- Following the procedure described before (see section 2.1), the reaction is simulated with QD. Additionally, the experimental signal is modeled from the wave packet propagation for a direct comparison. The first step hereby is the integration of parts of the wave packet along the bond cleavage coordinate. The integrals are afterwards modulated by the strong shift of radical and cation absorption with the planarization and the temporal resolution of the experiment. The resulting simulated signals for $\text{Ph}_2\text{CH}^\bullet$ and Ph_2CH^+ are in good agreement with the experimental absorption.

The comparison between experimental and simulated signals shown in this paper proves the reaction mechanism, which involves two consecutive CoIns. It demonstrates very clearly that a rate model is not sufficient for the description of the reaction, but the explicit motion of the wave packet and its splitting have to be considered.

Similar behavior can be inferred for other systems with two product channels and ultrafast delay times.

The article “Ultrafast photochemistry with two product channels: wavepacket motion through two distinct conical intersections” published by *Chemical Physics Letters* is reprinted here with permission from *Chem. Phys. Lett.* **683**, 128–134 (2017). Copyright 2017 Elsevier B.V. The supporting information for this article is available under <https://doi.org/10.1016/j.cpllett.2017.02.086>.



Contents lists available at ScienceDirect

Chemical Physics Letters

journal homepage: www.elsevier.com/locate/cplett

Research paper

Ultrafast photochemistry with two product channels: Wavepacket motion through two distinct conical intersections

Eberhard Riedle^{a,*}, Matthias K. Roos^b, Sebastian Thallmair^{a,b,1}, Christian F. Sailer^a, Nils Krebs^a, Benjamin P. Fingerhut^{b,2}, Regina de Vivie-Riedle^{b,*}^a Lehrstuhl für BioMolekulare Optik, Ludwig-Maximilians-Universität (LMU), Oettingenstr. 67, 80538 München, Germany^b Department Chemie, Ludwig-Maximilians-Universität (LMU), Butenandt-Str. 11, 81377 München, Germany

ARTICLE INFO

Article history:

Received 4 January 2017

In final form 27 February 2017

Available online 2 March 2017

Keywords:

Femtosecond photodissociation

Conical intersection

Competing channels

ABSTRACT

Light induced bond cleavage is an ubiquitous process in large molecules, yet its quantum nature is not fully understood. We present a comprehensive description of the ultrafast light induced C–Cl bond cleavage in diarylmethyl chlorides combining femtosecond transient absorption measurements with *ab initio* calculations. We observe a delayed appearance of radicals (80 fs) and cations (125 fs). The excited state wavepacket moves initially toward two conical intersections and the passing through these intersections determines the partitioning into the differing product channels. Different locations of the conical intersections explain the observed delay times.

© 2017 Elsevier B.V. All rights reserved.

1. Introduction

Photoinduced processes in molecules are omnipresent and are of relevance in various fields like biology, environmental science, synthetic chemistry and renewable energies. Thus, their in-depth understanding is of major importance. Pioneering work in all of these fields has been done by Ahmed Zewail [1–5]. Photoinduced bond cleavage constitutes an important subtopic of these processes and has been one of the early examples studied by Ahmed Zewail [6]. Typically, it proceeds ultrafast in the femtosecond regime. On this time scale, conical intersections (CoIn's) can decisively influence the reaction and determine its outcome [7–11]. Moreover, they can provide a connection between bound and dissociative electronic states and thus cause initially bound states to be depopulated very fast. At a CoIn, states with differing electronic configuration cross and their energy gap vanishes. Strictly speaking, the non-crossing rule of diatomics is not valid for larger systems and the displacement along nonsymmetric coupling modes leads to a CoIn [7–9]. In the vicinity of the CoIn the Born-Oppenheimer

separation breaks down completely and highly efficient and rapid photodissociation [12] or isomerization can take place [13,14].

Experimentally, the presence and effectiveness of a CoIn is detected as femtosecond decay of the optical signature attributed to the excited state and the equally fast recovery of the ground state absorption for a photophysical process. For a photochemical process the newly appearing product signal serves as indication with the same ultrafast rise. The detection and interpretation gets more complex as more than one CoIn is involved. Theory has shown convincing examples for this situation and it now seems to be rather the rule than the exception [7,8,15]. Once the existence of CoIns is accepted, the next step is to move away from the description of the ultrafast process in terms of populations toward the motion of a vibronic wavepacket from the Franck-Condon point toward the CoIn and beyond. This has recently been demonstrated in a particularly comprehensible study of the isomerization of rhodopsin [16].

For many chemical processes not only the channels of return to the ground state and a single product exist like in a ring opening reaction [17,18], but two or more product channels [10,11,19,20]. In a classical kinetic description – a rate model – one expects a decay of the excited state signal with $\tau = 1/(k_{IC} + k_1 + k_2)$ where k_1 and k_2 are the effective product formation rates and k_{IC} is the internal conversion rate. The products are expected to appear equally fast and the ratio of products is given by $r = k_1/k_2$. From the theoretical point of view the question arises whether one or two CoIns are responsible. To clarify this experimentally, the sole

* Corresponding authors.

E-mail addresses: riedle@physik.uni-muenchen.de (E. Riedle), Regina.de_Vivie@cup.uni-muenchen.de (R. de Vivie-Riedle).¹ Current address: Groningen Biomolecular Sciences and Biotechnology Institute and The Zernike Institute for Advanced Material, University of Groningen, Nijenborgh 7, 9747 AG Groningen, The Netherlands.² Current address: Max Born Institute for Nonlinear Optics and Short Pulse Spectroscopy, Max-Born-Str. 2a, 12489 Berlin, Germany.<http://dx.doi.org/10.1016/j.cplett.2017.02.086>

0009-2614/© 2017 Elsevier B.V. All rights reserved.

determination of the ultrafast rates is not sufficient. Additional and more specific signatures have to be found.

We investigate the bond cleavage of diphenylmethylchloride (DPMC) in solution that is known to either proceed homolytically (diphenylmethyl radical + chlorine radical) or heterolytically (diphenylmethyl cation + chloride anion). Previously it was found that both processes occur in well under 1 ps and the diphenylmethyl redox states can be easily distinguished spectroscopically [21–23]. The earlier experiments were performed with a broadband transient absorption spectrometer with high but still limited temporal resolution [24]. Theoretical investigations indicated the decisive role of CoIns during product formation and suggested a time scale of around 100 fs for the bond cleavage [21,25]. We now report a detailed analysis of two-color measurements [26] with 40 fs temporal resolution. Moreover, we calculate the expected experimental signal based on quantum dynamics simulations. In this way we can uniquely and unambiguously decipher the complex dynamics and show that one of two distinct CoIns is responsible for each reaction channel.

2. Experimental conditions

The investigated molecule DPMC absorbs at 270 nm and below by excitation in the phenyl rings (see Fig. 2a). The bond between the central sp^3 hybridized carbon and the chlorine is eventually broken. If the bond electrons are shared between the fragments (homolysis), the diphenylmethyl radical with a strong absorption at 327 nm results. If both electrons go to the chlorine (heterolysis), the diphenylmethyl cation with an absorption centered at 435 nm emerges.

For a full resolution of the temporal evolution we use two non-collinear optical parametric amplifiers (NOPA) and frequency doubling in 35 and 62 μm thin BBO crystals (see Fig. 1). Optimal compression with fused silica prisms only in the visible leads to pulses with about 25 fs duration [27,28]. A mechanical delay line affords the delay between the 270 nm pump pulse and the probe pulse at either 327 or 436 nm (for spectra see Fig. 2b). To avoid spurious contributions from the cell windows, the recordings were performed in a 50 μm free-flowing jet [29]. The evaporating solvent was continuously replenished to ensure a constant optical density. Special care was taken to determine the delay between pump and probe pulse to a single femtosecond accuracy. This was accomplished by splitting both pulses and a second “transfer experiment” with compensated dispersion (for details see SI). By referencing the transient signal with the shot-to-shot measured pump energy we increase the sensitivity [28].

In the ‘transfer experiment’ we monitor the two-photon-absorption (TPA) induced transmission change of the probe beam for temporal overlap with the pump beam in a 100 μm BBO crystal in non-phase-matching geometry [30]. In a first run the TPA in the BBO crystal (Fig. 2c) is recorded simultaneously with the TPA of the pure solvent (acetonitrile = ACN, Fig. 2d). In this way we measure the small but significant path length difference δt between pump and probe in the two arms of the experiment. The center of the curves is determined by fitting a Gaussian to the data. Then the pure solvent is exchanged by the molecular solution without any changes to the experimental geometry and a scan performed. As the BBO signal appears again at the overlap between pump and probe, it serves as marker for which position of the delay line there is temporal overlap in the dynamics measurement. Even if the delay between pump and probe has slightly changed over the 5 m paths, we can determine the differential changes with an accuracy of 10% of the crosscorrelation width of 38 fs, i.e. to 4 fs or 1.2 μm . Therefore we know the time-zero of the dynamics to this precision.

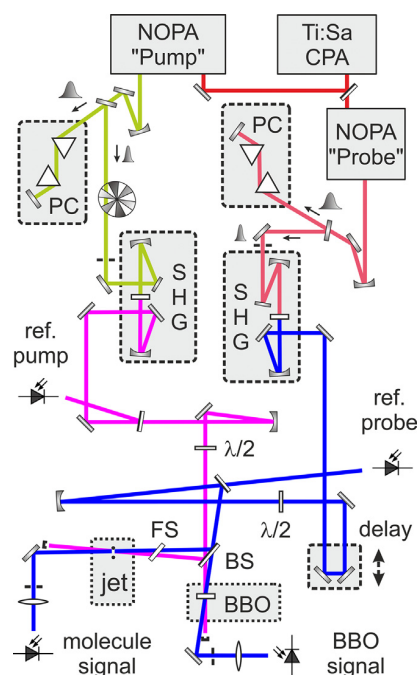


Fig. 1. Transient absorption setup. CPA: chirped pulse amplifier; NOPA: noncollinear optical parametric amplifier; PC: prism compressor; SHG: second harmonic generation; BS: beam splitter; FS: fused silica plate for compensation of dispersion.

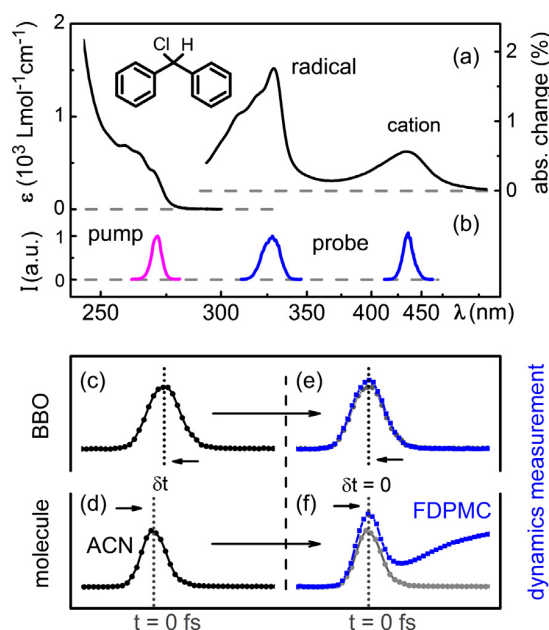


Fig. 2. (a) Absorption spectrum of DPMC in acetonitrile (left) and diphenylmethyl radical and cation transient absorption spectrum (right) 5 ps after 270 nm excitation. (b) Spectrum I_{pump} and I_{probe} of the pump and the probe pulses. (c)–(f) TPA signals used to determine the absolute time-zero between pump and probe pulses to 4 fs accuracy. The grey curves in (e) and (f) are the curves of (c) and (d) shifted to $\delta t = 0$. See text and SI for details.

With 200 nJ pump energy focused to 76 μm FWHM we excite about 2% of the DPMC molecules dissolved in ACN. The large molar absorption coefficient of the fragments (about 50,000 $\text{L/mol} \cdot \text{cm}$ as compared to 500 $\text{L/mol} \cdot \text{cm}$ for DPMC) leads to a sizable absorption change at the respective wavelength of each

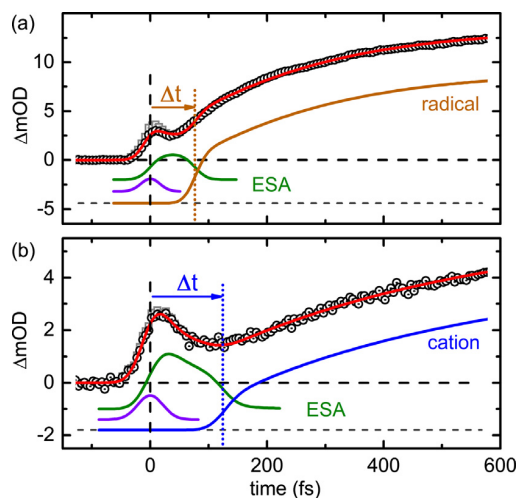


Fig. 3. Transient absorption (black circles) after UV excitation of DPMC in ACN at (a) 327 nm (diphenylmethyl radical) and (b) 436 nm (diphenylmethyl cation). The coherent signal from the solvent is subtracted from the raw data (open grey squares) to yield the pure molecular signal. The fit is shown with a solid line (red). The excited state absorption (ESA) (green) and the product absorption from the cation (blue) and radical (orange) are labeled in the plot. Below the ESA is the coherent signal from the molecule (purple). (For interpretation of the references to colour in this figure legend, the reader is referred to the web version of this article.)

diphenylmethyl redox state. The time dependence of the transient absorption (see Fig. 3) is the experimental observable that has to be evaluated and interpreted to recover the microscopic reaction dynamics. Through careful monitoring of the beam sizes, sample concentration and pulse energies we obtain not only a picture of the temporal behavior but even the quantitative yields [23].

3. Single wavelength pump-probe measurements

Roughly 40% of the excited DPMC dissociates homolytically. The transient signal rises with the cross correlation (CC) of the pump and probe pulse (38 fs FWHM) and falls off within the next tens of femtoseconds (see Fig. 3a). A comparison to the signal measured for pure acetonitrile shows that part of this early signal is due to two-photon absorption in the solvent that is proportional to the Gaussian shaped CC [31]. We correct the raw data (grey squares) by the properly scaled solvent contribution to obtain the pure molecular signal (black circles; compare SI). Even the pure molecular signal still contains a Gaussian shaped contribution centered exactly at delay zero and with a width equal to the optically measured CC. We assign this contribution to a coherent, nonresonant two-photon absorption. One of the pulses prepares a polarization in the molecule and the other pulse adds a second interaction leading to a higher electronic state. This interaction depletes the probe pulse as long as the pump-probe delay is within the CC convoluted with the electronic dephasing time of DPMC of likely a few tens of femtoseconds [32–34].

The remaining population part of the early molecular signal is proportional to the integral of the pump-probe CC as population in the S_1 state is accumulated from the initial polarization and the subsequent electronic dephasing. The signal strength is due to the excited state absorption (ESA) in the Franck-Condon (FC) region. Immediately after the pump pulse the wavepacket accelerates away from the FC point and the signal changes weakly. At a delay $\Delta t = 76$ fs the signal increases significantly within the time resolution. Finally it increases further with a quasi-exponential behavior and a time constant of 270 fs.

Only about 2% of the excited DPMC dissociates heterolytically and leads to a weak but well detectable transient absorption signal at 435 nm. The temporal behavior is analogous to the radical signal with two exceptions: the delay is now 124 fs and the signal increases much more at later times (see Fig. 3b). The increase from 76 to 124 fs for the delay in signal increase is the decisive difference between the homolytic and the heterolytic channel. Already the clearly non-exponential signal increase in the first 150 fs and even more the different times for the two distinct product channels deviate not only quantitatively but conceptually from the expectation of a rate model with two processes drawing from the same reservoir.

We used the described concepts of the signal evolution to model it quantitatively and to fit values to the data (see SI). The resulting fit is shown in Fig. 3 as red line and fits extremely well for both the radical and the cation. For demonstration of the various contributions we depict the time dependent ESA as green lines and the actual radical or cation contribution as orange and blue curve. For proper modeling the 20 ps electron transfer (ET) within the radical pairs that depletes the radical population and increases the cation population is included [23]. The effective 300 fs increase of both signals has been previously shown to originate from both planarization of the diphenylmethyl moieties after the bond cleavage and from solvation [22]. For a complete overview of all contributing processes see Ref. [35].

The ET in the radical pair is only possible if the cation is better stabilized than the radical. We therefore performed preliminary experiments with the transient absorption setup [24] and found that in methanol the ET does not contribute effectively to the cation generation. DPMC itself is not stable in methanol, but properly substituted derivatives are [36]. We chose the monofluoro-substituted diphenylmethylchloride (FDPMC) for additional measurements in methanol. The curves in Fig. 4 demonstrate that the general behavior is quite similar to DPMC and that the strong slow increase due to ET is indeed absent in the cation signal. FDPMC thus allows an even more unambiguous interpretation. As the same features are observed in DPMC and FDPMC, we can readily conclude that the bond cleavage is neither altered by the substitution nor the solvent. It is purely a property of the molecular core.

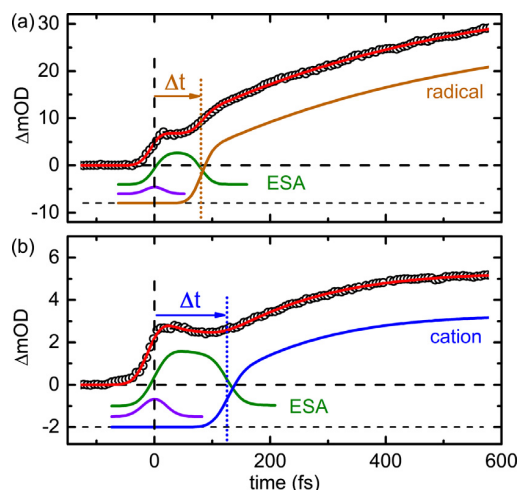


Fig. 4. Transient absorption (black circles) after UV excitation of FDPMC in methanol at (a) 327 nm (diphenylmethyl radical) and (b) 427 nm (diphenylmethyl cation). The coherent signal from the solvent is subtracted. The fit is shown with a solid line (red). The excited state absorption (ESA) (green) and the product absorption from the cation (blue) and radical (orange) are labeled in the plot. Below the ESA is the coherent signal from the molecule (purple). (For interpretation of the references to colour in this figure legend, the reader is referred to the web version of this article.)

Most importantly, we find times of 81 and 126 fs for the two delays, within experimental precision equal to the times found for DPMC.

4. Simulation of the absorption signal of the products

The experimental results are strong evidence for the involvement of Colns in the bond cleavage dynamics. No other reaction mechanism can be readily inferred from the ultrafast reaction times. In a previous quantum chemical investigation of DPMC the importance of Colns for the product channels was already demonstrated [21,25]. To connect directly to the experimental observables, the potential energy curves for DPMC, comprising the radical as well as the cation channel, were obtained at the ‘our own *n*-layered integrated molecular orbital and molecular mechanics’ (ONIOM) level of theory [37,38], using a program of our own design enabling to call different quantum chemistry program packages [39]. For the high-level system which was restricted to one of the two phenyl rings, we performed complete active space self-consistent field (CASSCF) calculations with an active space of 12 electrons in 10 orbitals. It includes the complete π system of one phenyl ring, the $\sigma_{\text{C-Cl}}$ and $\sigma_{\text{C-Cl}}^*$ orbitals of the C–Cl bond, and the two non-bonding *p* orbitals of the chlorine atom [25]. The low-level system, i.e. the complete system, was treated at the UB3LYP level of theory. The constrained low-level state (CLS) approximation for ONIOM was used [40] and the basis set employed was 6-31G(d). The CASSCF calculations were performed with the program package Molpro [41], the UB3LYP calculations with Gaussian [42]. We calculated the potential energy surfaces in a two-dimensional coordinate space spanned by the C–Cl distance $R_{\text{C-Cl}}$ and the quantity d_{py} describing the pyramidalization of the central methyl carbon atom [25,43]. The specially adapted reactive coordinate d_{py} includes relaxation in non-reactive coordinates like bond lengths or positioning of the phenyl rings which occur during planarization. By using the G-matrix formalism [43–45] this background relaxation is also included in the kinetic energy operator, which we demonstrated to have an important impact on the wavepacket dynamics. The design strategy for adapted reactive coordinates is given in Ref. [43]. The two coordinates $R_{\text{C-Cl}}$ and d_{py} have proven to be the most important for the ultrafast bond cleavage. A one-dimensional cut of the potential energy curves along $R_{\text{C-Cl}}$ is shown in Fig. 5.

The electronic states are shown in the diabatic representation. The optical excitation takes place in the phenyl ring and leads to the weakly bound S_1 state with $\pi\pi^*$ character (red line). The excitation energy is 4.88 eV (254 nm), which is in good agreement with the experimental value of 4.59 eV (270 nm) and previous CASPT2 calculations (4.90 eV, 253 nm) [21]. Close to the FC point the state is crossed by the repulsive S_2 and S_2' states, whose electronic structure corresponds to transitions from the Cl lone pairs to the π^* system of the phenyl ring (solid and dashed orange line). The S_2 and the S_2' state are located on the two phenyl rings, involve one chlorine *p* orbital each, and are nearly degenerate. The leading configurations of the S_3 state are of $\pi\pi^*$ and $\pi\sigma^*$ character. Due to the σ^* contribution the S_3 state is also repulsive (see blue line in Fig. 5).

The two spatially separated Colns can be easily recognized. At the first Coln, not only two but three electronic states are degenerate [25]. It leads to bond cleavage into the radical pair. The second Coln leads to the ion pair. Both Colns were also optimized and the structures are included in the SI. They are separated from the FC point by only 0.30 Å and 0.73 Å along $R_{\text{C-Cl}}$. A more detailed discussion can be found in Ref. [25]. The existence of Colns does not yet warrant an effective and ultrafast process, but it provides the possibility. Only dynamical calculations can clarify this question [9,46]. Coupling among all states is needed to describe the dynamic

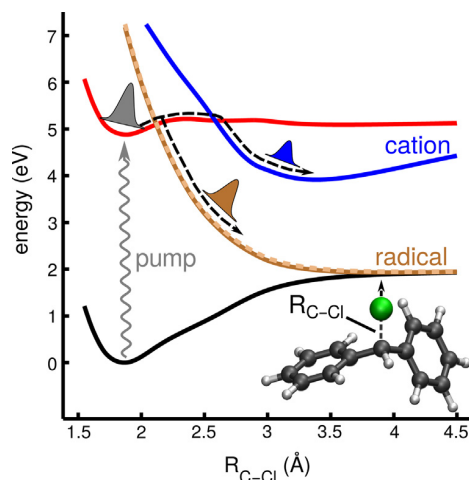


Fig. 5. Diabatic potential energy curves vs. C–Cl distance $R_{\text{C-Cl}}$ calculated on the ONIOM(CAS(12,10)/B3LYP) level of theory. Shown are the ground state S_0 (black), the excited states S_1 (red), S_2 (orange) and S_2' (orange-dashed) leading to the radical and S_3 (blue) leading to the cation. (For interpretation of the references to colour in this figure legend, the reader is referred to the web version of this article.)

situation appropriately. We performed the quantum dynamics calculations in the diabatic representation in order to treat the three-state Coln properly; the transformation of the coupling matrix elements can be found elsewhere [25]. The quantum dynamics were performed on the two-dimensional surfaces spanned by the selected reactive coordinates with a program of our own design which solves the time-dependent Schrödinger equation on a regular space grid using the Chebychev propagation scheme [47] and the G-matrix method for the kinetic Hamiltonian [43–45]. The ground state vibrational eigenfunction was transferred to the S_1 potential and slightly shifted to smaller $R_{\text{C-Cl}}$ and higher d_{py} to account for the minimal barrier being not contained in the ONIOM potential. The branching of the wavepacket at the Colns is followed in the diabatic representation, including the diabatic potential coupling matrix elements.

Based on the wavepacket dynamics the experimental signal can be calculated. First, the two-dimensional wavepacket Ψ is integrated along $R_{\text{C-Cl}}$

$$\Psi_{\text{sig}}(d_{\text{py}}, t) = \int_{R_{\text{C-Cl}}=2.8}^{\infty} \Psi(R_{\text{C-Cl}}, d_{\text{py}}, t) dR_{\text{C-Cl}} \quad (1)$$

which yields the wavepacket fraction Ψ_{sig} contributing to the signal. We assume that the wavepacket at C–Cl distances of $R_{\text{C-Cl}} < 2.8$ Å does not show any product absorption. This can be justified by the fact that the absorption of diphenylmethyl radicals and cations mainly involves the *p* orbital of the methyl carbon which still interacts strongly with the chlorine atom for $R_{\text{C-Cl}} < 2.8$ Å.

During planarization, the absorption of the diphenylmethyl cation changes strongly [22]. The same holds for the radical. Fig. 6 shows how the strongest absorption signature of each product evolves for $d_{\text{py}} = 0.5 - 0.0$ Å, which here is the relevant part of their full absorption spectra $S(d_{\text{py}}, \lambda)$. They are calculated at the DFT level of theory (M06-2X [48]/cc-pVTZ) including electrostatic solvent effects of acetonitrile using a polarizable continuum model [49].

The relaxed structure of both moieties is fully planarized with a $d_{\text{py}} = 0.0$ Å; the minimum structure of DPMC shows a $d_{\text{py}} = 0.42$ Å. Both spectra clearly show that the products only contribute to the absorption at the final position of the signal if the planarization has reached a value of d_{py} of approximately 0.2 Å. Thus, the coordinate

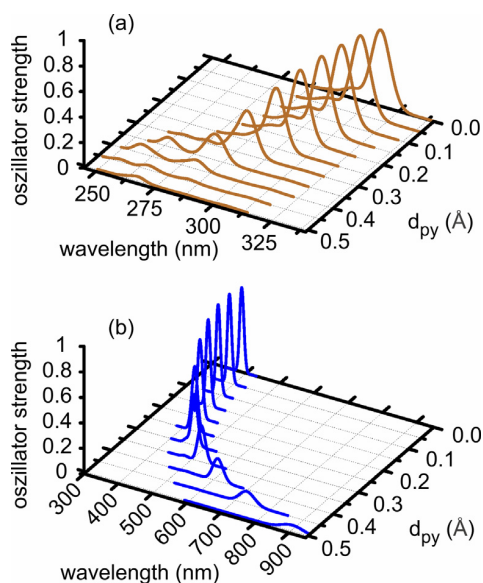


Fig. 6. Shift of the Gaussian broadened spectra $S(d_{py}, \lambda)$ ($\sigma = 400 \text{ cm}^{-1}$) for the DPM radical (a) and the DPM cation (b). The transition energies were calculated using TDDFT/M06-2X/ccpVTZ with PCM (acetonitrile). The geometries are reconstructed using the specially adapted coordinates introduced in [43]

d_{py} is not only important to describe the reaction properly but also enables to simulate the single wavelength absorption signal.

A closer look at the spectra (Fig. 6) reveals that the planarization has an opposite effect on how the strongest absorption band of the products develops. The radical shifts to the red (a) while the cation strongly shifts to the blue part of the spectrum (b). The reason for both effects is the energetic change of the non-bonding orbital of the central methyl C atom. During planarization, its character changes from sp^3 to p which entails a rise of the orbital energy due to the loss of s character. In the case of the radical, this orbital is occupied by one electron (singly occupied molecular orbital, SOMO). As the orbital energy rises, the energy of the electronic ground state D_0 rises accordingly. In the excited states D_4 and D_5 causing the absorption signal the electron density in the SOMO decreases. This means that their energy is less affected by the planarization. Thus, the energy gaps between D_4/D_5 and the ground state are reduced with decreasing d_{py} . In the case of the cation, the opposite effect occurs: The non-bonding orbital at the methyl C atom is unoccupied (lowest unoccupied molecular orbital, LUMO) in the ground state S_0 . In the excited state S_1 it is occupied. Thus, the energy of the S_1 state increases during the planarization while S_0 is unaffected. This causes the strong blue shift of the cation absorption. The absolute shift of the cation is about 2.5 times larger than the one of the radical because the radical has a more complex electronic structure. The states D_4 and D_5 entail excitation from the SOMO in π^* orbitals as well as from π orbitals in the SOMO resulting in a less pronounced effect of the orbital energy changes on the energy gaps.

Together with the wavepacket Ψ_{sig} , these spectra can now be employed to simulate the experimentally observed time-dependent single wavelength absorption $A(t)$:

$$A(t) = \int \left[\int \Psi_{sig}(d_{py}, t) \cdot S(d_{py}, \lambda) d(d_{py}) \right] I_{probe}(\lambda) d\lambda \quad (2)$$

$A(t)$ is the absorption at infinite time resolution, $S(d_{py}, \lambda)$ the calculated product spectrum and $I_{probe}(\lambda)$ the spectrum of the probe pulse. We first multiply Ψ_{sig} with the product spectrum S , which depends on d_{py} and λ . After integration along d_{py} , which yields

the total absorption of the product, we take into account the spectrum of the probe laser pulse via multiplication. We shifted the maximum of the probe pulse to account for the shift between the calculated and the measured maximum of the product. Integration along the wavelength yields the absorption of the total probe pulse with an infinite time resolution as for one point in time only the wavepacket at that time is taken into account. In the experiment the finite pulse length integrates over a range of times.

To include the temporal resolution of the experiment, we convoluted $A(t)$ with the Gaussian function $CC(t)$ with a FWHM of 40 fs found in the experiment:

$$A_{CC}(t) = A(t) \otimes CC(t) = \int A(t') CC(t - t') dt' \quad (3)$$

Fig. 7 depicts the simulated absorption signal of the diphenylmethyl radical and cation calculated according to Eqs. (1)–(3). It shows a good agreement with the experimental product absorption (blue and orange line in Fig. 3). The excited state wavepacket reaches the three-state CoIn and populates the repulsive S_2 and S_2^* states. After 67 fs the wavepacket has reached $R_{C-Cl} = 4.0 \text{ \AA}$ (black circles in Fig. 7a) [25] which results in a sudden rise of the signal after 130 fs (orange line). The latter is the time when the product population has reached a suitable planarization ($d_{py} \sim 0.2 \text{ \AA}$) to contribute to the signal. The simulation reveals that the sudden step-like increase of the signal is due to the major part of the wavepacket crossing through the first CoIn. The planarization mainly takes part subsequently and leads to the delay of the signal in comparison to the wavepacket population at $R_{C-Cl} = 4.0 \text{ \AA}$. The simulated absorption increase after the initial step is mainly due to further parts of the wavepacket which still pass through the CoIn but also due to ongoing planarization which increases the absorption strength. Additional effects caused by the relaxation of the solvent environment [22] and the subsequently arising electron transfer [23] are not included in the simulation.

In line with the small probability of 2% for heterolysis already found experimentally, only a minor fraction of the wavepacket stays on the S_1 surface. It crosses through the second CoIn leading to cation formation and reaches $R_{C-Cl} = 4.0 \text{ \AA}$ after approx. 143 fs [25]. As observed in the experiment, the simulated cation signal rises delayed compared to the radical absorption (Fig. 6(b)). It shows a sudden increase after 160 fs.

The quantum dynamical calculations show that both channels given by the two CoIns are indeed active on the ultrafast time scale.

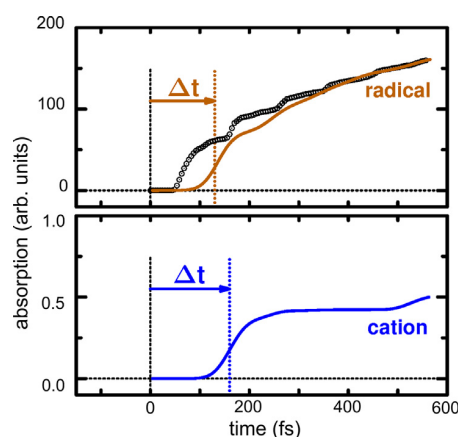


Fig. 7. Simulated absorption signal (solid lines) for the DPMC radical (top) and the DPMC cation (bottom) according to Eqs. (1)–(3). The black circles in the upper panel correspond to the part of the wavepacket which has reached $R_{C-Cl} > 4.0 \text{ \AA}$ on the S_2 and S_2^* states and is attributed to the radical fragments. For comparison it is normalized to the simulated absorption signal at the last time point.

They lead to the two distinct products, the diphenylmethyl radical and the diphenylmethyl cation. The radical is produced at a slightly earlier time than the cation as already indicated by the potential topology. The simulated time delay of 30 fs is in good agreement with the experimental results.

5. Conclusions

The following overall picture of the photoinitiated processes in DPMC evolves. The system (wavepacket) accelerates from the FC point upon optical excitation, but it stays in the shallow minimum for some tens of femtoseconds. Within less than 100 fs the weak potential barrier is crossed and the homolytic bond cleavage happens. The simulated signal appears only after 130 fs due to its dependence on the planarization coordinate. Similar effects occur for the cation. Thus, the delay time of both signals depends on the time scale when relevant Confs are crossed and on the time necessary to reach the geometry of the product absorption. The experiment suggests a time of 80 fs for the appearance of the radical pair in the electronic ground state. The remaining part of the wavepacket in the excited state proceeds to the second Con and at 125 fs ion pairs are detected. Interestingly, a very similar behavior is found for the DPMC analogon diphenylmethylbromide. Both dissociations are slowed down due to the heavier halogen leaving group and the processes can just be resolved with the broadband transient spectrometer [50].

The cooperative picture of highest temporal resolution and sensitivity measurements, thorough analysis and high level quantum chemical and dynamical calculation clearly establishes that the ultrafast photochemistry with two product channels is due to wavepacket motion through two distinct conical intersections. The relative reaction yield depends on the detailed motion of the wavepacket and the position of the Confs. A traditional rate model of two competing stochastic processes cannot explain the dynamics and branching ratio. For many other systems with two ultrafast appearing products, a similar behavior can be expected and a deviation from the traditional rate models will be needed for a correct description.

Acknowledgments

The authors thank H. Mayr for stimulating discussions, C. Nolte for the synthesis of the FDPMC, L. Maisenbacher for valuable experimental help and F. Milota and J. Hauer for the jet design. We gratefully acknowledge financial support by Deutsche Forschungsgemeinschaft through the excellence cluster 'Munich Center for Advanced Photonics' (MAP) and the SFB 749, as well as the Emmy Noether Programme (B.P.F., Grant No. FI 2034/1-1) and support by the Leibniz-Rechenzentrum der Bayerischen Akademie der Wissenschaften (LRZ) through allocation of computing time.

Appendix A. Supplementary material

Supplementary data associated with this article can be found, in the online version, at <http://dx.doi.org/10.1016/j.cplett.2017.02.086>.

References

- [1] A.H. Zewail, *Femtochemistry: Ultrafast Dynamics of the Chemical Bond*, vols. 1 and 2, World Scientific, Singapore, 1994.
- [2] M.J. Rosker, M. Dantus, A.H. Zewail, *J. Chem. Phys.* 89 (1988) 6113.
- [3] A.H. Zewail, *Angew. Chem. Int. Ed.* 39 (2000) 2586.
- [4] A.W.P. Fitzpatrick, G.M. Vanacore, A.H. Zewail, *Proc. Natl. Acad. Sci. USA* 112 (2015) 3380.
- [5] E. Najafi, T.D. Scarborough, J. Tang, A.H. Zewail, *Science* 347 (2015) 164.
- [6] M. Dantus, M.J. Rosker, A.H. Zewail, *J. Chem. Phys.* 89 (1988) 6128.
- [7] M. Olivucci, M.A. Robb, F. Bernardi, *Conformational Analysis of Excited States*, Wiley-VCH, New York, 2000.
- [8] D.R. Yarkony, *J. Phys. Chem. A* 105 (2001) 6277.
- [9] W. Domcke, D.R. Yarkony, H. Köppel, *Conical Intersections: Electronic Structure, Dynamics and Spectroscopy*, World Scientific Publishing, Singapore, 2004.
- [10] S. Thallmair, M. Kowalewski, J.P.P. Zauleck, M.K. Roos, R. de Vivie-Riedle, *J. Phys. Chem. Lett.* 5 (2014) 3480.
- [11] S. Thallmair, J.P.P. Zauleck, R. de Vivie-Riedle, *J. Chem. Theory Comput.* 11 (2015) 1987.
- [12] S.A. Harich, X. Yang, X. Yang, R.N. Dixon, *Phys. Rev. Lett.* 87 (2001) 253201.
- [13] Y.H. Jiang, A. Rudenko, O. Herrwerth, L. Foucar, M. Kurka, K.U. Kühnel, M. Lezius, M.F. Kling, J. van Tilborg, A. Belkacem, K. Ueda, S. Düsterer, R. Treusch, C.D. Schröter, R. Moshhammer, J. Ullrich, *Phys. Rev. Lett.* 105 (2010) 263002.
- [14] M.E.-A. Madjet, O. Vendrell, R. Santra, *Phys. Rev. Lett.* 107 (2011) 263002.
- [15] A. Nenov, T. Cordes, T.T. Herzog, W. Zinth, R. de Vivie-Riedle, *J. Phys. Chem. A* 114 (2010) 13016.
- [16] D. Polli, P. Altoè, O. Weingart, K.M. Spillane, C. Manzoni, D. Brida, G. Tomasello, G. Orlandi, P. Kukura, R.A. Mathies, M. Garavelli, G. Cerullo, *Nature* 467 (2010) 440.
- [17] J.L. White, J. Kim, V.S. Petrović, P.H. Bucksbaum, *J. Chem. Phys.* 136 (2012) 054303.
- [18] K. Kosma, S.A. Trushin, W. Fuß, W.E. Schmid, *Phys. Chem. Chem. Phys.* 11 (2009) 172.
- [19] N.J. Turro, V. Ramamurthy, J.C. Scaiano, *Modern Molecular Photochemistry of Organic Molecules*, University Science Books, Sausalito, 2010.
- [20] J. Knorr, P. Sokkar, S. Schott, P. Costa, W. Thiel, W. Sander, E. Sanchez-Garcia, P. Nuernberger, *Nat. Commun.* 7 (2016) 12968.
- [21] B.P. Fingerhut, D. Geppert, R. de Vivie-Riedle, *Chem. Phys.* 343 (2008) 329.
- [22] B.P. Fingerhut, C.F. Sailer, J. Ammer, E. Riedle, R. de Vivie-Riedle, *J. Phys. Chem. A* 116 (2012) 11064.
- [23] C.F. Sailer, S. Thallmair, B.P. Fingerhut, C. Nolte, J. Ammer, H. Mayr, I. Pugliesi, R. de Vivie-Riedle, E. Riedle, *ChemPhysChem* 14 (2013) 1423.
- [24] U. Megerle, I. Pugliesi, C. Schrieffer, C.F. Sailer, E. Riedle, *Appl. Phys. B* 96 (2009) 215.
- [25] S. Thallmair, M.K. Roos, R. de Vivie-Riedle, *Struct. Dyn.* 3 (2016) 043205.
- [26] C. Sailer, N. Krebs, B. Fingerhut, R. de Vivie-Riedle, E. Riedle, in: M. Chergui, S. Cundiff, A. Taylor, R. de Vivie-Riedle, K. Yamanouchi (Eds.), *Ultrafast Phenomena XVIII*, EPJ Web of Conferences 41 (2013) 05042.
- [27] P. Baum, S. Lochbrunner, E. Riedle, *Appl. Phys. B* 79 (2004) 1027.
- [28] C. Schrieffer, S. Lochbrunner, E. Riedle, D.J. Nesbitt, *Rev. Sci. Instrum.* 79 (2008) 013107.
- [29] F. Milota, J. Sperling, A. Nemeth, H.F. Kauffmann, *Chem. Phys.* 357 (2009) 45.
- [30] C. Homann, N. Krebs, E. Riedle, *Appl. Phys. B* 104 (2011) 783.
- [31] M. Lorenc, M. Ziolk, R. Naskrecki, J. Karolczak, J. Kubicki, A. Maciejewski, *Appl. Phys. B* 74 (2002) 19.
- [32] J.-Y. Bigot, M.T. Portella, R.W. Schoenlein, C.J. Bardeen, A. Migus, C.V. Shank, *Phys. Rev. Lett.* 66 (1991) 1138.
- [33] E.T.J. Nibbering, D.A. Wiersma, K. Duppen, *Phys. Rev. Lett.* 66 (1991) 2464.
- [34] N. Krebs, I. Pugliesi, J. Hauer, E. Riedle, *New J. Phys.* 15 (2013) 085016.
- [35] C.F. Sailer, E. Riedle, *Pure Appl. Chem.* 85 (2013) 1487.
- [36] B. Denegri, A. Streiter, S. Jurić, A.R. Ofial, O. Kronja, H. Mayr, *Chem. Eur. J.* 12 (2006) 1648.
- [37] M. Svensson, S. Humbel, R.D.J. Froese, T. Matsubara, S. Sieber, K. Morokuma, *J. Phys. Chem.* 100 (1996) 19357.
- [38] L.W. Chung, W.M.C. Sameera, R. Ramozzi, A.J. Page, M. Hatanaka, G.P. Petrova, T.V. Harris, X. Li, Z. Ke, F. Liu, H.-B. Li, L. Ding, K. Morokuma, *Chem. Rev.* 115 (2015) 5678.
- [39] B.P. Fingerhut, S. Oesterling, K. Haiser, K. Heil, A. Glas, W.J. Schreier, W. Zinth, T. Carell, R. de Vivie-Riedle, *J. Chem. Phys.* 136 (2012) 204307.
- [40] M.J. Bearpark, S.M. Larkin, T. Vreven, *J. Phys. Chem. A* 112 (2008) 7286.
- [41] H.-J. Werner, P.J. Knowles, G. Knizia, F.R. Manby, M. Schütz, P. Celani, T. Korona, R. Lindh, A. Mitrushenkov, G. Rauhut, K.R. Shamasundar, T.B. Adler, R.D. Amos, A. Bernhardsson, A. Berning, D.L. Cooper, M.J.O. Deegan, A.J. Dobbyn, F. Eckert, E. Goll, C. Hampel, A. Hesselmann, G. Hetzer, T. Hrenar, G. Jansen, C. Köppl, Y. Liu, A. W. Lloyd, R.A. Mata, A.J. May, S.J. McNicholas, W. Meyer, M.E. Mura, A. Nicklass, D.P. O'Neill, P. Palmieri, D. Peng, K. Pflüger, R. Pitzer, M. Reiher, T. Shiozaki, H. Stoll, A.J. Stone, R. Tarroni, T. Thorsteinsson, M. Wang, MOLPRO, Version 2012.1, A Package of Ab Initio Programs, 2012.
- [42] M.J. Frisch, G.W. Trucks, H.B. Schlegel, G.E. Scuseria, M.A. Robb, J.R. Cheeseman, G. Scalmani, V. Barone, B. Mennucci, G.A. Petersson, H. Nakatsuji, M. Caricato, X. Li, H.P. Hratchian, A.F. Izmaylov, J. Bloino, G. Zheng, J.L. Sonnenberg, M. Hada, M. Ehara, K. Toyota, R. Fukuda, J. Hasegawa, M. Ishida, T. Naka-jima, Y. Honda, O. Kitao, H. Nakai, T. Vreven, J.A. Montgomery, Jr., J.E. Peralta, F. Ogliaro, M. Bearpark, J.J. Heyd, E. Brothers, K.N. Kudin, V.N. Staroverov, R. Kobayashi, J. Normand, K. Raghavachari, A. Rendell, J.C. Burant, S.S. Iyengar, J. Tomasi, M. Cossi, N. Rega, J.M. Millam, M. Klene, J.E. Knox, J.B. Cross, V. Bak-ken, C. Adamo, J. Jaramillo, R. Gomperts, R.E. Stratmann, O. Yazyev, A.J. Austin, R. Cammi, C. Pomelli, J.W. Ochterski, R.L. Martin, K. Morokuma, V.G. Zakrzewski, G.A. Voth, P. Salvador, J.J. Dannenberg, S. Dapprich, A.D. Daniels, Ö. Farkas, J.B. Foresman, J.V. Ortiz, J. Cioslowski, D.J. Fox, Gaussian 09, Revision E.01, Gaussian Inc, Wallingford CT, 2009.
- [43] S. Thallmair, M.K. Roos, R. de Vivie-Riedle, *J. Chem. Phys.* 144 (2016) 234104.
- [44] E.B. Wilson Jr., J.C. Decius, P.C. Cross, *Molecular Vibrations*, McGraw-Hill, New York, 1955.

- [45] L. Schaad, J.J. Hu, *Mol. Struct. Theochem* 185 (1989) 203.
- [46] T.K. Allison, H. Tao, W.J. Glover, T.W. Wright, A.M. Stooke, C. Khurmi, J. van Tilborg, Y. Liu, R.W. Falcone, T.J. Martínez, A. Belkacem, *J. Chem. Phys.* 136 (2012) 124317.
- [47] H. Tal-Ezer, R. Kosloff, *J. Chem. Phys.* 81 (1984) 3967.
- [48] Y. Zhao, D.G. Truhlar, *Theor. Chem. Acc.* 120 (2008) 215.
- [49] J. Tomasi, B. Mennucci, R. Cammi, *Chem. Rev.* 105 (2005) 2999.
- [50] E. Riedle, M. Bradler, M. Wenninger, C.F. Sailer, I. Pugliesi, *Faraday Disc.* 163 (2013) 139.

2.3. The effect of a higher homologue on the reaction dynamics

The periodic table was built by clustering elements based on similar behavior [112]. For this reason, both chlorine and bromine are found in the same group, the halogens. Both can be used as leaving group in diphenylmethyl compounds to yield a radical or ion pair [88]. After studying the reaction dynamics for $\text{Ph}_2\text{CH}-\text{Cl}$ (section 2.1) and verifying its mechanism (section 2.2), it is now interesting to turn to the higher homologue bromine as leaving group. As both compounds hold the same number of valence electrons and, thus, have the same bonding situation, the excited states and their character are inferred to be similar with analogous CoIns. But as already mentioned in the introduction of this chapter, the experimental transient absorption measurements astounds with differences: Besides longer delay times for $\text{Ph}_2\text{CH}^\bullet$ (100 fs) and Ph_2CH^+ (200 fs) and a product ratio shifted towards a more balanced distribution (70%/30% radical/cation) [103], the signals of both channels are superimposed by a small-amplitude oscillation with a frequency of 300 cm^{-1} ($\text{Ph}_2\text{CH}^\bullet$) and 350 cm^{-1} (Ph_2CH^+), respectively [104].

In the article “Ultrafast non-adiabatic dynamics of excited diphenylmethyl bromide elucidated by quantum dynamics and semi-classical on-the-fly dynamics” published by *Physical Chemistry Chemical Physics* the initial bond cleavage reaction of $\text{Ph}_2\text{CH}-\text{Br}$ is simulated for the first time [113]. On the one hand, a QD approach is used. The extensive transfer of methods and solutions from the chlorine case is advantageous, using the same coordinate system $\{r, d_{py}\}$ based on the Wilson G-matrix method (chapter 1). On the other hand, full-dimensional MQCD is employed, allowing further insights into the molecular motions in the full configuration space and an evaluation of the dimensionality reduction. Combining these two complementary approaches can in this way result in a more complete picture of the reaction dynamics. It is chosen to especially unravel the role of vibrations during the bond cleavage. Analogously to $\text{Ph}_2\text{CH}-\text{Cl}$ the ONIOM method (see appendix A) is employed for the QC with only one phenyl ring in the model system and CASSCF as high level method. The application of ONIOM in semi-classical dynamics follows the implementation described in the literature [114].

The key points of the article are:

- Like for $\text{Ph}_2\text{CH}-\text{Cl}$ a three-state and a two-state CoIn are optimized, opening up the radical and the cationic channel, respectively. The barriers before these CoIns are significantly lower as for the chlorine case and the minima of S_0 and S_1 have a ellipsoidal shape in the two-dimensional subspace.
- In the QD delay times of 110 fs ($\text{Ph}_2\text{CH}^\bullet$) and 130 fs (Ph_2CH^+) result, in good agreement with the experiment. The radical pair is confirmed as the main product. Significant amounts of ion pairs are only obtained if the coordinate d_{py} is further triggered, an effect attributed to the reduced dimensionality. The wave packet initially follows the shape of the minima towards smaller d_{py} values, later oscillates back and forth in d_{py} direction, while propagating towards larger r values.
- The MQCD calculations confirm the reaction mechanism *via* two CoIns and show similar delay times as the QD. The product distribution is in good agreement with the experiment.
- The vibrations occurring during the bond cleavage are analyzed in detail. For the MQCD trajectories spectrograms are calculated using the velocity autocorrelation function (VACF). These spectrograms demonstrate the differences between

the product channel, where a band at 1300 cm^{-1} is characteristic for the radical channel and a band at 1100 cm^{-1} for the ion pair channel.

- Integrating the QD wave packet in distinct areas reveals an oscillation occurring in the S_1 minimum deemed responsible for the signal fluctuations in the experiment.

This work not only demonstrates the benefit of using complementary methods to elucidate the ongoing dynamics and the involved vibrations, but also clearly works out the similarities and differences between $\text{Ph}_2\text{CH}-\text{Br}$ and $\text{Ph}_2\text{CH}-\text{Cl}$. It becomes apparent that this seemingly small change in the leaving group has a decisive impact on the PESs and, thus, the motions of the wave packet.

The article “Ultrafast non-adiabatic dynamics of excited diphenylmethyl bromide elucidated by quantum dynamics and semi-classical on-the-fly dynamics” published by *Physical Chemistry Chemical Physics* is reprinted here from *Phys. Chem. Chem. Phys.* **20**, 22753–22761 (2018) with permission from the PCCP Owner societies. The Supporting Information for this article is available under <https://doi.org/10.1039/c8cp03257b>.



PCCP

PAPER

View Article Online

View Journal | View Issue



Cite this: *Phys. Chem. Chem. Phys.*,
2018, 20, 22753

Ultrafast non-adiabatic dynamics of excited diphenylmethyl bromide elucidated by quantum dynamics and semi-classical on-the-fly dynamics†

Franziska Schüppel, Matthias K. Roos and Regina de Vivie-Riedle *

Carbocations and carboradicals are key intermediates in organic chemistry. Typically UV laser excitation is used to induce homolytical or heterolytical bond cleavage in suitable precursor molecules. Of special interest hereby are diphenylmethyl compounds ($\text{Ph}_2\text{CH-X}$) with $\text{X} = \text{Cl}, \text{Br}$ as a leaving group as they form diphenylmethyl radicals ($\text{Ph}_2\text{CH}^\bullet$) and cations (Ph_2CH^+) within a femtosecond time scale in polar solvents. In this work, we build on our methodology developed for the chlorine case and investigate the photodissociation reaction of $\text{Ph}_2\text{CH-Br}$ by state-of-the-art theoretical methods. On the one hand, we employ specially adapted reactive coordinates for a grid-based wave packet dynamics in reduced dimensionality using the Wilson G-matrix ansatz for the kinetic part of the Hamiltonian. On the other hand, we use full-dimensional semiclassical on-the-fly dynamics with Tully's fewest switches surface hopping routine for comparison. We apply both methods to explain remarkable differences in experimental transient absorption measurements for Cl or Br as the leaving group. The wave packet motion, visible only for the bromine leaving group, can be related to the crucial role of the central carbon atom, which undergoes rehybridization from sp^3 to sp^2 during the photoinduced bond cleavage. Comparable features are the two consecutive conical intersections near the Franck-Condon region controlling the product splitting to $\text{Ph}_2\text{CH}^\bullet/\text{Br}^\bullet$ and $\text{Ph}_2\text{CH}^+/\text{Br}^-$ as well as the difference in delay time for the respective product formation.

Received 22nd May 2018,
Accepted 15th August 2018

DOI: 10.1039/c8cp03257b

rsc.li/pccp

1 Introduction

Carbocations and to a lesser extent carboradicals are important building blocks in organic synthesis.^{1,2} Furthermore, carbocations are used to study the kinetics of reactions with nucleophiles to build reference scales to predict reactivities.^{3,4} The highly reactive species can be prepared by irradiating a suitable precursor molecule with UV light,⁵⁻⁷ and in this way initiating a bond cleavage that can occur homolytically or heterolytically. Widely used^{4,7-9} precursors are diphenylmethyl compounds $\text{Ph}_2\text{CH-X}$ with *e.g.* $\text{X} = \text{Cl}, \text{Br}$ as leaving groups. These compounds are distinguishable by clearly distinct spectra of their photo-products and thus can be easily studied by transient absorption measurements.

In the case of chlorine this was done extensively,⁸⁻¹² lately also with extremely high temporal resolution allowing changes to be resolved in the few femtosecond regime.¹² Delay times of 76 fs for the formation of the radical pair and 124 fs for the

formation of the ion pair were reported.^{11,12} With 95% radical pairs, the product ratio was clearly biased towards the homolytic channel, with only 5% ion pairs. Recently, we could elucidate the initial processes occurring during the ultrafast dissociation of $\text{Ph}_2\text{CH-Cl}$ with theoretical methods.^{12,13} Especially, we discovered the leading role of the chlorine lone pairs. They provide an effective connection between the initial photo-accessible $\pi\pi^*$ state and the radical-pair product channel. The coupling into the lone pair states occurs at a three-state conical intersection (CoIn), the first in a sequence of two CoIns near the Franck-Condon (FC) region. The second CoIn at slightly larger carbon-chlorine distance is a two-state CoIn and connects the $\pi\pi^*$ state with the ion-pair product channel. This sequence of CoIns completely defines the product ratio. The delay times were in good agreement with the experimental ones and we could confirm the radical pair as the main product of the initial bond cleavage. Overall, we could successfully explain the reaction process in the first hundreds of femtoseconds.

Bromine, the heavier homologue of chlorine, was also studied experimentally as a leaving group.^{14,15} Here, the dissociation reaction is slower compared to the chlorine case. The reported delay times with respect to the optical excitation are slightly longer for the rise of both product signals. The radical pair is

Department of Chemistry, Ludwig-Maximilians-Universität München,
Butenandtstraße 5-13, 81377 Munich, Germany.

E-mail: Regina.de_Vivie@cup.uni-muenchen.de

† Electronic supplementary information (ESI) available. See DOI: 10.1039/c8cp03257b

detected after 100 fs and the ion pair after 200 fs. The product ratio still favors the homolytic channel, but with 70% radical pairs and 30% ion pairs the excess of radicals is not so pronounced. More remarkable is a small-amplitude oscillation superimposed on the rise of the transient absorption signals that was associated with a vibrational mode of the remaining carbon backbone.¹⁴ To the best of our knowledge, there are no theoretical studies on the photodissociation of Ph₂CH–Br or this oscillation in particular.

In this work, we investigate the photo-induced bond cleavage of Ph₂CH–Br by quantum dynamical and mixed quantum-classical (semi-classical) methods. Specific geometry points that are important for the product splitting such as CoIns are identified and optimized with quantum chemical methods. For the dynamics simulation we apply two different approaches. On the one hand, like in the chlorine case, we employ grid-based wave packet dynamics in reduced dimensionality using the Wilson G-matrix^{16–18} ansatz for the kinetic energy operator. This ansatz allows us to adequately treat arbitrary coordinates in the Hamiltonian, in this case our specially adapted reactive coordinates.¹⁹ With these coordinates, we can take into account the relaxation of the carbon backbone during the bond cleavage without optimizations for each grid point. On the other hand, we use Tully's fewest switches surface hopping routine²⁰ in on-the-fly semi-classical dynamics simulations. Here, due to its full-dimensional nature, we can analyze the motions of the molecule in the complete configuration space using the velocity autocorrelation function to calculate the spectrogram. Both dynamics methods are based on the same electronic structure method. We choose an "Our Own N-Layered Integrated Molecular Orbital and Molecular Mechanics" (ONIOM)^{21–23} quantum chemical description with complete active space self-consistent field (CASSCF) as a high level of theory. The focus of our work is to discuss and explain the differences caused in the photodissociation dynamics by changing the leaving group from chlorine to bromine.

This article is structured as follows: In Section 2, we first introduce the partitioning of the ONIOM layers used in both dynamics simulations, and then discuss details of each of these methods. Section 3.1 deals with optimized minima and CoIns and shows first potential energy surfaces. In Section 3.2, we discuss the results of the quantum dynamical simulations. Section 3.3 concerns the semi-classical dynamical simulations. Section 3.4 discusses the vibrational motions driving the reaction and relates them to the experimental observables. Finally, Section 4 summarizes our findings and concludes this work.

2 Computational details

As shown for the lighter homologue Ph₂CH–Cl the π -systems of the phenyl rings are not coupled and can be separated.^{13,24} In Ph₂CH–Br they form an angle of 72.5° at the FC point. Since Ph₂CH–Br is a rather large molecule to treat at the CASSCF level of theory, the computational effort is reduced by using an ONIOM two-layer ansatz.^{21,22} We do so by employing a program of our own design²³ with interfaces to various

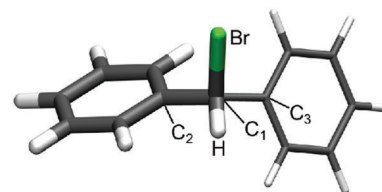


Fig. 1 Geometry of Ph₂CH–Br showing the ONIOM partitioning. The thick part shows the model system PhCH₂–Br calculated at the high level of theory CAS(12,10). The second phenyl ring is only included for calculations at the low level of theory and replaced by an H atom in the model system.

quantum chemistry program packages. Thus, one phenyl ring is replaced by an H atom for the ONIOM model system forming PhCH₂–Br (Fig. 1) treated at the CASSCF level of theory with the program package Molpro2012.^{25,26} The active space (Fig. S10, ESI[†]) consists of 12 electrons in 10 orbitals, CAS(12,10), and contains all π orbitals of the one phenyl ring, the σ/σ^* orbitals of the C₁–Br bond and two lone pair orbitals (n_1 , n_2) of the bromine atom. It is analogous to the active space used for the description of Ph₂CH–Cl.¹³ Following the argument of uncoupled π -systems, the excitation can be seen as localized on only one phenyl ring and so the constraint low-level state (CLS) approximation²⁷ is used. The complete system is either calculated at the B3LYP level of theory with the program package Gaussian09²⁸ (in the quantum dynamics part) or at the HF level of theory with Molpro2012 (in the semi-classical part). Minima and the two-state CoIn of the model system, PhCH₂–Br, were optimized at the CAS(12,10) level of theory using the program package Molpro2012. The optimization of the three-state CoIn was done at the same level of theory using the program package Columbus.^{29–32} For all calculations we employed the binning-SVP basis set for the bromine atom and the 6-31G(d) basis set for all other atoms.

2.1 Quantum dynamics

For the quantum dynamical simulation, we reduce the number of coordinates because a full-dimensional simulation on *ab initio* potential energy surfaces (PESs) is not feasible. The photodissociation is described by two specially adapted reactive coordinates¹⁹ that already proved to capture the ultrafast dynamics of the lighter homologue.¹³ The first one is the C₁–Br distance r describing the bond cleavage. The second coordinate describes the change of the pyramidalization of the C₁ atom due to rehybridization from sp³ to sp² along the bond cleavage. It is quantified as the distance d_{py} from atom C₁ to the plane spanned by its three neighboring atoms. Both reactive coordinates are shown in Fig. 2.

To include relaxation in the reduced coordinate system, we used the already mentioned concept of specially adapted reactive coordinates¹⁹ that was developed in our group. Significant changes of further internal coordinates during the bond cleavage were considered *via* fit functions derived from a relaxed scan along the C₁–Br bond length. Besides the second active coordinate d_{py} , changes along bonds and angles including the central C₁ atom and the relative position between the phenyl

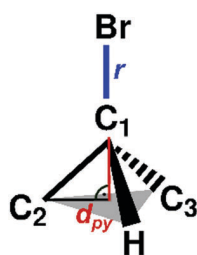


Fig. 2 Reactive coordinates r and d_{py} for the quantum dynamical simulation.

rings emerge as most important. A detailed description of this procedure is reviewed in the ESI†

The Hamiltonian has to be transformed from Cartesian coordinates into the chosen reactive coordinates. The challenging part hereby is the kinetic energy operator $\hat{T}(x,y,z)$ which can be expressed in the reactive coordinates using the Wilson G-Matrix formalism.^{16–19} The transformed operator $\hat{T}(r,d_{py})$ is of the form:

$$\hat{T}(r, d_{py}) = -\frac{\hbar^2}{2} \left[\frac{\partial}{\partial r} G_{rr} \frac{\partial}{\partial r} + \frac{\partial}{\partial r} G_{rd_{py}} \frac{\partial}{\partial d_{py}} + \frac{\partial}{\partial d_{py}} G_{d_{py}r} \frac{\partial}{\partial r} + \frac{\partial}{\partial d_{py}} G_{d_{py}d_{py}} \frac{\partial}{\partial d_{py}} \right],$$

with the diagonal elements G_{rr} , $G_{d_{py}d_{py}}$ and the equal, off-diagonal elements $G_{rd_{py}}$, $G_{d_{py}r}$. The G-Matrix elements are shown in Fig. S3 (ESI†).

We used a diabatic description of the potential energy operator for our simulation and included the five lowest singlet states (π^2 , $\pi\pi^*$, $n_1\pi^*$, $n_2\pi^*$ and $\pi\sigma^*$) at the ONIOM(CAS(12,10):B3LYP) level of theory (Fig. S2, ESI†). The transformation into the diabatic picture was implemented as described in ref. 13 using the dipole and transition dipole moment. The diabatic coupling matrix elements (DCMEs), necessary to describe population transfer between diabatic states, result from this transformation, as well. The diabatic representation is essential for the quantum dynamics simulation because it allows us to avoid population transfer between the degenerate lone pair states ($n_1\pi^*$ and $n_2\pi^*$). In the diabatic description we can set this coupling to zero and completely eliminate the interaction that is unimportant for the product distribution. Instead, we only include DCMEs (Fig. S4, ESI†) in the area of the optimized CoIns between the states of interest.

The wave packet simulation was performed with a program of our own design. For the time propagation we used the Chebychev propagator³³ with a time step of $\Delta t = 10$ a.u. The laser excitation is simulated in the dipole approximation with a Gaussian shaped laser pulse adapted to the experimental parameters (FWHM = 18 fs; $\lambda = 250$ nm; $I_{\max} = 5.63 \times 10^{13}$ W cm⁻²; $t_0 = 0$ fs). More technical details of the simulation are listed in the ESI†

2.2 Semi-classical dynamics

We used our modified version of the program package NewtonX^{34,35} with an interface for Molpro2012^{25,26} implementing the ONIOM

code²³ for the semi-classical dynamics. The five lowest singlet states were considered for the simulation calculated at the ONIOM(CAS(12,10):HF) level of theory. We ran 100 trajectories with different initial conditions generated from a Wigner distribution³⁶ based on a frequency analysis of Ph₂CH–Br in the ground state at the B3LYP level of theory. 69 trajectories reached the end of the selected simulation time and showed C₁–Br bond cleavage. Three trajectories remained in the FC region and did not show any reaction after 250 fs. The other 28 trajectories broke down in the beginning of the simulation in the FC region because the CASSCF calculation did not converge. The 69 reactive trajectories are used as the basis for our analysis which results in a maximum statistical error of less than 12%.³⁷ Investigating a two-pathway mechanism with an experimental distribution of 70%/30% is therefore possible with the given number of trajectories. The Wigner distribution was transferred to the $\pi\pi^*$ state to start the simulation. Transitions between the electronic states were treated according to Tully's fewest switches surface hopping routine.²⁰ A simulation time of 250 fs and a time step of 0.5 fs were applied. The integration of Newton's equations was done with the Velocity Verlet algorithm.

Furthermore, we performed trajectory calculations for the diphenylmethyl radical and cation in the ground state after C₁–Br bond cleavage. This simulation was performed with NewtonX^{34,35} and its interface to Gaussian09.²⁸ To obtain the initial conditions, we used the geometry and velocity at 250 fs of each of the previous trajectories describing the dynamics of the precursor Ph₂CH–Br and discarded the bromine atom. In doing so, we could follow the ground state dynamics of the two fragments (Ph₂CH•/Ph₂CH⁺) at the B3LYP level of theory for a further 1000 fs.

3 Results and discussion

3.1 Potential energy surfaces of Ph₂CH–Br

Within the applied CLS approximation the electronic excitation is restricted to the model system PhCH₂–Br. Optimized geometry points on the PESs that are important during the dissociation are shown in Fig. 3. The closed shell ground state minimum (Fig. 3a) has a C₁–Br bond length r of 2.02 Å and the central carbon atom C₁ is completely sp³ hybridized with a value of $d_{py} = 0.34$ Å. The S₁ minimum with $\pi\pi^*$ character lies close to the FC region (Fig. 3b) with a slightly larger r of 2.06 Å and almost no change in d_{py} (0.32 Å). A three-state CoIn (S₃/S₂/S₁, CoIn₁) between the $\pi\pi^*$ state and the two degenerate $n_1\pi^*/n_2\pi^*$ states (Fig. 3c) is located at $r = 2.21$ Å and $d_{py} = 0.25$ Å. A second CoIn (S₄/S₃, CoIn₂) between the $\pi\pi^*$ state and a state with $\pi\sigma^*$ character is found at $r = 2.80$ Å and $d_{py} = 0.06$ Å. Here, the central C₁ atom is already sp² hybridized (Fig. 3d).

Ground and excited state PESs along the bond cleavage coordinate r and the hybridization coordinate d_{py} are calculated at the ONIOM(CAS(12,10):B3LYP) level of theory. For a first overview, a one-dimensional cut along r for constant $d_{py} = 0.35$ Å is shown in Fig. 4 for the corresponding diabatic PESs. The photodissociation reaction starts with a $\pi\pi^*$ excitation from the ground state to the S₁ state. The excitation energy of 4.85 eV

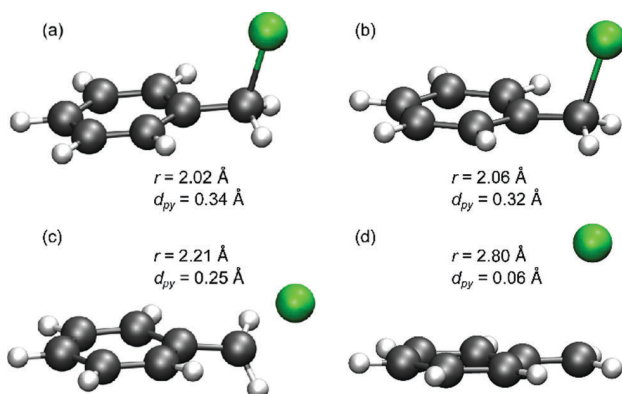


Fig. 3 Optimized geometries at the CAS(12,10) level of theory of the model system PhCH₂-Br of (a) the S₀ minimum, (b) the S₁ minimum, (c) the three-state Con (Con₁) and (d) the two-state Con (Con₂).

(255 nm) is hereby in good agreement with the experimental value of 4.59 eV (270 nm).¹⁴ Close to the FC region, the two lone pair states ($n_1\pi^*/n_2\pi^*$) cross the $\pi\pi^*$ state (CoIn₁). With larger distance r , the $n_1\pi^*/n_2\pi^*$ states are stabilized and become degenerate to the ground state (π^2), correlating with the homolytic reaction channel leading to radical pairs (Ph₂CH•/Br•). The second Con (CoIn₂) between the $\pi\sigma^*$ and the $\pi\pi^*$ state can be reached *via* a small barrier at a slightly larger C₁-Br bond length and leads to heterolytic bond cleavage forming ion pairs (Ph₂CH⁺/Br⁻).

For both homologues, the location of CoIn₁ closer to the FC region than CoIn₂ makes it the decisive factor for the product splitting. Compared to the chlorine case, however, all significant points lie at larger C₁-Br distance. This is expected since the bromine atom is larger than the chlorine atom. The main difference shows in the relative position of the CoIns to the S₁ minimum leading to different barrier heights. Note that the

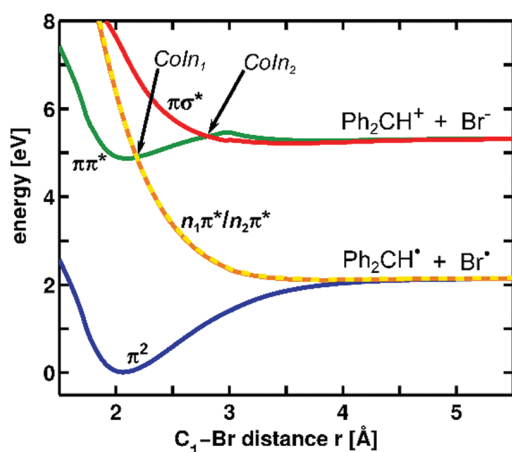


Fig. 4 Diabatic potential energy surfaces of the five lowest singlet states at the ONIOM(CAS(12,10):B3LYP) level of theory along the C₁-Br bond length r with constant $d_{py} = 0.35$ Å. The d_{py} value is chosen to depict the FC point correctly. The reaction starts with an excitation from the ground state (π^2 , blue) to a $\pi\pi^*$ state (green). The $n_1\pi^*/n_2\pi^*$ (yellow/orange dashed) describe the homolytic bond cleavage channel and the $\pi\sigma^*$ state (red) describes the heterolytic bond cleavage channel. For better comparison, the PESs of Ph₂CHCl are shown in Fig. S7 (ESI†).

respective smallest barrier does not lie on the one-dimensional cut for $d_{py} = 0.35$ Å (Fig. 4). In the bromine case the two lone pair states cross the $\pi\pi^*$ state (CoIn₁) almost at the S₁ minimum resulting in a smaller barrier of only 0.04 eV compared to the barrier of 0.22 eV in the chlorine case. The same tendency is found for the relative position of CoIn₂. Again the barrier is smaller in the bromine case (0.11 eV) compared to the chlorine case (0.32 eV).¹³ Especially the lower barrier towards CoIn₂ might explain the experimentally found increase in ion pair formation from 5% to 30%.^{11,14,15} We further investigated the influence of triplet states. The respective spin-orbit coupling becomes significant only for the homolytic channel after passing CoIn₁ (see ESI†). Thus intersystem crossing does not influence the dynamics. In contrast to the chlorine case, the S₁ minimum well extends significantly to smaller and larger d_{py} values (Fig. S2b, ESI†), with an ellipsoidal rather than a circular shape in the two-dimensional subspace. The special shape of the minimum well points to a higher coupling probability between the two reactive coordinates and results from a larger C₁-Br distance allowing higher flexibility for the phenyl rings.

3.2 Quantum dynamics

The two-dimensional PESs for the five lowest diabatic states (π^2 , $\pi\pi^*$, $n_1\pi^*$, $n_2\pi^*$ and $\pi\sigma^*$) considered in the quantum dynamical simulation are shown in Fig. 5 along both reactive coordinates r and d_{py} . Both conical intersections form each a crossing seam in these two dimensions (Fig. S6, ESI†).

The propagation starts with the first vibrational eigenfunction of the ground state. The wave packet is excited *via* dipole-laser interaction from the ground state to the $\pi\pi^*$ state (Fig. 6, green curve). After successful excitation, the wave packet evolves in the $\pi\pi^*$ state. Population is transferred to the $n_1\pi^*$ and $n_2\pi^*$ states when the wave packet reaches CoIn₁ with a time delay of around 50 fs (orange curve) after excitation. CoIn₂ is reached later with a delay of about 110 fs but only marginal population left in the $\pi\pi^*$ state is transferred to the $\pi\sigma^*$ state (red curve). The homolytic bond cleavage clearly dominates the dissociation. To compare the delay times with the rise in the experimentally observable absorption signals, we must take into account that the products are not

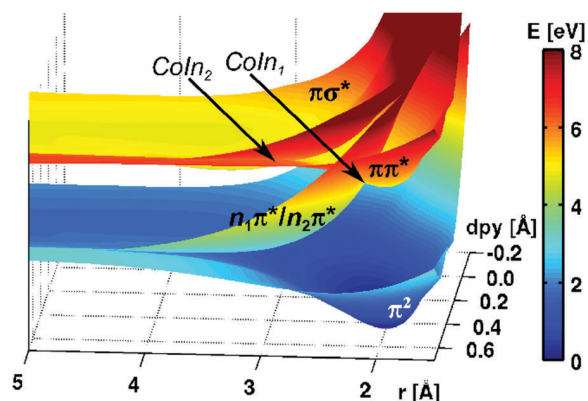


Fig. 5 Two-dimensional diabatic potential energy surfaces of the five lowest singlet states at the ONIOM(CAS(12,10):B3LYP) level of theory along the reactive coordinates r and d_{py} .

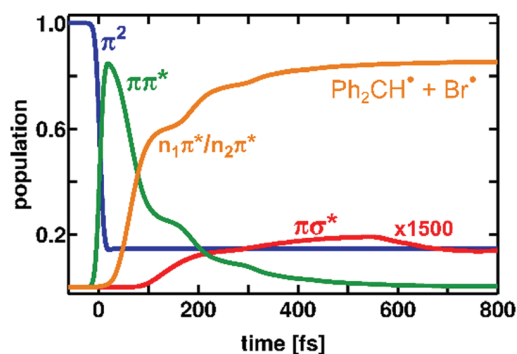


Fig. 6 Population as a function of time. The laser pulse has its maximum at $t = 0$ fs. As the laser pulse occurs, population is transferred from the π^2 state (blue) to the $\pi\pi^*$ state (green). The wave packet reaches CoIn₁ after around 50 fs as the population of the two lone pair states (orange) rises. CoIn₂ is reached later after around 120 fs but almost no population ($\sim 0.1 \times 10^{-3}$) is transferred to the $\pi\sigma^*$ state (red; curve enlarged by a factor of 1500). This means no ion pairs ($\text{Ph}_2\text{CH}^+/\text{Br}^-$) are built in this simulation. The population of the $n_1\pi^*$ and $n_2\pi^*$ states is summed because both lead to the same product.

instantaneously detectable as soon as the wave packet has passed the respective CoIn, but the C₁-Br bond has to be broken. By comparing the orbital interaction¹² of the lone pair and the π orbital transforming to the C-Br σ bond, we obtained the threshold of $r = 3.1$ Å for nearly vanishing interaction with the leaving group. Accordingly, we define as the delay time, the point in time when more than 50% of the wave packet after excitation has passed this threshold in its corresponding electronic state. With this definition the delay time for the radical pairs is 110 fs and for the ion pairs 190 fs, which is in good agreement with the experimental results ($\text{Ph}_2\text{CH}^*/\text{Br}^*$: 100 fs; $\text{Ph}_2\text{CH}^+/\text{Br}^-$: 200 fs).^{14,15} For the product distribution, the experimental ratio of 70% radical pairs and 30% ion pairs^{14,15} is not reached, but we also found that the radical pairs are the dominant products. However, in our simulation almost no ion pairs are formed. This means the barrier to CoIn₂ might be overestimated at the ONIOM(CAS(12,10):B3LYP) level of theory in the reduced coordinate space. A correct description of the barrier may be obtained by introducing a third reactive coordinate. As a rather large simulation grid is used, the introduction of a further reactive coordinate is computationally demanding. Therefore, we slightly shifted the initial wave packet by $\Delta r = -0.13$ Å and $\Delta d_{\text{py}} = 0.04$ Å (Fig. S5, ESI†) to overcome the barrier. By this, the resulting product distribution changes to 85% radical pairs ($\text{Ph}_2\text{CH}^*/\text{Br}^*$) and 15% ion pairs ($\text{Ph}_2\text{CH}^+/\text{Br}^-$), which matches better the experimental results. After the laser excitation, the shifted wave packet oscillates more strongly in the $\pi\pi^*$ minimum. Especially the motion along the coordinate d_{py} is enhanced, which corresponds to an activation in this reactive mode. It points to the significance of this motion and related ones to effectively lower the barrier to CoIn₂ when all dimensions are included. With chlorine as the leaving group^{12,13} this was of no concern because the wave packet did not propagate in the direction of the reactive coordinate d_{py} .

In the following, the motion of the wave packet with the original, unmodified starting conditions is discussed for the

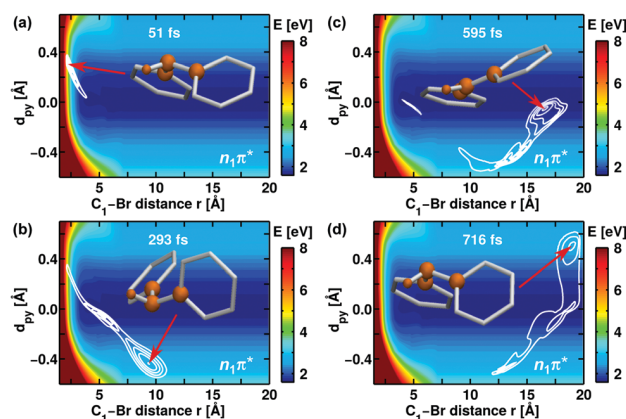


Fig. 7 Wave packet in the $n_1\pi^*$ state at different delay times. (a) The wave packet is transferred to the $n_1\pi^*$ state after around 51 fs. (b) There, it starts immediately leaving the FC region towards smaller d_{py} and larger r values. (c) The wave packet gets decelerated in negative d_{py} as the potential rises and moves back towards $d_{\text{py}} = 0.0$ Å. (d) The wave packet moves further to larger r and d_{py} values reaching the turning point at $d_{\text{py}} \approx 0.5$ Å. For a better overview only the geometry of the carbon backbone without the bromine atom and the hydrogen atoms of the phenyl rings is shown at the location of the maximum of the wave packet in each snapshot.

main product channel, the $n_1\pi^*$ state. Fig. 7 shows snapshots of the wave packet motion together with the geometry of the carbon backbone corresponding to the maximum of the wave packet. During dissociation the wave packet strongly oscillates along d_{py} . The first snapshot (Fig. 7a) shows the wave packet at its first appearance in the $n_1\pi^*$ state after 51 fs where the central carbon atom C₁ is still sp³ hybridized. The wave packet propagates immediately towards smaller d_{py} and larger r values. At 293 fs (Fig. 7b) the maximum of the wave packet has passed $d_{\text{py}} = 0.0$ Å and has reached the turning point at negative d_{py} values. Now the sp³ hybridization at the C₁ atom is inverted, after quickly passing the planar sp² hybridization. Furthermore, the C₁-Br bond can be considered as broken as the wave packet is localized at $r > 3.1$ Å. After 595 fs (Fig. 7c) the wave packet returns to $d_{\text{py}} \approx 0.0$ Å to form again a sp² hybridized C₁ atom. The last snapshot at 716 fs (Fig. 7d) shows the wave packet close to the turning point for positive d_{py} values. At $d_{\text{py}} \approx 0.5$ Å the C₁ atom is back in the original sp³ hybridization. In summary, the wave packet oscillates within the grid between $r = 1.5$ Å and $r = 20.0$ Å from $d_{\text{py}} = 0.0$ Å to $d_{\text{py}} = -0.5$ Å and back in around 500 fs propagation time.

3.3 Semi-classical dynamics

To include all degrees of freedom we performed a full dimensional semi-classical trajectory simulation based on the same electronic structure method. Overall, the 69 trajectories follow the same reaction paths and exhibit the same CoIns as in the quantum dynamics calculation. For the analysis, we separated the trajectories according to their finally populated product channel corresponding either to the radical or ion pair. For each channel, the adiabatic energy is averaged over all respective trajectories, which are 41 for the radical pair and 28 for the ion pair channel (Fig. 8). All states participating in the photoreaction are shown and the leading

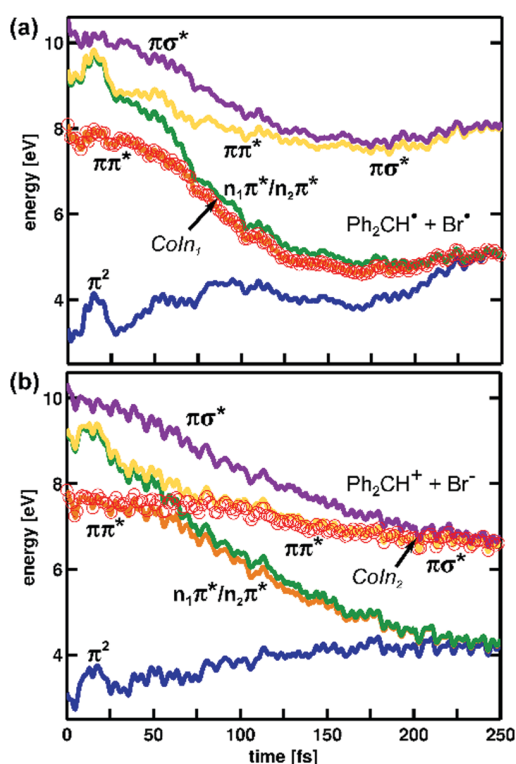


Fig. 8 Averaged adiabatic energies of the five lowest states along the trajectories leading to the homolytic bond cleavage channel (a) and leading to the heterolytic bond cleavage channel (b). The S_0 state is shown in blue, the S_1 in orange, the S_2 in green, the S_3 in yellow and the S_4 in violet. The respective electronic character is also indicated for clarity. The red circles mark the currently occupied state. All energy values are given in reference to the energy of the ground state minimum optimized at the ONIOM(CAS(12,10):HF) level of theory.

configurations are indicated. The currently populated state is marked with red circles. Fig. 8a shows the temporal evolution for the homolytic bond cleavage. The dynamics starts in the S_1 state (orange) which has $\pi\pi^*$ character in the FC region. The system reaches CoIn_1 in a time window between 60 and 80 fs. Thereafter the trajectories follow the lone pair states $n_1\pi^*$ and $n_2\pi^*$ (green, orange) towards the lowest dissociation channel $\text{Ph}_2\text{CH}^+ + \text{Br}^-$. Fig. 8b shows the temporal evolution of the heterolytic bond cleavage. The first conical intersection CoIn_1 has been passed on the $\pi\pi^*$ state and the trajectories reach CoIn_2 in a time window between 180 and 220 fs where the transition to the $\pi\sigma^*$ state takes place. This state correlates with the second dissociation channel $\text{Ph}_2\text{CH}^+ + \text{Br}^-$. The product ratio of about 60% homolytic bond cleavage to 40% heterolytic bond cleavage and the appearance time of the products are in good agreement with the experimental results.^{14,15} The good agreement for the product distribution supports our previous assumption in context with the results from quantum dynamics that additional degrees of freedom are important to reach the heterolytic bond cleavage.

3.4 Molecular motions promoting the reaction

Classical nuclear motion. To identify further important molecular degrees of freedom for the reaction we calculated a spectrogram for each product channel using the velocity

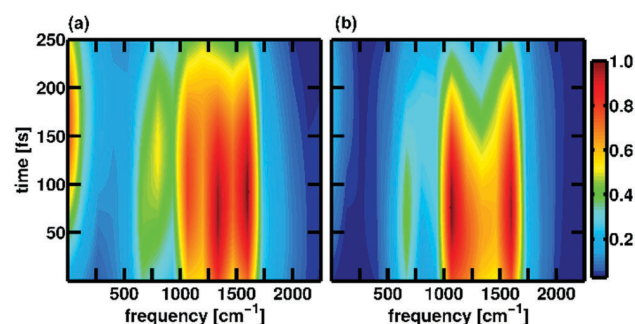


Fig. 9 Spectrogram in the range of 0 to 2500 cm^{-1} for (a) the trajectories leading to the homolytic bond cleavage channel and (b) the trajectories leading to the heterolytic bond cleavage channel. The intensity is normalized to the maximal peak intensity of each spectrogram. The complete spectrograms with the dominant, but non-specific C–H stretch vibrations are shown in Fig. S8 (ESI[†]).

autocorrelation function (VACF) derived from the semi-classical trajectories.^{38,39} Details of the calculation are explained in the ESI.[†] As expected C–H stretch vibrations are responsible for the broadest band around 3300 cm^{-1} (Fig. S8, ESI[†]). These are activated by the Wigner distribution and not specific to one of the product channels. More interesting is the range between 0 and 2500 cm^{-1} (Fig. 9). Both spectrograms show a strong band around 1600 cm^{-1} that can be attributed to normal modes mainly characterized by in-plane C–C–H bending vibrations at the phenyl rings. The weak band around 700 cm^{-1} can be attributed to normal modes mainly characterized by out of plane C–C–H bending vibrations at the phenyl rings. All assigned normal mode vectors are shown in Fig. S11 (ESI[†]). They are based on the frequency analysis used for the Wigner distribution. Significant differences between both channels are visible in the bands at 1300 cm^{-1} and 1100 cm^{-1} . While the higher frequency band is the strongest for the homolytic channel, it does not appear in the spectrogram of the heterolytic channel. The strongest band there is the lower frequency band that is only weak in the spectrogram of the homolytic channel. The band at 1300 cm^{-1} can be assigned to a normal mode mainly characterized by an asymmetric stretch motion at the carbon center C_1 . Its activation favors the homolytic bond cleavage. The band at 1100 cm^{-1} can be assigned to a normal mode mainly characterized by the pyramidalization at the carbon center C_1 . Its activation leads preferentially to the heterolytic bond cleavage. This finding is in good agreement with the quantum dynamical results discussed before, where an extra activation of the reactive coordinate d_{py} is needed to populate the heterolytic bond cleavage channel. The required activation can be interpreted as a cost for the reduced flexibility in the reactive coordinates compared to the full dimensions. The fast frequencies between 1000 cm^{-1} to 1600 cm^{-1} do not appear in the experiment. A reason might be that the time resolution of 50 fs^{14,15} is not sufficient to resolve those frequencies.

The oscillations observed in the experimental transient absorption signal^{14,15} appear most distinctly after 250 fs. To identify possible mechanisms behind this signature, the simulation time for the trajectories was elongated to the ps regime.

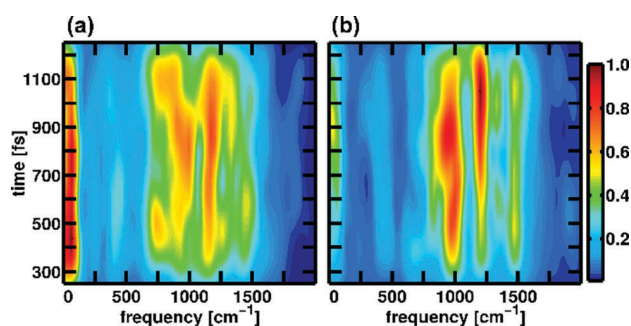


Fig. 10 Spectrogram in the range of 0 to 2000 cm^{-1} of (a) the Ph_2CH^* trajectories and (b) the Ph_2CH^+ trajectories. The intensity is normalized to the maximal peak intensity of each spectrogram. For the complete spectrograms, see Fig. S9 (ESI†).

For that, we discarded the bromine atom and continued the propagation for all trajectories after 250 fs where the $\text{C}_1\text{-Br}$ bond can be regarded as broken. Now the calculations can be performed at the B3LYP level of theory only considering the ground state of either Ph_2CH^* or Ph_2CH^+ . The corresponding spectrograms for the relevant bands up to 2000 cm^{-1} are shown in Fig. 10. The bands are slightly shifted compared to the short time spectrogram (Fig. 9), which reflects the change of computational method. Overall, both spectra are remarkable similar with a band around 50 cm^{-1} emerging stronger, especially for the homolytic channel. This band can be assigned to a normal mode mainly characterized by a butterfly-like motion of the phenyl rings (Fig. S12, ESI†). In the area of the experimentally reported vibrations at 300 cm^{-1} (110 fs) for Ph_2CH^* and 350 cm^{-1} (100 fs) for Ph_2CH^+ only very weak signatures occur. This unexpected finding needs further reflection, therefore the wave packet motion from the QD simulation has to be considered in more detail.

Wave packet motion. The discrepancy between the outcome of the VACF for the trajectory calculations and the experimental signature may be attributed to the presence of an observation window in the experiment. Thus, we adapt the experimental observation window and apply it for the analysis of the wave packet dynamics in the $n_1\pi^*$ state. The observation window is defined as a restricted area on our grid, which reflects the geometric structures for which the experimental signal becomes maximal. Ph_2CH^* has the highest absorption when the carbon center is sp^2 hybridized ($d_{\text{py}} = 0.0 \text{ \AA}$).¹² Therefore, the wave packet's motion is visualized by its integral $F(t)$ evaluated at every time step within the restricted area in the $n_1\pi^*$ state (for details see ESI†). These results show pronounced oscillations (Fig. 11b) with strong recurrences with a period of 500 fs and recurrences of decreasing amplitudes with a period of 120 fs.

The slow oscillation can be assigned to the motion of the wave packet's main part in the $n_1\pi^*$ state (see Fig. 7). The fast oscillations are induced by the motion of the wave packet in the $\pi\pi^*$ minimum leading to a stepwise depopulation through CoIn_1 (Fig. 6). To support this statement a second observation window is set along the CoIn_1 seam in the $\pi\pi^*$ state recording the fast oscillations in the S_1 minimum (Fig. 11a). The decrease

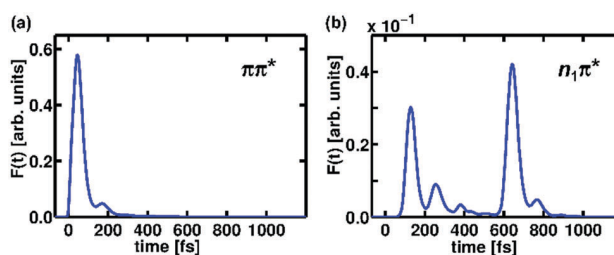


Fig. 11 Time-dependent evaluation of the wave packet's motion as its integral $F(t)$ in the defined restricted area (a) along the CoIn_1 seam in the $\pi\pi^*$ state and (b) along the coordinate r with constant $d_{\text{py}} = 0.0 \text{ \AA}$ in the $n_1\pi^*$ state (for details see ESI†).

in amplitude directly reflects the depopulation of the $S_1 \pi\pi^*$ state. Their frequency of 280 cm^{-1} matches the experimentally reported frequency of 300 cm^{-1} for Ph_2CH^* .^{14,15} However, in this area only weak bands occur in the spectrogram (Fig. 10) evaluated from the VACF, so we assume that the measured oscillation contains contributions from several normal modes. These modes are activated during the dissociation reaction and are triggered by the planarization motion of the central carbon atom C_1 .

The slow oscillations cannot be distinguished in the experiment because they have the fast oscillations (Fig. 11b) superimposed on them. To find their corresponding frequencies in the spectrogram we have to take into account that the detection window only records their half cycle. The full period, thus, corresponds to 1000 fs, which means a frequency of 33 cm^{-1} . This frequency is comparable to the band at 50 cm^{-1} in the spectrogram. The difference can be attributed to the reduced coordinate space optimized for the fast part of the dissociation reaction from the FC region through the CoIns . After the bond cleavage, motions of and within the phenyl rings are activated in the full dimensional trajectories. In the QD simulation only the relative motion of the phenyl rings is indirectly considered. The more pronounced amplitude oscillations in the temporal signal of the QD simulation compared to the experimental signal can be explained by the reduced coordinate space, as well. Here, no competing pathways enhance the background signal. The discussed wave packet motion does not occur for chlorine as the leaving group.⁸⁻¹² The differences in the shape of the potential, especially in the FC region, as well as in the mass of the halogen atoms are decisive for this effect. With respect to the experimental observation window, the semi-classical calculations recover only the slow reactive motion of the pyramidalization but not the fast one showing as a frequency of 300 cm^{-1} extracted from the pump-probe experiment. This frequency is attributed to the excited state wavepacket motion crossing the barrier close to the FC-region and can be regarded as a pure quantum effect which cannot be recovered in the semi-classical trajectory calculations.

4 Conclusions

The photodissociation of $\text{Ph}_2\text{CH-Br}$ was studied with quantum chemical, quantum dynamical and semi-classical dynamical methods. Using an effective ONIOM partitioning of the system

and thus reducing the computational effort, we were able to come up with a balanced description of the PESs. Hereby, CAS(12,10) was used as a high-level method. Both in our quantum chemical and semi-classical simulations we could successfully accomplish the passing through two consecutive CoIns. We were able to describe the product splitting into the homolytic and the heterolytic reaction path and explain the different delay times for both product channels as reported in the experiment.^{14,15} In our two-dimensional quantum dynamical simulation, we were able to rely on the framework of specially adapted reactive coordinates. However, it was necessary to further trigger a vibrational mode related to the pyramidalization of the central carbon atom C₁ to enhance the amount of ion pair formation to approach the experimental findings. In the simulated spectra of the full-dimensional semi-classical trajectories, the band of a corresponding mode was a significant indicator for heterolytic dissociation. Therefore, with both our simulations, we could clearly demonstrate the considerable impact of such a mode for the activation of the ion pair channel. The importance of the pyramidalization in general for the dissociation reaction is a huge difference compared to Ph₂CH-Cl where the dynamics in this coordinate is very limited. In Ph₂CH-Br activation of this coordinate explains the difference in the ratio between the homolytic and the heterolytic product channel and leads to a wave packet oscillation accompanying the bond cleavage process observable in the experimental transient absorption signal. Overall, in this work we explained the microscopic details of the photodissociation mechanism of Ph₂CH-Br and successfully pointed out the similarities and contrasts of the photo-induced dissociation reaction of Ph₂CH-Br compared to the case with chlorine as the leaving group.

Conflicts of interest

There are no conflicts of interest to declare.

Acknowledgements

Financial support of this work from the Deutsche Forschungsgemeinschaft through the SFB749 and the excellence cluster 'Munich-Centre for Advanced Photonics' (MAP) is gratefully acknowledged. We thank Chaochen Lu for his contributions to the first calculations.

References

- 1 D. Ravelli, S. Protti and M. Fagnoni, *Chem. Rev.*, 2016, **116**, 9850–9913.
- 2 R. R. Naredla and D. A. Klumpp, *Chem. Rev.*, 2013, **113**, 6905–6948.
- 3 H. Mayr, *Tetrahedron*, 2015, **71**, 5095–5111.
- 4 H. Mayr, J. Ammer, M. Baidya, B. Maji, T. A. Nigst, A. R. Ofial and T. Singer, *J. Am. Chem. Soc.*, 2015, **137**, 2580–2599.
- 5 P. K. Das, *Chem. Rev.*, 1993, **93**, 119–144.
- 6 R. A. McClelland, *Tetrahedron*, 1996, **52**, 6823–6858.
- 7 J. Ammer and H. Mayr, *J. Phys. Org. Chem.*, 2013, **26**, 956–969.
- 8 J. Bartl, S. Steenken, H. Mayr and R. A. McClelland, *J. Am. Chem. Soc.*, 1990, **112**, 6918–6928.
- 9 M. Lipson, A. A. Deniz and K. S. Peters, *Chem. Phys. Lett.*, 1998, **288**, 781–784.
- 10 C. F. Sailer, S. Thallmair, B. P. Fingerhut, C. Nolte, J. Ammer, H. Mayr, I. Pugliesi, R. de Vivie-Riedle and E. Riedle, *Chem-PhysChem*, 2013, **14**, 1423–1437.
- 11 C. F. Sailer, N. Krebs, B. P. Fingerhut, R. de Vivie-Riedle and E. Riedle, *EPJ Web Conf.*, 2013, **41**, 05042.
- 12 E. Riedle, M. K. Roos, S. Thallmair, C. F. Sailer, N. Krebs, B. P. Fingerhut and R. de Vivie-Riedle, *Chem. Phys. Lett.*, 2017, **683**, 128–134.
- 13 S. Thallmair, M. K. Roos and R. de Vivie-Riedle, *Struct. Dyn.*, 2016, **3**, 043205.
- 14 E. Riedle, M. Bradler, M. Wenninger, C. F. Sailer and I. Pugliesi, *Faraday Discuss.*, 2013, **163**, 139.
- 15 C. F. Sailer and E. Riedle, *Pure Appl. Chem.*, 2013, 85.
- 16 B. Podolsky, *Phys. Rev.*, 1928, **32**, 812–816.
- 17 J. E. B. Wilson, J. C. Decius and P. C. Cross, *Molecular Vibrations: The Theory of Infrared and Raman Vibrational Spectra*, Dover Publ., 1980.
- 18 L. J. Schaad and J. Hu, *J. Mol. Struct. THEOCHEM*, 1989, **185**, 203–215.
- 19 S. Thallmair, M. K. Roos and R. de Vivie-Riedle, *J. Chem. Phys.*, 2016, **144**, 234104.
- 20 J. C. Tully, *J. Chem. Phys.*, 1990, **93**, 1061.
- 21 M. Svensson, S. Humbel, R. D. J. Froese, T. Matsubara, S. Sieber and K. Morokuma, *J. Phys. Chem.*, 1996, **100**, 19357–19363.
- 22 L. W. Chung, W. M. C. Sameera, R. Ramozzi, A. J. Page, M. Hatanaka, G. P. Petrova, T. V. Harris, X. Li, Z. Ke, F. Liu, H.-B. Li, L. Ding and K. Morokuma, *Chem. Rev.*, 2015, **115**, 5678–5796.
- 23 B. P. Fingerhut, S. Oesterling, K. Haiser, K. Heil, A. Glas, W. J. Schreier, W. Zinth, T. Carell and R. de Vivie-Riedle, *J. Chem. Phys.*, 2012, **136**, 204307.
- 24 B. P. Fingerhut, D. Geppert and R. de Vivie-Riedle, *Chem. Phys.*, 2008, **343**, 329–339.
- 25 H. J. Werner, P. J. Knowles, G. Knizia, F. R. Manby, M. Schütz, P. Celani, T. Korona, R. Lindh, A. Mitrushenkov, G. Rauhut, K. R. Shamasundar, T. B. Adler, R. D. Amos, A. Bernhardsson, A. Berning, D. L. Cooper, M. J. O. Deegan, A. J. Dobbyn, F. Eckert, E. Goll, C. Hampel, A. Hesselmann, G. Hetzer, T. Hrenar, G. Jansen, C. Köppl, Y. Liu, A. W. Lloyd, R. A. Mata, A. J. May, S. J. McNicholas, W. Meyer, M. E. Mura, A. Nicklass, D. P. O'Neill, P. Palmieri, D. Peng, K. Pflüger, R. Pitzer, M. Reiher, T. Shiozaki, H. Stoll, A. J. Stone, R. Tarroni, T. Thorsteinsson and M. Wang, *MOLPRO, version 2012.1, a package of ab initio programs*, 2012, see www.molpro.net.
- 26 H.-J. Werner, P. J. Knowles, G. Knizia, F. R. Manby and M. Schütz, *WIREs Comput. Mol. Sci.*, 2012, **2**, 242–253.
- 27 M. J. Bearpark, S. M. Larkin and T. Vreven, *J. Phys. Chem. A*, 2008, **112**, 7286–7295.
- 28 M. J. Frisch, G. W. Trucks, H. B. Schlegel, G. E. Scuseria, M. A. Robb, J. R. Cheeseman, G. Scalmani, V. Barone,

- B. Mennucci, G. A. Petersson, H. Nakatsuji, M. Caricato, X. Li, H. P. Hratchian, A. F. Izmaylov, J. Bloino, G. Zheng, J. L. Sonnenberg, M. Hada, M. Ehara, K. Toyota, R. Fukuda, J. Hasegawa, M. Ishida, T. Nakajima, Y. Honda, O. Kitao, H. Nakai, T. Vreven, J. J. A. Montgomery, J. E. Peralta, F. Ogliaro, M. Bearpark, J. J. Heyd, E. Brothers, K. N. Kudin, V. N. Staroverov, R. Kobayashi, J. Normand, K. Raghavachari, A. Rendell, J. C. Burant, S. S. Iyengar, J. Tomasi, M. Cossi, N. Rega, J. M. Millam, M. Klene, J. E. Knox, J. B. Cross, V. Bakken, C. Adamo, J. Jaramillo, R. Gomperts, R. E. Stratmann, O. Yazyev, A. J. Austin, R. Cammi, C. Pomelli, J. W. Ochterski, R. L. Martin, K. Morokuma, V. G. Zakrzewski, G. A. Voth, P. Salvador, J. J. Dannenberg, S. Dapprich, A. D. Daniels, Ö. Farkas, J. B. Foresman, J. V. Ortiz, J. Cioslowski and D. J. Fox, *Gaussian 09, Revision D.01*, Gaussian, Inc., Wallingford, CT, 2009.
- 29 H. Lischka, R. Shepard, I. Shavitt, R. M. Pitzer, M. Dallos, T. Müller, P. G. Szalay, F. B. Brown, R. Ahlrichs, H. J. Böhm, A. Chang, D. C. Comeau, R. Gdanitz, H. Dachsel, C. Ehrhardt, M. Ernzerhof, P. Höchtl, S. Irlé, G. Kedziora, T. Kovar, V. Parasuk, M. J. M. Pepper, P. Scharf, H. Schiffer, M. Schindler, M. Schüler, M. Seth, E. A. Stahlberg, J.-G. Zhao, S. Yabushita, Z. Zhang, M. Barbatti, S. Matsika, M. Schuurmann, D. R. Yarkony, S. R. Brozell, E. V. Beck, J.-P. Blaudeau, M. Ruckebauer, B. Sellner, F. Plasser and J. J. Szymczak, *COLUMBUS, an ab initio electronic structure program, release 7.0*, 2015.
- 30 H. Lischka, T. Müller, P. G. Szalay, I. Shavitt, R. M. Pitzer and R. Shepard, *WIREs Comput. Mol. Sci.*, 2011, **1**, 191–199.
- 31 H. Lischka, R. Shepard, R. M. Pitzer, I. Shavitt, M. Dallos, T. Müller, P. G. Szalay, M. Seth, G. S. Kedziora, S. Yabushita and Z. Zhang, *Phys. Chem. Chem. Phys.*, 2001, **3**, 664–673.
- 32 S. Matsika and D. R. Yarkony, *J. Chem. Phys.*, 2002, **117**, 6907–6910.
- 33 H. Tal-Ezer and R. Kosloff, *J. Chem. Phys.*, 1984, **81**, 3967.
- 34 M. Barbatti, G. Granucci, M. Ruckebauer, F. Plasser, R. Crespo-Otero, J. Pittner, M. Persico and H. Lischka, *NEWXTON-X: a package for Newtonian dynamics close to the crossing seam, version 1.4*, 2014, see www.newtonx.org.
- 35 M. Barbatti, M. Ruckebauer, F. Plasser, J. Pittner, G. Granucci, M. Persico and H. Lischka, *WIREs Comput. Mol. Sci.*, 2013, **4**, 26–33.
- 36 M. Barbatti, A. J. A. Aquino and H. Lischka, *Phys. Chem. Chem. Phys.*, 2010, **12**, 4959.
- 37 R. Crespo-Otero and M. Barbatti, *Chem. Rev.*, 2018, **118**, 7026–7068.
- 38 M. Tamaoki, Y. Yamauchi and H. Nakai, *J. Comput. Chem.*, 2005, **26**, 436–442.
- 39 B. P. Fingerhut, PhD thesis, Ludwigs-Maximilians-Universität, 2010.

Chapter 3.

Photophysics of elongated π systems in organic molecules

A prominent feature of a molecule is its color. This feature is induced by the molecule's ability to absorb light in a certain range of the visible spectrum. The color, in turn, is then determined by the remaining, non-absorbed part of the spectrum. The molecular group responsible for the absorption of light is called chromophore. The most prevalent chromophores in organic molecules are conjugated π bonds [115]. The π orbitals forming these bonds hereby combine and constitute the π system, where photon absorption leads to excitation from the outstretched π to π^* orbitals.

With the molecule in the excited state after absorption, photophysical or photochemical processes can occur. While photochemical processes lead to new products, *e.g.* by photodissociation as shown in chapter 2, photophysical processes do not change the absorbing molecule. Instead radiative or radiationless processes can happen like fluorescence or internal conversion.

As the absorption and the fluorescence occur at definite wave lengths, different species can be distinguished by their spectroscopic signature. To understand these signatures and gain further knowledge about the system at hand, theoretical methods are often a useful tool. In this chapter, two organic molecules with elongated π systems, pyrene and the dye Cy3, are studied concerning their photophysics. Both are used as dyes and fluorescence probes [116, 117]. For pyrene (section 3.1), it is to understand how the fluorescent state is reached after the absorption as this process was measured to be ultrafast [50, 118]. QD and non-adiabatic MQCD are employed to simulate this process. For Cyanine 3 (Cy3) (section 3.2), DNA is used as scaffold to bring two dye molecules in close proximity. These constructs are investigated experimentally and theoretically to prove the dimerization as H-aggregates.

3.1. Ultrafast relaxation from 1L_a to 1L_b in pyrene

Pyrene is a typical polycyclic aromatic hydrocarbon (PAH), consisting of four fused benzene rings, thus completely flat and aromatic. It is used in fluorescence studies [117] as it combines long excited state lifetimes [48, 119] with a high fluorescence quantum yield [46, 119]. Furthermore, absorption and emission do not involve the same state meaning that no self-absorption can occur after fluorescence. Namely, the first photo-accessible state is S_2 or 1L_a following Platt's nomenclature [120], whereas emission only occurs from the S_1 or 1L_b , even after excitation to higher-lying states [49, 121] and in accordance with Kasha's rule [122]. Therefore, an internal conversion process must occur. It can be followed by transient absorption spectroscopy, which reveals a time constant of 85 fs [118]. However, to date there is still no complete microscopic picture of this process.

In the article "Ultrafast relaxation from 1L_a to 1L_b in pyrene: a theoretical study" published in *Chemical Physics* this ultrafast relaxation process is theoretically mod-

eled for the first time with two different methods [123]. The first one is reduced dimensionality QD on a regular grid. The second one is non-adiabatic MQCD. Besides providing an answer to a long standing question, the article also compares two state-of-the-art dynamical methods using the same QC method as basis. The balanced QC description of both the 1L_a state with its transition moment along the long molecular axis and 1L_b with its transition moment along the short molecular axis is rather difficult. Compared to benzene the symmetry in pyrene is reduced from D_{6h} to D_{2h} leading to non-equivalent in-plane axes and, thus, to different character for 1L_a and 1L_b .

The key statements of the article are:

- In a benchmark and review of literature values, CASSCF(4,4) is selected as the method of choice. While time-dependent density functional theory (TDDFT) gives a wrong ordering of the minima, larger active spaces separate both states by up to 2 eV inhibiting the experimentally observed ultrafast relaxation. With CASSCF(4,4) a CoIn is successfully optimized. This minimal active space does not inherently favor one of the states and is the best estimate for the intricate QC of pyrene.
- Displacement vectors between the minima are chosen as coordinate system for a two-dimensional QD simulation. The G-matrix (see chapter 1) is constant for these linear coordinates and the non-adiabatic couplings are projected onto the used subspace. The minima appear as two very close-lying, only slightly shifted, almost harmonic potential wells in this subspace. While a masking function is necessary to inhibit immediate back coupling, the excitation and relaxation through the CoIn is successfully modeled. Therein, the wave packet moves from the FC region through the CoIn towards the excited state minima, where it lies highly delocalized in the end.
- In non-adiabatic MQCD, the relaxation is described in full dimensionality. It takes place with a time constant of 43 fs, which is faster than in the experiment probably due to the shortcomings of CASSCF(4,4) and especially its gradients. The statistical analysis of the trajectories shows that many hoppings per trajectory occur, proving the fact that both states are close in energy for a considerable area of the PES. The final population clearly confirms 1L_b as the fluorescent state.
- Projecting the locations of starting, end, and hopping geometries of the non-adiabatic MQCD trajectories onto the two-dimensional subspace used in the QD reveals the similarity of the results from both approaches. The movement away from the FC region is clearly visible and the very widespread hopping points indicate very efficient coupling between both states.

Overall, both dynamical methods give a consistent and convergent picture of the ultrafast relaxation. They both show the strong coupling between 1L_a and 1L_b and confirm the time frame, relaxation efficiency and 1L_b as the fluorescent state. The small oscillator strength of 1L_b in turn explains the long excited state lifetime.

The article "Ultrafast relaxation from 1L_a to 1L_b in pyrene: a theoretical study" published in *Chemical Physics* is reprinted here with permission from *Chem. Phys.* (2018), DOI: 10.1016/j.chemphys.2018.08.002. Copyright 2018 Elsevier B.V. The Supporting Information for this article is available under <https://doi.org/10.1016/j.chemphys.2018.08.002>.



ELSEVIER

Contents lists available at ScienceDirect

Chemical Physics

journal homepage: www.elsevier.com/locate/chemphysUltrafast relaxation from 1L_a to 1L_b in pyrene: a theoretical study

Matthias K. Roos, Sebastian Reiter, Regina de Vivie-Riedle*

Department Chemie, Ludwig-Maximilians-Universität München, Butenandstr. 11, D-81377 München, Germany

ARTICLE INFO

Keywords:

Quantum dynamics
Semi-classical dynamics
Ultrafast relaxation
Conical intersection
CASSCF
Pyrene

ABSTRACT

Pyrene and its photophysics have been extensively studied, especially experimentally. Yet to this day there is no conclusive theoretical description of the relaxation from the photo-accessible 1L_a state to the fluorescent 1L_b state, which is partly due to the challenge of adequately modeling both states without over-stabilizing one or the other. We first compare several quantum chemical methods to find the best model that offers a good trade-off between a balanced description of both states and computational effort. On the basis of the selected electronic structure method, we simulate this relaxation process with two state-of-the-art dynamical techniques. We perform wave packet propagations in reduced dimensions and full-dimensional on-the-fly surface hopping to corroborate our choice of coordinates and obtain a more complete picture of the relaxation mechanism. Our results confirm the important role of a conical intersection between the two excited states that has been postulated in the literature.

1. Introduction

Pyrene is one of the most well-studied organic molecules with respect to its photophysics [1]. It is known for the formation of excimers [2–4], excited state lifetimes on the timescale of several hundred nanoseconds [5,6] and a high fluorescence quantum yield [6,7]. Since the spectral gap between monomer and the broad-range excimer fluorescence allows a clear distinction of the respective signals, pyrene is used as a fluorescent probe for the labeling of DNA [8–10] and for studying the conformational changes in proteins [11]. In organic electronics, pyrene and its derivatives find applications for example as chromophores in OLEDs [1].

As a representative [12] of polycyclic aromatic hydrocarbons (PAH), pyrene has a large π -system that absorbs in the near UV range. It belongs to the D_{2h} point group, so compared to benzene, its symmetry is reduced, implicating that the axes forming the molecular plane are no longer equivalent. For this paper, the z-axis is oriented along the long side of the molecule and the y-axis along the short side, whereas the x-axis is perpendicular to the molecular plane (Fig. 1).

The first bright state is the $\pi\pi^*$ -state S_2 , with its transition moment oriented along the z-axis [13]. It is labeled 1L_a according to Platt's notation [14]. In contrast, the absorption of the lowest-lying singlet state S_1 (1L_b) is almost two orders of magnitude smaller [13] and therefore negligible compared to 1L_a . Its transition moment is oriented along the y-axis.

Emission, however, is solely reported from the 1L_b state, even after

excitation to higher-lying states such as 1L_a [15,16]. This implies internal conversion between 1L_a and 1L_b which can be monitored by transient absorption spectroscopy. Indeed, an ultrafast decay from 1L_a to 1L_b was observed [17,18] with a time constant of 85 fs [18]. A conical intersection (CoIn) [19,20] connecting the two states is the prime suspect for such a process [21], but so far not confirmed. The nuclear dynamics in 1L_a and its related electronic fluctuation were studied to simulate non-linear spectra, but non-adiabatic coupling was not included in this single trajectory ansatz [21]. Therefore, a conclusive theoretical simulation of the complete excitation and relaxation process and thus a convincing microscopic picture of it is still lacking.

In the literature, various theoretical methods have been used to study the excited states of pyrene: time-dependent density functional theory (TDDFT) [22–26], complete active space self-consistent field (CASSCF) [21,24,25,27] and perturbation theory methods based on CASSCF [24,25,28,29]. In all these reports, the challenge to describe the two low-lying excited states of pyrene becomes manifest. While TDDFT often predicts a wrong state ordering, modern methods like XMCQDPT2 [30] are quantitatively in very good agreement to the experiment [29], but come with tremendous computational cost.

In this work, we simulate the relaxation process from the bright 1L_a to the dark 1L_b state with state-of-the-art dynamical methods [31]. For this purpose, we first carefully assess the quantum chemistry to find the theoretical method with the best combination of accuracy and computational cost. Next, we discuss some critical molecular geometries. Our approach for simulating the ultrafast relaxation process after

* Corresponding author.

E-mail address: regina.de.vivie@cup.uni-muenchen.de (R. de Vivie-Riedle).<https://doi.org/10.1016/j.chemphys.2018.08.002>

Received 2 May 2018; Accepted 2 August 2018

0301-0104/ © 2018 Elsevier B.V. All rights reserved.

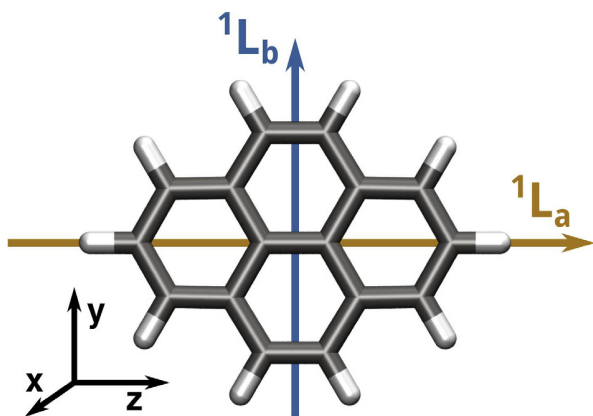


Fig. 1. Spatial orientation of pyrene in this paper. The molecular structure is overlaid with sketches of the transition dipole moments of the two excited states studied here. Note that the 1L_b transition dipole moment is scaled up by a factor of 15 in this picture for better visualization.

photoexcitation is two-part: The first method is grid-based quantum dynamics which is performed in reduced dimensionality. We therefore construct a reduced coordinate space out of the critical points and profit from the quantum nature of the wave packet description for the nuclear motion in this subspace. Contrary to MCTDH [32] (and references therein) where more modes could be used, here in the quantum dynamics we can benefit from the complete potential energy surfaces. As second method we use trajectory-based non-adiabatic on-the-fly molecular dynamics. Here, we can simulate in full dimensionality at the expense of treating the nuclear motion in a classical way. This method gives us further insight in the occurring processes and validates our choice of geometrical subspace for the quantum dynamics.

This paper is structured as follows: In Section 2 the procedures and programs we used are listed. Section 3.1 deals with the choice of an appropriate method for the quantum-chemical treatment of pyrene. Afterwards, the results of the quantum dynamics are presented in Section 3.2, while Section 3.3 contains the analysis of the semiclassical simulations. Finally, Section 4 summarizes and concludes this work.

2. Computational details

2.1. Optimizations and simulation of spectra

Structures (S_0 , S_1 , S_2) were optimized on both the (TD)DFT/CAM-B3LYP/6-31G(d) and CASSCF(4,4)/6-31G(d) levels of theory. For the latter, state-averaging over three states was employed. Each optimized minimum structure was verified by a frequency analysis. DFT calculations were performed with the *Gaussian09* [33] software package, while *Molpro 2012.1* [34,35] was employed for CASSCF [36–38] calculations. All optimized geometries are included in the [Supporting Information](#). Vibrationally resolved spectra were simulated within the Franck–Condon (FC) approximation using the FCclasses code [39–43]. Gaussian functions with a full-width-half-maximum (FWHM) of $\sigma = 135 \text{ cm}^{-1}$ were used for line broadening.

2.2. Quantum dynamical calculations

Quantum dynamical calculations were performed with a program of our own design by solving the time-dependent Schrödinger equation (TDSE) on a spatial grid spanned by the orthonormalized coordinate vectors pointing from the FC point to the 1L_a and 1L_b minimum, respectively. The short iterative Lanczos algorithm [44,45] was used with a time step of 0.02 a.u. to simulate the propagation of the wave packet in time. We employed the Wilson G-matrix formalism to represent the kinetic energy operator in reduced coordinates [46–49]. The potential

energy was obtained by CASSCF(4,4)/6-31G(d) calculations with *Molpro 2012.1*. Working in an adiabatic representation, we constructed non-adiabatic coupling elements (NACME) by projecting the full-dimensional couplings obtained from the quantum chemical calculations into the two-dimensional (2D) ${}^1L_a/{}^1L_b$ space.

To include the exact geometry of the S_1/S_2 CoIn in our reduced coordinate space, a third coordinate would be necessary, implying a significant increase in computational effort. To at least take into account the coupling at the geometry of the S_1/S_2 CoIn, we displaced all geometries of the initial 2D potential energy surface (PES) along the orthogonalized coordinate vector from the FC point to the optimized structure of the CoIn ($q_{\text{FC} \rightarrow \text{CoIn}}$) and computed the NACME that were then projected on the grid. Along this small displacement ($6.93 \times 10^{-4} \text{ \AA}$) the change of the 2D PES is negligible, but the NACME increase drastically towards the optimized CoIn geometry, facilitating a more realistic modeling of the ultrafast relaxation process of pyrene.

During the quantum dynamical simulation, the population in S_1 was absorbed by a masking function to suppress back coupling to S_2 and smooth the population decay curve.

2.3. Semi-classical on-the-fly dynamical calculations

Non-adiabatic on-the-fly dynamics were carried out with a modified version of the program *NewtonX 1.4* [50,51], using a self-written interface [52] to the program package *Molpro 2012.1*. State-averaged CASSCF with the active space of four electrons in four orbitals (CASSCF(4,4)) was used as quantum chemical method with state-averaging over three states. The basis set was 6-31G(d) [53,54]. 198 trajectories were calculated, starting from a Wigner distribution [55] of geometry distortion and momentum around the ground-state minimum structure optimized on the CASSCF/6-31G(d) level of theory. The Wigner distribution was transferred to the second excited state (1L_a) to simulate the excitation process. The trajectories were propagated for 250 fs with the Velocity Verlet integrator [56], using a timestep of 0.5 fs. Tully’s fewest switches surface hopping routine [57] was used for transitions between the electronic states, as it is implemented in *NewtonX*.

3. Results and discussion

3.1. Method of choice

As we want to describe the transition from the bright 1L_a to the dark 1L_b state, we first need to find a suitable quantum chemical methodology to adequately treat both states. In the literature, TDDFT has been employed extensively for calculations on pyrene [22,23,25,26]. Using the range-separated density functional CAM-B3LYP [59], we can simulate a vibrationally resolved absorption spectrum for the 1L_a state. The spectrum is depicted in Fig. 2 and dominated by the 0-0 transition at $\tilde{\nu} = 0 \text{ cm}^{-1}$. As it is typical for polycyclic aromatic hydrocarbons (PAH) [60], four distinct peaks with decreasing intensity are clearly visible. The spectrum is in very good agreement with the experiment [16] (see Fig. S3 in the [Supporting Information](#)), so this level of theory sufficiently describes the vibronic structure of 1L_a . However, the question of how accurately both states are treated regarding their relative energy remains.

Calculated energies on the TDDFT level of theory are listed in Table 1, showing vertical excitation energies ΔE^{vert} of 4.07 eV for 1L_b and of 4.11 eV for 1L_a . Compared to the experiment, these energies are slightly higher and the states lie very close to each other. At least, they seem to be in the correct order and the oscillator strength f_{vert} also confirms the interpretation of 1L_a as the bright state. Nevertheless, a look at the emission energies ΔE^{fluor} reveals that the minimum of 1L_a is lower than the one of 1L_b , contradicting the experimental findings.

In Fig. 3 the most important transitions for both states are visualized. 1L_b is described by two almost equally weighted transitions, one from π_2 to π_1^* and one from π_1 to π_2^* . In contrast, 1L_a is dominated by the

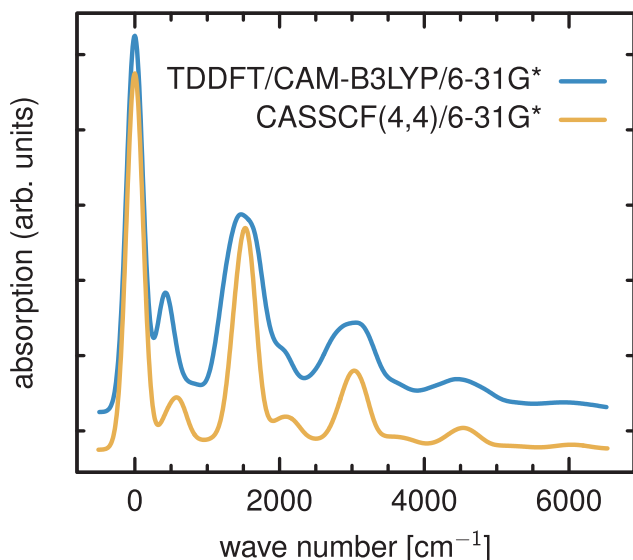


Fig. 2. Vibrationally resolved absorption spectra for the bright 1L_a state of pyrene on the TDDFT and CASSCF(4,4) levels of theory in comparison. Note that the baselines of the two spectra are vertically shifted against each other for better visibility. Additionally, the absorption maximum, corresponding to the vibronic 0–0 transition, is shifted by 3.78 eV for the TDDFT spectrum and 5.43 eV for the CASSCF(4,4) spectrum.

Table 1

Vertical excitation and emission energies for 1L_a and 1L_b on the TDDFT/6-31G(d) and CASSCF(4,4)/6-31G(d) levels of theory. The values in parentheses represent the oscillator strengths of the respective transitions. Furthermore, vertical excitation energies for CAS(12,12)/MIDI-4 and CAS(14,15)/aug-cc-pVDZ are listed as taken from the literature.

Method	ΔE^{vert} [eV]		ΔE^{fluor} [eV]	
	1L_b	1L_a	1L_b	1L_a
TDDFT	4.07 (0.000)	4.11 (0.316)	3.81 (0.000)	3.69 (0.409)
CAS(4,4)	5.44 (0.001)	5.52 (0.300)	5.11 (0.001)	5.15 (0.475)
CAS(12,12) ^a	4.12	5.85	–	–
CAS(14,15) ^b	4.35	5.51	–	–
Exp.	3.36 ^c	3.72 ^d	3.36 ^c	–

^a Ref. [27].

^b Ref. [25].

^c ΔE^{0-0} from Ref. [58].

^d ΔE^{0-0} from Ref. [16].

HOMO–LUMO ($\pi_1-\pi_1^*$) transition while the transition from π_2 to π_2^* (dashed) is less relevant. Both states are symmetry allowed (1L_b : B_{2u} ; 1L_a : B_{1u}). The low oscillator strength for 1L_b can be explained by cancellation effects already hypothesized by Becker et al. [13] and also found for the similar tryptamine molecule [61]. As both transitions contribute to the electronic transition dipole moment with opposite sign, the resulting sum almost vanishes and 1L_b is dark.

The contribution of two transitions clearly renders 1L_b a multi-reference state. In the literature [62] it was also assigned a more covalent character in a valence-bond picture, whereas 1L_a was attributed an ionic nature. All these differences explain why TDDFT might treat both states differently. Indeed, it was first noted by Grimme and co-workers [62,63,22] that TDDFT— independent of functional—significantly underestimates the singlet 1L_a states present in the large π systems of polycyclic aromatic hydrocarbons (PAH). Subsequently, this

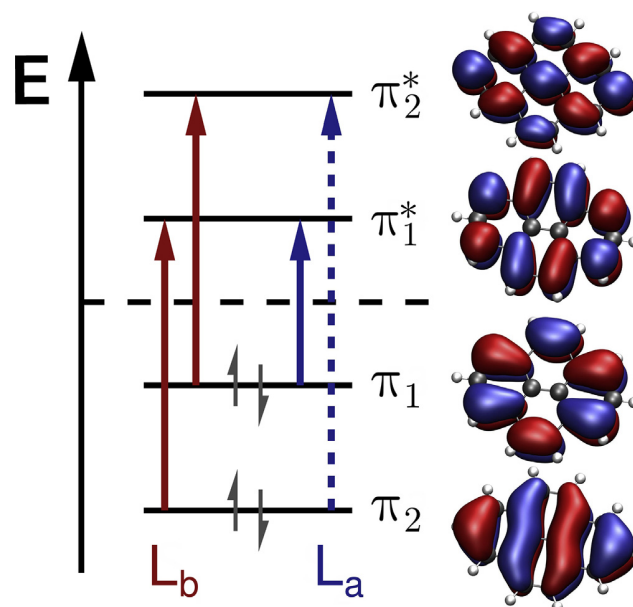


Fig. 3. Visualisation of the transitions of the excited states 1L_a and 1L_b and the corresponding molecular orbitals. Hereby, 1L_b is described by two almost equally weighted transitions, from π_2 to π_2^* and from π_1 to π_2^* , respectively. The description of 1L_a is dominated by the HOMO–LUMO transition, $\pi_1-\pi_1^*$, and the transition $\pi_2-\pi_2^*$ (dashed) is less important.

topic drew some attention and several studies discussed 1L_a and 1L_b states of oligoacenes and similar polycyclic aromatic hydrocarbons (PAH) [64–72]. On the one hand, new or optimized functionals improved the description of 1L_a states, but simultaneously worsened the picture for 1L_b . On the other hand, 1L_a was attributed a more hidden charge-transfer character, whose description is one of the major caveats of TDDFT [73,74].

Hence, it is reasonable to resort to a multi-configuration method like CASSCF that is inherently capable of treating phenomena like charge-transfer states. Here, the choice of active space is crucial for meaningful results, as it is no black-box method. In the subset of orbitals titled active space, a full configuration interaction (CI) expansion is applied so that the electrons therein are fully correlated. Concerning nomenclature, the term CASSCF(x,y) means x electrons in y orbitals. So for pyrene, CASSCF(16,16) would contain the complete π system in the active space, but is computationally too demanding for our purposes. Additionally, we noticed that the vertical excitation energies of the two states were too far apart with a difference of more than 2 eV on the CASSCF(16,16)/6-31G(d) level of theory. A possible explanation might be that intruder orbitals with totally delocalized character shifts the orbitals of 1L_a character towards the outer limits of the active space where excitations are less likely. In contrast the orbitals of 1L_b character remain more centered and thus this state becomes more favored.

In the literature, various possible ways of restricting the active space to describe 1L_a and 1L_b states of pyrene have been reported: Bito et al. chose two different active spaces, depending on the state in question [27]. For 1L_b , they employed CASSCF(8,8), while using CASSCF(12,12) for 1L_a , with each active space consisting of π and π^* orbitals only. Excitation energies are reported on the CASSCF(12,12) level of theory as 4.12 eV and 5.85 eV for 1L_b and 1L_a , respectively. Thus, both states are separated by more than 1.7 eV at the FC point, prohibiting the interaction necessary for ultrafast relaxation.

Kerkines et al. performed calculations on the CASSCF(14,15) level of theory [25]. This active space is derived from the full valence π active space by replacing the two lowest-lying bonding π orbitals with the highest-lying σ orbital and therefore including $\sigma-\pi^*$ transitions. Again, both states are clearly separated as the vertical excitation

energies are 4.35 eV for 1L_b and 5.51 eV for 1L_a .

These results show that the CASSCF method can reproduce the experimental order of states. However, the two states in question are energetically too far apart. Typically, either one state is overstabilized or the other one is underestimated or both. Test calculations for the active spaces CASSCF(8,8), CASSCF(10,10) and CASSCF(12,12) reveal the reason behind these observations: The molecular orbitals of the active space tend to have a bias toward one direction and unilaterally stabilize one state. For example, in the CASSCF(8,8) framework, 1L_b is the favored state as the orbitals are dominantly located along the short molecular axis. For CASSCF(10,10), the symmetry of D_{2h} for the orbitals is broken, rendering the results useless.

Nenov et al. recently presented [21] a RASSCF [75,76] based restriction of CASSCF(16,16) by only allowing up to quadruple excitations. But here, as in other papers [24,29], no excitation energies on CASSCF level of theory are stated, since the CASSCF wavefunction is used as basis for further calculations employing perturbation theory methods. These methods give reliable results, but are not feasible for dynamical calculations in terms of computational effort.

Overall, it is evident that CASSCF also has its problems with 1L_a and 1L_b states and especially the inclusion of further orbitals does not *per se* improve the results. This fact is in line with observations by Coe and Martínez [77] who deemed it “naive” to select the active space only according to size. Therefore, after having performed the mentioned test calculations we took a minimal approach and chose the minimal active space necessary to describe both states. As stated before, the two most important transitions for both states are depicted in Fig. 3. We restricted our active space to these four orbitals, which means CASSCF(4,4). As no further orbitals are included, no asymmetry is introduced with respect to the molecular axes and no state is inherently favored. From the test calculations, CASSCF(4,4) also emerged as the best candidate. The energies and oscillator strengths obtained on this level of theory are listed in Table 1. With vertical excitation energies ΔE^{vert} of 5.44 eV for 1L_b and 5.52 eV for 1L_a , both states are energetically close, but the optimized minima are in the correct order so that emission from 1L_b can be expected in accordance with the experiment. Furthermore, the small oscillator strength ($f = 0.001$) for the 1L_b minimum provides an excellent explanation for the already mentioned long excited state lifetimes reported in the literature [5,6]: The calculated fluorescence lifetime of 1430 ns (see Supporting Information) is in good agreement with the value of 1420 ns measured in a supersonic jet [5]. This confirms that the dominant character for emission in pyrene is 1L_b . Note that the high quantum yield is due to lack of competing non-adiabatic decay pathways. While the excitation energies are overestimated, an effect that can be attributed to CASSCF [78], the simulated vibrationally resolved absorption spectrum for 1L_a (Fig. 2) strongly resembles the one calculated with TDDFT and is also in close agreement with the experimental one. Note that the absorption maxima of both theoretical spectra are shifted to 0cm^{-1} in Fig. 2 for better comparability. A discussion of the optimized geometries is given at the beginning of the next chapter. The optimization of a CoIn between 1L_a and 1L_b on this level of theory was successful. With an excitation energy of 5.17 eV, it lies energetically between the FC point and the excited state minima and therefore within reach.

3.2. Quantum dynamical calculations

Quantum dynamics for a molecule like pyrene is currently only feasible in reduced coordinates. To include any relevant molecular structures in our simulations, we constructed a 2D coordinate space out of the orthonormalized displacement vectors from the FC point to the 1L_a minimum ($q_{\text{FC}\rightarrow L_a}$) as well as to the 1L_b minimum ($q_{\text{FC}\rightarrow L_b}$). Both coordinate vectors are overlaid on the optimized S_0 geometry in Fig. 4 with a magnification factor of 6.12. As the pictures suggest, both vectors lie in the molecular plane and all of the minimum structures are planar, as required by symmetry reasons. The large magnification factor

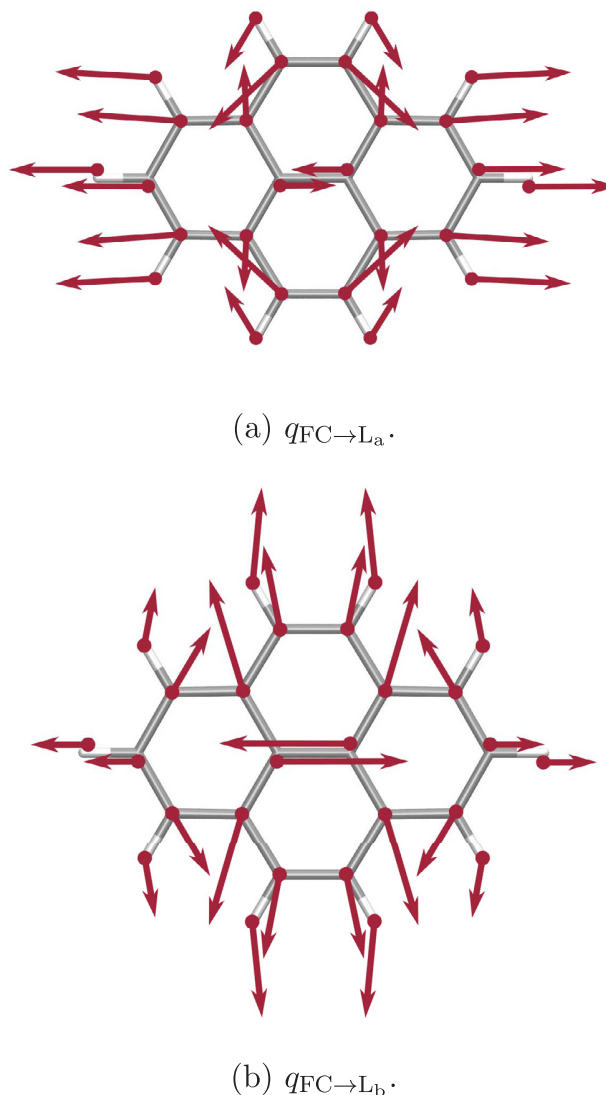


Fig. 4. Coordinate vectors used to represent pyrene in quantum dynamical simulations built from displacement vectors from the optimized S_0 minimum to the respective excited state minimum. $q_{\text{FC}\rightarrow L_b}$ is orthogonalized with respect to $q_{\text{FC}\rightarrow L_a}$.

however demonstrates the small deviation between these structures and therefore the strong delocalization of the excitation over the complete π system. This fact is also corroborated by the small RMSD of 0.015 Å for the 1L_b minimum and 0.020 Å for the 1L_a minimum, each compared to the S_0 minimum structure. The difference between both vectors is conspicuous: While $q_{\text{FC}\rightarrow L_a}$ describes a stretching motion along the long axis of the molecule, the orthogonal $q_{\text{FC}\rightarrow L_b}$ is best characterized as a stretching along the short axis. These preferred directions agree with the directions of the electronic transition dipole moment of these excitations.

Using the Wilson G-matrix formalism for the kinetic energy operator, this choice of coordinates has two major consequences: As we employ linear coordinates, we obtain constant G-matrix elements throughout the whole grid. Furthermore, the necessary orthogonalization prevents kinetic coupling between the coordinates and the off-diagonal G-matrix element is zero.

The resulting excited adiabatic PESs spanned by these two coordinates are shown in Fig. 5. The S_2 PES is very harmonic. The projection of the optimized CoIn geometry onto the subspace is located in

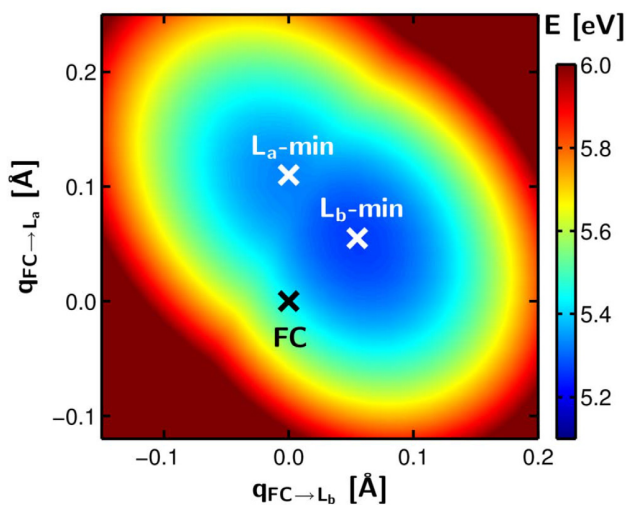
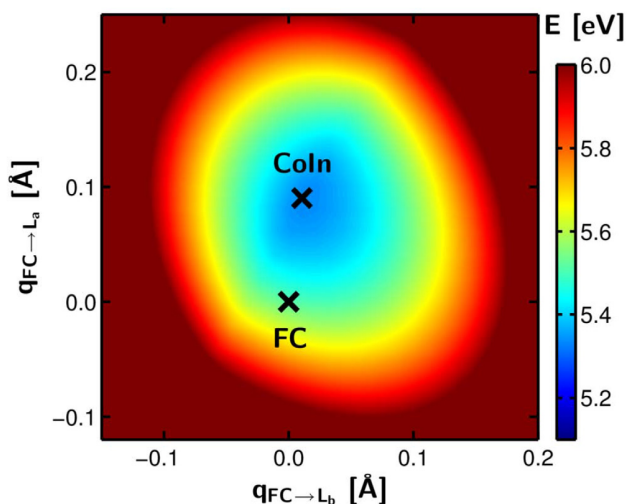
(a) S_1 potential energy surface.(b) S_2 potential energy surface.

Fig. 5. Adiabatic potential energy surfaces used to represent pyrene in the quantum dynamical simulations calculated with CASSCF(4,4)/6-31G(d). The S_0 minimum is set to 0 eV. The location of the optimized geometries are marked.

the minimum of the potential. The S_1 PES exhibits a double well structure with the 1L_b and 1L_a minimum. It is clearly visible that the 1L_b minimum is lower in energy and its minimum well is much more pronounced. Between the minima, there is a small barrier that can be interpreted as the crossing seam of the 1L_a and 1L_b PESs in a diabatic picture.

Due to the narrow harmonic potential well in S_2 , the low vibrational eigenfunctions are energetically far apart. Therefore, we simulated an ultrashort laser pulse with a FWHM of only 6.8 fs in the intensity domain to model the excitation of a wave packet from the electronic ground state to S_2 . The resulting wave packet (Fig. 6, black) is quite delocalized and starts to decay through the CoIn to S_1 immediately after photoexcitation. In the course of the simulation, the wave packet moves from the FC region towards the S_2 minimum while continuously decaying (Fig. 6, white). Apart from that, the wave packet does not move on the S_2 PES, which we attribute to its high degree of delocalization and the corresponding lack of initial momentum in a particular direction.

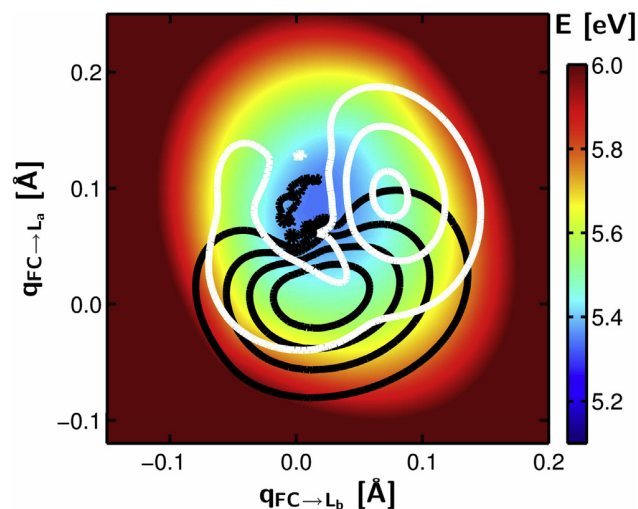


Fig. 6. Wavepacket on the S_2 potential energy surface at $t = 0$ fs (black) and $t = 150$ fs (white). Immediately after excitation to S_2 , the strongly delocalized wave packet starts to couple to S_1 , causing a visible disruption around the CoIn. During the simulation, the wave packet evolves towards the S_2 minimum and continues to decay.

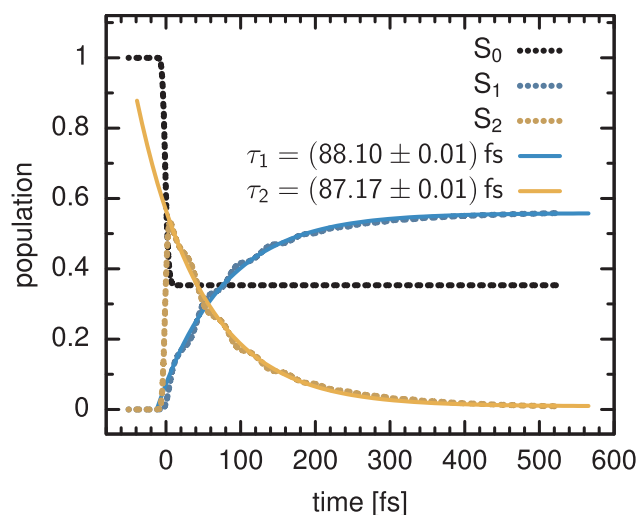


Fig. 7. Population dynamics after laser pulse excitation of pyrene in the quantum dynamical simulation. The lifetimes τ were obtained by mono-exponentially fitting the population curves for S_1 and S_2 , respectively.

In Fig. 7 the population of all three states, S_0 , S_1 , and S_2 is plotted. At $t = 0$ fs the laser is at its maximum and excites around 60% of the ground state population (dotted black) to S_2 (dotted orange). Almost immediately after the excitation, the population of S_1 (dotted blue) is rising, indicating successful population transfer through the CoIn. After 600 fs the population is almost completely transferred from S_2 to S_1 . Small oscillations of the population curves are due to immediate backcoupling between the states.

To obtain a relaxation time τ for the ultrafast S_2/S_1 transition from the population curves, we fitted both the rise in population in S_1 and the decay from S_2 with an exponential function $f(x)$ and $g(x)$, respectively (Fig. 7, solid lines):

$$f(x) = y_0 - \exp\left(\frac{x_0 - x}{\tau_1}\right), \quad (1)$$

$$g(x) = \exp\left(-\frac{x - x_0}{\tau_2}\right) + y_0. \quad (2)$$

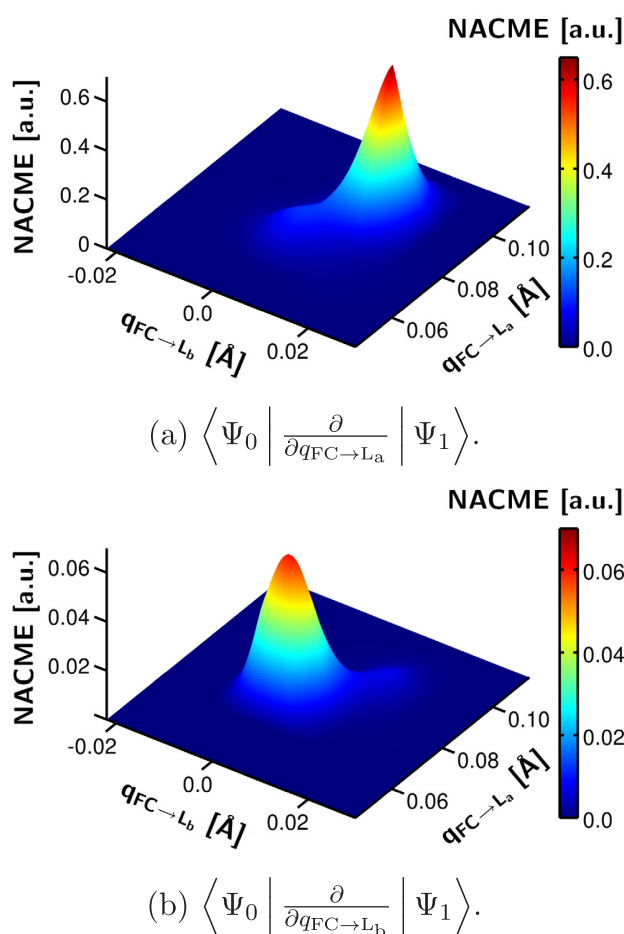


Fig. 8. Non-adiabatic coupling matrix elements (NACME) in the vicinity of the investigated S_1/S_2 conical intersection. Note that the NACME in $q_{\text{FC} \rightarrow L_a}$ direction (a) are an order of magnitude higher than those in $q_{\text{FC} \rightarrow L_b}$ direction (b).

The two resulting time constants $\tau_1 = 88.10$ fs and $\tau_2 = 87.17$ fs are in close agreement with each other and also resemble the experimentally determined decay time of 85 fs [18].

However, these results have to be taken with a grain of salt, since the rate limiting factor in our simulations is not the path of the wave packet towards the CoIn but the coupling to S_1 and the amount of back-coupling to S_2 . The former is fixed by the size of the NACME (Fig. 8) but the latter can be strongly influenced by the masking function we employed in S_1 to cut off the wave packet and effectively simulate its further decay from S_1 . Removing all the population in S_1 immediately after coupling through the CoIn yields a lower limit of 33 fs for the relaxation time, while moving the masking function outward from the CoIn produces lifetimes of over 400 fs. This means that the relaxation time is dependent on the exact position of this cut-off function on the S_1 PES and was modeled in our simulations to reproduce the experimental findings.

3.3. Semi-classical on-the-fly dynamical calculations

The semi-classical dynamics was started in the 1L_a state. Out of 198 trajectories, 72 ran the complete simulation time of 250 fs. In Fig. 9 the average energies for the 1L_a (orange) and 1L_b states (blue) are shown together with the energy of the current state (red dots) and the total energy (black). The point of reference for the energies is the ground state energy of the minimum structure on the CASSCF(4,4) level of theory. Due to the averaging, the marker for the current state either lies on the curve for the 1L_a or the 1L_b state, or between them. This way it

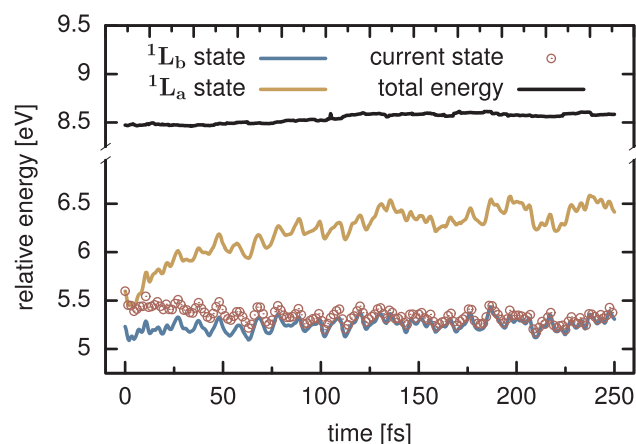


Fig. 9. Relative energies of 1L_a (orange), 1L_b (blue) and the current state (red dots) averaged over 198 trajectories. The energies are relative to the average energy of the electronic ground state at the starting point of the trajectories.

indicates the proportion of trajectories currently running in one or the other state. After around 10 fs many trajectories already show transitions into the 1L_b state. Thereafter, the 1L_a state is more and more depopulated and 1L_b becomes the dominant state.

The temporal evolution of the population of both states highlights this even more. It is depicted in Fig. 10 together with the number of running trajectories at a given time. The population transfer from 1L_a (orange dots) to 1L_b (blue dots) is clearly visible, beginning right after the start of the trajectories, as 1L_a has a sharp decrease at this early stage. After 30 fs, both states are equally populated, while the population transfer continues. At the end of the simulation time of 250 fs, 1L_b is populated with 85.9%, 1L_a with 14.1%. The residual population in the 1L_a state differs from experimental observations [17] where it approaches zero and emission is only reported from 1L_b . A possible explanation might be the omission of triplet states in our dynamics simulation. Like in Section 3.2, it is possible to use exponential fit functions to model the data and extract time constants from the on-the-fly population data. These fit functions are shown in Fig. 10 as solid lines. The time constant for decrease and increase, respectively, is 43 ± 0.6 fs, which is very close to the lower limit for the time constant found in the quantum dynamics. In both cases the deviation from the experimentally found 85 fs stems from the quantum chemical

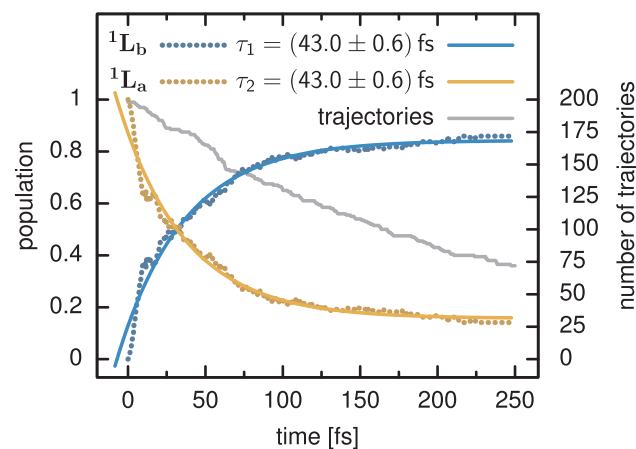


Fig. 10. Population dynamics of the on-the-fly simulation. The population of 1L_a (orange dots) decreases exponentially with a time constant $\tau = 43.0 \pm 0.6$ fs, while the population of 1L_b (blue dots) simultaneously rises. After 250 fs, the ratio of populations is 85.9:14.1 in favor of 1L_b . The fit functions are drawn as continuous lines. In gray, the number of running trajectories at each point in time is plotted.

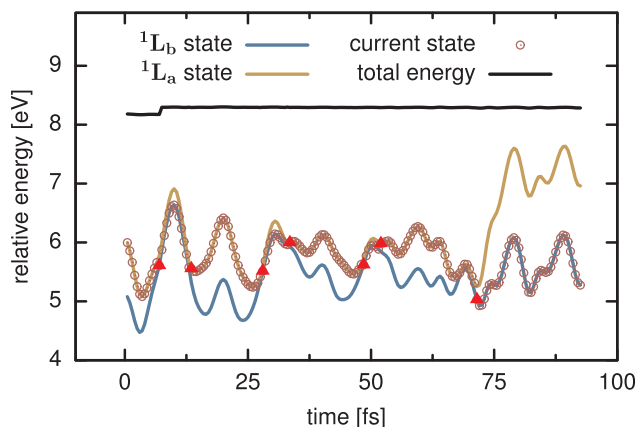


Fig. 11. First 100 fs of an example trajectory of the on-the-fly simulation. The continuous lines represent the energies of the 1L_a state (orange) and the 1L_b state (blue) as well as the total energy (black). The current state is marked with dark red dots, hops are marked with bright red triangles. There are seven hops occurring in the shown time span, the first after 7.0 fs, the last after 71.5 fs. Up until 75 fs, both states run very close in energy, afterwards 1L_a is destabilized by ca. 1.5 eV and no further hop is happening until the end of the simulation time at 250 fs. The energies are relative to the energy of the ground state at the beginning of the trajectory.

description, as the minimum wells on CASSCF(4,4) level of theory are too steep and lie too close together.

To get a better understanding of the occurring dynamics, it is worthwhile to take a closer look at the trajectories. In Fig. 11 the temporal evolution of the first 100 fs of an example trajectory is shown. In the course of this time span, seven hops occur, marked with bright red triangles, the first already at 7.0 fs and the last at 71.5 fs. This demonstrates that there is not just one, but multiple transitions between these two states. Both states are energetically close across a relatively large part of the PES, resulting in a long amount of time before the energies diverge, here up to an energy difference of 1.5 eV, and the dynamics continues only in 1L_b . Geometrically speaking, at this point in time the trajectory enters and then further explores a part of the configuration space where 1L_a is clearly destabilized compared to 1L_b . The initial phase with multiple hops back and forth corresponds to the immediate back coupling already observed in the quantum dynamics.

Using the number of hops as well as the points in time of the first and last hop for all trajectories, we can perform a statistical analysis of the on-the-fly dynamics. The results are listed in Table 2. Each line gives the data averaged over all hops and exclusively over the hops going into 1L_a and 1L_b , respectively. On average, each trajectory displays three hops occurring between 21.2 fs and 56.8 fs. Thereby, 1.1 hops go into 1L_a and 1.9 hops into 1L_b . These values already demonstrate the prevalence of the 1L_b state, which is further established by the fact that out of 198 trajectories, the vast majority of 170 finish in 1L_b . Since all trajectories start in the 1L_a state, the first hops must go into 1L_b and take place after 21.2 fs. The first hops back occur a little later after

Table 2

Statistical data for the on-the-fly simulation. Listed are the average number of hops and the average point in time of the first and last hop, respectively. The values are given separately for the hops going into 1L_a and 1L_b , respectively, and for all hops together. For the number of hops the standard deviation is shown as error margin.

hops into	1L_a and 1L_b	1L_a	1L_b
No. of hops	3.0 ± 2.9	1.1 ± 1.5	1.9 ± 1.5
first hop [fs]	21.2	34.0	21.2
last hop [fs]	56.8	65.1	55.0

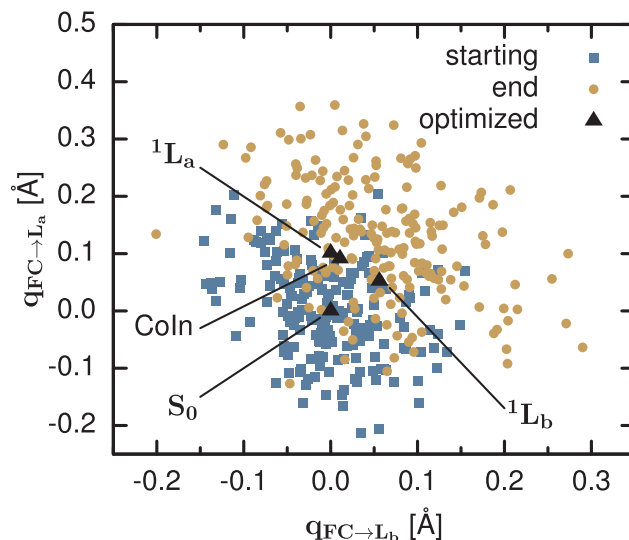


Fig. 12. Projection of starting (blue) and end geometries (orange) of the on-the-fly trajectories onto the surface spanned by the optimized minimum geometries. The location of the optimized geometries of the S_0 , 1L_a , 1L_b minimum and of the CoIn are marked with black triangles.

34.0 fs. The last hops into 1L_b occur after 55.0 fs, the last ones into 1L_a again around 10 fs later. As the latter implies trajectories finishing in 1L_a , here the divergence in energy shown in the example trajectory above is not occurring or not lasting. Only a minority of 28 trajectories end in 1L_a , which corresponds well to the experimentally observed fluorescence solely from 1L_b .

However, the mentioned average values should not obscure the large diversity occurring in this set of trajectories. The standard deviation of the number of hops is listed as an error margin in Table 2. It is almost as large or even larger as the average value, owing to the fact that in the set of trajectories the number of hops varies between zero and 14.

Since we used a reduced subspace for our quantum dynamics, it is now interesting to project important geometry points of the on-the-fly trajectories onto this subspace to evaluate if the subspace is meaningful. In Fig. 12, the projections of both the starting (blue) and the end geometries (orange) are shown. Furthermore, the location of the optimized geometries of the S_0 , 1L_b and 1L_a minimum and of the CoIn are marked in black. The starting points display very clearly the effect of the Wigner distribution: The blue squares are randomly spread around the S_0 minimum geometry, from -0.2 \AA to 0.2 \AA in $q_{FC \rightarrow L_a}$ and from -0.15 \AA to 0.15 \AA in $q_{FC \rightarrow L_b}$, with the highest point density located directly at the S_0 minimum. The finishing points are shifted towards the minima of 1L_a and 1L_b and are even more widespread. While outliers are located at almost 0.4 \AA in $q_{FC \rightarrow L_a}$ and 0.3 \AA in $q_{FC \rightarrow L_b}$, the main portion of trajectories finishes within the minimum wells of 1L_a and 1L_b shown in Fig. 5a. The points, however, are also not evenly distributed around the excited states minima, but shifted towards positive coordinate values in both directions enhancing the stretching of pyrene along both molecular axes. A comparison with the PES in Fig. 5a confirms that the area of negative coordinate values is highly unstable. Overall, a similar motion from the FC point to the minima and subsequent spreading as found in the quantum dynamics is recognizable.

At this point, the question arises at which geometries the hops occur. In Fig. 13 all hopping geometries are projected onto the 2D surface. It is apparent that the highest density of hopping points is located near the optimized CoIn geometry, but nevertheless hoppings can occur anywhere in the S_1 2D subspace. Thus, in full dimensionality the state degeneracy is not only restricted to the optimized CoIn or the

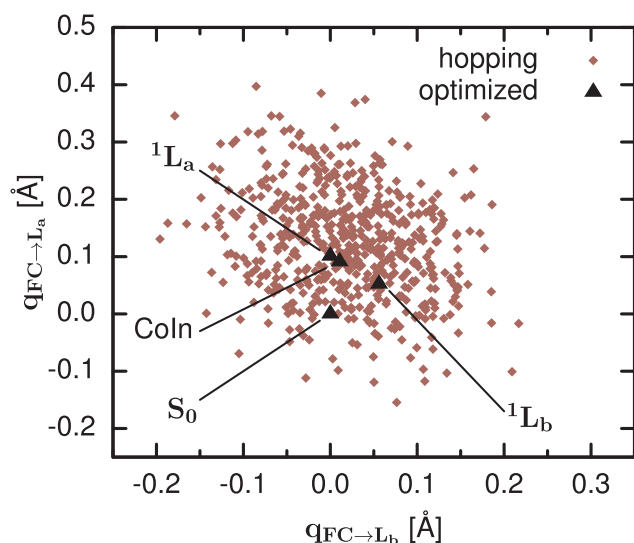


Fig. 13. Projection of the hopping geometries of the on-the-fly trajectories onto the surface spanned by the optimized minimum geometries. The location of the optimized geometries of the S_0 , 1L_a , 1L_b minimum and the CoIn are marked with black triangles.

small barrier. It is again a hint for a very efficient coupling between these two states.

4. Conclusions

Quantum chemically, pyrene is a very challenging molecule, because not only the state ordering and energies in the FC region, but also the relative position of the 1L_a and 1L_b state minima are important. Nevertheless, we were able to simulate for the first time its ultrafast relaxation from the bright 1L_a state to the fluorescent 1L_b state. Thereto, we employed two dynamical methods that complement each other. Both were based on the carefully chosen multireference *ab initio* method leading to CASSCF(4,4) as the most balanced description for the quantum chemistry, where neither 1L_a nor 1L_b state is inherently favored.

In the grid-based quantum dynamics we used a 2D subspace generated from displacement vectors between minimum structures. Due to the large π system and the rigid molecular structure, these displacements are strongly delocalized and hence small. With non-adiabatic coupling matrix elements projected on our subspace we were able to account for the coupling between these two states. By observing the wave packet passing through the ${}^1L_a/{}^1L_b$ CoIn we could substantiate the relaxation mechanism postulated in the literature, while only allowing the immediate back coupling *via* a masking function.

Furthermore, we performed full-dimensional non-adiabatic on-the-fly dynamics. Here, multiple hops back and forth occurred per trajectory comparable to the back coupling in the quantum dynamics, with the 1L_b as lowest excited state minimum containing in the end the vast majority of population. Similar to the wave packet picture there was an overall movement from the FC area towards the minima. The location of the hopping events were widespread around the optimized minima resembling the respective PES and demonstrating that not the optimized conical intersection alone was responsible for the population transfer, but hopping could occur on a large part of the subspace. So by thorough analysis of the trajectory geometries we could confirm our coordinate choice for the quantum dynamics and in this way further legitimate our dimensionality reduction. By fitting an exponential function to the population curves we were able to extract decay time constants comparable to the experiment and in this way also verify the time scale of the relaxation.

Acknowledgments

Financial support by the Deutsche Forschungsgemeinschaft through the SFB749 is gratefully acknowledged. We thank Teresa Küblböck for her contributions to the first calculations and Bastian Baudisch and Eberhard Riedle for fruitful discussions.

Appendix A. Supplementary data

Supplementary data associated with this article can be found, in the online version, at <https://doi.org/10.1016/j.chemphys.2018.08.002>.

References

- [1] T.M. Figueira-Duarte, K. Müllen, Pyrene-based materials for organic electronics, *Chem. Rev.* 111 (2011) 7260–7314, <https://doi.org/10.1021/cr100428a>.
- [2] T. Förster, K. Kasper, Ein konzentrationsumschlag der fluoreszenz des pyrens, *Z. Elektrochem., Ber. Bunsenges. Phys. Chem.* 59 (1955) 976–980, <https://doi.org/10.1002/bbpc.19550591018>.
- [3] J.B. Birks, Excimers, *Rep. Prog. Phys.* 38 (1975) 903–974, <https://doi.org/10.1088/0034-4885/38/8/001>.
- [4] F.M. Winnik, Photophysics of preassociated pyrenes in aqueous polymer solutions and in other organized media, *Chem. Rev.* 93 (1993) 587–614, <https://doi.org/10.1021/cr00018a001>.
- [5] E.A. Mangle, M.R. Topp, Excited-state dynamics of jet-cooled pyrene and some molecular complexes, *J. Phys. Chem.* 90 (1986) 802–807, <https://doi.org/10.1021/j100277a020>.
- [6] D.S. Karpovich, G.J. Blanchard, Relating the polarity-dependent fluorescence response of pyrene to vibronic coupling. Achieving a fundamental understanding of the py polarity scale, *J. Phys. Chem.* 99 (1995) 3951–3958, <https://doi.org/10.1021/j100012a014>.
- [7] F.P. Schwarz, S.P. Wasik, Fluorescence measurements of benzene, naphthalene, anthracene, pyrene, fluoranthene, and benzo[*e*]pyrene in water, *Anal. Chem.* 48 (1976) 524–528, <https://doi.org/10.1021/ac60367a046>.
- [8] P. Conlon, C.J. Yang, Y. Wu, Y. Chen, K. Martinez, Y. Kim, N. Stevens, A.A. Marti, S. Jockusch, N.J. Turro, W. Tan, Pyrene excimer signaling molecular beacons for probing nucleic acids, *J. Am. Chem. Soc.* 130 (2008) 336–342, <https://doi.org/10.1021/ja076411y>.
- [9] X. Su, X. Xiao, C. Zhang, M. Zhao, Nucleic acid fluorescent probes for biological sensing, *Appl. Spectrosc.* 66 (2012) 1249–1261, <https://doi.org/10.1366/12-06803>.
- [10] O.A. Krasheninina, D.S. Novopashina, E.K. Apartsin, A.G. Venyaminova, Recent advances in nucleic acid targeting probes and supramolecular constructs based on pyrene-modified oligonucleotides, *Molecules* 22 (2017) 2108, <https://doi.org/10.3390/molecules22122108>.
- [11] G. Bains, A.B. Patel, V. Narayanaswami, Pyrene: a probe to study protein conformation and conformational changes, *Molecules* 16 (2011) 7909–7935, <https://doi.org/10.3390/molecules16097909>.
- [12] J. Wu, M. Dobrowolski, M. Cyrański, B. Merner, G. Bodwell, Y. Mo, P. Schleyer, On the aromatic stabilization energy of the 4N π electron pyrene, *Mol. Phys.* 107 (2009) 1177–1186, <https://doi.org/10.1080/00268970902784918>.
- [13] R.S. Becker, I.S. Singh, E.A. Jackson, Comprehensive spectroscopic investigation of polynuclear aromatic hydrocarbons. i. absorption spectra and state assignments for the tetracyclic hydrocarbons and their alkyl-substituted derivatives, *J. Chem. Phys.* 38 (1963) 2144, <https://doi.org/10.1063/1.1733946>.
- [14] J.R. Platt, Classification of spectra of cata-condensed hydrocarbons, *J. Chem. Phys.* 17 (1949) 484, <https://doi.org/10.1063/1.1747293>.
- [15] P. Foggi, L. Pettini, I. Santa, R. Righini, S. Califano, Transient absorption and vibrational relaxation dynamics of the lowest excited singlet state of pyrene in solution, *J. Phys. Chem.* 99 (1995) 7439–7445, <https://doi.org/10.1021/j100019a029>.
- [16] B. Baudisch, Time resolved broadband spectroscopy from uv to nir: beneficial use of the coherent artifact and pyrene dynamics (Ph.D. thesis), Ludwig-Maximilians-Universität München, 2018 <https://edoc.ub.uni-muenchen.de/21902/>.
- [17] F.V.R. Neuwahl, P. Foggi, Direct observation of s₂–s₁ internal conversion in pyrene by femtosecond transient absorption, *Laser Chem.* 19 (1999) 375–379, <https://doi.org/10.1155/1999/37692>.
- [18] N. Krebs, New insights for femtosecond spectroscopy (Ph.D. thesis), Ludwig-Maximilians-Universität München, 2013 <http://edoc.ub.uni-muenchen.de/16299/>.
- [19] W. Domcke, D. Yarkony, H. Köppel (Eds.), Conical Intersections: Electronic Structure, Dynamics & Spectroscopy (Advanced Series in Physical Chemistry), World Scientific, Singapur, 2004, <https://doi.org/10.1142/9789812565464>.
- [20] W. Domcke, D.R. Yarkony, Role of conical intersections in molecular spectroscopy and photoinduced chemical dynamics, *Annu. Rev. Phys. Chem.* 63 (2012) 325–352, <https://doi.org/10.1146/annurev-physchem-032210-103522>.
- [21] A. Nenov, A. Giussani, B.P. Fingerhut, I. Rivalta, E. Dumont, S. Mukamel, M. Garavelli, Spectral lineshapes in nonlinear electronic spectroscopy, *Phys. Chem. Chem. Phys.* 17 (2015) 30925–30936, <https://doi.org/10.1039/c5cp01167a>.
- [22] M. Dierksen, S. Grimme, Density functional calculations of the vibronic structure of electronic absorption spectra, *J. Chem. Phys.* 120 (2004) 3544, <https://doi.org/10.1063/1.1642595>.

- [23] M. Dierksen, S. Grimme, The vibronic structure of electronic absorption spectra of large molecules: a time-dependent density functional study on the influence of exact hartree-fock exchange, *J. Phys. Chem. A* 108 (2004) 10225–10237, <https://doi.org/10.1021/jp047289h>.
- [24] Y.H. Park, B.-S. Cheong, Theoretical investigation of electronic structures of the ground and excited states of pyrene and its derivatives, *Curr. Appl. Phys.* 6 (2006) 700–705, <https://doi.org/10.1016/j.cap.2005.04.023>.
- [25] I.S.K. Kerkines, I.D. Petsalakis, G. Theodorakopoulos, W. Klopper, Low-lying absorption and emission spectra of pyrene, 1,6-dithiaprene, and tetrathiafulvalene: A comparison between ab initio and time-dependent density functional methods, *J. Chem. Phys.* 131 (2009) 224315, <https://doi.org/10.1063/1.3271347>.
- [26] H. Öricü, N. Acar, Effects of substituent groups and solvent media on pyrene in ground and excited states: A DFT and tddft study, *Comp. Theor. Chem.* 1056 (2015) 11–18, <https://doi.org/10.1016/j.comptc.2015.01.001>.
- [27] Y. Bito, N. Shida, T. Toru, Ab initio mrsd-ci calculations of the ground and the two lowest-lying excited states of pyrene, *Chem. Phys. Lett.* 328 (2000) 310–315, [https://doi.org/10.1016/s0009-2614\(00\)00936-2](https://doi.org/10.1016/s0009-2614(00)00936-2).
- [28] K. Yamazaki, N. Niitsu, K. Nakamura, M. Kanno, H. Kono, Electronic excited state paths of stone-wales rearrangement in pyrene: Roles of conical intersections, *J. Phys. Chem. A* 116 (2012) 11441–11450, <https://doi.org/10.1021/jp306894x>.
- [29] A.Y. Freidzon, R.R. Valiev, A.A. Bereznoy, Ab initio simulation of pyrene spectra in water matrices, *RSC Adv.* 4 (2014) 42054–42065, <https://doi.org/10.1039/c4ra05574h>.
- [30] A.A. Granovsky, Extended multi-configuration quasi-degenerate perturbation theory: The new approach to multi-state multi-reference perturbation theory, *J. Chem. Phys.* 134 (2011) 214113, <https://doi.org/10.1063/1.3596699>.
- [31] W. Domcke, G. Stock, Theory of ultrafast nonadiabatic excited-state processes and their spectroscopic detection in real time, *Adv. Chem. Phys.* 100 (1997) 1, <https://doi.org/10.1002/9780470141595.ch1>.
- [32] H.R. Larsson, D.J. Tannor, Dynamical pruning of the multiconfiguration time-dependent hartree (DP-MCTDH) method: An efficient approach for multidimensional quantum dynamics, *J. Chem. Phys.* 147 (2017) 044103, <https://doi.org/10.1063/1.4993219>.
- [33] M.J. Frisch, G.W. Trucks, H.B. Schlegel, G.E. Scuseria, M.A. Robb, J.R. Cheeseman, G. Scalmani, V. Barone, B. Mennucci, G.A. Petersson, H. Nakatsuji, M. Caricato, X. Li, H.P. Hratchian, A.F. Izmaylov, J. Bloino, G. Zheng, J.L. Sonnenberg, M. Hada, M. Ehara, K. Toyota, R. Fukuda, J. Hasegawa, M. Ishida, T. Nakajima, Y. Honda, O. Kitao, H. Nakai, T. Vreven, J.A. Montgomery, Jr., J.E. Peralta, F. Ogliaro, M. Bearpark, J.J. Heyd, E. Brothers, K.N. Kudin, V.N. Staroverov, R. Kobayashi, J. Normand, K. Raghavachari, A. Rendell, J.C. Burant, S.S. Iyengar, J. Tomasi, M. Cossi, N. Rega, J.M. Millam, M. Klene, J.E. Knox, J.B. Cross, V. Bakken, C. Adamo, J. Jaramillo, R. Gomperts, R.E. Stratmann, O. Yazyev, A.J. Austin, R. Cammi, C. Pomelli, J.W. Ochterski, R.L. Martin, K. Morokuma, V.G. Zakrzewski, G.A. Voth, P. Salvador, J.J. Dannenberg, S. Dapprich, A.D. Daniels, Ö. Farkas, J.B. Foresman, J.V. Ortiz, J. Cioslowski, D.J. Fox, Gaussian 09, Revision D.01, <http://www.gaussian.com>, Gaussian Inc., Wallingford CT 2009.
- [34] H.-J. Werner, P.J. Knowles, G. Knizia, F.R. Manby, M. Schütz, P. Celani, T. Korona, R. Lindh, A. Mitrushenkov, G. Rauhut, K.R. Shamasundar, T.B. Adler, R.D. Amos, A. Bernhardsson, A. Berning, D.L. Cooper, M.J.O. Deegan, A.J. Dobbyn, F. Eckert, E. Goll, C. Hampel, A. Hesselmann, G. Hetzer, T. Hrenar, G. Jansen, C. Köppl, Y. Liu, A.W. Lloyd, R.A. Mata, A.J. May, S.J. McNicholas, W. Meyer, M.E. Mura, A. Nicklass, D.P. O'Neill, P. Palmieri, D. Peng, K. Pflüger, R. Pitzer, M. Reiher, T. Shiozaki, H. Stoll, A.J. Stone, R. Tarroni, T. Thorsteinsson, M. Wang, Molpro, version 2012.1, a package of ab initio programs, see <http://www.molpro.net>.
- [35] H.-J. Werner, P.J. Knowles, G. Knizia, F.R. Manby, M. Schütz, Molpro: a general-purpose quantum chemistry program package, *WIREs Comput. Mol. Sci.* 2 (2012) 242–253, <https://doi.org/10.1002/wcms.82>.
- [36] B.O. Roos, P.R. Taylor, P.E. Siegbahn, A complete active space Scf method (CASSCF) using a density matrix formulated super-ci approach, *Chem. Phys.* 48 (1980) 157–173, [https://doi.org/10.1016/0301-0104\(80\)80045-0](https://doi.org/10.1016/0301-0104(80)80045-0).
- [37] P.J. Knowles, H.-J. Werner, An efficient second-order mc scf method for long configuration expansions, *Chem. Phys. Lett.* 115 (1985) 259–267, [https://doi.org/10.1016/0009-2614\(85\)80025-7](https://doi.org/10.1016/0009-2614(85)80025-7).
- [38] H.-J. Werner, P.J. Knowles, A second order multiconfiguration scf procedure with optimum convergence, *J. Chem. Phys.* 82 (1985) 5053, <https://doi.org/10.1063/1.448627>.
- [39] F. Santoro, R. Improta, A. Lami, J. Bloino, V. Barone, Effective method to compute franck-condon integrals for optical spectra of large molecules in solution, *J. Chem. Phys.* 126 (2007) 084509, <https://doi.org/10.1063/1.2437197>.
- [40] F. Santoro, R. Improta, A. Lami, J. Bloino, V. Barone, Erratum: effective method to compute franck-condon integrals for optical spectra of large molecules in solution [J. Chem. Phys. 126, 084509 (2007)], *J. Chem. Phys.* 126 (2007) 169903, <https://doi.org/10.1063/1.2722259>.
- [41] V. Barone, J. Bloino, M. Biczysko, F. Santoro, Fully integrated approach to compute vibrationally resolved optical spectra: From small molecules to macrosystems, *J. Chem. Theory Comput.* 5 (2009) 540–554, <https://doi.org/10.1021/ct8004744>.
- [42] J. Bloino, M. Biczysko, F. Santoro, V. Barone, General approach to compute vibrationally resolved one-photon electronic spectra, *J. Chem. Theory Comput.* 6 (2010) 1256–1274, <https://doi.org/10.1021/ct9006772>.
- [43] F. Santoro, FcClasses: a Fortran 77 code, release 2.1, <http://www.piccom.cnr.it/fcClasses> (07.12.2015), 2008.
- [44] C. Lanczos, An iteration method for the solution of the eigenvalue problem of linear differential and integral operators, *J. Res. Nat. Bur. Stand.* 45 (1950) 255, <https://doi.org/10.6028/jres.045.026>.
- [45] D.J. Tannor, *Introduction to Quantum Mechanics: a Time-dependent Perspective*, University Science Books, Sausalito, CA, 2007.
- [46] B. Podolsky, Quantum-mechanically correct form of hamiltonian function for conservative systems, *Phys. Rev.* 32 (1928) 812–816, <https://doi.org/10.1103/PhysRev.32.812>.
- [47] E.B. Wilson Jr., J.C. Decius, P.C. Cross, *Molecular Vibrations: The Theory of Infrared and Raman Vibrational Spectra*, Dover Publ, New York, NY, 1980.
- [48] L. Schaad, J. Hu, The schrödinger equation in generalized coordinates, *J. Mol. Struct. THEOCHEM* 185 (1989) 203–215, [https://doi.org/10.1016/0166-1280\(89\)85014-6](https://doi.org/10.1016/0166-1280(89)85014-6).
- [49] S. Thallmair, M.K. Roos, R. de Vivie-Riedle, Design of specially adapted reactive coordinates to economically compute potential and kinetic energy operators including geometry relaxation, *J. Chem. Phys.* 144 (2016) 234104, <https://doi.org/10.1063/1.4953667>.
- [50] M. Barbatti, G. Granucci, M. Ruckebauer, F. Plasser, R. Crespo-Otero, J. Pittner, M. Persico, H. Lischka, NewtonX: a package for Newtonian dynamics close to the crossing seam, version 1.4, <http://www.newtonx.org>, 2014.
- [51] M. Barbatti, M. Ruckebauer, F. Plasser, J. Pittner, G. Granucci, M. Persico, H. Lischka, Newton-x: a surface-hopping program for nonadiabatic molecular dynamics, *WIREs Comput. Mol. Sci.* 4 (2014) 26–33, <https://doi.org/10.1002/wcms.1158>.
- [52] S. Oesterling, *Ab initio studies on photorelaxation: exploring, altering and crossing the excited state landscape*, Ph.D. thesis Ludwig-Maximilians-Universität München, 2017 <https://edoc.ub.uni-muenchen.de/20910/>.
- [53] W.J. Hehre, R. Ditchfield, J.A. Pople, Self-consistent molecular orbital methods. XII. Further extensions of Gaussian-type basis sets for use in molecular orbital studies of organic molecules, *J. Chem. Phys.* 56 (1972) 2257–2261, <https://doi.org/10.1063/1.1677527>.
- [54] P.C. Hariharan, J.A. Pople, The influence of polarization functions on molecular orbital hydrogenation energies, *Theor. Chim. Acta* 28 (1973) 213–222, <https://doi.org/10.1007/bf00533485>.
- [55] M. Barbatti, A.J.A. Aquino, H. Lischka, The UV absorption of nucleobases: semi-classical ab initio spectra simulations, *Phys. Chem. Chem. Phys.* 12 (2010) 4959, <https://doi.org/10.1039/b924956g>.
- [56] W.C. Swope, H.C. Andersen, P.H. Berens, K.R. Wilson, A computer simulation method for the calculation of equilibrium constants for the formation of physical clusters of molecules: application to small water clusters, *J. Chem. Phys.* 76 (1982) 637–649, <https://doi.org/10.1063/1.442716>.
- [57] J.C. Tully, Molecular dynamics with electronic transitions, *J. Chem. Phys.* 93 (1990) 1061, <https://doi.org/10.1063/1.459170>.
- [58] K.P. Geigle, J. Wolf, G. Hohlneicher, Franck-condon/herzberg-teller interferences in the 11b transitions of pyrene and chrysenes, *J. Photochem. Photobiol., A* 105 (1997) 183–187, [https://doi.org/10.1016/S1010-6030\(96\)04607-2](https://doi.org/10.1016/S1010-6030(96)04607-2).
- [59] T. Yanai, D.P. Tew, N.C. Handy, A new hybrid exchange-correlation functional using the coulomb-attenuating method (cam-b3lyp), *Chem. Phys. Lett.* 393 (2004) 51–57, <https://doi.org/10.1016/j.cplett.2004.06.011>.
- [60] A.M. Rivera-Figueroa, K.A. Ramazan, B.J. Finlayson-Pitts, Fluorescence, absorption, and excitation spectra of polycyclic aromatic hydrocarbons as a tool for quantitative analysis, *J. Chem. Educ.* 81 (2004) 242, <https://doi.org/10.1021/ed081p242>.
- [61] M. Schmitt, R. Brause, C.M. Marian, S. Salzmann, W.L. Meerts, Electronically excited states of tryptamine and its microhydrated complex, *J. Chem. Phys.* 125 (2006) 124309, <https://doi.org/10.1063/1.2354494>.
- [62] M. Parac, S. Grimme, A tddft study of the lowest excitation energies of polycyclic aromatic hydrocarbons, *Chem. Phys.* 292 (2003) 11–21, [https://doi.org/10.1016/s0301-0104\(03\)00250-7](https://doi.org/10.1016/s0301-0104(03)00250-7).
- [63] S. Grimme, M. Parac, Substantial errors from time-dependent density functional theory for the calculation of excited states of large π systems, *ChemPhysChem* 4 (2003) 292–295, <https://doi.org/10.1002/cphc.200390047>.
- [64] B.M. Wong, T.H. Hsieh, Optoelectronic and excitonic properties of oligoacenes: substantial improvements from range-separated time-dependent density functional theory, *J. Chem. Theory Comput.* 6 (2010) 3704–3712, <https://doi.org/10.1021/ct100529s>.
- [65] R.M. Richard, J.M. Herbert, Time-dependent density-functional description of the 11a state in polycyclic aromatic hydrocarbons: charge-transfer character in disguise? *J. Chem. Theory Comput.* 7 (2011) 1296–1306, <https://doi.org/10.1021/ct100607w>.
- [66] N. Kuritz, T. Stein, R. Baer, L. Kronik, Charge-transfer-like $\pi \rightarrow \pi^*$ excitations in time-dependent density functional theory: a conundrum and its solution, *J. Chem. Theory Comput.* 7 (2011) 2408–2415, <https://doi.org/10.1021/ct2002804>.
- [67] L. Goerigk, S. Grimme, Double-hybrid density functionals provide a balanced description of excited 11a and 11b states in polycyclic aromatic hydrocarbons, *J. Chem. Theory Comput.* 7 (2011) 3272–3277, <https://doi.org/10.1021/ct200380v>.
- [68] M. Krykunov, S. Grimme, T. Ziegler, Accurate theoretical description of the 11a and 11b excited states in acenes using the all order constricted variational density functional theory method and the local density approximation, *J. Chem. Theory Comput.* 8 (2012) 4434–4440, <https://doi.org/10.1021/ct300372x>.
- [69] Y. Kurashige, T. Yanai, Theoretical study of the $\pi \rightarrow \pi^*$ excited states of oligoacenes: a full π -valence DMRG-CASPT2 Study, *Bull. Chem. Soc. Jpn.* 87 (2014) 1071–1073, <https://doi.org/10.1246/bcsj.20140180>.
- [70] B. Moore, H. Sun, N. Govind, K. Kowalski, J. Autschbach, Charge-transfer versus charge-transfer-like excitations revisited, *J. Chem. Theory Comput.* 11 (2015) 3305–3320, <https://doi.org/10.1021/acs.jctc.5b00335>.
- [71] H.F. Bettinger, C. Tönshoff, M. Doerr, E. Sanchez-Garcia, Electronically excited states of higher acenes up to nonacene: a density functional theory/multireference configuration interaction study, *J. Chem. Theory Comput.* 12 (2016) 305–312, <https://doi.org/10.1021/acs.jctc.5b00671>.
- [72] F. Bettanin, L.F.A. Ferrão, M. Pinheiro, A.J.A. Aquino, H. Lischka, F.B.C. Machado, D. Nachtigallova, Singlet 1a and 1b bands for n-acenes (n = 2–7): A CASSCF/

- CASPT2 Study, *J. Chem. Theory Comput.* 13 (2017) 4297–4306, <https://doi.org/10.1021/acs.jctc.7b00302>.
- [73] N.T. Maitra, Perspective: fundamental aspects of time-dependent density functional theory, *J. Chem. Phys.* 144 (2016) 220901, <https://doi.org/10.1063/1.4953039>.
- [74] H.S. Yu, S.L. Li, D.G. Truhlar, Perspective: Kohn-sham density functional theory descending a staircase, *J. Chem. Phys.* 145 (2016) 130901, <https://doi.org/10.1063/1.4963168>.
- [75] J. Olsen, B.O. Roos, P. Jrgensen, H.J.A. Jensen, Determinant based configuration interaction algorithms for complete and restricted configuration interaction spaces, *J. Chem. Phys.* 89 (1988) 2185, <https://doi.org/10.1063/1.455063>.
- [76] P.-Å. Malmqvist, A. Rendell, B.O. Roos, The restricted active space self-consistent-field method, implemented with a split graph unitary group approach, *J. Phys. Chem.* 94 (1990) 5477–5482, <https://doi.org/10.1021/j100377a011>.
- [77] J.D. Coe, T.J. Martínez, Ab initio molecular dynamics of excited-state intramolecular proton transfer around a three-state conical intersection in malonaldehyde, *J. Phys. Chem. A* 110 (2006) 618–630, <https://doi.org/10.1021/jp0535339>.
- [78] L. González, D. Escudero, L. Serrano-Andrés, Progress and challenges in the calculation of electronic excited states, *ChemPhysChem* 13 (2012) 28–51, <https://doi.org/10.1002/cphc.201100200>.

3.2. Identification of the absorbing species in a cyanine dye-DNA construct

Bringing two dye molecules in close proximity allows the π systems of both of them to interact with each other. In this way, a new electronic structure is created by combining the orbitals of the individual molecules, leading to an energetic stabilization. This process is called dimerization and new spectroscopic properties ensue from it. Therefore, absorption spectroscopy is able to distinguish between monomeric and dimeric form. But the shift in absorption occurring between the signals of the new formed dimer and the monomer can further tell the type of aggregation. Two types are possible, H- and J-aggregates, as can be seen in fig. 3.1 following molecular exciton theory [124, 125]. The two molecules are outlined by blue ellipsoids and the polarization

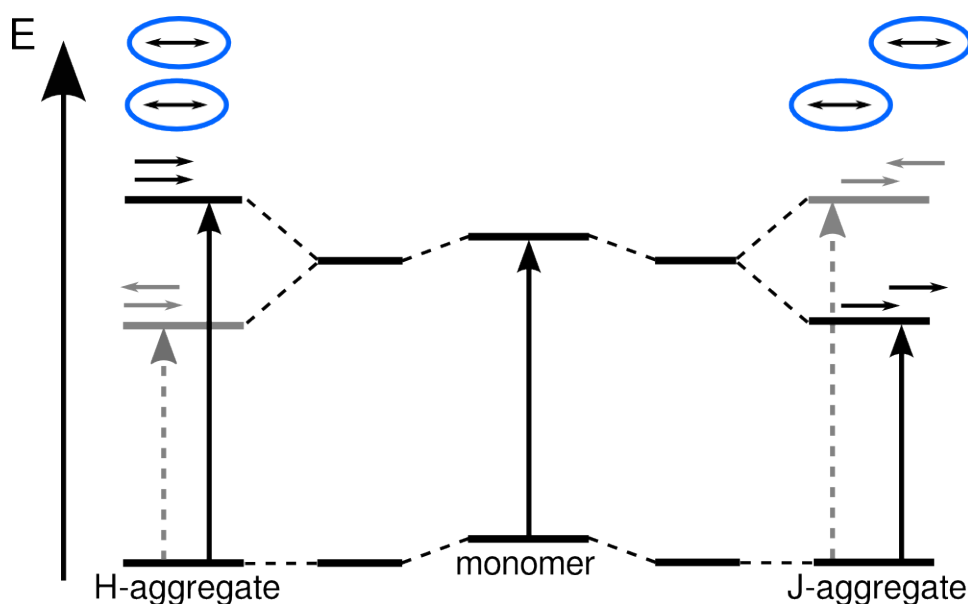


Figure 3.1.: Scheme of ground and excited states of monomer, H- and J-aggregates. The molecules are outlined as blue ellipsoids with the polarization axis of the transition dipole moment as vectors inside. The strong component with the vectors in-phase is each drawn as solid black excitation vector, the weak component with out-of-phase vectors in dashed gray.

axis of their transition dipole moment as vectors inside. In both cases, the transition dipole moments are parallel to each other. In H-aggregates, the molecules are stacked directly above each other in a “side-by-side” fashion, whereas in J-aggregates, the molecules are shifted against each other. These seemingly small difference has dramatic effects on the electronic structure. As seen in the figure, going from the ground and excited state of the monomer, both forms of aggregation lead to a stabilization. In both cases, the new formed excited states split up depending on the orientation of the transition dipole moment. For in-phase orientation the strong component with high oscillator strength f results, drawn here with a solid black vector, in contrast to the out-of-phase arrangement which is the weak component with small f , drawn as dashed gray vector. For H-aggregates, the strong component lies at higher energy, thus, at smaller wave length, meaning a blue or hypsochromic shift, whereby the “h” in hypsochromic give the H-aggregates their name [126]. For J-aggregates (named after their discoverer E. E. Jelley [127, 128]), the strong component lies at lower energy, hence, shorter wave length and implies a red or bathochromic shift.

In this thesis, the shift caused by dimerization is investigated experimentally and theoretically to elucidate the nature of the formed dimer. In the following article “Proximity-Induced H-Aggregation of Cyanine Dyes on DNA-Duplexes” published in *The Journal of Physical Chemistry A* Cy3 dye molecules (see fig. 3.2 top) covalently anchored in DNA are characterized using, on the one hand, absorption and circular dichroism (CD) spectroscopy, and, on the other hand, TDDFT calculations and MD simulations [129]. The DNA serves as scaffold to bring the dye molecules in close proximity. The investigation is based on the already known ability of Cy3 to form aggregates in aqueous solution [130]. It is an effort to artificially create dimers in a controlled manner, a task crucial for the design of future light harvesting devices, as it allows the manipulation of light.

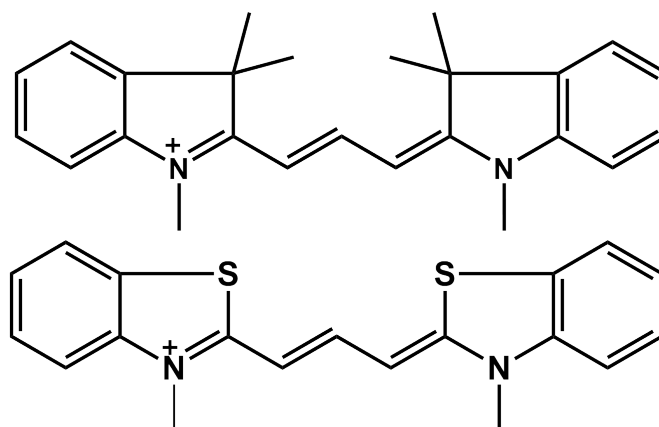


Figure 3.2.: Cyanine 3 (Cy3) as used in the experiments and MD simulations (top). Model system for the TDDFT calculations (bottom).

Key points of the article are:

- In a series of absorption spectroscopy experiments, singly and doubly Cy3 labeled DNA is studied. The used DNA is both single-stranded DNA (ssDNA) and double-stranded DNA (dsDNA) and the Cy3 molecules are either anchored on directly adjacent base pairs or with a spacer base pair in between. In all doubly labeled samples, a new peak at 512 nm is visible, about 38 nm blue-shifted compared to the monomer peak at 550 nm. It is more pronounced if the dyes were closer to each other and for dsDNA. The latter is attributed to the stronger rigidity of the dsDNA. This new peak is a strong hint for H-aggregation [131].
- To verify the H-aggregation hypothesis, monomer and dimer of a model system (see fig. 3.2 bottom) consisting only of the π system responsible for the absorption are optimized with TDDFT. The resulting dimer is stabilized by π stacking in parallel dipole orientation. Simulated vibrationally resolved absorption spectra are in very good agreement with the experiment. The dimer peak exhibits a blue-shift of 42 nm, representing the strong component of molecular exciton theory [124, 131]. Fitting simulated monomer and dimer spectrum to the experimental data reveal a mixing ratio of monomer to dimer of 2:1.
- In CD spectroscopy for the dsDNA samples, strong signals are visible for the dimer constructs with dyes adjacent to each other, hinting on a slightly angled parallel dipole configuration of the dyes.

- The results of the CD spectroscopy are confirmed by MD simulations of a 14-base pair DNA strand tagged with two Cy3 molecules adjacent to each other. The dyes stay close together at the negatively charged backbone and do not intercalate in the major groove as the monomer. The dyes are on average rotated 11° against each other.

Overall, the results in this article show that DNA can successfully be used as a scaffold to create artificial Cy3 H-aggregates.

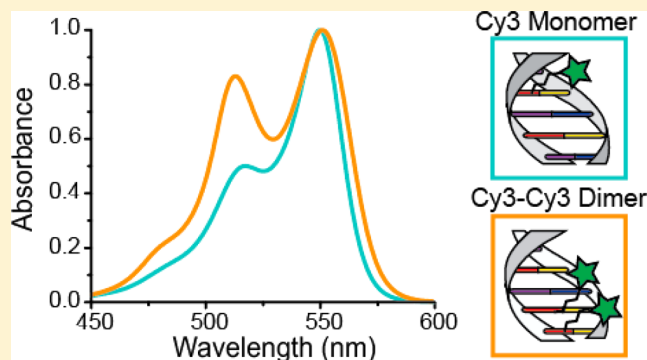
Hereafter, the article “Proximity-Induced H-Aggregation of Cyanine Dyes on DNA-Duplexes” published in *The Journal of Physical Chemistry A* is reprinted with permission from *J. Phys. Chem. A* **120**, 9941–9947 (2016). Copyright 2016 American Chemical Society. The Supporting Information for this article is available under <https://doi.org/10.1021/acs.jpca.6b10939>.

Proximity-Induced H-Aggregation of Cyanine Dyes on DNA-Duplexes

Francesca Nicoli,[†] Matthias K. Roos,[‡] Elisa A. Hemmig,[§] Marco Di Antonio,^{||} Regina de Vivie-Riedle,[‡] and Tim Liedl^{*,†,||}[†]Faculty of Physics and Center for NanoScience (CENS), Ludwig-Maximilians-Universität München (LMU), Geschwister-Scholl-Platz 1, 80539 Munich, Germany[‡]Department Chemie, Ludwig-Maximilians-Universität München (LMU), Butenandt Straße 11, 81377 Munich, Germany[§]Cavendish Laboratory, University of Cambridge, JJ Thomson Avenue, CB3 0HE Cambridge, United Kingdom^{||}Chemistry Department, University of Cambridge, Lensfield Road, CB2 1EW Cambridge, United Kingdom

Supporting Information

ABSTRACT: A wide variety of organic dyes form, under certain conditions, clusters known as J- and H-aggregates. Cyanine dyes are such a class of molecules where the spatial proximity of several dyes leads to overlapping electron orbitals and thus to the creation of a new energy landscape compared to that of the individual units. In this work, we create artificial H-aggregates of exactly two Cyanine 3 (Cy3) dyes by covalently linking them to a DNA molecule with controlled subnanometer distances. The absorption spectra of these coupled systems exhibit a blue-shifted peak, whose intensity varies depending on the distance between the dyes and the rigidity of the DNA template. Simulated vibrational resolved spectra, based on molecular orbital theory, excellently reproduce the experimentally observed features. Circular dichroism spectroscopy additionally reveals distinct signals, which indicate a chiral arrangement of the dye molecules. Molecular dynamic simulations of a Cy3–Cy3 construct including a 14-base pair DNA sequence verified chiral stacking of the dye molecules.



INTRODUCTION

The manipulation of light on the nanometer scale is of fundamental importance for designing efficient light harvesting and photonic devices.^{1–4} Fluorescent emitters such as quantum dots, fluorescence dyes, and NV centers are highly sensitive to their environment. In particular, organic fluorescent molecules are known to aggregate and stack on top of each other under certain conditions, resulting in changes of their absorption and emission properties.^{5–11} Many applications demand the precise tuning of the dye's spectroscopic properties, such as dipole orientation and coupling strength, for which control over their interactions is highly desired.^{4,12,13} Aggregation of fluorescent molecules has been vastly exploited by tuning experimental parameters such as solvent polarity, ionic concentration and temperature.^{14–16} Nonetheless, these methods are rather nonspecific and do not yield fine control over the resulting aggregate, making it difficult to fully characterize the resulting supramolecular dye structure.^{8,17} Natural light harvesting complexes, on the other hand, offer an example of full control over spectral coupling. In nature, a protein scaffold organizes the relative position and orientation of chromophores, so that their coupling strength and optical properties can be tuned into the desired frequency window.^{1,18}

In a similar way, DNA base pair recognition offers unprecedented spatial control over the assembly of nano-

meter-scale objects, including optically active components, such as dyes,¹⁹ quantum dots,²⁰ and metallic nanoparticles.^{21,22} Simple double-stranded DNA constructs have already been employed in a variety of photonics applications, which require a precise spatial organization of dyes, such as the creation of artificial aggregates of dyes. For example, the aggregation of cyanine dyes can occur via their intercalation in the minor groove of a DNA double strand.²³ With the goal of improving the control over the positioning of dyes, DNA bases were substituted with the molecule of interest, for example methyl red,²⁴ biphenyl, and bipyridyl.²⁵ In a different conjugation scheme, porphyrin aggregates have been created on a DNA strand through covalent linkage of porphyrin rings to thymine bases in a defined sequence.^{26,27} Owing to the wide variety of commercially available dyes that are covalently linked to DNA bases, covalent coupling today is the method of choice for imaging and energy transfer studies.

In this work, we exploit this excellent addressability of DNA strands and in particular thymine bases to induce cyanine dye dimerization in a controlled manner and create new molecular excitonic states. With the ultimate goal of mimicking multidye

Received: October 31, 2016

Revised: November 17, 2016

Published: December 9, 2016

coupling similar to that found in light harvesting complexes, we are here interested in studying interactions between pairs of Cyanine 3 (Cy3) dyes brought into close proximity in synthetic DNA single- and double-strands. Our DNA – dye hybrid structures are characterized by absorption spectroscopy and circular dichroism (CD). Because of the *a priori* design of the system, the interaction between the dyes can further be modeled by time-dependent density functional theory (TD-DFT) calculations, allowing the comparison of spectral properties with simulated absorption spectra. Finally, the dynamics of the dye–DNA complex is investigated through molecular dynamics (MD) simulations.

MATERIALS AND METHODS

The constructs used in this work consist of a synthetic DNA strand where one or two Cy3 molecules are linked to thymine bases through NHS coupling and the corresponding, unmodified, complementary sequence. The DNA strands were purchased from IBA GmbH (Göttingen, Germany). The following sequences were used:

Monomer 5'-ATC GTA TC T_{cy3} GTG TCT ATG CTA-3'

Dimer 1 base distance 5'-ATCGTATC T_{cy3} G T_{cy3} GTCTATGCTA-3'

Dimer 0 base distance 5'-ATCGTATCTG T_{cy3} T_{cy3} TGTCTATGCTA-3'

T_{cy3} indicates the modified thymine bases.

To hybridize the modified strand with their complement a mixture of both strands with a 1 to 1 ratio was mixed with buffer containing 1xTE (10 mM Tris, 1 mM EDTA) and 150 mM NaCl at pH 8.0. The solution was heated to 65 °C for 5 min and slowly cooled to room temperature over 2 h.

The absorption measurements were performed using a 10 mm optical path length quartz cuvette (Hellma-analytics) and a V-650 Spectrometer (Jasco) with 0.5 nm resolution and 1 s/point integration time. The CD signal was acquired with Chirascan-Plus Circular Dichroism Spectrometer (Applied Photophysics Ltd.) 1 nm resolution and 1 s/point integration time and the samples (DNA constructs concentration 10 μ M in 1xTE and 150 mM NaCl buffer) placed in a 3 mm optical path length quartz cuvette (Hellma-analytics). Absorption and CD measurements were all performed at room temperature.

We also test a construct with a different Cy3–DNA linker. In this case one Cy3 molecule is located on each of two complementary DNA strands, the dye effectively acts as a substitute for the sugar-base complex at a specific location on the oligonucleotide. This substitution is accomplished by conjugating the 3' and 5' ends of two shorter strands to the two free hydroxy groups of the dye (Supporting Information, Scheme S1). Such modified oligos and the relative complements were purchased from IDT (Integrated DNA Technologies Inc.). The following sequences were used:

Dimer $N = 0$

5'-ATT CAG ATT TTT TTT TTT TTT TTT TTT T/ $iCy3$ /TT TTT AGT TGA A-3'

5'-TTC AAC TAA AAA/ $iCy3$ /AAA AAA AAA AAA AAA AAA AAA TCT GAA T-3'

Dimer $N = 6$

5'-ATT CAG ATT TTT TTT TT TTT TT/ $iCy3$ /TTTTTTTT TTT AGT TGA A-3'

5'-TTC AAC TAA AAA/ $iCy3$ /AAA AAA AAA AAA AAA AAA AAA TCT GAA T-3'

Monomer:

5'-ATT CAG ATT TTT TTT TT TTT TTTTTTTTTTTT
TTTT AGT TGA A-3'

5'-TTC AAC TAA AAA/ $iCy3$ /AAA AAA AAA AAA AAA
AAA AAA TCT GAA T-3'

The doubly labeled Cy3 strands were hybridized by mixing equimolar amounts of the two complementary strands at a concentration of 2 μ M in 1xTE, followed by heating to 70 °C and linear cooling to 25 °C over 45 min in a thermocycler (Bio-Rad Laboratories, Inc.).

Absorbance measurements were performed using a Cary 300 Bio UV–visible Spectrophotometer (Agilent Technologies) with 1 nm resolution and 0.1 s/point integration time. The DNA duplex samples were diluted to a final concentration of 0.7 μ M in 1xTE in a low volume cuvette (100 μ L) (10 mm path length) (Sigma-Aldrich). CD spectra were recorded on an Applied Photophysics Chirascan circular dichroism spectropolarimeter using a 1 mm path length quartz cuvette. CD measurements were performed at room temperature over a range of 450–600 nm using a response time of 0.5 s, 1 nm pitch and 0.5 nm bandwidth. The recorded spectra represent a smoothed average of three scans, zero-corrected at 600 nm and normalized (Molar ellipticity θ is quoted in 10⁵ deg cm² dmol⁻¹). The absorbance of the buffer was subtracted from the recorded spectra. The sample was diluted to a final concentration of 5 μ M in 1xTE.

COMPUTATIONAL METHODS

We generate simulated vibrational resolved absorption spectra using TD-DFT and a polarizable continuum model (PCM). All first principle calculations were carried out with the program package Gaussian09.²⁸ The functional B3LYP and the basis set 6-31G(d) were used throughout. To account for solvent effects the polarizable continuum model²⁹ was used. For the optimization of the dimer the dispersion correction D3 from Grimme³⁰ was added. The simulation of the vibrationally resolved spectra was done using the implementation of Santoro et al.³¹ in Gaussian09.²⁸ The Franck–Condon method and a spectral broadening of 300 cm⁻¹ was used.

The molecular dynamics (MD) simulations were carried out with the program Gromacs 5.1.^{32,33} The following DNA sequence was used: 5'-TAT CTG T_{cy3} T_{cy3} T GTC TA-3'. A starting structure for the double-stranded DNA was generated with model.it.³⁴ The amber99bsc0^{35,36} force field was used for the DNA and GAFF³⁷ for the Cy3 molecule. The parameter for Cy3 were taken from Graen et al.,³⁸ the ones for the modified thymine and the linker were generated using ANTECHAMBER relying on HF/6-31G(d) optimizations. The simulations were performed in TIP3P water,³⁹ sodium ions were added to neutralize the system. A rectangular box with side lengths of 55 \times 55 \times 43 Å was used. After energy minimization, the system was first equilibrated for 200 ps while restraining the DNA and then again for 1 ns without any constraints, before running production simulations.

RESULTS AND DISCUSSION

Dyes located at distances below \sim 10 nm can exchange energy via nonradiative, incoherent dipole–dipole interaction known as Förster resonance energy transfer (FRET).⁴⁰ When the molecules are brought into even closer proximity, to distances comparable to their physical size, they can instead have coherent energy exchange.⁴¹ This type of interaction gives rise to new energy states compared to those observed in individual

dyes. Consequently, this coupling creates a new energy landscape and therefore leads to new optical properties, which can be quantified via absorption spectroscopy.^{5,7,23,42,43}

Our system of study is a short DNA duplex consisting of a single-stranded DNA (ssDNA) oligonucleotide carrying either one or two Cy3 molecules, which are covalently attached to selected thymine bases through NHS coupling (Scheme S1.a) and an unmodified complementary DNA sequence. We arranged the dyes in two different configurations: Dimer 1 (Cy3–G–Cy3) contains two Cy3 dyes coupled to a thymine with one unmodified guanine in between while Dimer 0 (Cy3–Cy3) has no separating base (Figure 1, parts B and C). A single labeled strand serves as a control sample (Figure 1A).

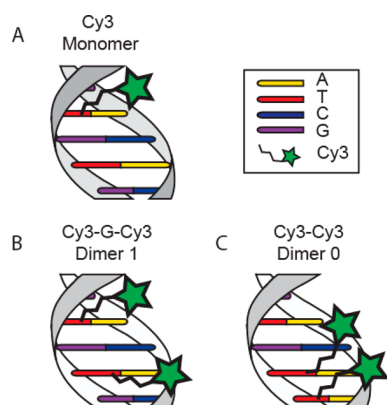


Figure 1. Schematic representation of experimental dye-DNA constructs with relative nomenclature and dye positions. (A) Cy3 monomer, only one thymine base is modified with the dye. (B) Cy3 “dimer 1” with one base (guanine) separation between dyes. (C) Cy3 “dimer 0” consisting of two Cy3 molecules linked to adjacent bases.

To investigate the interactions between the dyes in their different configurations we performed absorption spectroscopy measurements on both the ssDNA and the dsDNA constructs. The results are summarized in Figure 2. For the ssDNA constructs (Figure 2A), the Cy3 monomer displays the expected absorption maximum at 550 nm with two small shoulders at 520 nm and at 480 nm (Supporting Information, Figure S1). Constructs containing two Cy3 molecules display a

new, blue-shifted peak around 512 nm (hypsochromic peak), which increases in intensity as the dyes get closer to each other. Additionally, the shoulder in the region around 480 nm becomes more pronounced in the 2-dye constructs. Similar trends are observed in the dsDNA constructs (Figure 2B) but with an even more pronounced intensity increment of the blue-shifted hypsochromic peak. The spectral change is so pronounced that it is visible with bare eyes (see Supporting Information, Figure S2). As the only structural difference compared to the ssDNA constructs is the presence of the hybridized, unmodified complement, we conclude that the higher rigidity of the duplex (persistence length $P_{dsDNA} \sim 50$ nm) compared to ssDNA ($P_{ssDNA} \sim 1$ nm) leads to a decreased orientation fluctuation of the two dyes and therefore to a modified spectrum.⁴⁴ Further, the average distance between two bases in a single-stranded configuration is on the order of 6 Å while it is 3.4 Å in dsDNA⁴⁵ also resulting in closer proximity of the dyes in the duplex configuration. The fact that the relative distance between dyes plays a crucial role in the strength of their interaction becomes obvious when comparing the increased intensity of the hypsochromic peak of the construct with 0 bases in between the dyes with that containing a spacer guanine. We attribute the formation of the hypsochromic peak to Cy3–Cy3 interaction and not to interaction of the dyes with adjacent DNA bases as the single-labeled control sample does not display any additional spectral peaks.

Cyanine dye molecules are known to interact with each other via π -orbital stacking thereby forming H-aggregates in aqueous solutions.^{11,16,17} The appearance of the blue-shifted peak in our experiments is consistent with this picture of H-aggregation of two polarized molecules with parallel dipoles.^{4,10,42,43} To demonstrate that the dimer formation is a result of the controlled positioning of the dyes mediated by the DNA scaffold and not caused by spontaneous aggregation, we performed a series of control experiments: First, the observed spectra were not significantly affected by varying the concentration of the constructs (Supporting Information, Figure S3). Second, in order to exclude the possibility of H-aggregation being mediated by DNA groove intercalation,²³ we mixed free dye with unmodified dsDNA at varying ratios and again observed no changes of the spectra compared to those

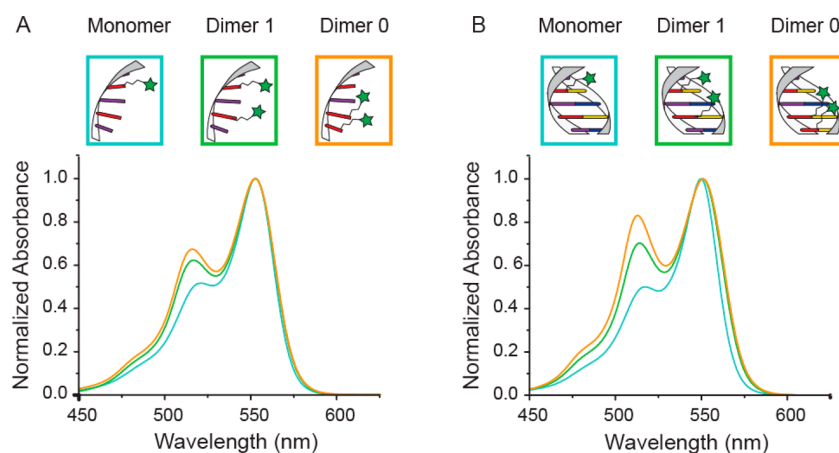


Figure 2. Absorption spectra of the dye-DNA constructs. (A) Normalized absorption of the ssDNA and (B) dsDNA constructs. The light blue curves correspond to the Cy3 monomer, while the green and orange curves correspond to the Cy3 dimer with 1 base and 0 base distance, respectively.

originating from monodye-labeled samples (Supporting Information, Figure S4).

We also tested a different construct where one single Cy3 dye was located on each of two complementary DNA strands and we again observed the same spectral changes that are typical for H-aggregate dimerization (Supporting Information, Figure S5).

Simulated vibrational resolved absorption spectra were generated using TD-DFT, and a PCM was applied. To reduce the computational cost, we neglected the surrounding DNA and chose a model system (Supporting Information, Figure S6) consisting only of the π -system, which is responsible for the absorption properties of the dye. Figure 3 shows the simulated

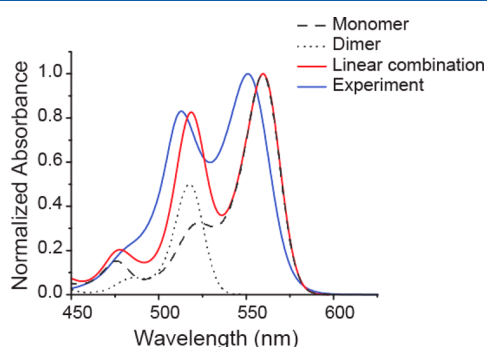


Figure 3. Comparison of weighted linear combination of TD-DFT simulated spectra (solid red line) and experimentally obtained spectra from the construct “dimer 0” on dsDNA (solid blue line). Simulated spectra of monomer and dimer are shown in black (dashed and dotted lines corresponding to monomer and dimer, respectively). The intensities of the experimental spectra were fitted best when assuming one-third dimer and two-third monomer contributions.

absorption spectrum for the strongly dipole-allowed S_1 state of the monomer and its excellent agreement with our experiments. The 0–0 band is located at 560 nm with a smaller peak at 523 nm, characteristic for cyanine dyes.^{46,47} This excitation corresponds to a transition from the highest occupied molecular orbital (HOMO) to the lowest unoccupied molecular orbital (LUMO), as shown in Table 1.

Stacking two of these monomers in a parallel dipole configuration leads to the dimer structure shown in the Supporting Information, Figure S6. Both molecules are completely flat and the distance between their molecular

planes is 3.4 Å, as by design in the “Dimer 0” construct. In this configuration, the HOMO and LUMO of the monomers combine resulting in four different orbitals and hence, four different excited states. Each new state consists of two transitions between these four orbitals which are built by positive or negative linear combination of the monomer’s HOMO and LUMO. The contributions of the S_1 and S_3 states result in a zero net contribution. The S_2 and the S_4 states consist of the same transitions, but with inverse weight. The S_2 state has a vertical excitation energy of 2.22 eV and is thus red-shifted compared to the monomer. Its oscillator strength is 2 orders of magnitude smaller (0.0424) than the one of the S_4 state and is, as a consequence, the weak component in molecular exciton theory.^{48,49} In contrast, the S_4 state is blue-shifted (2.80 eV) and has a significant oscillator strength (2.8945) that is almost twice the monomer value. It is the strong component in molecular exciton theory and the only relevant transition here. The resulting absorption spectrum is shown in Figure 3. It consists of the 0–0 transition at 518 nm with almost none vibrational progression. Comparing this outcome to the monomer, we observe a blue shift of the absorption signal by 42 nm resulting from dimerization. The hypsochromic peak observed in the experimental spectrum is 38 nm shifted from the monomer absorption, which is very close to the difference displayed by the simulated spectra. The absolute simulated values of the vertical excitation of the monomer and dimer are shifted bathochromatically in respect to the experimental peaks by 0.04 and 0.03 eV, respectively, which constitutes very good agreement for a first principle method such as TD-DFT.⁵⁰ This overall agreement between experimental data and theory strengthens our hypothesis of controlled H-aggregation.

The simulations show either the original peak for the monomers at 560 nm or the blue-shifted peak for the dimers at 518 nm. In our dimer samples, we observe not only the blue-shifted peak but also the original peak indicating that not all dyes form the H-aggregate state or that this state is not formed permanently, as also indicated by the MD simulations discussed below (see MD video included as Supporting Information). To account for the mixed spectrum of the monomer and dimer species, we created a linear combination of the two simulated spectra. The superimposed modeled spectrum fitted the experimental spectrum best with one-third contribution from the dimer population and two-thirds originating from the

Table 1. Vertical Excitation Energies E_{vert} , Oscillator Strengths f , and the Involved Transitions for the Lowest-Lying Excited States of Monomer and Stacked Dimer Obtained with TD-DFT/B3LYP/6-31G(d) in Water (PCM)^a

	state	transition	weight (%)	E_{vert} (eV)	f
monomer	S_1	HOMO \rightarrow LUMO	100	2.61	1.6014
dimer	S_1	HOMO-1 \rightarrow LUMO	11	2.18	$<5 \times 10^{-5}$
		HOMO \rightarrow LUMO+1	89		
	S_2	HOMO-1 \rightarrow LUMO+1	40	2.22	0.0424
		HOMO \rightarrow LUMO	60		
	S_3	HOMO-1 \rightarrow LUMO	89	2.43	$<5 \times 10^{-5}$
		HOMO \rightarrow LUMO+1	11		
	S_4	HOMO-1 \rightarrow LUMO+1	60	2.80	2.8945
		HOMO \rightarrow LUMO	40		

^aThe calculations are performed for a model system with inserted sulfur atoms instead of $C(\text{CH}_3)_2$ shown in the Supporting Information, Figure S6. For the monomer there is only one excitation of importance with an energy of 2.61 eV. In the case of the dimer, only the S_4 state contributes significantly to the absorption and is clearly blue-shifted compared to the monomer with an energy of 2.8 eV. The corresponding orbitals can be seen in the Supporting Information, Figure S7.

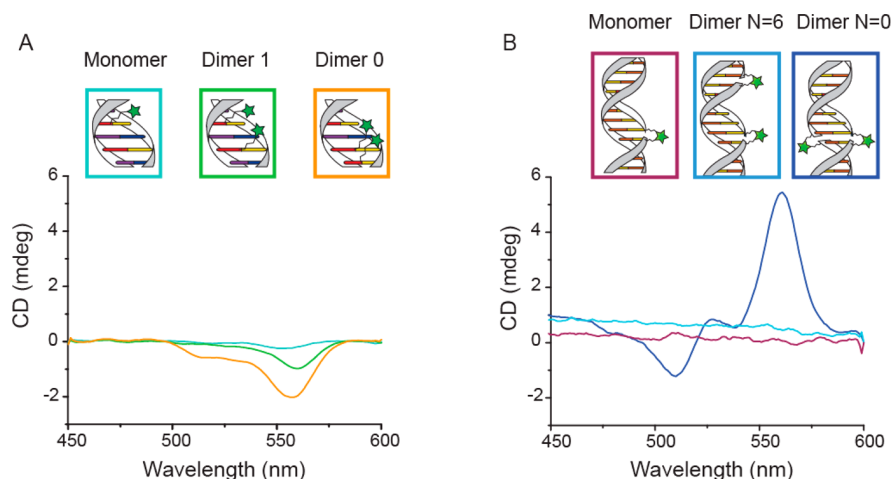


Figure 4. CD measurements of all dsDNA constructs. (A) Spectra of thymine-labeled Cy3–dsDNA constructs, showing an increasing CD signal as the distance between dyes decreases. (B) Spectra of doubly labeled Cy3–dsDNA constructs, showing a CD signal for the dimer with 0 bases in between dyes and no signal for both the monomer and the dimer with six bases in between dyes.

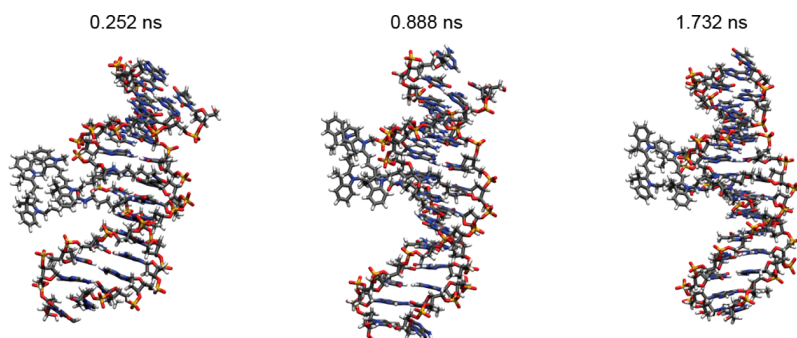


Figure 5. Snapshots of MD simulations at the specified time frames. The Cy3 molecules are visible on the left and they are located, throughout the whole simulation, close to the DNA backbone. No intercalation is observed during the observation time of 2 ns. The molecules show a nonperfect parallel alignment and a fluctuating reciprocal position, which is consistent with the experimental observations of CD and the coexistence of monomer and dimer peaks.

monomers. Also the appearance of the more pronounced shoulder at 480 nm could in this way be attributed to the convolution of the two minor peaks of the monomer and dimer spectra around these wavelengths.

In the simulations, the dyes are stacked one above the other in a parallel dipole configuration, where the energy level of the excited state corresponds to the main absorption peak of the dimer spectrum. To test for chiral arrangements of the dyes we also conducted circular dichroism (CD) measurements. All constructs containing two cyanines in close proximity exhibited a measurable CD signal (see Figure 4). In contrast, all samples with only a single dye did not exhibit chiral signatures, indicating that CD transfer, i.e., coupling between the chiral dsDNA and the achiral individual dyes, is not the origin of the recorded CD.⁵¹ In accordance with this observation, the Cy3 dimer with dyes in closest proximity displays the strongest CD signal. The same behavior has been reported for DNA–porphyrin constructs.²⁷ Our MD simulations further confirm that the measured signal is not a result of Cy3–DNA intercalation but a result of chiral stacking of the dyes. Interestingly, the constructs with the doubly anchored Cy3 exhibit even stronger CD signals and a different spectral shape compared to that of the thymine-modified constructs. Previous studies have shown that doubly linked Cy3 can intercalate between DNA bases,⁵² suggesting that dyes can stack on top of

each other but also between adjacent base pairs resulting in strong, bisignate CD signals.^{51,53} Generally, CD spectroscopy cannot be used to gather full structural information and additional modeling would be required to quantitatively understand the recorded spectra.⁵⁴ Nevertheless, we can infer that all the constructs showing the hypsochromic shift also exhibit chiral arrangements of dyes and that different strategies of linking the same dyes to DNA duplexes lead to structural and spectral variations.

Molecular dynamics simulations of the Cy3–Cy3 construct including a 14-base pair DNA sequence were used to investigate the dynamics of the system. We considered the experimental Cy3 molecule with the original $C(CH_3)_2$ groups here. Snapshots at different points in time shown in Figure 5 and Supporting Information movieS1 reveal that the dyes stay in close proximity throughout the simulation (2 ns). While the Cy3 monomer preferably lies in the major groove of the DNA (see *Cy3_monomer.pdb* file in the Supporting Information), the dyes in the dimer configuration stay near the negatively charged backbone, as it can be expected for a positively charged molecule. For some time during the propagation, the attraction between the molecules is visible as one or both leave their planar form, which is normally the natural configuration for molecules with such a π -system. The edges are bent toward each other to maximize the interaction. Furthermore, as the

bulky C(CH₃)₂ groups prevent the molecule from aligning perfectly, the dye molecules rotate slightly against each other, forming an average angle of 11.1°, confirming the results of the CD spectroscopy.

CONCLUSION

In conclusion, we demonstrated that with our relatively simple system of cyanine dyes covalently attached to DNA backbones, we can artificially create molecular excitonic states by deterministically changing the reciprocal distance of the dyes and the rigidity of the scaffolding constructs. Our preprogrammable DNA-based approach demonstrates excellent control over dye assembly and designed dimer interaction strengths thus allowing optical tuning and theoretical modeling of dye aggregates. Furthermore, the use of DNA as the underlying scaffolding material opens the possibility for complex integrated nanostructures, thereby widening the toolbox of nano-optical components available for photonics and nano-optics.

ASSOCIATED CONTENT

Supporting Information

The Supporting Information is available free of charge on the ACS Publications website at DOI: 10.1021/acs.jpca.6b10939.

DNA–dye coupling scheme; free monomeric Cy3 absorption spectrum; samples images; absorption spectra of control experiments, i.e., different construct concentration and ds-DNA/dye mixture; absorption spectrum of constructs with alternative DNA–Cy3 functionalization scheme; optimized molecular structures for theoretical modeling; and calculated molecular orbitals (PDF)

Pdb file of MD simulations corresponding to the Cy3–DNA monomer construct (PDB)

Video of MD simulations corresponding to the Cy3–DNA dimer construct (AVI)

AUTHOR INFORMATION

Corresponding Author

*(T.L.) E-mail: tim.liedl@physik.lmu.de. Telephone: +49-(0) 89-2180-3725.

ORCID

Tim Liedl: 0000-0002-0040-0173

Notes

The authors declare no competing financial interest.

ACKNOWLEDGMENTS

This work was supported by the European Commission through ERC Grant Agreement No. 336440, by ORCA, and by the Deutsche Forschungsgemeinschaft through the SFB749. M.D.A. is thankful to CRUK for program funding and E.A.H. acknowledges support from the Schweizerischer Nationalfonds (SNF). We thank Prof. Ulrich Keyser, Dr. Alex Chin, Dr. Celestino Creatore, and Dr. Mauricio Pilo Pais for useful discussions. F.N. acknowledges Timon Funk for the help with CD measurements and Luisa Kneer for initial support of the project.

REFERENCES

(1) Scholes, G. D.; Fleming, G. R.; Olaya-Castro, A.; van Grondelle, R. Lessons from Nature about Solar Light Harvesting. *Nat. Chem.* **2011**, *3* (10), 763–774.

(2) Wasielewski, M. R. Self-Assembly Strategies for Integrating Light Photosynthetic Systems. *Acc. Chem. Res.* **2009**, *42* (12), 1910–1921.

(3) Tame, M. S.; McEnery, K. R.; Özdemir, Ş. K.; Lee, J.; Maier, S. A.; Kim, M. S. Quantum Plasmonics. *Nat. Phys.* **2013**, *9* (6), 329–340.

(4) Saikin, S. K.; Eisfeld, A.; Valleau, S.; Aspuru-Guzik, A. Photonics Meets Excitonics: Natural and Artificial Molecular Aggregates. *Nanophotonics* **2013**, *2* (1), 21–38.

(5) Czikkely, V.; Försterling, H. D.; Kuhn, H. Light Absorption and Structure of Aggregates of Dye Molecules. *Chem. Phys. Lett.* **1970**, *6* (1), 11–14.

(6) Reers, M.; Smith, T. W.; Chen, L. B. J-Aggregate Formation of a Carbocyanine as a Quantitative Fluorescent Indicator of Membrane Potential. *Biochemistry* **1991**, *30* (18), 4480–4486.

(7) Tiddy, G. J. T.; Mateer, D. L.; Ormerod, A. P.; Harrison, W. J.; Edwards, D. J. Highly Ordered Aggregates in Dilute Dye-Water Systems. *Langmuir* **1995**, *11* (2), 390–393.

(8) Harrison, W. J.; Mateer, D. L.; Tiddy, G. J. T. Liquid-Crystalline J-Aggregates Formed by Aqueous Ionic Cyanine Dyes. *J. Phys. Chem.* **1996**, *100* (6), 2310–2321.

(9) Würthner, F.; Kaiser, T. E.; Saha-möller, C. R. J-Aggregates: From Serendipitous Discovery to Supra-Molecular Engineering of Functional Dye Materials. *Angew. Chem., Int. Ed.* **2011**, *50*, 3376–3410.

(10) Eisfeld, A.; Briggs, J. S. The J- and H-Bands of Organic Dye Aggregates. *Chem. Phys.* **2006**, *324*, 376–384.

(11) Kopainsky, B.; Hallermeier, J. K.; Kaiser, W. The First Step of Aggregation of Pic: The Dimerization. *Chem. Phys. Lett.* **1981**, *83* (3), 498–502.

(12) Roller, E.-M.; Argyropoulos, C.; Högele, A.; Liedl, T.; Pilo-Pais, M. Plasmon–Exciton Coupling Using DNA Templates. *Nano Lett.* **2016**, *16* (9), 5962–5966.

(13) Zengin, G.; Johansson, G.; Johansson, P.; Antosiewicz, T. J.; Käll, M.; Shegai, T. Approaching the Strong Coupling Limit in Single Plasmonic Nanorods Interacting with J-Aggregates. *Sci. Rep.* **2013**, *3*, 3074.

(14) Slavnova, T. D.; Chibisov, A. K.; Görner, H. Kinetics of Salt-Induced J-Aggregation of Cyanine Dyes. *J. Phys. Chem. A* **2005**, *109*, 4758–4765.

(15) Armitage, B.; Retterer, J.; O'Brien, D. F. Dimerization of Cyanine Dyes in Water Driven by Association with Hydrophobic Borate Anions. *J. Am. Chem. Soc.* **1993**, *115* (20), 10786–10790.

(16) Renge, I.; Wild, U. P. Solvent, Temperature, and Excitonic Effects in the Optical Spectra of Pseudoisocyanine Monomer and J-Aggregates. *J. Phys. Chem. A* **1997**, *101* (43), 7977–7988.

(17) von Berlepsch, H.; Böttcher, C.; Ouart, A.; Burger, C.; Dähne, S.; Kirstein, S. Supramolecular Structures of J-Aggregates of Carbocyanine Dyes in Solution. *J. Phys. Chem. B* **2000**, *104* (22), 5255–5262.

(18) Cheng, Y.-C.; Fleming, G. R. Dynamics of Light Harvesting in Photosynthesis. *Annu. Rev. Phys. Chem.* **2009**, *60*, 241–262.

(19) Stein, I. H.; Schüller, V.; Böhm, P.; Tinnefeld, P.; Liedl, T. Single-Molecule FRET Ruler Based on Rigid DNA Origami Blocks. *ChemPhysChem* **2011**, *12* (3), 689–695.

(20) Mitchell, G. P.; Mirkin, C. A.; Letsinger, R. L. Programmed Assembly of DNA Functionalized Quantum Dots. *J. Am. Chem. Soc.* **1999**, *121* (10), 8122–8123.

(21) Mirkin, C. A.; Letsinger, R. L.; Mucic, R. C.; Storhoff, J. J. A DNA-Based Method for Rationally Assembling Nanoparticles into Macroscopic Materials. *Nature* **1996**, *382*, 607–609.

(22) Alivisatos, A. P.; Johnsson, K. P.; Peng, X.; Wilson, T. E.; Loweth, C. J.; Bruchez, M. P.; Schultz, P. G. Organization of “Nanocrystal Molecules” Using DNA. *Nature* **1996**, *382*, 609–611.

(23) Hannah, K. C.; Armitage, B. A. DNA-Templated Assembly of Helical Cyanine Dye Aggregates: A Supramolecular Chain Polymerization. *Acc. Chem. Res.* **2004**, *37*, 845–853.

(24) Asanuma, H.; Shirasuka, K.; Takarada, T.; Kashida, H.; Komiyama, M. DNA - Dye Conjugates for Controllable H* Aggregation. *J. Am. Chem. Soc.* **2003**, *125*, 2217.

- (25) Brotschi, C.; Leumann, C. J. DNA with Hydrophobic Base Substitutes: A Stable, Zipperlike Recognition Motif Based On Interstrand-Stacking Interactions. *Angew. Chem., Int. Ed.* **2003**, *42* (14), 1655–1658.
- (26) Bouamaied, I.; Nguyen, T.; Rühl, T.; Stulz, E. Supramolecular Helical Porphyrin Arrays Using DNA as a Scaffold. *Org. Biomol. Chem.* **2008**, *6*, 3888–3891.
- (27) Fendt, L.; Bouamaied, I.; Thoni, S.; Amiot, N.; Stulz, E. DNA as Supramolecular Scaffold for Porphyrin Arrays on the Nanometer Scale. *J. Am. Chem. Soc.* **2007**, *129* (49), 15319.
- (28) Frisch, M. J.; Trucks, G. W.; Schlegel, H. B.; Scuseria, G. E.; Robb, M. A.; Cheeseman, J. R.; Scalmani, G.; Barone, V.; Mennucci, B.; Petersson, G. A.; et al.; *Gaussian 09*, Revision D.1; Gaussian Inc.: Wallingford, CT, 2009.
- (29) Miertuš, S.; Scrocco, E.; Tomasi, J. Electrostatic Interaction of a Solute with a Continuum. A Direct Utilization of {AB} Initio Molecular Potentials for the Prediction of Solvent Effects. *Chem. Phys.* **1981**, *55*, 117–129.
- (30) Grimme, S.; Antony, J.; Ehrlich, S.; Krieg, H. A Consistent and Accurate Ab Initio Parametrization of Density Functional Dispersion Correction (DFT-D) for the 94 Elements H-Pu. *J. Chem. Phys.* **2010**, *132* (15), 154104.
- (31) Santoro, F.; Improta, R.; Lami, A.; Bloino, J.; Barone, V. Effective Method to Compute Franck-Condon Integrals for Optical Spectra of Large Molecules in Solution. *J. Chem. Phys.* **2007**, *126*, 084509.
- (32) Pronk, S.; Pall, S.; Schulz, R.; Larsson, P.; Bjelkmar, P.; Apostolov, R.; Shirts, M. R.; Smith, J. C.; Kasson, P. M.; van der Spoel, D.; et al. E. GROMACS 4.5: A High-Throughput and Highly Parallel Open Source Molecular Simulation Toolkit. *Bioinformatics* **2013**, *29*, 845–854.
- (33) Abraham, M. J.; Murtola, T.; Schulz, R.; Páll, S.; Smith, J. C.; Hess, B.; Lindahl, E. GROMACS: High Performance Molecular Simulations through Multi-Level Parallelism from Laptops to Supercomputers. *SoftwareX* **2015**, *1–2*, 19–25.
- (34) Vlahovicek, K.; Pongor, S. Model.it: Building Three Dimensional DNA Models from Sequence Data. *Bioinformatics* **2000**, *16* (11), 1044–1045.
- (35) Wang, J.; Cieplak, P.; Kollman, P. A. How Well Does a Restrained Electrostatic Potential (RESP) Model Perform in Calculating Conformational Energies of Organic and Biological Molecules? *J. Comput. Chem.* **2000**, *21* (12), 1049–1074.
- (36) Pérez, A.; Marchán, L.; Svozil, D.; Sponer, J.; Cheatham, T. E.; Laughton, C. A.; Orozco, M. Refinement of the AMBER Force Field for Nucleic Acids: Improving the Description of A/ γ Conformers. *Biophys. J.* **2007**, *92*, 3817–3829.
- (37) Wang, J.; Wolf, R. M.; Caldwell, J. W.; Kollman, P. A.; Case, D. A. Development and Testing of a General Amber Force Field. *J. Comput. Chem.* **2004**, *25*, 1157–1174.
- (38) Graen, T.; Hoefling, M.; Grubmüller, H. AMBER-DYES: Characterization of Charge Fluctuations and Force Field Parameterization of Fluorescent Dyes for Molecular Dynamics Simulations. *J. Chem. Theory Comput.* **2014**, *10* (12), 5505–5512.
- (39) Jorgensen, W. L.; Chandrasekhar, J.; Madura, J. D.; Impey, R. W.; Klein, M. L. Comparison of Simple Potential Functions for Simulating Liquid Water. *J. Chem. Phys.* **1983**, *79* (2), 926–935.
- (40) Scholes, G. D. Long-Range Resonance Energy Transfer in Molecular Systems. *Annu. Rev. Phys. Chem.* **2003**, *54* (18), 57–87.
- (41) Beljonne, D.; Curutchet, C.; Scholes, G. D.; Silbey, R. J. Beyond Förster Resonance Energy Transfer in Biological and Nanoscale Systems. *J. Phys. Chem. B* **2009**, *113* (19), 6583–6599.
- (42) Czikklely, V.; Forsterling, H. D.; Kuhn, H. Extended Dipole Model for Aggregates of Dye Molecules. *Chem. Phys. Lett.* **1970**, *6* (3), 207–210.
- (43) Fulton, R. L.; Gouterman, M. Vibronic Coupling. II. Spectra of Dimers. *J. Chem. Phys.* **1964**, *41* (8), 2280–2286.
- (44) Tinland, B.; Pluen, A.; Sturm, J.; Weill, G. Persistence Length of Single-Stranded DNA. *Macromolecules* **1997**, *30* (19), 5763–5765.
- (45) Murphy, M. C.; Rasnik, I.; Cheng, W.; Lohman, T. M.; Ha, T. Probing Single-Stranded DNA Conformational Flexibility Using Fluorescence Spectroscopy. *Biophys. J.* **2004**, *86* (4), 2530–2537.
- (46) Lin, K. T. H.; Silzel, J. W. Relation of Molecular Structure to Franck-Condon Bands in the Visible-Light Absorption Spectra of Symmetric Cationic Cyanine Dyes. *Spectrochim. Acta, Part A* **2015**, *142*, 210–219.
- (47) Bertolino, C. A.; Ferrari, A. M.; Barolo, C.; Viscardi, G.; Caputo, G.; Coluccia, S. Solvent Effect on Indocyanine Dyes: A Computational Approach. *Chem. Phys.* **2006**, *330*, 52–59.
- (48) Kasha, M.; Rawls, H. R.; Ashraf El-Bayoumi, M. The Exciton Model in Molecular Spectroscopy. *Pure Appl. Chem.* **1965**, *11*, 371–392.
- (49) Guthmuller, J.; Zutterman, F.; Champagne, B. Prediction of Vibronic Coupling and Absorption Spectra of Dimers from Time-Dependent Density Functional Theory: The Case of a Stacked Streptocyanine. *J. Chem. Theory Comput.* **2008**, *4* (12), 2094–2100.
- (50) Laurent, A. D.; Jacquemin, D. TD-DFT Benchmarks: A Review. *Int. J. Quantum Chem.* **2013**, *113* (17), 2019–2039.
- (51) Yamaoka, K.; Resnik, R. A. The Extrinsic Cotton Effect of Acridine Orange Bound to Native DNA and Helical Poly-L-Glutamic Acid. *J. Phys. Chem.* **1966**, *70* (14), 4051–4066.
- (52) Stennett, E. M. S.; Ma, N.; Van Der Vaart, A.; Levitus, M. Photophysical and Dynamical Properties of Doubly Linked Cy3-DNA Constructs. *J. Phys. Chem. B* **2014**, *118* (1), 152–163.
- (53) Seibt, J.; Engel, V. On the Calculation of Circular Dichroism Spectra Using Quantum Wave-Packet Dynamics with an Application to Molecular Dimers. *J. Chem. Phys.* **2007**, *126* (7), 074110.
- (54) Seibt, J.; Lohr, A.; Wurthner, F.; Engel, V. Circular Dichroism and Absorption Spectroscopy of Merocyanine Dimer Aggregates: Molecular Properties and Exciton Transfer Dynamics from Time-Dependent Quantum Calculations. *Phys. Chem. Chem. Phys.* **2007**, *9* (47), 6214–6218.

Chapter 4.

Chemical stability of two standard electrolytes used in lithium-ion batteries towards singlet oxygen

Storage of electricity is still one of the most prominent challenges in this second decade of the 21st century. Three major developments are responsible for the increasing demand for storage solutions: The more and more widespread use of mobile devices; the dawning age of electric based mobility and transportation; and the transition to renewable energy sources. In the first case, smaller yet more efficient batteries are asked for to power the high-performance chips in today's handheld devices. In the second case, especially the energy density of batteries is crucial to reach the driving range of internal combustion engine cars with future battery electric vehicles. At the same time, charging time needs to be reduced. In the third case, batteries are an important building block of modern power grids to counteract supply and demand surges as for example solar energy is not available at night. In all cases, lithium-ion batteries are a prominent solution [132–135].

Lithium has emerged to be the dominating element for batteries as it is the most electropositive and lightest metal. In these batteries, as the name suggests, lithium-ions function as charge carriers. The ions move between the electrodes in the electrolyte and get intercalated in the cathode active material (CAM) while under load and in the anode material while charging. Whereas the anode consists of graphite, many possible CAMs are already in use or still under research [135, 136]. One important class of CAMs are layered lithium nickel cobalt manganese oxides ($\text{LiNi}_x\text{Co}_y\text{Mn}_z\text{O}_2$, NCMs) that are already heavily commercialized. This class is favorable due to its high specific capacity and only minimal volume changes during charging and discharging [137], which leads to superior cycle stability compared to other CAMs [135].

To further increase the battery capacity and at the same time reduce the amount of expensive and toxic cobalt, nickel-rich NCMs are a promising candidate. However, the high amount of nickel diminishes the cycle stability counteracting a possible better initial capacity. Recently, it was shown by the Gasteiger group [137] that for certain nickel-rich NCMs this capacity fading occurs above a specific state of charge (SOC). In particular, it was demonstrated that this high SOC leads to the evolution of oxygen from the CAM. Simultaneously, the release of carbon monoxide and carbon dioxide (CO_2) was observed, leading to the hypothesis that the released lattice oxygen reacts with the electrolyte ethylene carbonate (EC) and all these effects ultimately cause a reduction in capacity with each cycle. In a subsequent work, the Gasteiger group [138] could prove that the released oxygen species is indeed the much more reactive singlet oxygen ($^1\text{O}_2$).

For this thesis, possible reaction pathways of electrolytes with $^1\text{O}_2$ were studied. In the article “Singlet Oxygen Reactivity with Carbonate Solvents used for Li-Ion Battery Electrolytes” submitted to *Journal of Physical Chemistry A* a joint experimental

and theoretical investigation of the reactivity of two common electrolytes with $^1\text{O}_2$ is presented. Several experimental techniques like on-line mass spectrometry, UV/Vis spectroscopy, and linear sweep voltammetry are used, complemented by QC and QD calculations.

Organic solvents are used for electrolytes in lithium-ion batteries, provided with a lithium salt like lithium hexafluorophosphate (LiPF_6) [133, 135]. Two of the commonly used organic solvents are chosen for this study, EC and dimethyl carbonate (DMC).

Key points of the article are:

- Using rose bengal as photosensitizer, $^1\text{O}_2$ is generated *in situ* in the pure electrolyte EC and DMC, respectively. With on-line mass spectrometry, changes in the gas phase above the sample are measured. While DMC shows no reactivity, EC is attacked by $^1\text{O}_2$ proven by the released CO_2 and the consumed $^1\text{O}_2$. The stoichiometry is quantified as 2:1 $^1\text{O}_2:\text{CO}_2$.
- With QC calculations a reaction mechanism is proposed initiated by the double hydrogen abstraction from EC, a step apparently described only once in the literature for a similar system [139]. The products vinylene carbonate (VC) and hydrogen peroxide (H_2O_2) are formed and VC can again react with $^1\text{O}_2$ or even triplet oxygen. Beginning at the TS of VC with $^1\text{O}_2$, ground state MQCD trajectories are run confirming CO_2 as the main gaseous decomposition product. For triplet oxygen intersystem crossing can occur, leading to the same product. For DMC the TSs lie too high for any reaction, confirming the experiment.
- The reaction mechanism is verified by colorimetric detection of H_2O_2 in the electrolyte solution *via* titanyle sulfate.
- The anodic oxidation of H_2O_2 in an aprotic electrolyte yields oxygen, which most likely shows proton and water formation, a reaction detrimental for every lithium-ion battery.

This joint experimental and theoretical work clearly demonstrates the power of collaboration as the calculated product of the rather unusual reaction of $^1\text{O}_2$ with an alkyl group was specifically searched for and successfully identified. It proves a mechanism very detrimental for the batteries and shows that the chemical stability against $^1\text{O}_2$ must not be overlooked in the search for new electrolytes. In the light of this research the standard electrolyte EC is probably not the best candidate for future lithium-ion batteries, contrary to DMC.

Hereafter, the article "Singlet Oxygen Reactivity with Carbonate Solvents used for Li-Ion Battery Electrolytes" submitted for publication to *Journal of Physical Chemistry A* is reprinted with permission from *J. Phys. Chem. A*. Unpublished work copyright 2018 American Chemical Society. The Supporting Information for this article is reprinted in Appendix B.

Singlet Oxygen Reactivity with Carbonate Solvents used for Li-Ion Battery Electrolytes

Anna T.S. Freiberg,^{‡a*} Matthias K. Roos,^{‡b} Johannes Wandt,^a Regina de Vivie-Riedle,^{b**} Hubert A. Gasteiger^a

^aChair of Technical Electrochemistry, Department of Chemistry and Catalysis Research Center, Technische Universität München, Garching, Germany

^bDepartment of Chemistry, Ludwig-Maximilians-Universität München, München, Germany

Singlet Oxygen, ab initio calculations, anodic oxidation of H₂O₂, chemical oxidation of ethylene carbonate

ABSTRACT: High degrees of delithiation of layered transition metal oxide cathode active materials (NCMs and HE-NCM) for lithium-ion batteries (LIBs) was shown to lead to the release of singlet oxygen, which is accompanied by enhanced electrolyte decomposition. Here we study the reactivity of chemically produced singlet oxygen with the commonly used cyclic and linear carbonate solvents for LIB electrolytes. On-line gassing analysis of the decomposition of ethylene carbonate (EC) and dimethyl carbonate (DMC) reveals different stability toward the chemical attack of singlet oxygen, which is produced in-situ by photo-excitation of the Rose bengal dye. *Ab initio* calculations and on-the-fly simulations reveal a possible reaction mechanism, confirming the experimental findings. In the case of EC, hydrogen peroxide and vinylene carbonate (VC) are found to be the products of the first reaction step of EC with singlet oxygen in the reaction cascade of the EC chemical decomposition. In contrast to EC, simulations suggested DMC to be stable in the presence of singlet oxygen, which was also confirmed experimentally. Hydrogen peroxide is detrimental for cycling of a battery, as for all known cathode materials the potential where singlet oxygen is released is found to be already high enough to electrochemically oxidize hydrogen peroxide, forming protons and/or water which both react with the typically used LiPF₆ salt to HF that then leads to transition metal dissolution from the cathode active materials. This study shows how important the chemical stability toward singlet oxygen is for today's battery systems and that a trade-off will have to be found between chemical and electrochemical stability of the solvent to be used.

INTRODUCTION

Lithium-ion batteries (LIBs) power today's consumer electronics such as laptops and mobile phones.¹⁻² Their use in battery electric vehicles (BEVs) promises to substantially reduce the (local) CO₂ emissions in the transportation sector.³ This, however, still requires significant increases in the gravimetric as well as volumetric energy density of LIBs in order to reduce battery weight/volume and to enable BEV driving ranges competitive with conventional combustion engine powered vehicles.⁴⁻⁵

Most state-of-the-art LIBs rely on a layered transition metal oxide cathode active material⁶ (CAM), currently paired with a graphite anode or, in the mid- to near-term with a higher energy density silicon anode.^{5, 7} To further increase the energy density, two types of mixed transition metal layered oxides are being investigated as high energy density CAMs, namely so-called Ni-rich NCMs (Li_x(Ni_xCo_yMn_z)O₂, with $x+y+z=1$)⁸ and Li-rich⁹ NCMs also referred to as HE-NCMs (Li_{1+w}(Ni_xCo_yMn_z)_{1-w}O₂, with

$x+y+z=1$ and w typically ≤ 0.2). While NCMs can theoretically deliver discharge capacities of up to 280 mAh/g upon complete delithiation, the long-term charge/discharge cycling stability of NCMs can only be met by limiting the degree of delithiation to ~70% state of charge (SOC),¹⁰⁻¹² i.e., by limiting the discharge capacity to ~190 mAh/g. Delithiation beyond ~70% SOC leads to higher charge cut-off potentials, which are reported to promote electrochemical electrolyte oxidation,¹³ whereby protic species proposed to result from electrolyte oxidation¹⁴ are the likely reason for the observed transition metal leaching from the CAM^{10-11, 15-18} and the cell impedance growth.¹⁰⁻¹¹ Furthermore, the reaction of electrolyte oxidation products and dissolved transition metal ions with the graphite anode can chemically delithiate the graphite anode, thereby leading to an irreversible active lithium loss.^{15, 17}

Oxygen release is another issue and has been known to occur for NCMs and HE-NCMs at high SOC,^{12, 19-23} indicating changes in the active material composition. The surface-near layers change from a layered to a spinel-like structure and/or a rock-salt structure.²⁴⁻²⁷ Simultaneous to

the O₂ release from the near-surface region, the formation of electrolyte decomposition products such as CO₂ and CO was detected by on-line electrochemical mass spectrometry (OEMS) by Jung et al.¹² and Guéguen et al.²³ Jung et al.¹² emphasized that the point at which O₂ is evolved depends on the SOC rather than on the cathode potential. The simultaneous evolution of O₂, CO₂ and CO was therefore assigned to a chemical reaction of the electrolyte with the released O₂ rather than to the electrochemical decomposition of the electrolyte, as the latter would depend on cathode potential and not on the SOC. The reactive O₂ released from the cathode was postulated to be singlet oxygen (excited state ¹Δ_g, further referred to as ¹O₂). Recently, we were indeed able to prove the SOC dependent release of ¹O₂ from NCMs and HE-NCM at high SOC using an *operando* photomultiplier set-up to record the 633 nm photon emission of the collision-induced bimolecular radiative decay of ¹O₂ to its triplet state.²⁸

As will be shown in this work, the following seemingly unrelated recent finding may also be linked to the release of singlet oxygen: It was demonstrated by the Dahn group^{13, 29-31} that electrolytes free of ethylene carbonate (EC) show superior capacity retention for NCM based CAMs operating at high cathode potentials (i.e., at high SOCs), whereby a lower overall impedance growth and a lower extent of gassing was observed.^{13, 30} This finding is somewhat puzzling, as it could not be explained by solely considering the electrochemical anodic stability of the solvents, as the cyclic ethylene carbonate has superior stability at high anodic potentials compared to the experimentally observed superior linear carbonate solvent (ethyl methyl carbonate (EMC)).³²⁻³⁴ A possible hypothesis to explain the inferior performance of EC solvent may be that it will react with ¹O₂ released at high SOC, forming reaction products, which are detrimental to battery durability.

Therefore, we will examine in this study the reactivity and the reaction products of the commonly used cyclic ethylene carbonate solvent with singlet oxygen and then compare it with the reactivity of a typical linear carbonate (dimethyl carbonate (DMC)) solvent. To this purpose, the reaction of in-situ formed ¹O₂ with EC and DMC was followed by analyzing the gaseous decomposition products and the consumption rate of oxygen by on-line mass spectrometry. To gain further insights into the reaction pathways and the nature of the reaction products, *ab initio* calculations are performed. The simulations identify the key characteristics, which govern the stability of aprotic electrolyte solvents toward ¹O₂. As H₂O₂ is predicted and found to be formed upon reaction of EC with ¹O₂, its decomposition pathway in the battery environment is further evaluated by on-line electrochemical mass spectrometry (OEMS) measurements. Finally, we will show that the here presented *ab initio* simulations and experimental findings on the reaction and reaction products of singlet oxygen with carbonate based electrolyte solvents are able to rationalize some of the observed aging mechanisms observed for LIBs employing NCM or HE-NCM cathodes. We there-

fore believe that our analysis will be able to guide the design of improved electrolyte solvents for use with oxygen releasing cathode active materials.

RESULTS AND DISCUSSION

On-line gas detection of solvent decomposition products

The chemical stability of carbonate solvents toward ¹O₂ is studied in a new experimental set-up adapted from our OEMS cell,³⁵ where the formation rates of gaseous reaction products between ¹O₂ generated in the electrolyte solvent (contained in a 4 ml cuvette) are quantified by on-line mass spectrometry (see Fig. S4 and experimental methods for details). Specifically, Rose bengal (RB) is used as photosensitizer to produce ¹O₂ in the electrolyte solvent saturated with triplet oxygen (ground state ³Σ_g⁻, from now entitled by ³O₂) by irradiating the reaction mixture with light at 523 nm. Furthermore, the use of 10% O₂ in argon allows a quantification of the oxygen consumption by on-line mass spectrometry (MS), enabling a more rigorous evaluation of the reaction stoichiometry between ¹O₂ and the electrolyte solvent. Background measurements by flushing the set-up with pure argon (excitation of the dye alone leads to no ¹O₂ formation) are performed for comparison in order to exclude thermal effects introduced by irradiation or side-reactions of the excited RB dye. The results of the on-line gas analysis for the reaction of EC and DMC with ¹O₂ are shown in Fig. 1, whereby the upper panels in each figure show the current applied to the LEDs: when current is applied (between 0 and 1 h), ¹O₂ is being generated by the RB dye in the ³O₂ saturated electrolyte solvent, while no ¹O₂ is generated in the absence of current (i.e., without irradiation). The gas evolution (middle panels) and the gas evolution rates (lower panels) for the reaction of ¹O₂ with EC for two different volumina of EC added into the cuvette are depicted in Fig. 1a (4 ml of EC) and Fig. 1b (1 ml of EC), while Fig. 1c shows the analogous experiment with DMC (4 ml). To assure that EC is present as a liquid (~-37°C melting temperature) and to provide the same reaction conditions for both carbonates, all measurements are conducted at 45°C. The dashed lines represent the gas evolution (rates) obtained while the set-up is set under argon, where no ¹O₂ is being produced.

In case of the EC solvent shown in Fig. 1a, the mass traces remain constant when the cuvette is radiated under argon (dashed lines, overlain by the blue CO line), meaning that no side-reaction from the excited RB dye is observed. After flushing the cuvette with 10% O₂ in argon, however, a clear signal at m/z=44 can be observed upon illumination (between 0-1 h), which is due to the formation of CO₂ (dark blue). Simultaneously, the oxygen concentration in the gas phase decreases (green), proving that upon excitation of triplet oxygen to its singlet state by the dye, singlet oxygen reacts with the solvent and thus leads to a consumption of oxygen from the gas phase (note that the molar consumption of O₂ is divided by 5 for better visibility). After a short delay, the CO₂ formation rate (Fig. 1a, lower panel) remains constant during illumination, as does the O₂ consumption rate. Moreover, after turning off the power-supply for the

LEDs (upper panel, $t > 1$ h), the CO_2 evolution and O_2 consumption rates decrease rapidly, which further proves that those gases are formed by a reaction of EC with $^1\text{O}_2$ that can only be generated during illumination. However, even 1 h after illumination, slight changes in the mass traces are still present, which suggests that a reaction product formed during illumination is reactive toward $^3\text{O}_2$ (see discussion later on), and/or that the diffusion of reaction products from the solution into the gas phase is slow (the diffusion length from the bottom of the cuvette to the liquid/gas interface is up to 4 cm). Finally, it should be noted that no CO is being evolved, which is in strong contrast to results obtained from an operating battery.^{12, 27-28}

To further elucidate the mechanism of CO_2 formation from the reaction of EC with $^1\text{O}_2$, the stoichiometry of evolved CO_2 and consumed O_2 shall be compared. As the on-line MS only samples the gas phase above the solvent, it must be considered that a significant fraction of the gases could be dissolved in the liquid. In relative terms, the amount of dissolved O_2 is negligible compared to that of CO_2 , as its temperature independent Henry coefficient in cyclic carbonates is at least one order of magnitude higher than that of CO_2 .³⁶ Assuming that the solvent and gas phase are in equilibrium, the amount of CO_2 in solution ($n_{\text{CO}_2(\text{solv})}$) based on its measured amount in the gas phase ($n_{\text{CO}_2(\text{gas})}$) can be calculated by Eq. 1, which is a combination of Henry's law and the ideal gas law:³⁷

$$\frac{n_{\text{CO}_2(\text{solv})}}{n_{\text{CO}_2(\text{gas})}} = \frac{V_{\text{solv}}}{V_{\text{gas}}} \cdot \frac{R \cdot T \cdot c_{\text{solv}}}{K_H^{\text{CO}_2, \text{solv}}} \quad (1)$$

where V_{solv} is the solvent volume (1 or 4 ml in Fig. 1), V_{gas} is the gas phase volume in the head-space of the cuvette which includes the connector to the MS ($V_{\text{gas}} = 6.7 \text{ ml} - V_{\text{solv}}$, equating to $V_{\text{solv}}/V_{\text{gas}} = 1.5$ for $V_{\text{solv}} = 4 \text{ ml}$), R is the universal gas constant, T is the temperature, c_{solv} is the molar concentration of the solvent ($\sim 15.3 \text{ mol/l}$ for pure EC at 45°C),³⁶ and $K_H^{\text{CO}_2, \text{solv}}$ is the Henry coefficient for CO_2 in the corresponding solvent. For our experimental temperature of $T = 318 \text{ K}$, the Henry constant for CO_2 in EC is approximately $K_H^{\text{CO}_2, \text{EC}} \approx 19 \text{ MPa}$.³⁶ For these values, the ratio of dissolved to gaseous CO_2 predicted by Eq. 1 amounts to $n_{\text{CO}_2(\text{solv})}/n_{\text{CO}_2(\text{gas})} \approx 3.1$, indicating that the amount of CO_2 dissolved in EC largely exceeds its amount in the gas-phase where its concentration is being measured by on-line MS. While in principle one could correct for this factor, the errors associated with this correction would likely be rather large due to the large value of $n_{\text{CO}_2(\text{solv})}/n_{\text{CO}_2(\text{gas})}$ in combination with the uncertainty in the Henry constant; furthermore, owing to the large diffusion length of up to 4 cm from the bottom of the cuvette to the liquid/gas interface, perfect equilibration of the CO_2 and O_2 gas/liq-uid concentrations may not be reached over the experimental time scale of 1 h, even though the liquid was mixed with a small stirrer (complete convective mixing over the 4 cm liquid height in the 1 cm^2 cross-section cuvette may not be achieved). Therefore, an additional experiment was performed in which the maximum diffusion/mixing length was reduced to $\sim 1 \text{ cm}$ by decreasing the EC volume to 1 ml, in which case sufficient convective mixing by the stirrer

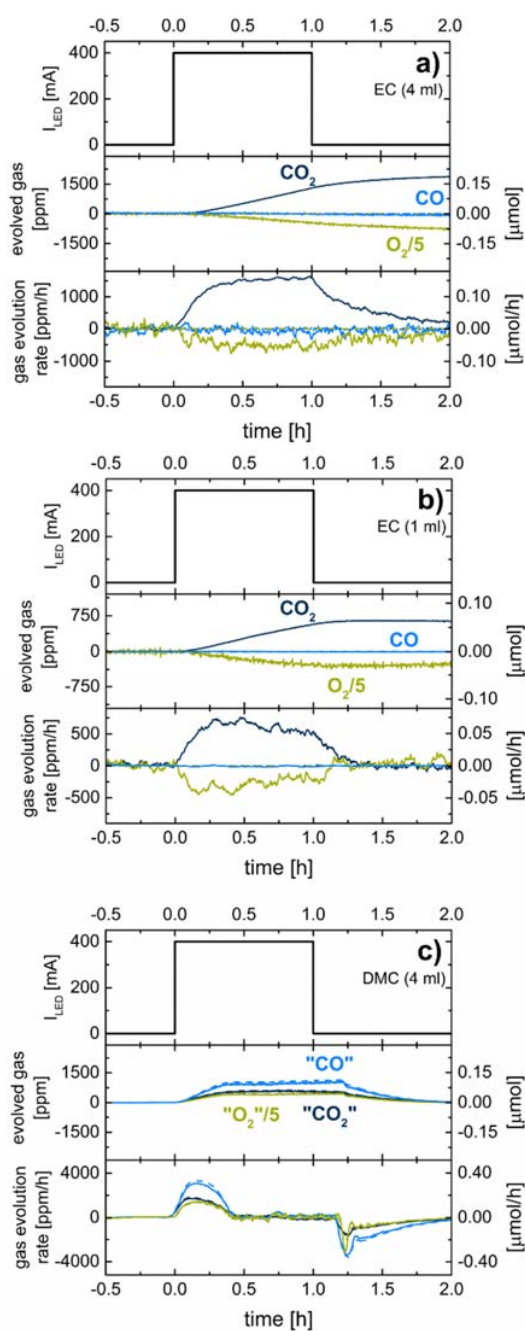


Fig. 1: Gas analysis of decomposition products. The upper panels show the current through the LEDs that irradiate the reaction vessel (cuvette) at 523 nm to enable the generation of $^1\text{O}_2$ by the dissolved Rose bengal dye, i.e., $^1\text{O}_2$ is generated between 0 and 1 h. The middle panels show the evolution of CO and CO_2 as well as the consumption of O_2 caused by the reaction of $^1\text{O}_2$ with carbonate solvents saturated with 10% O_2 in argon (at ambient pressure) at 45°C : **a)** for 4 ml EC; **b)** for 1 ml EC; and **c)** for 4 ml DMC placed into the cuvette. The lower panel shows the evolution rate for CO and CO_2 as well as the consumption rate of O_2 (smoothed over 50 points). Dashed lines show the background experiments conducted under argon, where no $^1\text{O}_2$ is being formed.

over the entire liquid height was observed. This also has the advantage that the fraction of dissolved CO_2 is reduced by nearly one order to magnitude to $n_{\text{CO}_2(\text{solv})}/n_{\text{CO}_2(\text{gas})} \approx 0.37$ (due to the lower value of $V_{\text{solv}}/V_{\text{gas}} = 0.18$), so that the percentage of the evolved CO_2 which ends up in the gas phase increases to $\sim 73\%$ compared to only $\sim 24\%$ when 4 ml of EC are used.

The results for the experiment with the reduced EC volume of 1 ml are shown in Fig. 1b. As expected, the amounts of evolved CO_2 and consumed O_2 are largely reduced compared to the experiment with 4 ml EC, even though the overall characteristics are similar. Now, however, the mass traces remain constant after illumination (Fig. 1b, central panel), contrary to what was observed with 4 ml EC (see Fig. 1a). This difference is also apparent in the gas evolution/consumption rates, which with 1 ml EC drop to zero only moments after the illumination is stopped (Fig. 1b, lower panel), clearly indicating that the low but finite gas evolution/consumption rates after illumination with 4 ml EC (Fig. 1a) must indeed be due to an incomplete equilibration between the liquid and the gas phase. Therefore, our estimate for the CO_2 and O_2 reaction stoichiometry is derived from the data with the lower EC volume of 1 ml, for which the amount of O_2 and CO_2 detected in the gas phase after 1h illumination as well as the calculated sum of CO_2 in the gas phase and in solution ($n_{\text{CO}_2(\text{sum})}$) are listed in Table 1, together with the resulting overall reaction stoichiometry ($n_{\text{CO}_2(\text{sum})}/n_{\text{O}_2(\text{gas})}$) which suggests that for each released CO_2 molecule two O_2 molecules are consumed. Possible microscopic reaction mechanisms will be discussed in the simulations part.

Table 1: Molar consumption of O_2 ($n_{\text{O}_2(\text{gas})}$) and formation of CO_2 ($n_{\text{CO}_2(\text{gas})}$) in the gas-phase over the 1 hour illumination period of 1 ml EC (0-1 h data shown in Fig. 1b). The total amount of CO_2 ($n_{\text{CO}_2(\text{sum})}$) calculated from its estimated partition into the liquid and the gas phase ($n_{\text{CO}_2(\text{solv})}/n_{\text{CO}_2(\text{gas})} \approx 0.37$; see text) is used to determine the overall reaction stoichiometry factor $n_{\text{CO}_2(\text{sum})}/n_{\text{O}_2(\text{gas})}$ of evolved CO_2 to consumed O_2 in the reaction of EC with $^1\text{O}_2$.

$n_{\text{O}_2(\text{gas})}$	$n_{\text{CO}_2(\text{gas})}$	$n_{\text{CO}_2(\text{sum})}$	$n_{\text{CO}_2(\text{sum})}$
[μmole]	[μmole]	[μmole]	n_{O_2}
-0.146	0.055	0.075	0.52

The gas analysis of DMC upon reaction with $^1\text{O}_2$ is shown in Fig. 1c. All mass traces assigned to CO_2 , CO , and O_2 show changes during the illumination phase. However, those changes are not caused by reactions with $^1\text{O}_2$, as the experiment under argon atmosphere (dashed lines) shows the same changes and as all mass traces return to their original values within ~ 0.5 h after turning off the illumination; furthermore, the O_2 mass signal would indicate an *increase* in the O_2 concentration during illumination. This clearly

points toward an experimental artefact when using solvents with a very high vapor pressure like DMC, caused by the heating of the solution during the illumination period. As a matter of fact, all mass channels assigned to the gases of interest also correspond to MS-fragments of the DMC molecule (see Fig. 3 in Ref. 37) and are therefore affected by the vapor pressure change of the solvent upon heating. This effect is not observable for the EC solvent, as its vapor pressure is several orders of magnitude lower than that of DMC (1913 Pa³⁸ for DMC vs 24 Pa³⁹ for EC at 45°C), leading to a strong temperature dependency of the solvent content in the gas phase in case of DMC, which explains the behavior observed in Fig. 1c. Therefore, we conclude that DMC shows an excellent stability toward $^1\text{O}_2$, as no oxygen is consumed even when $^1\text{O}_2$ is being generated. In summary, the data from this simple experimental set-up allows an easy evaluation of the reactivity of battery solvents with $^1\text{O}_2$, suggesting high stability for the linear alkyl carbonate DMC and significant reactivity with the cyclic carbonate EC.

Reaction mechanisms of carbonate solvents with singlet oxygen

Quantumchemical and dynamical methods are performed to elucidate the underlying microscopic reaction mechanism and to explain the different stability of EC and DMC toward $^1\text{O}_2$. We start our investigation with EC.

We could exclude a possible reaction of EC with $^3\text{O}_2$. The calculated reaction barrier on CASPT2 level of theory is 1.90 eV and will prevent the reaction. For the attack by $^1\text{O}_2$ we performed DFT and CASPT2 calculations. CASPT2 calculations were necessary when more than one electronic configuration becomes important in the wavefunction, which is often the case at transition states. A comparison of the critical energies is given in Table 2, while the reaction mechanism is shown in Fig. 2 (top, left). CASPT2 calculations were performed for EC, $^1\text{O}_2$, TS1, VC, $^3\text{O}_2$, TS2, the biradical and TS3. The $^1\text{O}_2$ aligns parallel to the C-C single bond, facing the H-atoms on one side. At the transition state (TS1) the oxygen π^* orbitals form new σ -bonds with the two H-atoms, resulting in a six membered ring consisting of the two carbon atoms, the two hydrogen atoms, and the two oxygen atoms. From TS1, the intermediate vinylene carbonate (VC) is produced by abstracting the two hydrogen atoms and eliminating an H_2O_2 molecule. The barrier height for this step lies between 0.92 eV (DFT) and 1.27 eV (CASPT2) and should allow the formation of VC (see first line in Table 2). With $\Delta G = -1.77$ eV, the reaction is clearly exergonic. This concerted dihydrogen abstraction is rather untypical compared to the well-known addition reactions of $^1\text{O}_2$ to C-C double bonds.⁴⁰ Sevin and McKee⁴¹ reported an analogous reaction for cyclohexadiene also based on calculations, yielding a barrier height of 0.96 eV on CASPT2 level of theory. While the thus predicted VC reaction product will exist only in low concentration compared to the EC educt, due to its C-C double bond it is substantially more reactive and contrary to EC can even react with $^3\text{O}_2$ (see below discussion and Fig. S5). As much more $^3\text{O}_2$ than $^1\text{O}_2$ is present, the reaction with $^3\text{O}_2$ should be more likely. This would also be the case in an operating battery,

Table 2: Reaction and activation free enthalpies (ΔG) and electronic energies with zero-point correction ($E+ZPC$) in eV for the reaction of the electrolyte with oxygen.

	B3LYP/6-311++G**		CASPT2	
	ΔG^*	ΔG	ΔE^*+ZPC	$\Delta E+ZPC$
$EC + {}^1O_2 \rightarrow VC + H_2O_2$	0.92	-1.77	1.27	-
$VC + {}^3O_2 \rightarrow \text{biradical}$	1.75	1.76	1.14	1.06
$VC + {}^1O_2 \rightarrow \text{dioxetane}$	1.32	-1.63	0.32	-
$\text{dioxetane} \rightarrow C_2H_2O_3 + CO_2$	1.24	-0.16	-	-

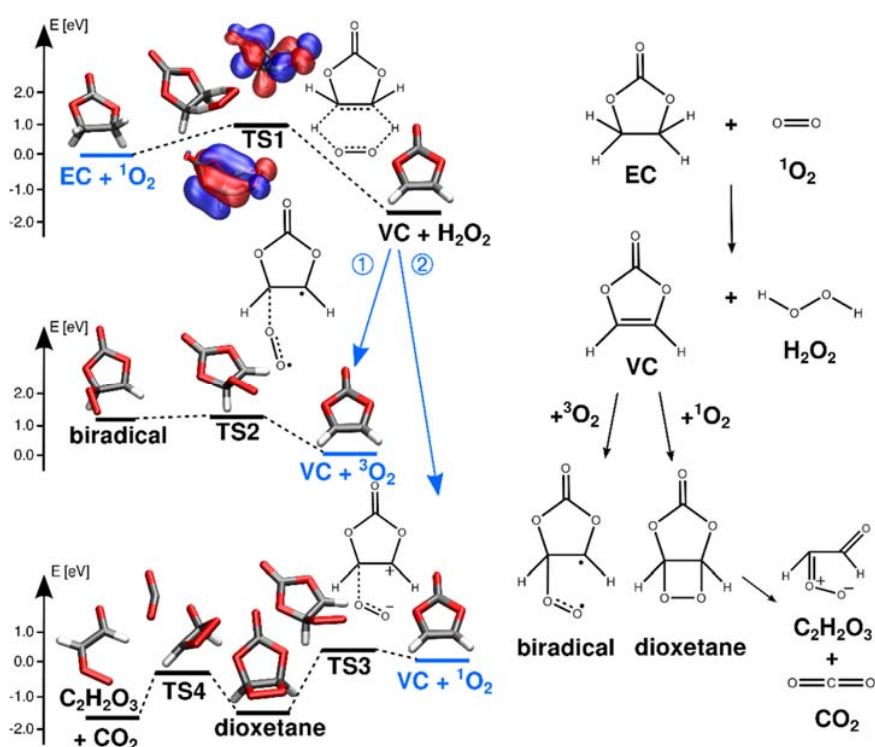


Fig. 2: Pathways for the reaction started by the attack of singlet oxygen on EC based on DFT and CASPT2 calculations.

as the lifetime of 1O_2 in solution is limited to the μs range,⁴² so that the concentration of 3O_2 in the bulk electrolyte will exceed the one of 1O_2 . For completeness we nevertheless calculated both pathways shown in Fig. 2 (middle and bottom, left). On the left-hand-side of Fig. 2, the calculated three-dimensional structures and their relative energies are given, on the right-hand-side the reaction pathways are visualized by a graphical representation.

In pathway ① (Fig. 2, middle), VC is attacked by 3O_2 . The oxygen molecule is bonding to one carbon atom of the C-C double bond, and a biradical is formed after passing

the transition state (TS2) with a barrier of 1.14 eV (CASPT2; see 2nd row of Table 2). Already TS2 is of biradical character, which requires a multi-configurational treatment. On CASPT2 level of theory, a frequency analysis is not feasible and therefore all values refer to the electronic energy plus zero point correction ($E+ZPC$). Despite the positive $E+ZPC$ of 1.06 eV for this reaction, it is a reasonable path, as the biradical is instable. Due to large spin-orbit coupling it will decay via inter-system crossing to the singlet pathway ②. Geometrically the TS2 and the biradical are similar to TS3. Thus, we assume the same reaction outcome as for the reaction of VC with 1O_2 . In this second reaction path (Fig. 2,

path ②, bottom), the ${}^1\text{O}_2$ is also attached to the C-C double bond, but almost parallel aligned to the C-C double bond, allowing direct ring closure to form the intermediate dioxetane in a [2+2] cycloaddition for which various reaction mechanisms are discussed.^{40, 43-45} The decisive barrier is very low (0.32 eV, TS₃; see 3rd row of Table 2) due to the high reactivity of ${}^1\text{O}_2$. The difference of 1 eV between DFT and CASPT₂ based barriers is again the result of the multi-configurational character of this TS. In a follow-up step, the carbonate moiety of dioxetane can split off and CO_2 is released, consistent with the experimental observations. In a subsequent step, the dioxetane ring opens to a $\text{C}_2\text{H}_2\text{O}_3$ fragment, probably instable in solution.

To search the configuration space for all possible final products, trajectory calculations were started at TS₃. With these calculations we can follow the change in potential energy as well as in geometry during the temporal evolution of the system. The calculations were performed for 900 fs, and from 110 started trajectories 103 converged. Within the propagation time, we could establish six different products, listed in Table 3. Next to dioxetane, $\text{C}_2\text{H}_2\text{O}_3 + \text{CO}_2$ (Fig. 2) is the main product. It is mostly generated from dioxetane when enough energy is available. The example trajectory in Fig. 3a shows a typical time trace of the potential energy profile leading to these final products as well as intermediate structures at selected points of the trajectory. The fast oscillations reflect the exchange between kinetic and potential energy, whereby their large amplitude indicates high activity in the vibrational motion. The overall energetic evolution shows two prominent steps. The reaction moves down-hill from the TS in around 100 fs and forms dioxetane, visible in the first plateau from ~150-450 fs. Thereafter, a second step is apparent where the C-O bonds in the five-membered ring break up and CO_2 is being released. Hereby potential energy is converted not only into vibrations, but also into rotational and translational motion. The second trajectory (Fig. 3b) is an example for a higher energetic trajectory, providing enough kinetic energy to further fragment dioxetane to $\text{HCO}^+ + \text{HCO}_2^- + \text{CO}_2$. The different, high-energy nature of this trajectory can also be seen in the even larger exchange between potential and kinetic energy.

The trajectory calculations shown in Fig. 3 and Table 3 confirm the thermodynamics established from the static calculations, i.e., dioxetane and $\text{C}_2\text{H}_2\text{O}_3 + \text{CO}_2$ are the main products. All further products found in the dynamical calculations are formed from dioxetane. Also a small amount of back reaction is observed.

The experimentally reported products $\text{CO}_2 + \text{CO}$ by Jung et al.¹² are also directly observable, but only to ~1% (see last row in Table 3). However, we expect that in the natural electrolyte environment (i.e., solvents plus a lithium salt), dioxetane as well $\text{C}_2\text{H}_2\text{O}_3$ will further fragment into CO_2 and CO . The abstraction of the H-atoms should be favored by the surrounding polar electrolyte and electrolyte salt, especially in an external potential field (i.e., in an operating battery).

In summary, the reaction of EC with ${}^1\text{O}_2$ passes through two central steps. The first one is the abstraction of two H-atoms from EC by ${}^1\text{O}_2$ to form VC and H_2O_2 ; the second step is the continuing reaction of VC with ${}^3\text{O}_2$ to form the final products. To further verify the first step, we tested the same situation for the linear DMC.

DMC does not provide two H-atoms at neighboring C-atoms and thus a transition state similar to that of TS₁ for EC cannot occur. All other possible transition states are so high in energy that they are unphysical and not found by the search algorithm. Thus, as to be expected based on the DMC molecular structure, no reaction takes place between ${}^1\text{O}_2$ and DMC.

Table 3: Distribution of products (based on 110 trajectories) for the trajectories starting from the transition state of VC + ${}^1\text{O}_2$. Italic pathways are also shown in Fig. 3.

Final geometry	%
dioxetane	63.6
<i>$\text{C}_2\text{H}_2\text{O}_3 + \text{CO}_2$ (Fig. 3a)</i>	25.5
VC + ${}^1\text{O}_2$	4.5
dioxirane-3-carbaldehyde + CO_2	3.6
<i>$\text{HCO}^+ + \text{HCO}_2^- + \text{CO}_2$ (Fig. 3b)</i>	0.9
$\text{H}_2\text{CO}_2 + \text{CO} + \text{CO}_2$	0.9
$2 \text{CO}_2 + \text{CO} + \text{H}_2$	0.9

Detection of liquid decomposition products and anodic oxidation of H_2O_2

The *ab initio* calculations for the reaction of EC with ${}^1\text{O}_2$ are in good agreement with the experimental results concerning the gaseous reaction products, i.e., CO_2 is the only product observed by gas-phase on-line MS and also the main gaseous product predicted by the calculations. The initial step of EC decomposition suggested by *ab initio* calculations is the abstraction of two H-atoms by ${}^1\text{O}_2$, forming H_2O_2 and VC, which poses the question whether VC could be detected after the reaction. Based on the results shown in Fig. 1a, where 0.38 $\mu\text{mol O}_2$ were consumed during the 2 h experiment and considering that according to the above mechanism one consumed O_2 molecule would produce one VC molecule, the maximum possible concentration of VC in solution (i.e., ignoring its follow-up reaction) would only amount to ~6 ppm (0.38 $\mu\text{mol}_{\text{VC}} \times 84 \text{ g/mol}_{\text{VC}} = 32 \mu\text{g}_{\text{VC}}$ in 5.2 g EC ($\equiv 4 \text{ ml}$)), which is far below the NMR detection limit and explains why it had not shown up in our ${}^1\text{H}$ - and ${}^{13}\text{C}$ -NMR analysis of the reaction mixture (data not shown). Even with more sensitive chemical analysis methods, we believe that VC will not be detectable, as the strong CO_2 gassing (see Fig. 1a) in combination with our calculations suggests that

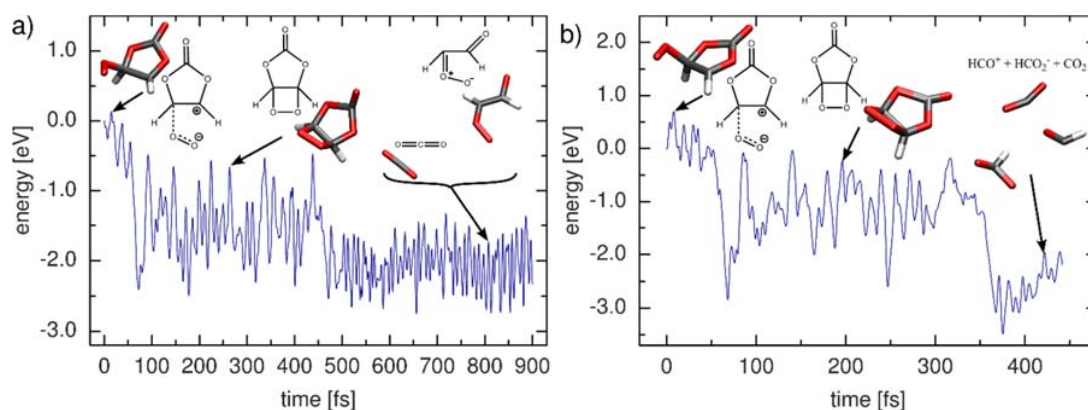


Fig. 3: Two example trajectories leading to a) $C_2H_2O_3 + CO_2$ and b) $HCO^+ + HCO_2^- + CO_2$ (right).

VC is a very reactive intermediate that can be readily decomposed and thus might only be present in the sub-ppm level. As a matter of fact, the instability of VC in solution is well-known and it can only be stabilized for use in battery electrolytes by radical inhibitors such as BHT (butylated hydroxytoluene),⁴⁶ which of course are absent here since VC is formed *in-situ* in pure EC solvent. Additionally, the above calculations revealed that even ground-state 3O_2 is able to initiate VC decomposition, which was also observed in a simple on-line MS experiment (see Supporting Information, Fig. S5).

Even though VC itself cannot be detected after the reaction of EC with 1O_2 , the above mechanism deduced from the *ab initio* calculations would result in the formation of H_2O_2 , which can be detected colorimetrically with very high sensitivity (few ppm),⁴⁷ following a standard procedure by the German Institute of Standardization (DIN 38 409, part 15), as explained in the experimental part.

The results of this analysis for the EC and DMC solution after exposure to 1O_2 (according to the experiments shown in Fig. 1a and c) are shown in Fig. 4a and b, respectively. As clearly seen in Fig. 4a, after reaction of the EC solution with 1O_2 , an additional absorption feature between 410-420 nm can be observed (orange line) that corresponds to the characteristic absorption of the $[Ti(O_2)]^{2+}$ complex formed in the presence of H_2O_2 (the features above that wavelength are caused by the RB dye). No signal at 410-420 nm can be observed for the experiment conducted under argon, where no 1O_2 is produced (black line). In contrast to that, the DMC solution shows no change after exposure to 1O_2 (orange line in Fig. 4b), as one would expect based on the on-line gas analysis (see Fig. 1c) as well as the *ab initio* calculations. Unfortunately, due to the background of the RB dye and possible chemical decomposition of H_2O_2 , a quantitative assessment is not feasible. Nevertheless, the result of this colorimetric analysis unambiguously verifies the formation of H_2O_2 and thus provides strong evidence for our calculated reaction mechanism, namely the formation of VC and H_2O_2 as the first step in the reaction of EC with 1O_2 .

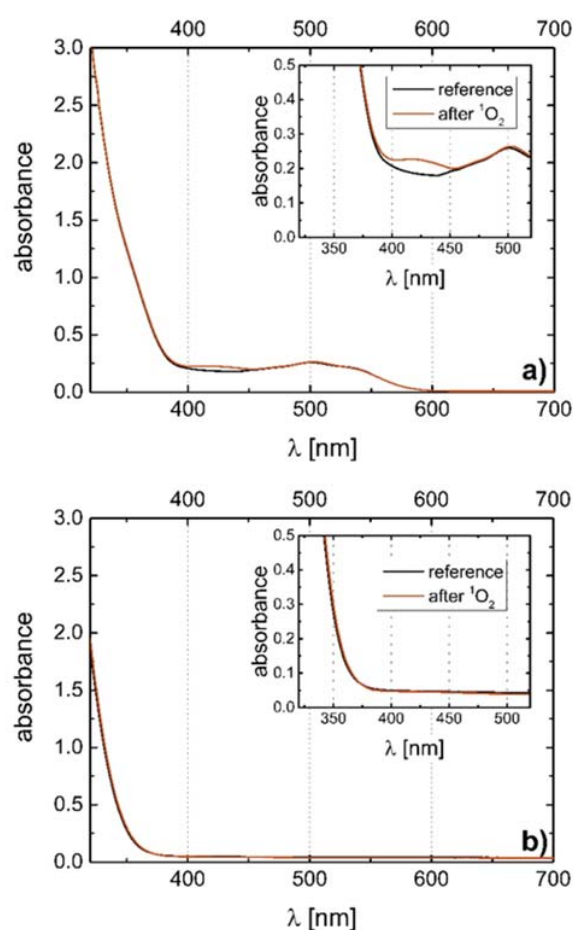


Fig. 4: Detection of H_2O_2 based on $[Ti(O_2)]^{2+}$ complex formation for 100 μM RB in EC (a) and DMC (b), with samples taken either before (black) or after reaction with 1O_2 (orange) according to the experimental procedures shown in Fig. 1a and c.

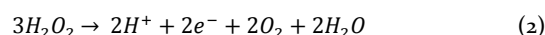
Does the formation of VC and H_2O_2 influence the battery's lifetime? The anodic oxidation of VC has already been studied by Pritzl et al.,⁴⁸ where it was found to initiate at 4.3 V vs Li⁺/Li. Still, it remains unknown whether the

lifetime of VC formed by ${}^1\text{O}_2$ is long enough to be oxidized electrochemically in an operating battery before its further chemical decomposition reaction with ${}^1\text{O}_2$ or ${}^3\text{O}_2$ (see Table 2). From the trajectory calculations we can extrapolate a chemical decomposition time on the order of several ps. In contrast to VC, H_2O_2 is chemically reasonably stable, which leads to the question how it might interact further in an operating battery after its formation at/near the layered transition metal oxide cathode. One possibility is its gradual chemical decomposition into water and oxygen, whereby water is known to react with the common LiPF_6 electrolyte salt forming POF_3 and HF ,⁴⁹⁻⁵⁰ ultimately leading to transition metal dissolution.^{10-11, 15-18} Another possibility which we will explore in the following is whether the potential is sufficiently high to drive the electrochemical oxidation of H_2O_2 to protons and oxygen (e.g., $\text{H}_2\text{O}_2 \rightarrow 2\text{H}^+ + 2\text{e}^- + \text{O}_2$); in this case, the PF_6^- anion would react with H^+ to HF and PF_5 .⁵¹

The remaining open question is whether the typical cathode potentials in LIBs with NCM or HE-NCM cathodes (~ 4.3 - 4.7 V vs Li^+/Li) is high enough to electrochemically oxidize H_2O_2 . Since no data are available in the literature on this reaction in aprotic electrolytes, it will be examined in the following by conducting linear sweep voltammetry (LSV) scans on a carbon black electrode (Super C65/PVdF) after deliberate addition of an aqueous H_2O_2 solution (50%_{wt}) to a DMC based electrolyte with 1.5 M LiPF_6 ; as H_2O_2 can only be obtained as an aqueous solution, the effect of H_2O addition is also examined for reference. To eliminate the reaction of H_2O_2 and H_2O at the lithium counter electrode, these experiments are conducted with our 2-compartment cell design where working and counter electrode are separated by a lithium ion conducting solid electrolyte (see experimental part and Metzger et al.¹⁴ for details). Fig. 5 shows the background measurements for the pure DMC based electrolyte without (a) and with 550 ppm H_2O (b). The upper panels show the anodic current vs potential during the 0.2 mV/s scan from the open circuit potential (OCV; ranging between ~ 3.1 - 3.7 V) up to 5.2 V vs Li^+/Li (see upper x-axes). The integral gas evolution and the gas evolution rates are shown in the middle and lower panels, respectively, whereby O_2 , CO_2 , and CO are the major gaseous products; dotted vertical lines mark the onset potentials of each gas (indicated by the respective color). As can be readily seen, no O_2 formation (green lines) is detected in the absence of H_2O_2 and the electrochemical oxidation of DMC is essentially unaffected by the presence of water (upper panels; note that the current peak at ~ 4.5 V is due to the corrosion/passivation of the current collector). For the DMC based electrolyte without and with added H_2O (Fig. 5a and b), CO_2 evolution sets in at ~ 4.87 V vs Li^+/Li (dark blue dotted line). The evolution of CO initiating at ~ 4.90 V vs Li^+/Li (blue dotted line) in the presence of H_2O (blue line in Fig. 5b) arises in major parts from the H_2O -induced oxidation of the carbon electrode as already studied by Metzger et al.⁵² and is thus absent for the H_2O -free electrolyte (Fig. 5a).

While the CO_2 and CO signals with the electrolyte containing 550 ppm of 50%_{wt} H_2O_2 in H_2O are identical to the

background measurement without H_2O_2 (except for an earlier CO_2 onset potential of ~ 4.4 V vs ~ 4.87 V), the presence of H_2O_2 results in a strong oxygen evolution, initiating at ~ 3.85 V vs Li^+/Li (green dotted line). The oxygen formation is completed by the time the potential has reached ~ 4.7 V, at which point the total amount of O_2 formed in the cell amounts to $3.9 \mu\text{mol}_{\text{O}_2}/\text{m}_c^2 \equiv 0.67 \mu\text{mol}_{\text{O}_2}$ (based on a total carbon surface area of 0.17 m_c^2 in the cell; see experimental section). This suggests that all of the H_2O_2 added to the cell ($275 \text{ ppm}_{\text{H}_2\text{O}_2} \equiv 1.05 \mu\text{mol}_{\text{H}_2\text{O}_2}$, based on 0.13 g of electrolyte) has been consumed, which would correspond to a reaction stoichiometry of 2 moles of O_2 produced per 3 moles of consumed H_2O_2 . Integrating the additional oxidation peak observed during the LSV scan between 3.8 and 4.65 V shown in the upper panel of Fig. 5c, the overall additional anodic charge in the presence of H_2O_2 can be estimated to be $\sim 0.67 \mu\text{mol}_e^-$. A comparison with the $0.67 \mu\text{mol}_{\text{O}_2}$ of evolved O_2 within this potential range indicates a 1-electron mechanism for the formation of O_2 from H_2O_2 . From this, from the above determined reaction stoichiometry of $\text{H}_2\text{O}_2/\text{O}_2 = 3/2$, and from the fact that the only observed gaseous product is O_2 , a plausible net electrochemical oxidation reaction can be formulated if one assumes that the electron charges are balanced by protons released into the solution:



While this net reaction does not give any insight into the elementary reaction steps and is still rather speculative, it illustrates that the electrooxidation of H_2O_2 is most likely accompanied by the release of protons. The initial elementary step is most likely the formation of a hydroperoxyl radical ($\text{HOO}\cdot$) by a 1-electron oxidation of H_2O_2 ($\text{HOOH} \rightarrow \text{HOO}\cdot + \text{H}^+ + \text{e}^-$), which has a standard potential of +1.44 V⁵³ (vs the standard hydrogen electrode, SHE). If referenced to the Li^+/Li scale (3.04 V vs SHE⁵³), this would correspond to ~ 4.5 V vs Li^+/Li at standard activities and ~ 3.7 V vs Li^+/Li if one were to assume activities of 10^{-7} for both $\text{HOO}\cdot$ and H^+ in the vicinity of the electrode, reasonably close to the OCV obtained in the DMC electrolyte containing 550 ppm of the added 50%_{wt} H_2O_2 solution (see Fig. 5c). The attack of intermediate $\text{HOO}\cdot$ radicals on DMC might also explain the earlier onset for CO_2 formation in the presence of H_2O_2 (compare Fig. 5a and 5c).

As shown and explained in the supporting information (paragraph E, Fig. S6), the evolution of H^+ can be traced and was proven for the anodic oxidation of H_2O_2 , matching the net reaction in Eq. 2 even quantitatively.

While further experiments would be required to gain mechanistic insights into the electrooxidation of H_2O_2 on carbon black, it is clear that H_2O_2 formed by the reaction of EC with ${}^1\text{O}_2$ would not be stable in the operating potential range of a layered transition metal oxide cathode material: while ${}^1\text{O}_2$ is released only above ~ 4.3 V vs Li^+/Li for NCM811 and above ~ 4.6 V vs Li^+/Li for NCM111 and HE-NCM,²⁸ the electrooxidation of H_2O_2 initiates already at potentials above ~ 3.85 V. If the here proposed net electrooxidation reaction of H_2O_2 in the cathode electrode were true

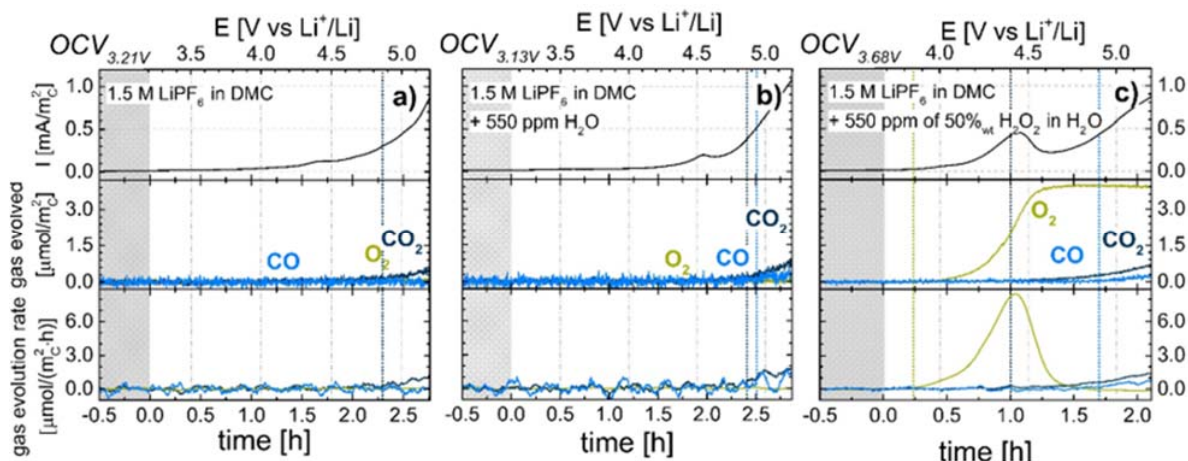


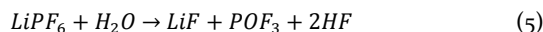
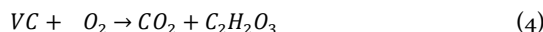
Fig. 5: Electrochemical oxidation of DMC electrolyte with 1.5 M LiPF₆ on a carbon black electrode (Super C65/PVdF) during a linear potential scan (0.2 mV/s) from OCV to 5.2 V vs Li⁺/Li (upper x-axes; OCV values are also indicated there) at 25°C: **a)** pure electrolyte; **b)** electrolyte with 550 ppm H₂O and, **c)** electrolyte with 550 ppm of 50%_{wt} H₂O₂ in H₂O. *Upper panels:* current vs potential; *middle panels:* total amount of formed gas for CO (blue lines), CO₂ (dark blue lines), and O₂ (green lines), referenced to the total BET surface area of the carbon electrode; *bottom panels:* gas evolution rates (smoothed over 50 points), whereby the onset of the evolution of each gas is marked by dashed vertical lines (in the respective color). Measurements are performed in a 2-compartment OEMS cell in which the lithium metal counter electrode is separated from the carbon black working electrode by an impermeable solid lithium ion conductor¹⁴.

(Eq. 2), the formation of protons and water with the commonly used LiPF₆ salt would lead to the formation of HF,⁴⁹⁻⁵¹ which in turn would lead to transition metal leaching from the cathode active material.^{10-11, 15-18}

In total, three different aging mechanism caused by the chemical reactivity of ¹O₂ with EC and by the resulting reaction products can be identified: i) EC consumption by its reaction with ¹O₂, accompanied by CO₂ formation; ii) chemical decomposition of H₂O₂ to oxygen and H₂O that further reacts with PF₆⁻ to POF₃ and HF and/or electrochemical oxidation of H₂O₂ to oxygen and H⁺ that further reacts with PF₆⁻ to PF₅ and HF; and, iii) chemical degradation of the cathode active material by the formed HF, accompanied by transition metal dissolution and migration to the anode, where it leads to a loss of active lithium and impedance growth.^{10, 17} All these mechanisms account for battery aging and show the importance of understanding the chemical reactivity of ¹O₂ with electrolyte solvents.

In summary, the release of singlet oxygen from layered transition metal oxide CAM for LIBs at high states of charge (above ~80%)²⁸ was shown here to lead to the decomposition of the commonly used EC electrolyte component, resulting in the formation of VC and H₂O₂ (see Eq. 3 or 1st row of Table 2). While VC can further react with both singlet and triplet oxygen (see Eq. 4 or 2nd and 3rd rows of Table 2), it will also get oxidized electrochemically at potentials above 4.3 V vs Li⁺/Li⁴⁸. At the same time, the generated H₂O₂ will get oxidized rapidly at the operating voltage of NCM and HE-NCM cathodes, most likely leading to the formation of H⁺ and H₂O (see Eq. 2), which would lead to the generation of HF from the typically used LiPF₆ salt (see Eqs. 5 and 6) which in turn would lead to transition metal leaching. Even though the impact of the organic residuals produced by the reaction of EC after reaction with

¹O₂ (VC, dioxetane, and further fragments) is still under investigation, the formation of H₂O₂ is seen as the major factor resulting in bad cycling performance of LIBs when NCM or HE-NCM cathodes are charged to high cut-off potentials or, more precisely, when they are charged above the SOC at which ¹O₂ is released.



CONCLUSION

In this study, we evaluated the chemical stability of the standard lithium-ion battery solvents ethylene carbonate (EC) and dimethyl carbonate (DMC) toward singlet oxygen (¹O₂) that was found to be released from layered transition metal oxides (NCM and HE-NCM) at high states of charge (SOC). A mass spectrometry set-up was developed, which enabled the on-line detection of gaseous reaction products upon the generation of ¹O₂ in triplet oxygen saturated EC or DMC with dissolved Rose bengal photosensitizer under irradiation with 525 nm light.

The ethylene group in EC was found to be the key reactive moiety allowing the attack of ¹O₂ as shown by *ab initio* calculations. Here, the decomposition of EC is initiated by the elimination of H₂O₂ and the formation of vinylene carbonate (VC), which can be further decomposed under CO₂ release, as confirmed by trajectory calculations. Calculations further suggested that no reaction would occur between ¹O₂ and the linear carbonate DMC. These predictions were tested by on-line gas analysis upon excitation of the photosensitizer, providing an unambiguous proof of the instability of EC and the high stability of DMC toward

$^1\text{O}_2$, as well as validating the formation of H_2O_2 upon decomposition of EC. On-line electrochemical mass spectrometry (OEMS) further revealed that H_2O_2 undergoes rapid electrochemical oxidation at a non-catalytic carbon black electrode at potentials above ~ 3.85 V vs Li^+/Li , i.e., at potentials below the operating potential of NCM and HE-NCM cathodes.

We believe that the formation of H_2O_2 is the key factor leading to the poor cycling stability of LIBs with (HE-)NCM based cathodes once the potential of O_2 -release is exceeded, as the anodic oxidation of H_2O_2 leads to the formation of protons and/or water that can further react to HF with the common LiPF_6 conducting salt. This mechanistic understanding of $^1\text{O}_2$ reactions with the EC solvent likely explains the experimental observation that EC-free electrolytes have been found to greatly improve capacity retention for oxygen-releasing cathodes.

MATERIALS AND METHODS

On-line gassing analysis during the reaction of $^1\text{O}_2$ with EC and DMC

The reaction of singlet oxygen with EC and DMC (both battery grade, < 10 ppm H_2O , BASF, Germany) is studied in a set-up adapted from our cell design for on-line electrochemical mass spectrometry (OEMS).³⁵ Here, singlet oxygen ($^1\text{O}_2$) is produced in triplet oxygen ($^3\text{O}_2$) saturated solutions of EC or DMC using Rose bengal (RB, disodium salt, $>95\%$, Sigma Aldrich) as photosensitizer to form $^1\text{O}_2$ in solution from $^3\text{O}_2$. Exciting RB with light at 525 nm ultimately leads to the formation of unstable triplet state RB with an excitation energy of 42 kcal/mol,⁵⁴ which transfers its excitation energy to a nearby $^3\text{O}_2$ by promoting it to the first singlet state. RB was chosen due to: i) its sufficient solubility in carbonate solvents; ii) its high quantum yield in solution and efficiency to convert $^3\text{O}_2$ to $^1\text{O}_2$,⁵⁵ and, iii) its high chemical stability.⁵⁶ The RB powder was dried for 72 h at 130°C under vacuum in a glass-oven (Büchi, Switzerland), and solutions of 100 μM RB in EC and DMC were prepared in an Ar-filled glovebox (MBraun, < 0.1 ppm H_2O , < 0.1 ppm O_2) by stirring on a hot-plate for several days at 50°C (i.e., above the melting temperature of EC). The set-up for the on-line mass spectrometry (MS) measurements was assembled inside the glovebox to avoid contamination from ambient air.

For on-line MS analysis, the electrochemical cell of our OEMS set-up was replaced by a standard UV-Vis cuvette (square 10 mm bottom, 2 transparent sides, 4 ml volume, Spectrosil glass, Starna, Germany) that is connected via a GL-tube-fitting (PPS, Bola, Germany) to a metal fitting, which in turn connects directly to the MS via a flow-restricting capillary (at a standard flow rate of ~ 1 $\mu\text{l}/\text{min}$). The cuvette was filled with either 4 or 1 ml of the carbonate solutions with RB dye, leaving a head-space volume of either 2.7 or 5.7 ml, respectively, which can be purged with argon or oxygen. A 6 mm magnetic stirrer was added to induce some convective mixing. The cuvette is located in a non-

transparent plastic encasing that prevents unintended excitation of the photosensitizer and that holds 4 LEDs (two on either side of the cuvette) with a characteristic wavelength of 525 nm at a maximum power of 3 W each (at an operating voltage of 3 V). The LEDs are connected in series and placed onto cooling fins to remove most of the heat generated during illumination. The LED power supply cables, the metal tube connecting the cuvette with the MS capillary inlet and the gas flushing valves are fed through the encasing. For details of the assembled cell and its location in the encasing see Fig. S4. After assembly, the set-up is placed onto a magnetic stirrer inside a temperature chamber at 45°C (chosen to be above the EC melting point), the capillary is connected to the mass spectrometer, and the set-up is flushed with pure argon and left to equilibrate for 4 h before starting an experiment. During these 4 h, the leak tightness of the assembly is assured prior to each measurement by following the MS signal for nitrogen; the measured nitrogen leaks were also negligible ($<< 0.05$ μl over 10 h, corresponding to $<< 0.2$ nmol over 1 h, which is negligible compared the measured gas formation/consumption shown in Fig. 1) proving the tightness of the set-up.

After the 4 h rest period, a current of 400 mA was applied to the LEDs while the set-up is still under argon atmosphere. Any gassing observed at that point of the experiment could only be attributed to a possible reactivity of the excited photosensitizer with the carbonate solvent or simply to a change in vapor-pressure due to the slight temperature increase of the solution by the LEDs. The light was turned off after 1 h of illumination and the mass traces are recorded for another hour to observe any delayed detection of evolved gases and to deconvolute true gas generation from the reaction and vapor pressure changes. Subsequently, the set-up was flushed with 10% O_2 in argon and left for equilibration for another 3 h. Then, the RB dye was excited again for 1 h recording the MS signals, followed by another hour without illumination. Finally, the set-up was flushed with calibration gases to quantify the evolved and consumed gases. The evolution of CO_2 , CO, and O_2 are assigned to the mass traces at $m/z=44$, $m/z=28$ and $m/z=32$, respectively (note that the CO signal was corrected for the contributions from CO_2 to the $m/z=28$ channel as described previously³²). No MS signals other than those related to these three gases were observed upon reaction of $^1\text{O}_2$ with the carbonate solvents (other than the constant background signals from the DMC solvent). Quantification is executed by dividing all mass-traces with the ion current on $m/z=36$ corresponding to the argon isotope and flushing the set-up after the measurement with calibration gases containing 2000 ppm of CO_2 , CO, and O_2 in argon.

Analysis of the carbonate solutions after reaction with $^1\text{O}_2$

Ab initio calculations have revealed several expected reaction products that remain in solution. H_2O_2 was detected by $[\text{Ti}(\text{O}_2)]^{2+}$ complex formation following a standard procedure by the German Institute of Standardization.⁵⁷ In the

presence of H_2O_2 , this complex of pertitanic acid is formed from TiOSO_4 with a characteristic absorption around 410 nm (in water). 3 ml of the carbonate solution were taken from the cuvette after on-line MS analysis and mixed with 3 ml of an aqueous TiOSO_4 solution (1.9–2.1%, for determination of hydrogen peroxide (H 15), according to DIN 38 409, part 15, DEV-18, Sigma Aldrich, USA) under inert atmosphere. 1.5 ml of the mixture was given into a quartz cuvette (Spectrosil glass, Starna, Germany) with a 2 mm path length and analyzed in transmission mode between 700 and 200 nm in a UV-Vis Spectrometer (Lambda35, Perkin Elmer, USA) at a scan rate of 240 nm/min, averaging 2 scans. All spectra were compared to the base solution without radiation exposure to deconvolute the signals from the RB dye and the pertitanic acid.

Anodic electrochemical decomposition of H_2O_2

Experiments and simulations indicate that H_2O_2 is formed after double H-abstraction from the ethylene group of EC. To examine the electrochemical reactivity of H_2O_2 in the lithium-ion battery environment, linear scan voltammetry (LSV) on a carbon black electrode in DMC based electrolyte without and with H_2O or $\text{H}_2\text{O}_2/\text{H}_2\text{O}$ was performed. For this, we used our 2-compartment OEMS set-up, where a Li^+ -conducting glass-ceramic (LICGC, diameter 1 inch, thickness 150 μm , Ohara, Japan) separates the carbon black working-electrode compartment from the lithium metal counter-electrode compartment, assuring (i) that no cross-diffusion of gas and solution species can occur and (ii) that gases evolved at the counter-electrode are not detected by the mass spectrometer which is connected to the head-space of the carbon black working-electrode.¹⁴

37

The carbon black working-electrodes were based on Super C65 (BET = 63 m^2/g , Timcal, Switzerland) and polyvinylidene fluoride (PVdF, Kynar HSV900, Arkema, France) at a 1:1 weight ratio. Slurries of Super C65 and PVdF in N-methyl-2-pyrrolidone (Sigma Aldrich, 99.5 %) were coated onto a stainless steel mesh (SS316, aperture 26 μm , wire diameter 25 μm , The Mesh Company Ltd, UK). The final carbon loading of the punched out 15 mm diameter electrodes was $1.45 \pm 0.1 \text{ mg}/\text{cm}^2$, corresponding to a carbon BET surface area of $0.16 \pm 0.02 \text{ m}^2$ for each electrode. As electrolyte, 1.5 M LiPF_6 (battery grade, BASF, Germany) in DMC (DMC electrolyte) was chosen for these measurements due to its slower hydrolysis compared to EC.⁵⁸ Either pure H_2O or a solution of 50%_w H_2O_2 in H_2O (pure, AppliChem, ITW reagents, Germany) were added to the electrolyte for a resulting concentration of 550 ppm H_2O and $\text{H}_2\text{O}_2/\text{H}_2\text{O}$, respectively. For each experiment, 100 μl ($\approx 0.13 \text{ g}$) of one of the three different electrolytes (pure DMC electrolyte, DMC + H_2O and DMC + H_2O_2 + H_2O) were placed into the working-electrode compartment by dropping it onto a 17 mm diameter glass-fiber separator (GF, 250 μm Glass microfiber filter 691, VWR, Germany; dried for 3 days at 300°C in a Büchi vacuum oven) which was sandwiched between the Ohara glass separator and the carbon black working-electrode. The electrolytes were mixed directly

before cell assembly to minimize the extent of the hydrolysis reaction of the carbonate and the chemical decomposition of H_2O_2 . Lithium metal (17 mm diameter, 450 μm thickness, 99.9% purity; Rockwood Lithium, USA) was used as counter electrode with an additional GF separator filled with pure DMC electrolyte sandwiched between the lithium metal and the Ohara glass. The cell was assembled inside an Ar-filled glovebox, placed into a temperature chamber at 25°C, and connected to the mass spectrometer and a potentiostat (SP300, BioLogic, France). A single oxidative scan from OCV (ranging from 3.2–3.7 V vs Li^+/Li) to 5.2 V was measured at 0.2 mV/s after an initial 4 h OCV period to obtain a well-defined mass signal background.

Computational methods

The geometries of minima and transition states (TS) were optimized using density functional theory (DFT) with the UB3LYP functional and the 6-311++G(d,p) basis set. Every stationary point was verified by frequency calculations. The path between reactants and products via the corresponding TS was established by Internal Reaction Coordinate (IRC) calculations. To take into account non-dynamic and dynamic electron correlation, CASPT2 calculations were carried out at the optimized geometries. This is important for structures with multi-configurational character, here especially for the reaction with triplet oxygen. This way, CASPT2/ANO-L-VDZP energies were calculated, taking into account the zero point energy (ZPE) on DFT level of theory. The active space used for the oxygen molecule consists of eight electrons in six orbitals (CAS(8,6)), the active space for EC and VC was CAS(4,4) and CAS(2,2), respectively. The difference in the active space reflects the fact that different orbitals are involved in the consecutive reaction steps. In the case of EC, the σ - and σ^* -orbitals of the two C-H bonds cleaved in the reaction are necessary; for VC, the π - and π^* -orbital at the neighboring sp^2 carbons are the reactive part. In the same way, the TS of the di-H-abstraction (TS₁) is described by CAS(12,10), and the TS of the reaction of VC with oxygen (TS₂ and TS₃) by CAS(10,8). In case of CAS(12,10), state averaging was used over three states with a ratio of 90:5:5. DFT calculations were carried out with the program package Gaussian09⁵⁹ and Gaussian16⁶⁰. The CASPT2 calculations were performed with MOLCAS 8.2.⁶¹⁻⁶²

Ground state on-the-fly simulations were carried out for the reaction of VC and $^1\text{O}_2$, starting from the optimized TS structure with the program NewtonX 2.0.⁶³⁻⁶⁴ and its interface to Gaussian09. The nuclear motion was treated classically, while the electrons were treated quantum mechanically using the DFT functional UB3LYP and the basis set 6-311++G(d,p). For the time propagation, we used the Velocity Verlet integrator with a time step of 0.5 fs. The TS was chosen as starting point, as we are mainly interested in the products that can be formed. The trajectories were started with a kinetic energy of 1 kcal/mol along the reaction vector pointing toward the products. All 3N-5 other normal modes were sampled according to a Wigner distribution⁶⁵ for both positions and momenta for the temperature of

300 K. no individual trajectories were calculated and analyzed.

ASSOCIATED CONTENT

Supporting Information. Visualization of the active spaces used for the CASSCF/CASPT2 calculations, listing of optimized geometries for all minima and transition states, picture of on-line MS set-up with cuvette and experimental results concerning the chemical reactivity of vinylene carbonate with $^3\text{O}_2$.

AUTHOR INFORMATION

Corresponding Author

* anna.freiberg@tum.de

**regina.de_vivie@cup.uni-muenchen.de

Author Contributions

The manuscript was written through contributions of all authors. / All authors have given approval to the final version of the manuscript. / ‡These authors contributed equally.

ACKNOWLEDGMENT

We would like to thank Alexander Ogrodnik and Sophie Solchenbach from TUM for very fruitful discussions. M. K. Roos and R. de Vivie-Riedle gratefully acknowledge financial support by the Deutsche Forschungsgemeinschaft through the SFB749 and thank Patrick Kölle for contributions to the first calculations.

ABBREVIATIONS

CAM, cathode active material; DMC, dimethyl carbonate; EC, ethylene carbonate; LED, light emitting diode; LiB, lithium-ion battery; LSV, linear sweep voltammetry; MS, mass spectrometry/mass spectrometer; OCV, open circuit voltage; RB, Rose Bengal; SOC, state of charge; VC, vinylene carbonate; ZPC, zero point correction.

REFERENCES

- (1) Tarascon, J. M.; Armand, M., *Nature*, **2001**, *414*, 359-367.
- (2) Blomgren, G. E., *J. Electrochem. Soc.*, **2016**, *164*, A5019-A5025.
- (3) Dunn, B.; Kamath, H.; Tarascon, J. M., *Science*, **2011**, *334*, 928-935.
- (4) Gröger, O.; Gasteiger, H. A.; Suchsland, J.-P., *J. Electrochem. Soc.*, **2015**, *162*, A2605-A2622.
- (5) Andre, D.; Kim, S.-J.; Lamp, P.; Lux, S. F.; Maglia, F.; Paschos, O.; Stiaszny, B., *J. Mater. Chem. A*, **2015**, *3*, 6709-6732.
- (6) Yabuuchi, N.; Makimura, Y.; Ohzuku, T., *J. Electrochem. Soc.*, **2007**, *154*, A314.
- (7) Gallagher, K. G.; Goebel, S.; Greszler, T.; Mathias, M.; Oelerich, W.; Eroglu, D.; Srinivasan, V., *Energy Environ. Sci.*, **2014**, *7*, 1555.
- (8) Noh, H.-J.; Yoon, S.; Yoon, C. S.; Sun, Y.-K., *J. Power Sources*, **2013**, *233*, 121-130.
- (9) Rozier, P.; Tarascon, J. M., *J. Electrochem. Soc.*, **2015**, *162*, A2490-A2499.
- (10) Buchberger, I.; Seidlmayer, S.; Pokharel, A.; Piana, M.; Hattendorff, J.; Kudejova, P.; Gilles, R.; Gasteiger, H. A., *J. Electrochem. Soc.*, **2015**, *162*, A2737-A2746.
- (11) Zheng, H.; Sun, Q.; Liu, G.; Song, X.; Battaglia, V. S., *J. Power Sources*, **2012**, *207*, 134-140.
- (12) Jung, R.; Metzger, M.; Maglia, F.; Stinner, C.; Gasteiger, H. A., *J. Electrochem. Soc.*, **2017**, *164*, A1361-A1377.
- (13) Petibon, R.; Xia, J.; Ma, L.; Bauer, M. K. G.; Nelson, K. J.; Dahn, J. R., *J. Electrochem. Soc.*, **2016**, *163*, A2571-A2578.
- (14) Metzger, M.; Strehle, B.; Solchenbach, S.; Gasteiger, H. A., *J. Electrochem. Soc.*, **2016**, *163*, A798-A809.
- (15) Wandt, J.; Freiberg, A.; Thomas, R.; Gorlin, Y.; Siebel, A.; Jung, R.; Gasteiger, H. A.; Tromp, M., *J. Mater. Chem. A*, **2016**, *4*, 18300-18305.
- (16) Gallus, D. R.; Schmitz, R.; Wagner, R.; Hoffmann, B.; Nowak, S.; Cekic-Laskovic, I.; Schmitz, R. W.; Winter, M., *Electrochim. Acta*, **2014**, *134*, 393-398.
- (17) Gilbert, J. A.; Shkrob, I. A.; Abraham, D. P., *J. Electrochem. Soc.*, **2017**, *164*, A389-A399.
- (18) Pieczonka, N. P. W.; Liu, Z.; Lu, P.; Olson, K. L.; Mootz, J.; Powell, B. R.; Kim, J.-H., *The Journal of Physical Chemistry C*, **2013**, *117*, 15947-15957.
- (19) Xiong, D. J.; Ellis, L. D.; Li, J.; Li, H.; Hynes, T.; Allen, J. P.; Xia, J.; Hall, D. S.; Hill, I. G.; Dahn, J. R., *J. Electrochem. Soc.*, **2017**, *164*, A3025-A3037.
- (20) Strehle, B.; Kleiner, K.; Jung, R.; Chesneau, F.; Mendez, M.; Gasteiger, H. A.; Piana, M., *J. Electrochem. Soc.*, **2017**, *164*, A400-A406.
- (21) Armstrong, A. R.; Holzapfel, M.; Novák, P.; Johnson, C. S.; Kang, S.-H.; Thackeray, M. M.; Bruce, P. G., *J. Am. Chem. Soc.*, **2006**, *128*, 8694-8698.
- (22) La Mantia, F.; Rosciano, F.; Tran, N.; Novák, P., *J. Appl. Electrochem.*, **2008**, *38*, 893-896.
- (23) Guéguen, A.; Streich, D.; He, M.; Mendez, M.; Chesneau, F. F.; Novák, P.; Berg, E. J., *J. Electrochem. Soc.*, **2016**, *163*, A1095-A1100.
- (24) Bak, S.-M.; Hu, E.; Zhou, Y.; Yu, X.; Senanayake, S. D.; Cho, S.-J.; Kim, K.-B.; Chung, K. Y.; Yang, X.-Q.; Nam, K.-W., *ACS Applied Materials & Interfaces*, **2014**, *6*, 22594-22601.
- (25) Jung, S.-K.; Gwon, H.; Hong, J.; Park, K.-Y.; Seo, D.-H.; Kim, H.; Hyun, J.; Yang, W.; Kang, K., *Adv. Ener. Mat.*, **2014**, *4*, 1300787.
- (26) Xu, B.; Fell, C. R.; Chi, M.; Meng, Y. S., *Energy Environ. Sci.*, **2011**, *4*, 2223.
- (27) Teufl, T.; Strehle, B.; Müller, P.; Gasteiger, H. A.; Mendez, M. A., *submitted for publication*, **2018**.
- (28) Wandt, J.; Freiberg, A. T. S.; Ogrodnik, A.; Gasteiger, H. A., *Mater. Today*, **2018**.
- (29) Xia, J.; Glazier, S. L.; Petibon, R.; Dahn, J. R., *J. Electrochem. Soc.*, **2017**, *164*, A1239-A1250.
- (30) Ma, L.; Glazier, S. L.; Petibon, R.; Xia, J.; Peters, J. M.; Liu, Q.; Allen, J.; Doig, R. N. C.; Dahn, J. R., *J. Electrochem. Soc.*, **2016**, *164*, A5008-A5018.
- (31) Xia, J.; Petibon, R.; Xiong, D.; Ma, L.; Dahn, J. R., *J. Power Sources*, **2016**, *328*, 124-135.
- (32) Xu, K.; Ding, S. P.; Jow, T. R., *J. Electrochem. Soc.*, **1999**, *146*, 4172.
- (33) Zhang, X.; Pugh, J. K.; Ross, P. N., *J. Electrochem. Soc.*, **2001**, *148*, E183.
- (34) Xing, L.; Li, W.; Wang, C.; Gu, F.; Xu, M.; Tan, C.; Yi, J., *J. Phys. Chem. B*, **2009**, *113*, 16596-602.
- (35) Tsiouvaras, N.; Meini, S.; Buchberger, I.; Gasteiger, H. A., *J. Electrochem. Soc.*, **2013**, *160*, A471-A477.
- (36) Kolar, P.; Nakata, H.; Shen, J. W.; Tsuboi, A.; Suzuki, H.; Ue, A., *Fluid Phase Equilib.*, **2005**, *228*, 59-66.

(37)Strehle, B.; Solchenbach, S.; Metzger, M.; Schwenke, K. U.; Gasteiger, H. A., *J. Electrochem. Soc.*, **2017**, *164*, A2513-A2526.

(38)Steele, W. V.; Chirico, R. D.; Knipmeyer, S. E.; Nguyen, A.; Smith, N. K.; Tasker, I. R., *Journal of Chemical & Engineering Data*, **1996**, *41*, 1269-1284.

(39)Pokorný, V.; Štejša, V.; Fulem, M.; Červinka, C.; Růžička, K., *Journal of Chemical & Engineering Data*, **2017**, *62*, 4174-4186.

(40)Maranzana, A.; Ghigo, G.; Tonachini, G., *J. Am. Chem. Soc.*, **2000**, *122*, 1414-1423.

(41)Sevin, F.; McKee, M. L., *J. Am. Chem. Soc.*, **2001**, *123*, 4591-4600.

(42)Ogilby, P. R.; Foote, C. S., *J. Am. Chem. Soc.*, **1983**, *105*, 3423-3430.

(43)Tonachini, G.; Schlegel, H. B.; Bernardi, F.; Robb, M. A., *J. Am. Chem. Soc.*, **1990**, *112*, 483-491.

(44)Yoshioka, Y.; Yamada, S.; Kawakami, T.; Nishino, M.; Yamaguchi, K.; Saito, I., *Bull. Chem. Soc. Jpn.*, **1996**, *69*, 2683-2699.

(45)Park, K.; West, A.; Raheja, E.; Sellner, B.; Lischka, H.; Windus, T. L.; Hase, W. L., *J. Chem. Phys.*, **2010**, *133*, 184306.

(46)Langer, R. Method for Storing and Transporting Vinylene Carbonate. US 2009/0131687 A1, May 21, 2009.

(47)Deadman, B. J.; Hellgardt, K.; Hii, K. K., *Reaction Chemistry & Engineering*, **2017**, *2*, 462-466.

(48)Pritzl, D.; Solchenbach, S.; Wetjen, M.; Gasteiger, H. A., *J. Electrochem. Soc.*, **2017**, *164*, A2625-A2635.

(49)Barlowz, C. G., *Electrochem. Solid-State Lett.*, **1999**, *2*, 362.

(50)Strmcnik, D.; Castelli, I. E.; Connell, J. G.; Haering, D.; Zorko, M.; Martins, P.; Lopes, P. P.; Genorio, B.; Østergaard, T.; Gasteiger, H. A.; Maglia, F.; Antonopoulos, B. K.; Stamenkovic, V. R.; Rossmeisl, J.; Markovic, N. M., *Nature Catalysis*, **2018**, *1*, 255-262.

(51)Solchenbach, S.; Metzger, M.; Egawa, M.; Beyer, H.; Gasteiger, H. A., *to be submitted*, **2018**.

(52)Metzger, M.; Marino, C.; Sicklinger, J.; Haering, D.; Gasteiger, H. A., *J. Electrochem. Soc.*, **2015**, *162*, A1123-A1134.

(53)Bratsch, S. G., *J. Phys. Chem. Ref. Data*, **1989**, *18*, 1-21.

(54)Redmond, R. W.; Gamlin, J. N., *Photochem. Photobiol.*, **1999**, *70*, 391-475.

(55)DeRosa, M., *Coord. Chem. Rev.*, **2002**, *233-234*, 351-371.

(56)Kochevar, I. E.; Redmond, R. W., *Methods Enzymol.*, **2000**, *319*, 20-8.

(57)Schwenke, K. U.; Metzger, M.; Restle, T.; Piana, M.; Gasteiger, H. A., *J. Electrochem. Soc.*, **2015**, *162*, A573-A584.

(58)Pacheco, M. A.; Marshall, C. L., *Energy & Fuels*, **1997**, *11*, 2-29.

(59)Frisch, M. J.; Trucks, G. W.; Schlegel, H. B.; Scuseria, G. E.; Robb, M. A.; Cheeseman, J. R.; Scalmani, G.; Barone, V.; Mennucci, B.; Petersson, G. A.; Nakatsuji, H.; Caricato, M.; Li, X.; Hratchian, H. P.; Izmaylov, A. F.; Bloino, J.; Zheng, G.; Sonnenberg, J. L.; Hada, M.; Ehara, M.; Toyota, K.; Fukuda, R.; Hasegawa, J.; Ishida, M.; Nakajima, T.; Honda, Y.; Kitao, O.; Nakai, H.; Vreven, T.; Montgomery, J. A. J.; Peralta, J. E.; Ogliaro, F.; Bearpark, M. J.; Heyd, J. J.; Brothers, E. N.; Kudin, K. N.; Staroverov, V. N.; Kobayashi, R.; Normand, J.; Raghavachari, K.; Rendell, A. P.; Burant, J. C.; Iyengar, S. S.; Tomasi, J.; Cossi, M.; Rega, N.; Millam, J. M.; Klene, M.; Knox, J. E.; Cross, J. B.; Bakken, V.; Adamo, C.; Jaramillo, J.; Gomperts, R.; Stratmann, R. E.; Yazyev, O.; Austin, A. J.; Cammi, R.; Pomelli, C.; Ochterski, J. W.; Martin, R. L.; Morokuma, K.; Zakrzewski, V. G.; Voth, G. A.; Salvador, P.; Dannenberg, J. J.; Dapprich, S.; Daniels, A. D.; Farkas, O.; Foresman, J. B.; Ortiz, J. V.; Cioslowski, J.; Fox, D. J., Gaussian, Inc., Wallingford, CT (2009).

(60)Frisch, M. J.; Trucks, G. W.; Schlegel, H. B.; Scuseria, G. E.; Robb, M. A.; Cheeseman, J. R.; Scalmani, G.; Barone, V.; Petersson,

G. A.; Nakatsuji, H.; Li, X.; Caricato, M.; Marenich, A. V.; Bloino, J.; Janesko, B. G.; Gomperts, R.; Mennucci, B.; Hratchian, H. P.; Ortiz, J. V.; Izmaylov, A. F.; Sonnenberg, J. L.; Williams-Young, D.; Ding, F.; Lipparini, F.; Egidi, F.; Goings, J.; Peng, B.; Petrone, A.; Henderson, T.; Ranasinghe, D.; Zakrzewski, V. G.; Gao, J.; Rega, N.; Zheng, G.; Liang, W.; Hada, M.; Ehara, M.; Toyota, K.; Fukuda, R.; Hasegawa, J.; Ishida, M.; Nakajima, T.; Honda, Y.; Kitao, O.; Nakai, H.; Vreven, T.; Throssell, K.; Montgomery, J. A. J.; Peralta, J. E.; Ogliaro, F.; Bearpark, M. J.; Heyd, J. J.; Brothers, E. N.; Kudin, K. N.; Staroverov, V. N.; Keith, T. A.; Kobayashi, R.; Normand, J.; Raghavachari, K.; Rendell, A. P.; Burant, J. C.; Iyengar, S. S.; Tomasi, J.; Cossi, M.; Millam, J. M.; Klene, M.; Adamo, C.; Cammi, R.; Ochterski, J. W.; Martin, R. L.; Morokuma, K.; Farkas, O.; Foresman, J. B.; Fox, D. J., Gaussian, Inc., Wallingford, CT (2016).

(61)Aquilante, F.; Autschbach, J.; Carlson, R. K.; Chibotaru, L. F.; Delcey, M. G.; De Vico, L.; Fdez Galvan, I.; Ferre, N.; Frutos, L. M.; Gagliardi, L.; Garavelli, M.; Giussani, A.; Hoyer, C. E.; Li Manni, G.; Lischka, H.; Ma, D.; Malmqvist, P. A.; Muller, T.; Nenov, A.; Olivucci, M.; Pedersen, T. B.; Peng, D.; Plasser, F.; Pritchard, B.; Reiher, M.; Rivalta, I.; Schapiro, I.; Segarra-Marti, J.; Stenrup, M.; Truhlar, D. G.; Ungur, L.; Valentini, A.; Vancoillie, S.; Veryazov, V.; Vysotskiy, V. P.; Weingart, O.; Zapata, F.; Lindh, R., *J. Comput. Chem.*, **2016**, *37*, 506-41.

(62)Vancoillie, S.; Delcey, M. G.; Lindh, R.; Vysotskiy, V.; Malmqvist, P. A.; Veryazov, V., *J. Comput. Chem.*, **2013**, *34*, 1937-48.

(63)Barbatti, M.; Ruckebauer, M.; Plasser, F.; Pittner, J.; Granucci, G.; Persico, M.; Lischka, H., *Wiley Interdisciplinary Reviews: Computational Molecular Science*, **2014**, *4*, 26-33.

(64)Barbatti, M.; Granucci, G.; Ruckebauer, M.; Plasser, F.; Crespo-Otero, R.; Pittner, J.; Persico, M.; Lischka, H., (2016), www.newtonx.org.

(65)Barbatti, M.; Aquino, A. J. A.; Lischka, H., *Phys. Chem. Chem. Phys.*, **2010**, *12*, 4959-4967.

TOC figure



Chapter 5.

Summary and outlook

In this thesis the reaction dynamics of various organic molecules with applications in kinetic studies, labeling and as battery electrolytes was investigated. The first two chapters were concerned with diphenylmethyl compounds used for reactivity studies and the quantum dynamics (QD) simulation of their bond cleavage. The third chapter discussed two molecules with elongated π system important for labeling. In the fourth chapter two common solvents used in lithium-ion batteries were tested for their reactivity towards singlet oxygen ($^1\text{O}_2$).

In the first chapter of this thesis, the concept of adapted reactive coordinates (aRCs) based on the Wilson G-matrix method was presented. It is a coordinate system to perform QD in reduced dimensionality, which includes the relaxation of non-reactive background coordinates. As first step, the most important reactive internal coordinates to describe the reaction were identified. In a second step major changes of further non-reactive coordinates were recorded using a minimum energy path (MEP), which were then fitted to the reactive coordinates. In this way, geometries could be constructed which were approximately relaxed without performing optimizations at each grid point. On the one hand, the computational cost is, thus, dramatically reduced as only single-point calculations have to be performed. On the other hand, unphysical discontinuities in the G-matrix are avoided. Comparative QD simulations for the bond cleavage of $\text{Ph}_2\text{CH}-\text{PPh}_3^+$ clearly demonstrated how the path of the wave packet is changed, if the background relaxation is included in the G-matrix or not. Without relaxation the propagation time to reach a conical intersection (CoIn) responsible for the formation of the experimental product was vastly prolonged.

In the second chapter of this thesis, the coordinate system from chapter 1 was used to simulate the initial photoinduced bond cleavage of diphenylmethyl chloride ($\text{Ph}_2\text{CH}-\text{Cl}$) and diphenylmethyl bromide ($\text{Ph}_2\text{CH}-\text{Br}$) with two-dimensional QD. In both molecules, the initial excitation leads to a local $\pi\pi^*$ state on one phenyl ring. Near the Franck-Condon region a three-state conical intersection (CoIn) seam is located, formed by the $\pi\pi^*$ and the lone pair states facilitating a direct connection with the heterolytic dissociation channel. A second CoIn—a two-state one—at larger bond length r opens up the homolytic channel. In both cases, wave packet motion through both consecutive CoIns was observed, delay times in good agreement with the experimental results were extracted, and the radical pair identified as main product. For $\text{Ph}_2\text{CH}-\text{Cl}$ the transient absorption signal was modeled from the wave packet data taking into account the experimental temporal resolution. With this, the assignment of the signals to the respective products was confirmed. While the second coordinate d_{py} —a measure for the pyramidalization of the central carbon atom—was of limited importance for $\text{Ph}_2\text{CH}-\text{Cl}$, it played a key role for $\text{Ph}_2\text{CH}-\text{Br}$, evident in the form of the minima and the emerging oscillations of the wave packet in this coordinate. Therefore, non-adiabatic mixed quantum-classical dynamics (MQCD) was additionally employed for $\text{Ph}_2\text{CH}-\text{Br}$ to specifically investigate the role of vibrations, further motivated by small-amplitude oscillations of the experimental signals. Spec-

trograms calculated from the trajectory geometries pointed to significant differences between the product channels. Further analysis of the motion of the wave packet in the QD found a vibration in the S_1 minimum, which was deemed responsible for the experimental oscillations. The comparison of all these results to the dynamics of $\text{Ph}_2\text{CH}-\text{PPh}_3^+$ published before revealed the strong influence of the leaving group on the excited states and, thus, the reaction dynamics.

The third chapter was devoted to the photophysics of elongated π systems in organic molecules. In the first part of this chapter the polycyclic hydrocarbon pyrene was investigated. The ultrafast relaxation from the bright 1L_a state to the fluorescent 1L_b state was simulated with two complementary dynamical methods, both based on the same carefully chosen QC description. For the QD a two-dimensional subspace generated from displacement vectors was used, relying on the Wilson G-matrix method as formulation of the kinetic part of the Hamiltonian. The passing of the wave packet through the CoIn backed the relaxation mechanism postulated in the literature. Full-dimensional non-adiabatic MQCD revealed a similar picture as the wave packet dynamics. Many back and forth hopping events underlined the strong coupling between the states even far from the CoIn. Fitted time constants verified the time scale of the reaction determined by transient absorption spectroscopy. The 1L_b state emerged as the mainly populated state in the end. A thorough analysis of the trajectory geometries further legitimated the dimensionality reduction done for the QD. Overall, both methods gave a clear and concise picture of the occurring relaxation process.

In the second part of chapter 3 the dimerization of Cyanine 3 (Cy3) dyes was investigated. These were covalently attached to DNA strands which acted as a scaffold. *Ab initio* calculations on a model system helped assigning a blue-shifted absorption signal to the formation of H-aggregates. Experimental circular dichroism (CD) spectroscopy and theoretical molecular dynamics (MD) simulations were employed to further characterize these aggregates, revealing a structure where the dye molecules are slightly rotated against each other. This study demonstrated that DNA can indeed be used as scaffold to artificially create dimers by defined changes of the distance between the dyes. Therefore, DNA can be added to the tool box of nano-optical components.

In the final chapter of this thesis, the chemical stability of the electrolytes ethylene carbonate (EC) and dimethyl carbonate (DMC) used in lithium-ion batteries towards $^1\text{O}_2$ was experimentally and theoretically investigated. From previous studies it is known that $^1\text{O}_2$ is released from specific cathode active materials (CAMs) like NCM for high state of charge (SOC). To prove its detrimental effect, $^1\text{O}_2$ was generated with the help of a photosensitizer in the pure electrolyte leading to the evolution of carbon dioxide (CO_2) in the case of EC, whereas DMC showed no reaction. *Ab initio* calculations suggested a concerted mechanism, which involved the ethylene moiety and lead to vinylene carbonate (VC) and hydrogen peroxide (H_2O_2) by double hydrogen abstraction. Ground state MQCD trajectories confirmed the further decay of VC to CO_2 . The detection of the theoretically proposed H_2O_2 by colorimetric experiments in solution proved the mechanism and demonstrated the strength of the collaborative *modus operandi*. Furthermore, the decay of H_2O_2 in an aprotic solvent was studied. It lead to the formation of water and free protons, both reacting with the lithium salt LiPF_6 to hydrofluoric acid, which is highly detrimental for the cycling of a battery. Altogether, it became apparent that the stability towards $^1\text{O}_2$ must not be overlooked in the search for new electrolytes.

Overall, in this thesis very different light-induced reactions from a multitude of applications were studied with QD and MQCD methods. Applied correctly both methods were able to elucidate the occurring processes at a microscopic level and in this way

contribute to a deeper understanding of these reactions. Furthermore, the synergy of both methods could be used to assess the effect of the reduced dimensionality. The results simultaneously showed that MQCD methods had not the ability to catch and explain all details, as they lack the character of a wave packet. If this character is decisive for the results, only true quantum methods as QD will prevail.

Appendix A.

The ONIOM method and its implementation

In the following sections, first a short introduction to the ONIOM method is given, then remarks on the specific implementations concerning different applications of the method are stated. The name and location of the specific codebase are given and the design decisions are shortly explained.

Short introduction to the ONIOM method

The well established [37] “our own n -layered integrated molecular orbital and molecular mechanics” (ONIOM) method was formulated by Morokuma and co-workers [32] based on already known hybrid methods [140, 141] to now combine an arbitrary number n of layers at different levels of theory, whereby here only $n = 2$ is considered. Like QM/MM it is devoted to the idea that only the reactive center has to be treated with the most accurate method. Unlike QM/MM it is an extrapolative scheme, replacing the calculation for the complete, here named real system at the high level of theory with three calculations, two for the smaller model system and one for the real system, but only at a low level of theory. The ONIOM energy E^{ONIOM} can then be calculated as follows:

$$E^{ONIOM} = E_{model}^{high} + E_{real}^{low} - E_{model}^{low}. \quad (\text{A.1})$$

While additive QM/MM can only combine quantum mechanics and molecular mechanics method, it is a unique advantage of ONIOM [37, 142] to allow more freedom in the choice of the low level method. Besides ONIOM with molecular mechanics [142–144] a combination of different QC methods as ONIOM(QC:QC) is feasible, which is the scope of ONIOM for this thesis. The coupling between the region only treated at low level of theory (low-level region) and the high-level region is in eq. A.1 automatically included at the low level of theory. In ONIOM(QC:QC) this already includes such electronic effects as polarization or charge transfer; strategies for a full electronic embedding are described in the literature [145, 146].

For building the model system, often covalent bonds have to be cut. An established method is the introduction of link atoms [33, 34], where hydrogen atoms cap all dangling bonds. A scaling factor is used to calculate the positions of the link atoms (see following section), setting the geometry of the model system in a functional dependence from the real system. As a consequence, no degree of freedom is added or lost in this procedure and, thus, the potential energy and its derivatives are well-defined [33, 142]. While the method is not intended to reproduce the absolute energy of the real system at the high-level method, it yields reliable energy differences [37].

Excited states can be treated with ONIOM as well. If the excitation can be seen as localized on the model system, the constraint low-level state (CLS) approximation [36] can be used and the energy of the excited state E^* is written as:

$$E^{*,ONIOM} \approx E_{model}^{*,high} + E_{real}^{low} - E_{model}^{low}. \quad (\text{A.2})$$

This approximation implies that the coupling between the high-level and low-level regions is state-independent.

A flexible ONIOM implementation interfacing various program packages

For the calculation of the PESs used in the QD simulations of chapter 1 and 2 of this thesis, a flexible implementation of the ONIOM code was developed. It is written in PERL5 and allows single-point calculations for a given set of geometries. Program options are chosen by an input file. Implemented are interfaces for the program packages GAUSSIAN09 [69], MOLPRO2012 [68], and MOLCAS7.8 [147].

After initializing the program starts a loop over all found geometries. In every loop the geometry is loaded, `scale_brokenbond()` builds the model system out of it (see comments below) and `get_energy()` is called three times, for each of the three necessary calculations. The latter subroutine is the key point of the algorithm. For each implemented program package, specific routines for generating the input, running the calculation, and reading the energy from the output file are called. For the addition of further methods or even program packages, only this central routine and the respective subroutines have to be changed or new ones added. After finishing the loop over all geometries, the ONIOM energies are calculated in `digest_oniom()` and written to `epot_ONIOM`. As the design decision with a loop already suggests, all calculations are performed in a serial manner. Two files, `ONIOM.log` and `shell.log`, log the run of the program.

Note that the atoms of the model system always have to be at the beginning of the geometry and that the code can handle the cutting of more than one covalent bond. This is realized by calling `scale_brokenbond()` multiple times, once for each inserted link atom. In this subroutine, first the nature of the cut bond is determined by the atoms forming it. Hence, a scaling factor g is chosen to reduce the length of the original A-B bond for the new A-H bond. The position r_H of the link atom can then be calculated from the positions of A and B (r_A , r_B) by:

$$r_H = r_A + g \cdot (r_B - r_A). \quad (\text{A.3})$$

At the moment, specific scaling factors are only implemented for C-C (0.709) and C-P (0.754) bonds according to the literature [33, 34], for other bonds 0.709 is used with a warning in the log files. Other g factors are conceivable by ratios of sums of covalent radii [33].

The codebase can be found in its own GIT repository on `/netfs`. A detailed documentation is found on the group's own wiki.

Optimizations in the ONIOM framework

The ONIOM energy is, like stated above, well-defined, enabling optimizations in the ONIOM framework. Based on eq. A.1, the energy can be rewritten as:

$$E^{ONIOM}(\mathbf{R}) = E_{model}^{high}(\mathbf{R}_{model}) + E_{real}^{low}(\mathbf{R}) - E_{model}^{low}(\mathbf{R}_{model}). \quad (\text{A.4})$$

Here, the geometry which the respective energy depends on is indicated in brackets, \mathbf{R} for the real system and \mathbf{R}_{model} for the model system. The gradient can now be also

written as a sum [33, 37]:

$$\frac{\partial E^{ONIOM}(\mathbf{R})}{\partial \mathbf{R}} = \frac{\partial E_{model}^{high}(\mathbf{R}_{model})}{\partial \mathbf{R}} + \frac{\partial E_{real}^{low}(\mathbf{R})}{\partial \mathbf{R}} - \frac{\partial E_{model}^{low}(\mathbf{R}_{model})}{\partial \mathbf{R}}. \quad (\text{A.5})$$

With the Jacobian $\mathbf{J} = \partial \mathbf{R}_{model} / \partial \mathbf{R}$ responsible for the transformation between the coordinate systems (details see below), the chain rule can be applied:

$$\frac{\partial E^{ONIOM}(\mathbf{R})}{\partial \mathbf{R}} = \frac{\partial E_{model}^{high}(\mathbf{R}_{model})}{\partial \mathbf{R}_{model}} \cdot \mathbf{J} + \frac{\partial E_{real}^{low}(\mathbf{R})}{\partial \mathbf{R}} - \frac{\partial E_{model}^{low}(\mathbf{R}_{model})}{\partial \mathbf{R}_{model}} \cdot \mathbf{J}. \quad (\text{A.6})$$

This formula implies that the gradients can be calculated separately for the respective number of atoms and the Jacobian provides the additional degrees of freedom for the model system calculations.

The implementation of `qext_oniom.pl` in PERL5 combines two different projects: On the one hand, the ONIOM program mentioned above, on the other hand the *Gaus-External* interface developed and used in the group. This interface allows optimizations using the “Berny algorithm” of GAUSSIAN with energies and gradients of any desired QC code. Ironically, it is docking on the ONIOM interface of GAUSSIAN itself. As the unchanged ONIOM code from the section above is called, the input is also identical. The input for the called QC program packages has to contain commands to calculate the gradient of the desired state. The code to readout the respective gradients is included in `qext_oniom.pl` for GAUSSIAN, MOLPRO and MOLCAS. The script `qext_oniom.pl` is called in the following manner:

```
qext_oniom.pl gaussian.com input_oniom <state>
```

with `gaussian.com` being the name of the GAUSSIAN input file containing the call of the external file `gau_external` and the starting geometry; `input_oniom` the input for the ONIOM program; followed by the number of the state to be optimized (ground state = 1).

Let us take a closer look at the Jacobian \mathbf{J} . Following the definition of the link atom in eq. A.3, the derivatives in the Jacobian for the atoms A and B yield:

$$\frac{\partial r_H}{\partial r_A} = 1 - g, \quad (\text{A.7})$$

$$\frac{\partial r_H}{\partial r_B} = g. \quad (\text{A.8})$$

In the code, the Jacobian is not used in its matrix form, but the gradients are added up accordingly, like the following pseudo code shows:

```
grad_A_oniom = grad_A_low_real + grad_A_high_model - grad_A_low_model
grad_B_oniom = grad_B_low_real
for all link atoms
  find scaling factor g according to bond A-B
  grad_H_diff = grad_H_high_level - grad_H_low_level
  grad_A_oniom = grad_A_oniom + grad_H_diff * (1-g)
  grad_B_oniom = grad_B_oniom + grad_H_diff * g
```

It is important to mark at this point: As the gradients of different calculations and program packages are added up, all must be in the same orientation to produce meaningful results. Since the geometries are in the same orientation, it is essential to prevent program packages from any kind of “standard orientation”. In GAUSSIAN this

can be done by “IOp(2/15=21)”, in MOLPRO by “orient,noorient;”, which is the default for XYZ input. This remark is also important for the following sections.

The codebase is included in the GIT repository for PERL in the `GausExternal` folder. A short documentation for the optimization with ONIOM is included on the ONIOM wiki page.

Conical intersections in ONIOM

A special group of geometry points are CoIns. Like minima or TSs CoIns can also occur in ONIOM calculations. For the optimization of a CoIn in ONIOM, Bearpark and co-workers suggested in their pioneering work [35, 36] a modified version of the established projected gradient method [148]. Their work is concerned with finding CoIns in ONIOM(QC:QC), in the literature also methods are reported for CoIn optimizations in ONIOM(QC:MM) [149].

Bearpark *et al.* employ the CLS approximation and use the gradient difference \mathbf{x} and the derivative coupling \mathbf{y} between the states of interest a, b of the high-level calculation:

$$\mathbf{x}_{model}^{high} = \frac{\partial(E_{model}^{b,high} - E_{model}^{a,high})}{\partial \mathbf{R}_{model}} \mathbf{J}, \quad (\text{A.9})$$

$$\mathbf{y}_{model}^{high} = \frac{\langle \mathbf{C}_a | \partial \hat{H}_{model}^{high} | \mathbf{C}_b \rangle}{\partial \mathbf{R}_{model}} \mathbf{J}. \quad (\text{A.10})$$

Here, $E_{model}^{a,high}$ and $E_{model}^{b,high}$ are the adiabatic energies for states a and b , \mathbf{C} are the CI eigenvectors and \hat{H} the electronic Hamiltonian. As before, the Jacobian \mathbf{J} transforms the matrices and considers the introduction of the link atoms. These two vectors \mathbf{x} and \mathbf{y} span the branching space [17] and distortions along these vectors lift the degeneracy.

The modified gradient $\tilde{\mathbf{g}}^{ONIOM}$ for the optimization consists of two parts:

$$\tilde{\mathbf{g}}^{ONIOM} = \mathbf{f} + \mathbf{g}_{IS}. \quad (\text{A.11})$$

With the first part \mathbf{f} the energy difference in the branching space is minimized:

$$\mathbf{f} = 2(E_{model}^{b,high} - E_{model}^{a,high}) \frac{\mathbf{x}_{model}^{high}}{|\mathbf{x}_{model}^{high}|}. \quad (\text{A.12})$$

The second part \mathbf{g}_{IS} consists of the intersection space gradient, which is orthogonal to the branching space and preserves the degeneracy. It can be calculated from the gradient of the upper state by projection:

$$\mathbf{g}_{IS} = \mathbf{P}' \frac{\partial E^{b,ONIOM}}{\partial \mathbf{R}}. \quad (\text{A.13})$$

The projection matrix \mathbf{P}' is given by

$$\mathbf{P}' = \mathbf{1} - \mathbf{A}(\mathbf{A}^T \mathbf{A})^{-1} \mathbf{A}^T \quad (\text{A.14})$$

with \mathbf{A} being a matrix containing $\mathbf{x}_{model}^{high}$ and $\mathbf{y}_{model}^{high}$ as columns.

At this point some thoughts should be put into the choice of methods. In ONIOM applications, often single-determinant methods like Hartree-Fock or DFT are used as low-level method [34, 36, 114]. This choice might turn out to be problematic if a S_0/S_1 CoIn occurs, because at such a point these methods do not yield a reliable

QC description [150]. Especially the term E_{model}^{low} in the energy expression (eq. A.1) is problematic, because the branching space is optimized for the model system only (eq. A.12). The other low-level term E_{real}^{low} is less determined to fail, as for the real system, the degeneracy of the CoIn in the model system tends to be lifted by the atoms in the low-level region. Furthermore, for a more accurate electronic description, the chosen low-level method has to match the character of the ground state in the high-level calculation [34, 36], which is possible by using open-shell, unrestricted or higher spin multiplicity solutions. It is essential for the ONIOM approximation to employ qualitatively the same wave function for real and model system [36].

The implementation in `qext_oniom_coin.pl` is a direct extension of the ONIOM optimization discussed before. The script is called analogously as stated above:

```
qext_oniom_coin.pl gaussian.com input_oniom <state>
```

where the number of the upper state has to be used. For tracking the progress of the optimization, the resulting gradient $\tilde{\mathbf{g}}^{ONIOM}$ and the energy difference $E_{model}^{b,high} - E_{model}^{a,high}$ are printed in each step. It is important that the latter value always stays positive. In case of convergence issues, the use of a steepest descent approach with slightly looser convergence criteria in GAUSSIAN (`opt=(steep, loose)`) is promising. GAUSSIAN is supported for low-level calculations, MOLPRO for both high- and low-level calculations.

The Jacobian \mathbf{J} is explicitly constructed by the routine `buildJacobian()`. The matrix is of the dimension $3N_{model} \times 3N$, where N_{model} and N are the number of atoms for the model and for the real system, respectively. It is sparse to a high degree, as it resembles a rectangular diagonal matrix with mostly "1" on the diagonal except for the link atoms. The only non-zero off-diagonal elements are the ones for the atoms the link atoms are bound to.

The codebase is included in the GIT repository for PERL in the `GausExternal` folder.

Vibrational analysis in the ONIOM framework

If an optimized geometry point is a true critical point can be verified by a vibrational analysis. For this analysis the Hessian containing the second derivatives along all coordinates is necessary. For the mass-weighted Hessian the eigenvectors correspond to normal modes. The vibrational modes are given by the square roots of the eigenvalues, disregarding translational and rotational modes with zero eigenvalue. For the ONIOM method the Hessian can be built as a sum like energy and gradients [33]:

$$\frac{\partial^2 E^{ONIOM}(\mathbf{R})}{\partial \mathbf{R}^2} = \mathbf{J}^T \cdot \frac{\partial^2 E_{model}^{high}(\mathbf{R}_{model})}{\partial \mathbf{R}_{model}^2} \cdot \mathbf{J} + \frac{\partial^2 E_{real}^{low}(\mathbf{R})}{\partial \mathbf{R}^2} - \mathbf{J}^T \cdot \frac{\partial^2 E_{model}^{low}(\mathbf{R}_{model})}{\partial \mathbf{R}_{model}^2} \cdot \mathbf{J}. \quad (\text{A.15})$$

Again, the Jacobian \mathbf{J} and here also its transpose \mathbf{J}^T are necessary to transform the matrices. Analysis methods for the ONIOM Hessian especially for TSs are described in the literature [151].

The implementation in PERL5 divides the task in three parts: In the first step, the script `builtInput.pl` generates the input for the three individual calculations, using template files and supporting GAUSSIAN and MOLPRO. Specific input to ensure additivity of the Hessian and correct output for step 3 is added automatically. The user submits these jobs in the second step by a submitter script of his/her own choice. The generation of the ONIOM Hessian and the vibrational analysis is done by the script `ONIOMfreq.pl` in the third step. Here, the non-mass weighted Hessians from

the subcalculations are read-in by specific routines and added up after multiplication with the Jacobian. The ONIOM Hessian is finally mass-weighted before the analysis.

Both mentioned scripts rely on functions, for better maintainability located in two perl modules, `basicRoutines.pm` and `FreqRoutine.pm`, specifically written for this project. The former contains read-in procedures for options (see Table A.1) and geometry and procedures to build the model system, using an only slightly modified version of the routine `scale_brokenbond()` mentioned before; the latter contains the vibrational analysis routine based on an implementation by A. Nenov. The resulting output file is formatted in GAUSSIAN style and can be read by MOLDEN [152] for visualization of the normal modes. The module files should be in the same folder as the scripts, as this location is assumed by the scripts. Both scripts expect the name of the options file as input parameter:

```
./builtInput.pl ONIOMinput
./ONIOMfreq.pl ONIOMinput
```

Table A.1.: Options for the ONIOM vibrational analysis

AtomsModel	<number>	number of atoms in model system
BrokenBond	A,B[,C,D...]	insert link atom for atom B, scale A-B bond
GeometryFile	<filename>	filename
ProgrammLow	<program name>	program for low level of theory
ProgrammHigh	<program name>	program for high level of theory
TemplateLow	<filename>	filename of template for low level
TemplateHigh	<filename>	filename of template for high level

The routine `buildJacobian()` to construct the Jacobian is re-used here from the optimization of the CoIn (see above).

The codebase is included in the GIT repository for PERL in the `ONIOMfreq` folder.

ONIOM in non-adiabatic mixed quantum-classical dynamics

Based on the interface for the program package MOLPRO2012 [68] written in PERL5 by Sven Oesterling [153] in NEWTONX 1.4 [154, 155], a flexible implementation of the ONIOM code invoking the CLS approximation (eq. A.2) was developed. It allows the usage of CASSCF as high-level method and HF as low-level method, but is in principle extendable to other low- or high-level methods like (TD)DFT. As the routine is implemented in the MOLPRO2012 interface `run-molpro.pl`, QC calculations are only possible with MOLPRO2012 and, thus, a mixing between different program packages is not yet possible. The implementation is based on Ref. [114].

The interface starts by calling `what_to_do()`, where the input file `molpro.par` is read. Here, three new options for ONIOM are inserted:

Table A.2.: Options for the ONIOM routine in `run-molpro.pl` of NEWTONX 1.4

<code>oniom_low</code>	<code>hf</code>	low-level of theory
<code>oniom_nat_mod</code>	<number>	number of atoms in model system
<code>oniom_brokenbond</code>	A,B[,C,D...]	insert link atom for atom B, scale A-B bond

If all parameters are present, the subroutine `oniom()` is called. Here, after reading the geometry, first both calculations for the model system are performed in one step, afterwards the low-level calculations for the real system. The modified routine `scale_brokenbond()` of the vibrational analysis was re-used to introduce the link atoms. For running the calculations, `oniom()` relies on `modify_input()` and `run_and_read()` of the original interface. Note that the hashes `%en` and `%grad` containing the energy and gradient of the low-level method have to be moved before running the second calculation. The ONIOM energies and gradients are calculated at the end according to the formulas in Ref. [114]. Afterwards, the main program calls `write_nx()` to store all values readable for NEWTONX.

Appendix B.

Supporting information for chapter 4

Supporting Information

Singlet Oxygen Reactivity with Carbonate Solvents used for Li-Ion Battery Electrolytes

Anna T.S. Freiberg,^{=a*} Matthias K. Roos,^{=b} Johannes Wandt,^a Regina de Vivie-Riedle,^{b**}
Hubert A. Gasteiger^a

^a*Chair of Technical Electrochemistry, Department of Chemistry and Catalysis Research Center, Technische Universität München, Garching, Germany*

^b*Department of Chemistry, Ludwig-Maximilians-Universität München, München, Germany*

* anna.freiberg@tum.de

** regina.de_vivie@cup.uni-muenchen.de

A: Background information on ab initio calculations

B: Photograph of on-line mass spectrometry set-up

C: Chemical reactivity of vinylene carbonate with $^3\text{O}_2$

D: H^+ evolution upon anodic oxidation of H_2O_2

A) Background information on ab initio calculations

In the following tables, the geometries of the optimized minimum structures are listed in Cartesian coordinates. The structures were optimized using UB3LYP/6-311++G(d,p) with the program packages Gaussian09¹ and Gaussian16². The geometries are given in Ångström and the respective total electronic energies in hartree. The transition states are numbered according to the main paper and designated with “TS”.

Table S1: Optimized structures for the reaction of EC + ¹O₂ and consecutive reactions**Ethylene carbonate (EC)**

absolute energy: -342.503368

O	-0.072049	1.110353	-0.109692
O	-0.072441	-1.110671	0.109281
C	-0.851828	-0.000065	-0.000096
O	-2.039801	0.000275	0.000196
C	1.300647	0.755393	0.122360
H	1.560631	1.014944	1.151617
H	1.927801	1.314283	-0.570320
C	1.300761	-0.755269	-0.122101
H	1.560867	-1.014838	-1.151273
H	1.927545	-1.314399	0.570713

Singlet oxygen (¹O₂)

absolute energy: -150.308956

O	0.000000	0.000000	0.602743
O	0.000000	0.000000	-0.602743

Triplet oxygen (³O₂)

absolute energy: -150.370417

O	0.000000	0.000000	0.602902
O	0.000000	0.000000	-0.602902

TS1

absolute energy: -492.786889

C	-0.288346	0.723178	0.872948
C	-0.288249	-0.722959	0.873144
H	-1.280153	1.002851	0.142283
H	-0.492354	1.301868	1.770883
H	-1.279406	-1.003258	0.142460
H	-0.492048	-1.301456	1.771243
O	0.874871	1.114520	0.203874
O	0.875179	-1.114451	0.204365
C	1.552997	-0.000009	-0.222967
O	2.554737	0.000033	-0.848568
O	-2.296902	-0.655858	-0.590465
O	-2.297190	0.655597	-0.589909

Vinylene carbonate (VC)

absolute energy: -341.270906

O	0.021352	1.107153	0.000269
O	0.021395	-1.107128	-0.000276
C	-0.788914	0.000009	-0.000003
O	-1.975005	-0.000024	0.000003
C	1.331275	0.664099	-0.000599
C	1.331249	-0.664110	0.000612
H	2.108210	1.406420	-0.000014

H 2.108199 -1.406415 -0.000016

Hydrogen peroxide (H₂O₂)

absolute energy: -151.602171

H -1.027061 0.668432 0.415171
H 1.027067 -0.668427 0.415174
O 0.717072 0.119674 -0.051897
O -0.717073 -0.119674 -0.051896

TS2

absolute energy: -491.591842

C -0.130380 1.292041 0.265458
C -0.601518 0.015870 0.704049
H -0.634477 2.231313 0.125577
H -1.197261 -0.110107 1.599949
O 1.091013 1.112619 -0.317292
O 0.499104 -0.821176 0.619775
C 1.496943 -0.184663 -0.075858
O 2.529991 -0.653563 -0.398872
O -2.813448 -0.102986 -0.361652
O -1.651477 -0.642482 -0.427885

Biradical

absolute energy: -491.592903

C -0.179942 1.263257 0.305405
C -0.654897 -0.083869 0.638478
H -0.733182 2.168019 0.123966
H -1.185185 -0.235079 1.575475
O 1.061355 1.137591 -0.250664
O 0.494257 -0.871104 0.542749
C 1.493062 -0.160633 -0.072371
O 2.552083 -0.577969 -0.380732
O -2.763807 -0.053218 -0.349851
O -1.597759 -0.640983 -0.427567

TS3

absolute energy: -491.546819

C -0.231713 1.165725 0.391958
C -0.587485 -0.164578 0.733160
H -0.794700 2.081786 0.414080
H -1.069259 -0.400393 1.676339
O 0.985292 1.168880 -0.155458
O 0.563254 -0.919492 0.499146
C 1.491652 -0.147853 -0.112969
O 2.549469 -0.462909 -0.522045
O -2.612884 0.143692 -0.591584
O -1.756477 -0.780316 -0.250473

Dioxetane

absolute energy: -491.661635

C 0.730736 -0.761144 0.550889
C 0.731061 0.761119 0.550915
H 1.092809 -1.385321 1.363860
H 1.092993 1.385724 1.363558
O -0.585408 -1.122770 0.226249
O -0.584449 1.123248 0.225288
C -1.325427 -0.000203 -0.057060
O -2.441365 0.000559 -0.438655

O 1.618923 0.747023 -0.568238
O 1.616796 -0.747939 -0.569129

TS4

absolute energy: -491.609745

C -0.672739 0.896878 0.512735
C -1.060260 -0.567513 0.682969
H -1.404941 1.574540 0.971108
H -1.070482 -1.262156 1.517151
O 0.515423 1.256856 0.389719
O 0.772156 -1.193052 0.138814
C 1.568712 -0.308276 -0.088359
O 2.612356 0.083600 -0.420048
O -1.873693 -0.729215 -0.273217
O -1.593599 0.526947 -0.976809

C₂O₃H₂

absolute energy: -302.994755

C -1.000156 -0.388245 0.000259
C -0.003548 0.700711 0.000045
H -0.615728 -1.416942 0.000794
H -0.309425 1.741421 0.000999
O -2.180801 -0.112240 -0.000257
O 1.257984 0.533439 -0.000154
O 1.791239 -0.696109 -0.000041

Carbon dioxide (CO₂)

absolute energy: -188.646915

C 0.000000 0.000000 0.000000
O 0.000000 0.000000 1.160755
O 0.000000 0.000000 -1.160755

Fig. S1, S2, and S3 depict the active spaces used in the CASSCF/CASPT2/ANO-L-VDZP calculations performed on UB3LYP/6-311++G(d,p) optimized geometries. The choice of active space is an essential parameter in these calculations, as in these orbital spaces all electrons are fully correlated. Further correlation is only included by perturbation theory. In Fig. S1, the active space for ethylene carbonate (a) and vinylene carbonate (b) is shown. The active space for oxygen is shown in Fig. S2, and the one for TS1 in Fig. S3. The numbering of the molecular orbitals (MO##) follows the numbering in the respective calculation. The captions contain further, essential details of the respective calculations.

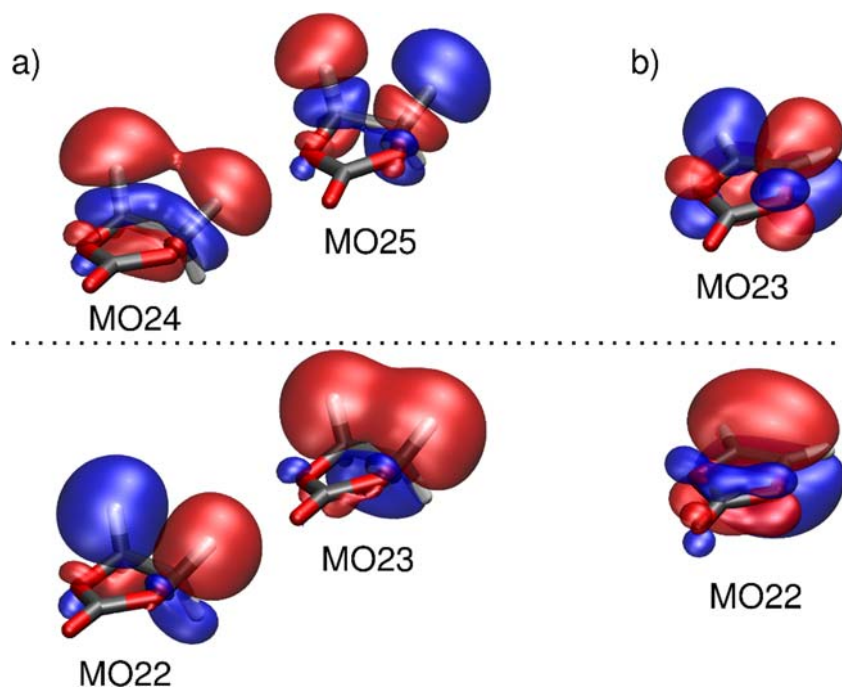


Fig. S1: Active Space for **a)** ethylene carbonate (EC) and **b)** vinylene carbonate (VC). For EC, the active space consists of the σ - and σ^* -orbitals of the two H-atoms on one side, i.e., CAS(4,4). For VC, the π - and π^* -orbitals of the C-C double bond constitute the active space, i.e., CAS(2,2). Iso-value: 0.02.

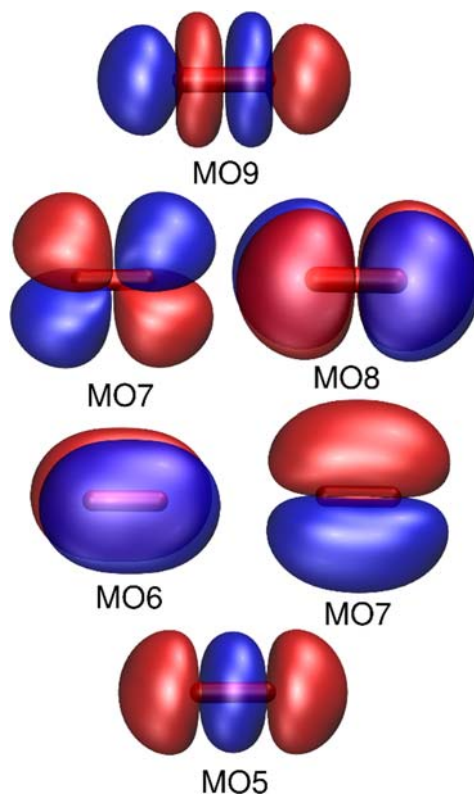


Fig. S2: Active space for $^1\text{O}_2$ and $^3\text{O}_2$ (CAS(8,6)). Iso-value: 0.02.

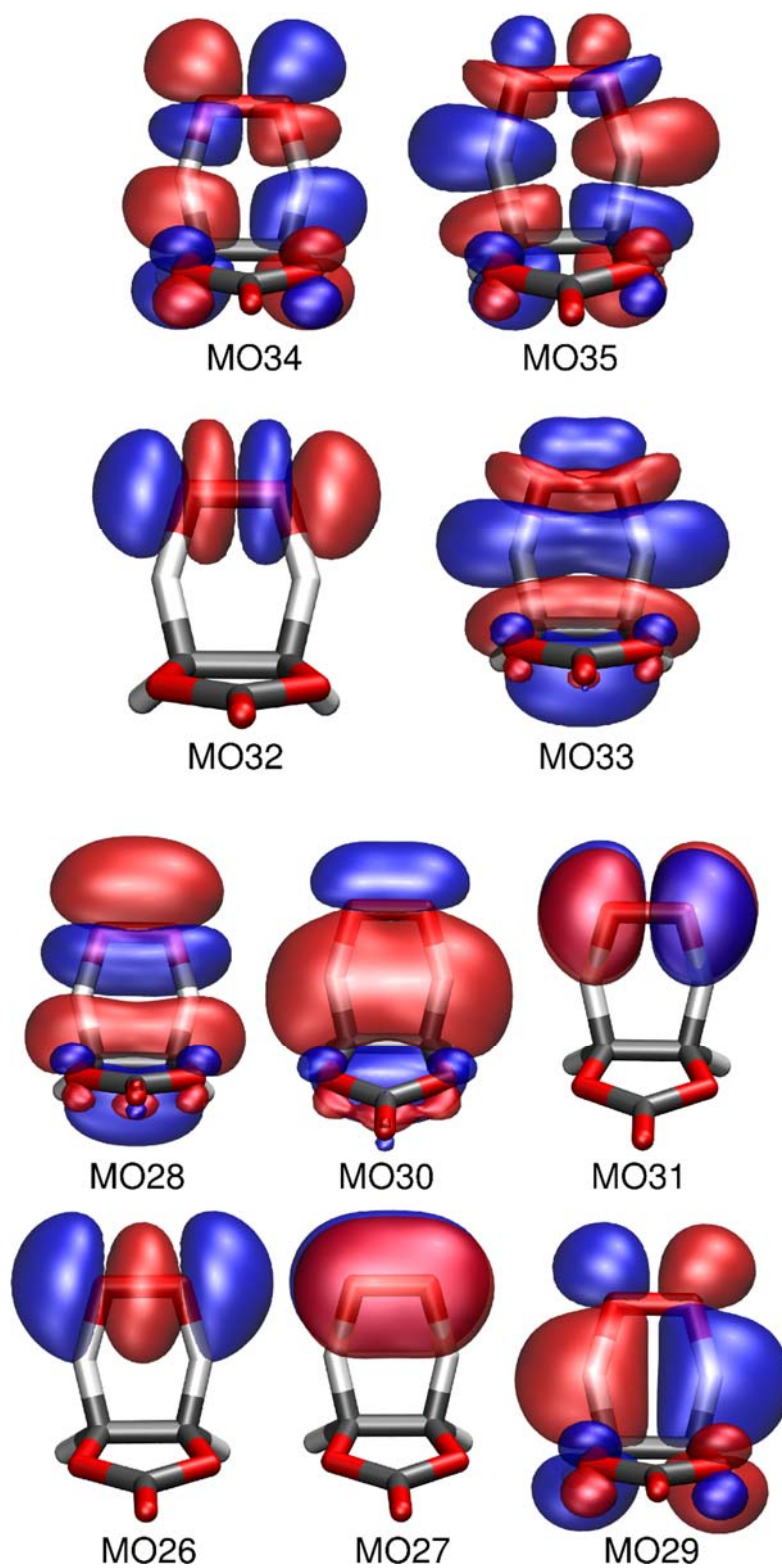


Fig. S3: Active space for TS1 (CAS(12,10)), calculated with state-averaging over three states with the weight 90:5:5. Iso-value: 0.02.

B: Photograph of on-line mass spectrometry set-up

Fig. S4 shows two pictures depicting the on-line mass spectrometry set-up as explained in the main text. The front plate ensuring opacity is removed.

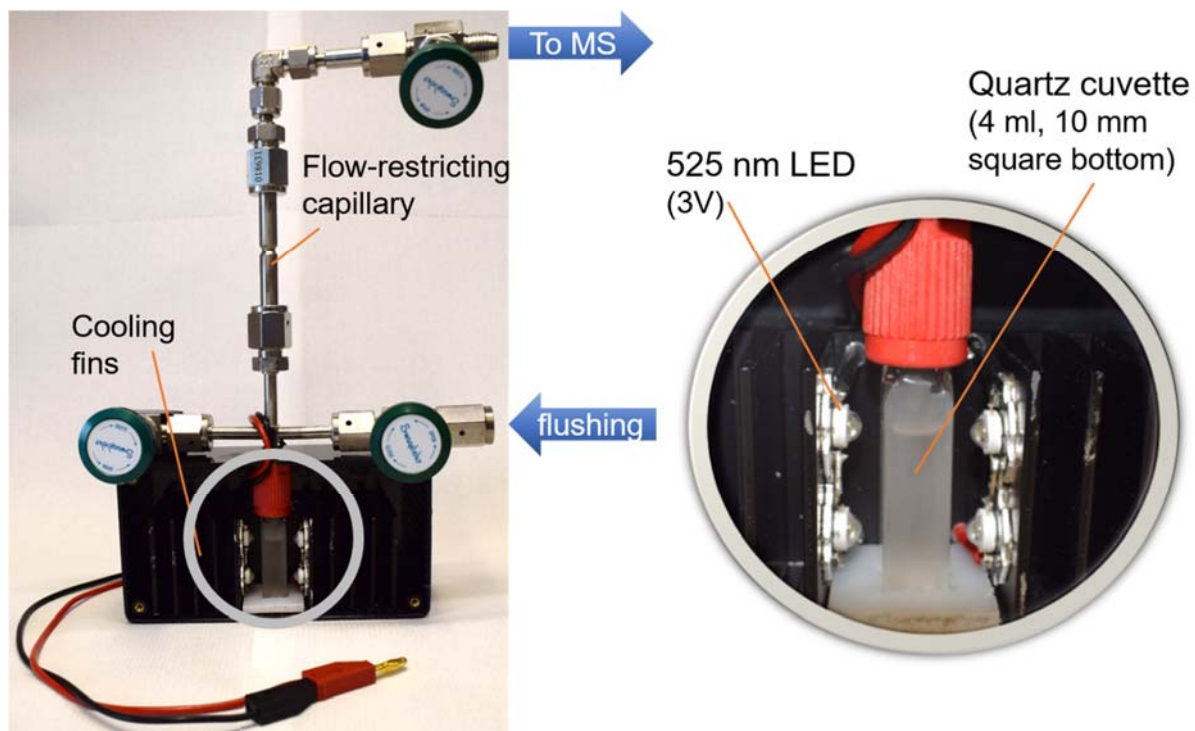


Fig. S4: Photos of the on-line mass spectrometry set-up for analysis of the gaseous decomposition products from the reaction of electrolyte solvents or electrolytes with $^1\text{O}_2$ (note that the front plate of the reactor was removed for taking these photographs). The flushing valves allow measurements in different gas atmospheres. The zoom on the right-hand-side shows the cuvette filled with 4 ml of carbonate solvent without photosensitizer.

C: Chemical reactivity of vinylene carbonate with $^3\text{O}_2$

According to *ab initio* calculations, the decomposition of vinylene carbonate (VC), formed after double H-abstraction from ethylene carbonate by $^1\text{O}_2$, can be initiated by another $^1\text{O}_2$ or even by a $^3\text{O}_2$ molecule, in both cases leading to CO_2 evolution as sole gaseous decomposition product.

In our on-line gas analysis of reactivity of different solvents toward $^1\text{O}_2$, $^1\text{O}_2$ is formed from $^3\text{O}_2$ using a photosensitizer. The amount of $^3\text{O}_2$ in our set-up – as well as in an operating battery – exceeds by far the concentration of $^1\text{O}_2$. As for now, only the consumption of O_2 (without differentiation of its electronic spin state) and the evolution of CO_2 allows the determination of the reaction stoichiometry; the reactivity of VC with $^3\text{O}_2$ shall be further evaluated experimentally. Please note that a chemical reactivity of ethylene carbonate with $^3\text{O}_2$ can be already excluded, considering the fact that the CO_2 baseline of the set-up under 10% $^3\text{O}_2$ in Ar (i.e., in absence of the light-driven generation of $^1\text{O}_2$) is not changing over time (see the CO_2 evolution rate between -0.5 and 0 h in the bottom panels of Fig. 1a and b in the main text), which is consistent with the result of the *ab initio* calculations.

For the determination of the reactivity of VC with $^3\text{O}_2$, we used a 1-compartment OEMS cell in our conventional OEMS set-up.⁴ The cell was assembled in an Ar-filled glovebox with two glass-fiber separators soaked with 200 μl of pure VC (battery grade, 200 ppm BHT as stabilizer, BASF, Germany), without any other components inside the cell. The cell was then connected to the MS via the flow-restricting capillary and the mass-traces were recorded for 4.5 h under Ar atmosphere. Afterwards, the cell was flushed for 2 minutes with 10% O_2 in Ar and the mass-traces were again recorded for 4.5 h before calibration of the MS signals with a calibration gas. Fig. S5 shows the results of this analysis at 25°C.

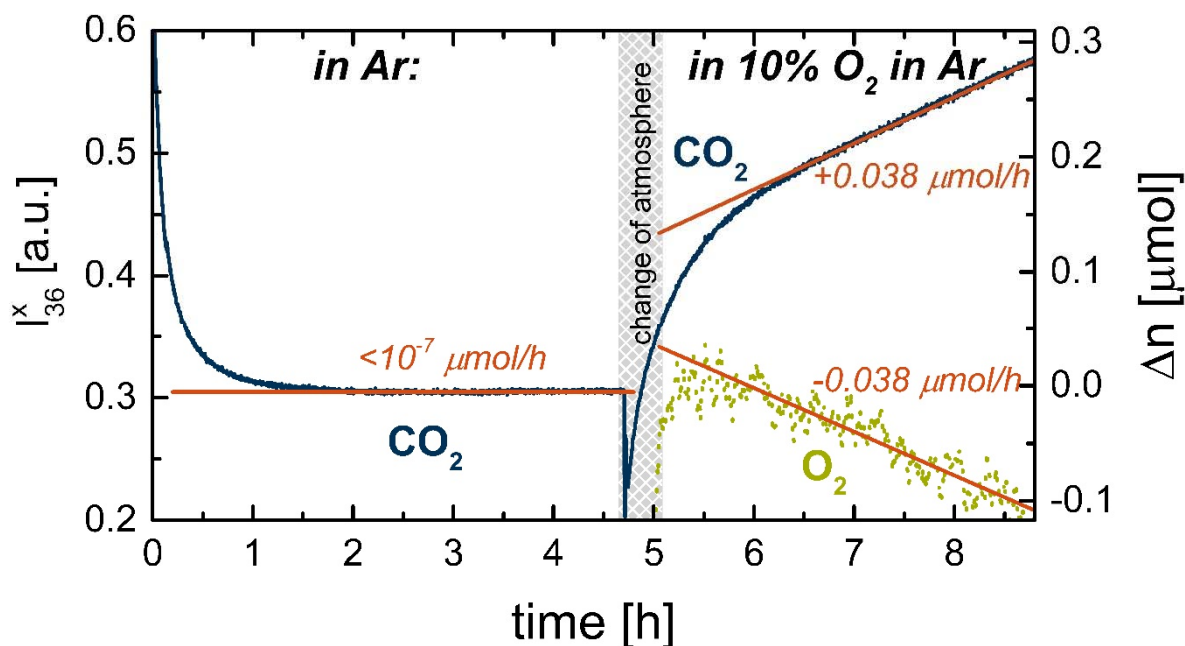
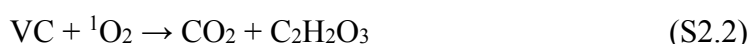
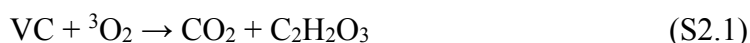


Fig. S5: CO_2 mass signals ($m/z=44$; blue line) from an OEMS cell at 25°C filled with 200 μl of VC (imbibed into two glass fiber separators), obtained under Ar ($t < 4.7$ h) for about two minutes; CO_2 signals are either given as CO_2 mass currents normalized by the current of the ^{36}Ar isotope (left y-axis) or calibrated to $\mu\text{mol CO}_2$ in the cell, setting its zero value after the initial background signal equilibration (after ≈ 2 h). The O_2 mass signal ($m/z=32$) in the presence of 10% O_2 in Ar (right-hand side green signal) is converted into μmol and offset such that the change in O_2 content with time can be followed in this figure. The slopes of the linear fits of concentration vs time (orange lines) over the last 2 h under each atmosphere represent the gas evolution/consumption rate.

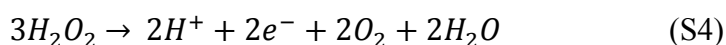
Fig. S5 displays the evolution of the CO_2 signal ($m/z=44$) initially under Ar ($t < 4.7$ h) and then after a two-minute flushing of the cell with 10% O_2 in Ar ($t > 4.7$ h), whereas baseline correction of the mass signals has been omitted, displaying only the raw data normalized by the ^{36}Ar isotope current (left-hand y-axis). Over the first 2 h in Ar, the CO_2 mass trace is gradually decreasing, reaching an essentially constant value; converting the mass signals into concentrations, the change of the CO_2 concentration between 2-5 h is $< 10^{-5} \mu\text{mol/h}$, and at this point the CO_2 concentration is set to 0 μmol (see right-hand y-axis). Except for the Ar and O_2 signals, CO_2 is the only mass signal that increases upon changing the gas atmosphere from Ar to 10% O_2 in Ar, indicating that it is the only gaseous reaction product of VC with $^3\text{O}_2$. That CO_2 is indeed due to a reaction of VC with $^3\text{O}_2$ is further evidenced by the observation that the O_2 mass signal after flushing the cell with 10% O_2 in Ar starts to decrease after an initial equilibration to the 10% level (green data points). As a matter of fact, after the initial equilibration period, the CO_2 evolution rate equals the O_2 consumption rate, as indicated by the red linear regression lines on the right-hand side of Fig. S5, with slopes of $+0.038 \mu\text{mol}_{\text{CO}_2}/\text{h}$

and $-0.038 \mu\text{mol}_{\text{O}_2}/\text{h}$. This clearly shows that $^3\text{O}_2$ does react with VC, producing one CO_2 molecule per consumed $^3\text{O}_2$. While the formation of VC from ethylene carbonate is only possible in the presence of $^1\text{O}_2$ (as shown experimentally and computationally here), as marked by Eqs. S1.1 and S1.2, the formed VC readily decomposes with both singlet and triplet O_2 (see Eqs. S2.1 and S2.2). The overall reaction (Eq. S3) thus is consistent with our observations that two moles of O_2 are consumed for each evolved mol of CO_2 (see Table 1, main text).

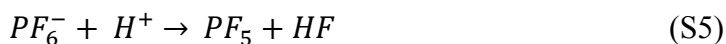


D: H^+ evolution upon anodic oxidation of H_2O_2

The net anodic oxidation reaction of H_2O_2 , Eq. 2 of the main text, suggests the evolution of a significant amount of protons if one assumes that the electron charges are balanced by protons released into the solution:



The bare H^+ concentration in solution can not be monitored by MS, but the instantaneous reaction of protons with the LiPF_6 conductive salt shown in Eq. S5 allows quantification of the protons formed as recently shown by Solchenbach et al.⁵



PF_5 that is formed in the presence of protons is detected as POF_3 due to its high reactivity with any oxygen-containing surface, i.e. the tubing connecting the cell to the MS. For quantification, the MS channel $m/z=85$ is used, employing the calibration factor of Solchenbach et al.⁵ The corresponding MS signals of the anodic oxidation of H_2O_2 with the reference measurements of the pure DMC electrolyte and the DMC electrolyte with H_2O are shown in Fig. S6, i.e. containing the same information as Fig. 5 in the main text, complemented with the POF_3 evolution, which should picture the H^+ concentration in solution without large time shift and in a quantity of 1:1. In comparison to Fig. 5 of the main text, scales of the middle and central panels containing the integral gas evolution and gas evolution rate are changed in order to accommodate the POF_3 signal.

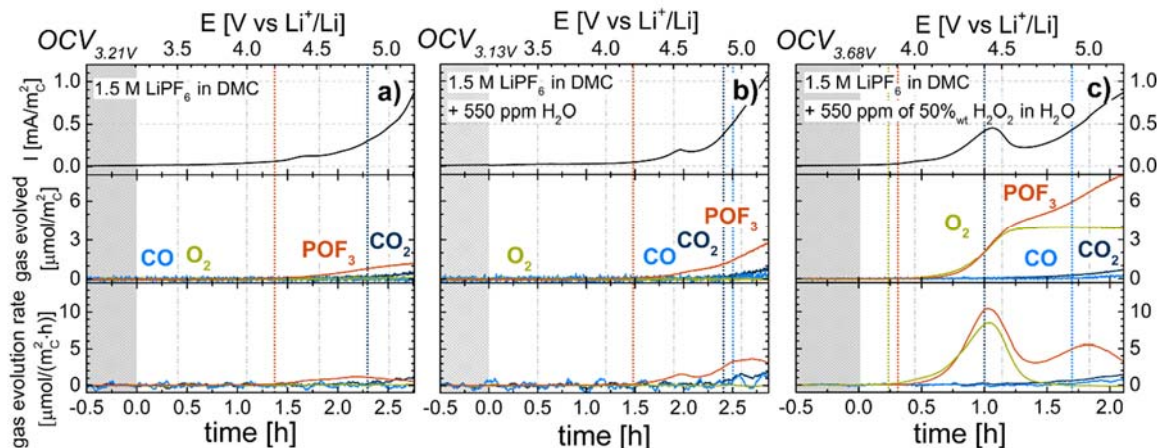


Fig. S6: Electrochemical oxidation of DMC electrolyte with 1.5 M LiPF₆ on a carbon black electrode (Super C65/PVdF) during a linear potential scan (0.2 mV/s) from OCV to 5.2 V vs Li⁺/Li (upper x-axes; OCV values are also indicated there) at 25°C: **a)** pure electrolyte; **b)** electrolyte with 550 ppm H₂O and, **c)** electrolyte with 550 ppm of 50%_{wt} H₂O₂ in H₂O. Upper panels: current vs potential; middle panels: total amount of formed gas for CO (blue lines), CO₂ (dark blue lines), POF₃ (orange lines) and O₂ (green lines), referenced to the total BET surface area of the carbon electrode; bottom panels: gas evolution rates (smoothed over 50 points), whereby the onset of the evolution of each gas is marked by dashed vertical lines (in the respective color). Measurements are performed in a 2-compartment OEMS cell in which the lithium metal counter electrode is separated from the carbon black working electrode by an impermeable solid lithium ion conductor.³

The POF₃ signal in the bare DMC electrolyte (Fig. S6a) arises around 4.2 V vs Li⁺/Li and maintains a rather constant rate of $1 \frac{\mu\text{mol}}{\text{m}^2 \cdot \text{h}}$ until the end of the measurement. In the presence of water (Fig. S6b), the onset of POF₃ evolution remains unchanged but a second process setting in at roughly 4.7 V vs Li⁺/Li leads to a significant higher integral gas evolution of POF₃ of $2.8 \frac{\mu\text{mol}}{\text{m}^2}$ at the end of the experiment. The first process setting in at 4.2 V vs Li⁺/Li is assigned to the anodic oxidation of DMC as the POF₃ onset well coincides with the onset of a significant current drawn from the carbon electrode, shown in the upper panel. The second evolution of POF₃ in the presence of water (Fig. S6b) can be explained by the electrochemical oxidation of the carbon electrode with water leading to CO gassing and H⁺ as explained by Metzger et al.⁶

Fig. S6c shows the evolution of POF₃ upon anodic oxidation of H₂O₂ in the DMC electrolyte containing 550 ppm of an aqueous H₂O₂ solution. The first rise in POF₃ signal sets in at 3.9 V vs Li⁺/Li, which is reasonably close to the onset of O₂ (3.85 V vs Li⁺/Li, ≈ 4 min difference) to correlate the evolution of O₂ and H⁺ – monitored as POF₃ – to the same anodic reaction. The O₂ evolution is terminated at roughly 4.7 V vs Li⁺/Li ($3.9 \frac{\mu\text{mol}_{\text{O}_2}}{\text{m}^2}$), which we assign to a complete conversion of the added amount of H₂O₂. The strong similarity of O₂ evolution behavior and POF₃ formation characteristics up to this point supports the hypothesis that these two processes are correlated. The ratio of evolved O₂ and POF₃ is always very close to a 1:1 relation, which is in agreement with Eqs. S4 and S5.

After complete conversion of the H₂O₂, the evolution of O₂ stops but an additional amount of POF₃ is formed above 4.5 V vs Li⁺/Li, accumulating to $7.5 \frac{\mu\text{mol}}{\text{m}^2}$ ($= 3.9 \frac{\mu\text{mol}_{\text{POF}_3, E < 4.5 \text{ V}}}{\text{m}^2} + 3.4 \frac{\mu\text{mol}_{\text{POF}_3, E > 4.5 \text{ V}}}{\text{m}^2}$). Comparing the additional amount of POF₃ formed after H₂O₂

consumption (i.e., above 4.5 V vs Li⁺/Li) in Fig. S6c and the amount formed in the bare presence of H₂O in Fig. S6b, the former can be considered to arise from the same processes as the overall concentration of water present in both cases is comparable (550 ppm for Fig. S6b and $\frac{550}{2} \text{ ppm}_{\text{H}_2\text{O added}} + \frac{550}{2} \cdot \frac{2}{3} \text{ ppm}_{\text{H}_2\text{O out of Eq. S4}} \approx 408 \text{ ppm}_{\text{H}_2\text{O}, E > 4.5 \text{ V}}$ for Fig. S6c). This correlation can further be seen in the rate plot (lower panels of Fig. S6b and c) where the POF₃ formation at high potential leads to a maximum rate at 5.0 V vs Li⁺/Li in both cases.

In conclusion, the amount of POF₃ gas detected is a direct probe for the amount of free H⁺ formed by anodic processes in this set-up and supports the net equation of the anodic oxidation of H₂O₂ as shown in Eq. 2 of the main text and Eq. S4 presented here.

References:

- (1) Frisch, M. J.; Trucks, G. W.; Schlegel, H. B.; Scuseria, G. E.; Robb, M. A.; Cheeseman, J. R.; Scalmani, G.; Barone, V.; Mennucci, B.; Petersson, G. A.; Nakatsuji, H.; Caricato, M.; Li, X.; Hratchian, H. P.; Izmaylov, A. F.; Bloino, J.; Zheng, G.; Sonnenberg, J. L.; Hada, M.; Ehara, M.; Toyota, K.; Fukuda, R.; Hasegawa, J.; Ishida, M.; Nakajima, T.; Honda, Y.; Kitao, O.; Nakai, H.; Vreven, T.; Montgomery, J. A. J.; Peralta, J. E.; Ogliaro, F.; Bearpark, M. J.; Heyd, J. J.; Brothers, E. N.; Kudin, K. N.; Staroverov, V. N.; Kobayashi, R.; Normand, J.; Raghavachari, K.; Rendell, A. P.; Burant, J. C.; Iyengar, S. S.; Tomasi, J.; Cossi, M.; Rega, N.; Millam, J. M.; Klene, M.; Knox, J. E.; Cross, J. B.; Bakken, V.; Adamo, C.; Jaramillo, J.; Gomperts, R.; Stratmann, R. E.; Yazyev, O.; Austin, A. J.; Cammi, R.; Pomelli, C.; Ochterski, J. W.; Martin, R. L.; Morokuma, K.; Zakrzewski, V. G.; Voth, G. A.; Salvador, P.; Dannenberg, J. J.; Dapprich, S.; Daniels, A. D.; Farkas, O.; Foresman, J. B.; Ortiz, J. V.; Cioslowski, J.; Fox, D. J., Gaussian, Inc., Wallingford, CT (2009).
- (2) Frisch, M. J.; Trucks, G. W.; Schlegel, H. B.; Scuseria, G. E.; Robb, M. A.; Cheeseman, J. R.; Scalmani, G.; Barone, V.; Petersson, G. A.; Nakatsuji, H.; Li, X.; Caricato, M.; Marenich, A. V.; Bloino, J.; Janesko, B. G.; Gomperts, R.; Mennucci, B.; Hratchian, H. P.; Ortiz, J. V.; Izmaylov, A. F.; Sonnenberg, J. L.; Williams-Young, D.; Ding, F.; Lipparini, F.; Egidi, F.; Goings, J.; Peng, B.; Petrone, A.; Henderson, T.; Ranasinghe, D.; Zakrzewski, V. G.; Gao, J.; Rega, N.; Zheng, G.; Liang, W.; Hada, M.; Ehara, M.; Toyota, K.; Fukuda, R.; Hasegawa, J.; Ishida, M.; Nakajima, T.; Honda, Y.; Kitao, O.; Nakai, H.; Vreven, T.; Throssell, K.; Montgomery, J. A. J.; Peralta, J. E.; Ogliaro, F.; Bearpark, M. J.; Heyd, J. J.; Brothers, E. N.; Kudin, K. N.; Staroverov, V. N.; Keith, T. A.; Kobayashi, R.; Normand, J.; Raghavachari, K.; Rendell, A. P.; Burant, J. C.; Iyengar, S. S.; Tomasi, J.; Cossi, M.; Millam, J. M.; Klene, M.; Adamo, C.; Cammi, R.; Ochterski, J. W.; Martin, R. L.; Morokuma, K.; Farkas, O.; Foresman, J. B.; Fox, D. J., Gaussian, Inc., Wallingford, CT (2016).
- (3) Metzger, M.; Strehle, B.; Solchenbach, S.; Gasteiger, H. A., *J. Electrochem. Soc.*, **2016**, *163*, A798-A809.
- (4) Tsiouvaras, N.; Meini, S.; Buchberger, I.; Gasteiger, H. A., *J. Electrochem. Soc.*, **2013**, *160*, A471-A477.
- (5) Solchenbach, S.; Metzger, M.; Egawa, M.; Beyer, H.; Gasteiger, H. A., *to be submitted*, **2018**.
- (6) Metzger, M.; Marino, C.; Sicklinger, J.; Haering, D.; Gasteiger, H. A., *J. Electrochem. Soc.*, **2015**, *162*, A1123-A1134.

List of abbreviations

aRC	adapted reactive coordinate
CAM	cathode active material
CASSCF	complete active space self consistent field
CASPT2	complete active space second-order perturbation theory
CC	cross correlation
CD	circular dichroism
CLS	constraint low-level state
CO₂	carbon dioxide
CoIn	conical intersection
Cy3	Cyanine 3
DCME	diabatic coupling matrix element
DFT	density functional theory
DMC	dimethyl carbonate
dsDNA	double-stranded DNA
EC	ethylene carbonate
ESA	excited state absorption
ET	electron transfer
FC	Franck-Condon
FWHM	full-width-half-maximum
H₂O₂	hydrogen peroxide
LG	leaving group
MCTDH	multi-configuration time-dependent Hartree
MD	molecular dynamics
MEP	minimum energy path
MM	molecular mechanics
MQCD	mixed quantum-classical dynamics
NCM	lithium nickel cobalt manganese oxide

NACME	non-adiabatic coupling matrix element
NOPA	non-collinear optical parametric amplifiers
$^1\text{O}_2$	singlet oxygen
OEMS	on-line electrochemical mass spectrometry
ONIOM	our own n-layered integrated molecular orbital and molecular mechanics
PAH	polycyclic aromatic hydrocarbon
PES	potential energy surface
Ph_2CH^+	diphenylmethyl cation
$\text{Ph}_2\text{CH}^\bullet$	diphenylmethyl radical
$\text{Ph}_2\text{CH}-\text{Br}$	diphenylmethyl bromide
$\text{Ph}_2\text{CH}-\text{Cl}$	diphenylmethyl chloride
$\text{Ph}_2\text{CH}-\text{PPh}_3^+$	diphenylmethyltriphenylphosphonium ion
PCM	polarizable continuum model
QC	quantum chemistry
QD	quantum dynamics
QM/MM	quantum mechanics/molecular mechanics
RB	rose bengal
RMSD	root-mean-square deviation
ssDNA	single-stranded DNA
SOC	state of charge
TDDFT	time-dependent density functional theory
TPA	two-photon-absorption
TS	transition state
VACF	velocity autocorrelation function
VC	vinylene carbonate

Bibliography

- [1] R. Levine, *Molecular Reaction Dynamics*, Cambridge University Press, Cambridge (2005).
- [2] A. H. Zewail, *Laser selective chemistry—is it possible?*, *Phys. Today* **33**, 27 (1980).
- [3] M. Dantus, M. J. Rosker and A. H. Zewail, *Real-time femtosecond probing of “transition states” in chemical reactions*, *J. Chem. Phys.* **87**, 2395 (1987).
- [4] A. H. Zewail, *Laser Femtochemistry*, *Science* **242**, 1645 (1988).
- [5] A. H. Zewail, *Femtochemistry: Recent Progress in Studies of Dynamics and Control of Reactions and Their Transition States*, *J. Phys. Chem.* **100**, 12701 (1996).
- [6] A. H. Zewail, *Femtochemistry: Atomic-Scale Dynamics of the Chemical Bond Using Ultrafast Lasers (Nobel Lecture)*, *Angew. Chem. Int. Ed.* **39**, 2586 (2000).
- [7] W. Demtröder, *Laser Spectroscopy: Basic Concepts and Instrumentation*, *Advanced Texts in Physics*, Springer-Verlag Berlin Heidelberg, 3rd ed. (2003).
- [8] B. Lasorne, G. A. Worth and M. A. Robb, *Excited-state dynamics*, *WIREs Comput. Mol. Sci.* **1**, 460 (2011).
- [9] R. Marquardt, *Theoretical Methods for Ultrafast Spectroscopy*, *ChemPhysChem* **14**, 1350 (2013).
- [10] J. C. Tully, *Perspective: Nonadiabatic dynamics theory*, *J. Chem. Phys.* **137**, 22A301 (2012).
- [11] A. R. Leach, *Molecular Modelling: Principles and Applications*, Prentice Hall, Harlow, England, 2nd ed. (2001).
- [12] W. Kohn, *Nobel Lecture: Electronic structure of matter—wave functions and density functionals*, *Rev. Mod. Phys.* **71**, 1253 (1999).
- [13] J. A. Pople, *Quantum Chemical Models (Nobel Lecture)*, *Angew. Chem. Int. Ed.* **38**, 1894 (1999).
- [14] M. Born and R. Oppenheimer, *Zur Quantentheorie der Molekeln*, *Ann. Phys.* **389**, 457 (1927).
- [15] J. von Neumann and E. P. Wigner, *On the behaviour of eigenvalues in adiabatic processes*, *Phys. Z.* **30**, 467 (1929).
- [16] E. Teller, *The Crossing of Potential Surfaces*, *J. Phys. Chem.* **41**, 109 (1937).
- [17] G. J. Atchity, S. S. Xantheas and K. Ruedenberg, *Potential energy surfaces near intersections*, *J. Chem. Phys.* **95**, 1862 (1991).

- [18] D. R. Yarkony, *Conical Intersections: The New Conventional Wisdom*, J. Phys. Chem. A **105**, 6277 (2001).
- [19] W. Domcke, D. Yarkony and H. Köppel (ed.), *Conical Intersections: Electronic Structure, Dynamics & Spectroscopy (Advanced Series in Physical Chemistry)*, World Scientific, Singapur (2004).
- [20] B. G. Levine and T. J. Martínez, *Isomerization Through Conical Intersections*, Annu. Rev. Phys. Chem. **58**, 613 (2007).
- [21] S. Matsika and P. Krause, *Nonadiabatic Events and Conical Intersections*, Annu. Rev. Phys. Chem. **62**, 621 (2011).
- [22] W. Domcke and D. R. Yarkony, *Role of Conical Intersections in Molecular Spectroscopy and Photoinduced Chemical Dynamics*, Annu. Rev. Phys. Chem. **63**, 325 (2012).
- [23] A. L. Sobolewski and W. Domcke, *Molecular mechanisms of the photostability of life*, Phys. Chem. Chem. Phys. **12**, 4897 (2010).
- [24] D. Polli, P. Altoe, O. Weingart, K. M. Spillane, C. Manzoni, D. Brida, G. Tomasello, G. Orlandi, P. Kukura, R. A. Mathies, M. Garavelli and G. Cerullo, *Conical intersection dynamics of the primary photoisomerization event in vision*, Nature **467**, 440 (2010).
- [25] D. J. Tannor, *Introduction to quantum mechanics : a time-dependent perspective*, University Science Books, Sausalito, CA (2007).
- [26] B. Podolsky, *Quantum-Mechanically Correct Form of Hamiltonian Function for Conservative Systems*, Phys. Rev. **32**, 812 (1928).
- [27] E. B. Wilson, Jr., J. C. Decius and P. C. Cross, *Molecular Vibrations: The Theory of Infrared and Raman Vibrational Spectra*, McGraw-Hill, New York, NY (1955).
- [28] L. Schaad and J. Hu, *The schrödinger equation in generalized coordinates*, J. Mol. Struct.: THEOCHEM **185**, 203 (1989).
- [29] V. Alexandrov, D. M. A. Smith, H. Rostkowska, M. J. Nowak, L. Adamowicz and W. McCarthy, *Theoretical study of the O-H stretching band in 3-hydroxy-2-methyl-4-pyrone*, J. Chem. Phys. **108**, 9685 (1998).
- [30] B. P. Fingerhut, D. Geppert and R. de Vivie-Riedle, *Ultrafast dissociation pathways of diphenylmethyl chloride to generate reactive carbo cations*, Chem. Phys. **343**, 329 (2008).
- [31] J. C. Tully, *Molecular dynamics with electronic transitions*, J. Chem. Phys. **93**, 1061 (1990).
- [32] M. Svensson, S. Humbel, R. D. J. Froese, T. Matsubara, S. Sieber and K. Morokuma, *ONIOM: A Multilayered Integrated MO + MM Method for Geometry Optimizations and Single Point Energy Predictions. A Test for Diels-Alder Reactions and Pt(P(*t*-Bu)₃)₂ + H₂ Oxidative Addition*, J. Phys. Chem. **100**, 19357 (1996).
- [33] S. Dapprich, I. Komáromi, K. Byun, K. Morokuma and M. J. Frisch, *A new ONIOM implementation in Gaussian98. Part I. The calculation of energies, gradients, vibrational frequencies and electric field derivatives*, J. Mol. Struct.: THEOCHEM **461-462**, 1 (1999).

- [34] T. Vreven and K. Morokuma, *The ONIOM (our own N-layered integrated molecular orbital + molecular mechanics) method for the first singlet excited (S_1) state photoisomerization path of a retinal protonated Schiff base*, *J. Chem. Phys.* **113**, 2969 (2000).
- [35] M. J. Bearpark, F. Ogliaro, T. Vreven, M. Boggio-Pasqua, M. J. Frisch, S. M. Larkin, M. Morrison and M. A. Robb, *CASSCF calculations for photoinduced processes in large molecules: Choosing when to use the RASSCF, ONIOM and MMVB approximations*, *J. Photochem. Photobiol. A* **190**, 207 (2007).
- [36] M. J. Bearpark, S. M. Larkin and T. Vreven, *Searching for Conical Intersections of Potential Energy Surfaces with the ONIOM Method: Application to Previtamin D*, *J. Phys. Chem. A* **112**, 7286 (2008).
- [37] L. W. Chung, W. M. C. Sameera, R. Ramozzi, A. J. Page, M. Hatanaka, G. P. Petrova, T. V. Harris, X. Li, Z. Ke, F. Liu, H.-B. Li, L. Ding and K. Morokuma, *The ONIOM Method and Its Applications*, *Chem. Rev.* **115**, 5678 (2015).
- [38] A. Warshel and M. Levitt, *Theoretical studies of enzymic reactions: Dielectric, electrostatic and steric stabilization of the carbonium ion in the reaction of lysozyme*, *J. Mol. Biol.* **103**, 227 (1976).
- [39] M. J. Field, P. A. Bash and M. Karplus, *A combined quantum mechanical and molecular mechanical potential for molecular dynamics simulations*, *J. Comput. Chem.* **11**, 700 (1990).
- [40] R. B. Murphy, D. M. Philipp and R. A. Friesner, *A mixed quantum mechanics/molecular mechanics (QM/MM) method for large-scale modeling of chemistry in protein environments*, *J. Comput. Chem.* **21**, 1442 (2000).
- [41] R. A. Friesner and V. Guallar, *Ab initio quantum chemical and mixed quantum mechanics/molecular mechanics (QM/MM) methods for studying enzymatic catalysis*, *Annu. Rev. Phys. Chem.* **56**, 389 (2005).
- [42] H. Lin and D. G. Truhlar, *QM/MM: what have we learned, where are we, and where do we go from here?*, *Theor. Chem. Acc.* **117**, 185 (2007).
- [43] S. C. L. Kamerlin, M. Haranczyk and A. Warshel, *Progress in Ab Initio QM/MM Free-Energy Simulations of Electrostatic Energies in Proteins: Accelerated QM/MM Studies of pK_a , Redox Reactions and Solvation Free Energies*, *J. Phys. Chem. B* **113**, 1253 (2009).
- [44] E. Brunk and U. Rothlisberger, *Mixed Quantum Mechanical/Molecular Mechanical Molecular Dynamics Simulations of Biological Systems in Ground and Electronically Excited States*, *Chem. Rev.* **115**, 6217 (2015).
- [45] T. Förster and K. Kasper, *Ein Konzentrationsumschlag der Fluoreszenz des Pyrens*, *Z. Elektrochem., Ber. Bunsenges. Phys. Chem.* **59**, 976 (1955).
- [46] F. P. Schwarz and S. P. Wasik, *Fluorescence measurements of benzene, naphthalene, anthracene, pyrene, fluoranthene, and benzo[e]pyrene in water*, *Anal. Chem.* **48**, 524 (1976).
- [47] J. Ferguson, L. W. Reeves and W. G. Schneider, *Vapor absorption spectra and oscillator strengths of naphthalene, anthracene, and pyrene*, *Can. J. Chem.* **35**, 1117 (1957).

- [48] E. A. Mangle and M. R. Topp, *Excited-state dynamics of jet-cooled pyrene and some molecular complexes*, *J. Phys. Chem.* **90**, 802 (1986).
- [49] P. Foggi, L. Pettini, I. Santa, R. Righini and S. Califano, *Transient absorption and vibrational relaxation dynamics of the lowest excited singlet state of pyrene in solution*, *J. Phys. Chem.* **99**, 7439 (1995).
- [50] F. V. R. Neuwahl and P. Foggi, *Direct Observation of S_2 - S_1 Internal Conversion in Pyrene by Femtosecond Transient Absorption*, *Laser Chem.* **19**, 375 (1999).
- [51] T. M. Figueira-Duarte and K. Müllen, *Pyrene-Based Materials for Organic Electronics*, *Chem. Rev.* **111**, 7260 (2011).
- [52] J. C. Tully, *Mixed quantum-classical dynamics*, *Faraday Discuss.* **110**, 407 (1998).
- [53] R. Crespo-Otero and M. Barbatti, *Recent Advances and Perspectives on Nonadiabatic Mixed Quantum-Classical Dynamics*, *Chem. Rev.* **118**, 7026 (2018).
- [54] M. Ben-Nun, J. Quenneville and T. J. Martínez, *Ab Initio Multiple Spawning: Photochemistry from First Principles Quantum Molecular Dynamics*, *J. Phys. Chem. A* **104**, 5161 (2000).
- [55] B. F. E. Curchod and T. J. Martínez, *Ab Initio Nonadiabatic Quantum Molecular Dynamics*, *Chem. Rev.* **118**, 3305 (2018).
- [56] H.-D. Meyer, U. Manthe and L. Cederbaum, *The multi-configurational time-dependent Hartree approach*, *Chem. Phys. Lett.* **165**, 73 (1990).
- [57] U. Manthe, H.-D. Meyer and L. S. Cederbaum, *Wave-packet dynamics within the multiconfiguration Hartree framework: General aspects and application to NOCl*, *J. Chem. Phys.* **97**, 3199 (1992).
- [58] H.-D. Meyer, *Studying molecular quantum dynamics with the multiconfiguration time-dependent Hartree method*, *WIREs Comput. Mol. Sci.* **2**, 351 (2011).
- [59] D. Kosloff and R. Kosloff, *A fourier method solution for the time dependent Schrödinger equation as a tool in molecular dynamics*, *J. Comput. Phys.* **52**, 35 (1983).
- [60] R. Kosloff, *Propagation Methods for Quantum Molecular Dynamics*, *Annu. Rev. Phys. Chem.* **45**, 145 (1994).
- [61] J. P. P. Zauleck, S. Thallmair and R. de Vivie-Riedle, *Revisiting an approximation in the Wilson G-matrix formalism and its impact on molecular quantum dynamics*, arXiv:1712.10170 [physics.chem-ph] (2017).
- [62] J. P. P. Zauleck, S. Thallmair, M. Loipersberger and R. de Vivie-Riedle, *Two New Methods To Generate Internal Coordinates for Molecular Wave Packet Dynamics in Reduced Dimensions*, *J. Chem. Theory Comput.* **12**, 5698 (2016).
- [63] G. Capano, T. J. Penfold, M. Chergui and I. Tavernelli, *Photophysics of a copper phenanthroline elucidated by trajectory and wavepacket-based quantum dynamics: a synergetic approach*, *Phys. Chem. Chem. Phys.* **19**, 19590 (2017).

- [64] X. Li, Y. Xie, D. Hu and Z. Lan, *Analysis of the Geometrical Evolution in On-the-Fly Surface-Hopping Nonadiabatic Dynamics with Machine Learning Dimensionality Reduction Approaches: Classical Multidimensional Scaling and Isometric Feature Mapping*, *J. Chem. Theory Comput.* **13**, 4611 (2017).
- [65] J. P. P. Zauleck and R. de Vivie-Riedle, *Constructing Grids for Molecular Quantum Dynamics Using an Autoencoder*, *J. Chem. Theory Comput.* **14**, 55 (2018).
- [66] S. Thallmair, M. K. Roos and R. de Vivie-Riedle, *Design of specially adapted reactive coordinates to economically compute potential and kinetic energy operators including geometry relaxation*, *J. Chem. Phys.* **144**, 234104 (2016).
- [67] S. Thallmair, B. P. Fingerhut and R. de Vivie-Riedle, *Ground and Excited State Surfaces for the Photochemical Bond Cleavage in Phenylmethylphenylphosphonium Ions*, *J. Phys. Chem. A* **117**, 10626 (2013).
- [68] H.-J. Werner, P. J. Knowles, G. Knizia, F. R. Manby, M. Schütz, P. Celani, T. Korona, R. Lindh, A. Mitrushenkov, G. Rauhut, K. R. Shamasundar, T. B. Adler, R. D. Amos, A. Bernhardsson, A. Berning, D. L. Cooper, M. J. O. Deegan, A. J. Dobbyn, F. Eckert, E. Goll, C. Hampel, A. Hesselmann, G. Hetzer, T. Hrenar, G. Jansen, C. Köppl, Y. Liu, A. W. Lloyd, R. A. Mata, A. J. May, S. J. McNicholas, W. Meyer, M. E. Mura, A. Nicklass, D. P. O'Neill, P. Palmieri, D. Peng, K. Pflüger, R. Pitzer, M. Reiher, T. Shiozaki, H. Stoll, A. J. Stone, R. Tarroni, T. Thorsteinsson and M. Wang, *MOLPRO, version 2012.1, a package of ab initio programs* (2012).
- [69] M. J. Frisch, G. W. Trucks, H. B. Schlegel, G. E. Scuseria, M. A. Robb, J. R. Cheeseman, G. Scalmani, V. Barone, B. Mennucci, G. A. Petersson, H. Nakatsuji, M. Caricato, X. Li, H. P. Hratchian, A. F. Izmaylov, J. Bloino, G. Zheng, J. L. Sonnenberg, M. Hada, M. Ehara, K. Toyota, R. Fukuda, J. Hasegawa, M. Ishida, T. Nakajima, Y. Honda, O. Kitao, H. Nakai, T. Vreven, J. A. Montgomery, Jr., J. E. Peralta, F. Ogliaro, M. Bearpark, J. J. Heyd, E. Brothers, K. N. Kudin, V. N. Staroverov, R. Kobayashi, J. Normand, K. Raghavachari, A. Rendell, J. C. Burant, S. S. Iyengar, J. Tomasi, M. Cossi, N. Rega, J. M. Millam, M. Klene, J. E. Knox, J. B. Cross, V. Bakken, C. Adamo, J. Jaramillo, R. Gomperts, R. E. Stratmann, O. Yazyev, A. J. Austin, R. Cammi, C. Pomelli, J. W. Ochterski, R. L. Martin, K. Morokuma, V. G. Zakrzewski, G. A. Voth, P. Salvador, J. J. Dannenberg, S. Dapprich, A. D. Daniels, O. Farkas, J. B. Foresman, J. V. Ortiz, J. Cioslowski and D. J. Fox, *GAUSSIAN09, Revision D.01*, Gaussian, Inc., Wallingford, CT (2009).
- [70] S. Thallmair, M. Kowalewski, J. P. P. Zauleck, M. K. Roos and R. de Vivie-Riedle, *Quantum Dynamics of a Photochemical Bond Cleavage Influenced by the Solvent Environment: A Dynamic Continuum Approach*, *J. Phys. Chem. Lett.* **5**, 3480 (2014).
- [71] C. Eckart, *Some Studies Concerning Rotating Axes and Polyatomic Molecules*, *Phys. Rev.* **47**, 552 (1935).
- [72] H. M. Pickett and H. L. Strauss, *Conformational Structure, Energy, and Inversion Rates of Cyclohexane and Some Related Oxanes*, *J. Am. Chem. Soc.* **92**, 7281 (1970).

- [73] W. Kabsch, *A solution for the best rotation to relate two sets of vectors*, Acta Cryst. Sect. A **32**, 922 (1976).
- [74] R. Diamond, *A note on the rotational superposition problem*, Acta Cryst. Sect. A **44**, 211 (1988).
- [75] S. K. Kearsley, *On the orthogonal transformation used for structural comparisons*, Acta Cryst. Sect. A **45**, 208 (1989).
- [76] D. R. Flower, *Rotational Superposition: A Review of Methods*, J. Mol. Graph. Model. **17**, 238 (1999).
- [77] A. Y. Dymarsky and K. N. Kudin, *Computation of the pseudorotation matrix to satisfy the Eckart axis conditions*, J. Chem. Phys. **122**, 124103 (2005).
- [78] E. A. Coutsiias, C. Seok and K. A. Dill, *Using quaternions to calculate RMSD*, J. Comput. Chem. **25**, 1849 (2004).
- [79] D. L. Theobald, *Rapid calculation of RMSDs using a quaternion-based characteristic polynomial*, Acta Cryst. Sect. A **61**, 478 (2005).
- [80] S. V. Krasnoshchekov, E. V. Isayeva and N. F. Stepanov, *Determination of the Eckart molecule-fixed frame by use of the apparatus of quaternion algebra*, J. Chem. Phys. **140**, 154104 (2014).
- [81] F. Jørgensen, *Orientation of the Eckart frame in a polyatomic molecule by symmetric orthonormalization*, Int. J. Quantum Chem. **14**, 55 (1978).
- [82] K. N. Kudin and A. Y. Dymarsky, *Eckart axis conditions and the minimization of the root-mean-square deviation: Two closely related problems*, J. Chem. Phys. **122**, 224105 (2005).
- [83] I. N. Bronstein, K. A. Semendjajew, G. Musiol and H. Mühlig (ed.), *Taschenbuch der Mathematik*, Harri Deutsch, Frankfurt/Main, 7th ed. (2008).
- [84] J. Bartl, S. Steenken, H. Mayr and R. A. McClelland, *Photo-heterolysis and -homolysis of substituted diphenylmethyl halides, acetates, and phenyl ethers in acetonitrile: characterization of diphenylmethyl cations and radicals generated by 248-nm laser flash photolysis*, J. Am. Chem. Soc. **112**, 6918 (1990).
- [85] P. K. Das, *Transient carbocations and carbanions generated by laser flash photolysis and pulse radiolysis*, Chem. Rev. **93**, 119 (1993).
- [86] R. A. McClelland, *Flash photolysis generation and reactivities of carbenium ions and nitrenium ions*, Tetrahedron **52**, 6823 (1996).
- [87] M. Lipson, A. A. Deniz and K. S. Peters, *The sub-picosecond dynamics of diphenylmethylchloride ion pairs and radical pairs*, Chem. Phys. Lett. **288**, 781 (1998).
- [88] J. Ammer and H. Mayr, *Photogeneration of carbocations: applications in physical organic chemistry and the design of suitable precursors*, J. Phys. Org. Chem. **26**, 956 (2013).

- [89] C. F. Sailer, S. Thallmair, B. P. Fingerhut, C. Nolte, J. Ammer, H. Mayr, I. Pugliesi, R. de Vivie-Riedle and E. Riedle, *A Comprehensive Microscopic Picture of the Benzhydryl Radical and Cation Photo-Generation and Interconversion through Electron Transfer*, *ChemPhysChem* **14**, 1423 (2013).
- [90] H. Mayr and M. Patz, *Scales of Nucleophilicity and Electrophilicity: A System for Ordering Polar Organic and Organometallic Reactions*, *Angew. Chem. Int. Ed.* **33**, 938 (1994).
- [91] H. Mayr, T. Bug, M. F. Gotta, N. Hering, B. Irrgang, B. Janker, B. Kempf, R. Loos, A. R. Ofial, G. Remennikov and H. Schimmel, *Reference Scales for the Characterization of Cationic Electrophiles and Neutral Nucleophiles*, *J. Am. Chem. Soc.* **123**, 9500 (2001).
- [92] H. Mayr and A. R. Ofial, *Kinetics of electrophile-nucleophile combinations: A general approach to polar organic reactivity*, *Pure Appl. Chem.* **77**, 1807 (2005).
- [93] H. Mayr and A. R. Ofial, *Do general nucleophilicity scales exist?*, *J. Phys. Org. Chem.* **21**, 584 (2008).
- [94] H. Mayr, *Reactivity scales for quantifying polar organic reactivity: the benzhydrylium methodology*, *Tetrahedron* **71**, 5095 (2015).
- [95] H. Mayr and A. R. Ofial, *Philicities, Fugalities, and Equilibrium Constants*, *Acc. Chem. Res.* **49**, 952 (2016).
- [96] K. S. Peters and B. Li, *Picosecond dynamics of contact ion pairs and solvent-separated ion pairs in the photosolvolysis of diphenylmethyl chloride*, *J. Phys. Chem.* **98**, 401 (1994).
- [97] K. S. Peters, S. Gasparrini and L. R. Heeb, *Dynamic Nature of the Transition State for the S_N1 Reaction Mechanism of Diphenylmethyl Acetates*, *J. Am. Chem. Soc.* **127**, 13039 (2005).
- [98] K. S. Peters, *Nature of Dynamic Processes Associated with the S_N1 Reaction Mechanism*, *Chem. Rev.* **107**, 859 (2007).
- [99] C. F. Sailer, R. B. Singh, J. Ammer, E. Riedle and I. Pugliesi, *Encapsulation of diphenylmethyl phosphonium salts in reverse micelles: Enhanced bimolecular reaction of the photofragments*, *Chem. Phys. Lett.* **512**, 60 (2011).
- [100] J. Ammer, C. F. Sailer, E. Riedle and H. Mayr, *Photolytic Generation of Benzhydryl Cations and Radicals from Quaternary Phosphonium Salts: How Highly Reactive Carbocations Survive Their First Nanoseconds*, *J. Am. Chem. Soc.* **134**, 11481 (2012).
- [101] B. P. Fingerhut, C. F. Sailer, J. Ammer, E. Riedle and R. de Vivie-Riedle, *Buildup and Decay of the Optical Absorption in the Ultrafast Photo-Generation and Reaction of Benzhydryl Cations in Solution*, *J. Phys. Chem. A* **116**, 11064 (2012).
- [102] C. Sailer, *Tracking the short life of highly reactive carbocations*, PhD thesis, Ludwig-Maximilians-Universität München (2012).
- [103] C. F. Sailer and E. Riedle, *Photogeneration and reactions of benzhydryl cations and radicals: A complex sequence of mechanisms from femtoseconds to microseconds*, *Pure Appl. Chem.* **85**, 1487 (2013).

- [104] E. Riedle, M. Bradler, M. Wenninger, C. F. Sailer and I. Pugliesi, *Electronic transient spectroscopy from the deep UV to the NIR: unambiguous disentanglement of complex processes*, Faraday Discuss. **163**, 139 (2013).
- [105] E. Riedle, M. K. Roos, S. Thallmair, C. F. Sailer, N. Krebs, B. P. Fingerhut and R. de Vivie-Riedle, *Ultrafast photochemistry with two product channels: Wavepacket motion through two distinct conical intersections*, Chem. Phys. Lett. **683**, 128 (2017).
- [106] S. Thallmair, J. P. P. Zauleck and R. de Vivie-Riedle, *Quantum Dynamics in an Explicit Solvent Environment: A Photochemical Bond Cleavage Treated with a Combined QD/MD Approach*, J. Chem. Theory Comput. **11**, 1987 (2015).
- [107] C. F. Sailer, N. Krebs, B. P. Fingerhut, R. de Vivie-Riedle and E. Riedle, *Wavepacket Splitting in the First 100 fs Determines the Products from the Bond Cleavage of Diphenylmethylchloride*, in: M. Chergui, A. Taylor, S. Cundiff, R. de Vivie-Riedle and K. Yamagouchi (ed.), *Ultrafast Phenomena XVIII*, vol. 41, p. 05042, Lausanne, Switzerland (2013).
- [108] S. Thallmair, *Photogeneration of reactive intermediates*, PhD thesis, Ludwig-Maximilians-Universität München (2015).
- [109] L. E. Manring and K. S. Peters, *Picosecond dynamics of the photodissociation of triarylmethanes*, J. Phys. Chem. **88**, 3516 (1984).
- [110] T. Bizjak, J. Karpiuk, S. Lochbrunner and E. Riedle, *50-fs Photoinduced Intramolecular Charge Separation in Triphenylmethane Lactones*, J. Phys. Chem. A **108**, 10763 (2004).
- [111] S. Thallmair, M. K. Roos and R. de Vivie-Riedle, *Molecular features in complex environment: Cooperative team players during excited state bond cleavage*, Struct. Dyn. **3**, 043205 (2016).
- [112] D. Mendeleev, *Über die Beziehungen der Eigenschaften zu den Atomgewichten der Elemente*, Z. Chem. **12**, 405 (1869).
- [113] F. Schüppel, M. K. Roos and R. de Vivie-Riedle, *Ultrafast non-adiabatic dynamics of excited diphenylmethyl bromide elucidated by quantum dynamics and semi-classical on-the-fly dynamics*, Phys. Chem. Chem. Phys. **20**, 22753 (2018).
- [114] B. P. Fingerhut, S. Oesterling, K. Haiser, K. Heil, A. Glas, W. J. Schreier, W. Zinth, T. Carell and R. de Vivie-Riedle, *ONIOM approach for non-adiabatic on-the-fly molecular dynamics demonstrated for the backbone controlled Dewar valence isomerization*, J. Chem. Phys. **136**, 204307 (2012).
- [115] M. Klessinger and J. Michl, *Excited states and photochemistry of organic molecules*, VCH, New York, NY (1995).
- [116] H. Yu, J. Chao, D. Patek, R. Mujumdar, S. Mujumdar and A. S. Waggoner, *Cyanine dye dUTP analogs for enzymatic labeling of DNA probes*, Nucleic Acids Res. **22**, 3226 (1994).
- [117] O. A. Krasheninina, D. S. Novopashina, E. K. Apartsin and A. G. Venyaminova, *Recent Advances in Nucleic Acid Targeting Probes and Supramolecular Constructs Based on Pyrene-Modified Oligonucleotides*, Molecules **22**, 2108 (2017).

- [118] N. Krebs, *New insights for femtosecond spectroscopy*, PhD thesis, Ludwig-Maximilians-Universität München (2013).
- [119] D. S. Karpovich and G. J. Blanchard, *Relating the polarity-dependent fluorescence response of pyrene to vibronic coupling. Achieving a fundamental understanding of the py polarity scale*, *J. Phys. Chem.* **99**, 3951 (1995).
- [120] J. R. Platt, *Classification of Spectra of Cata-Condensed Hydrocarbons*, *J. Chem. Phys.* **17**, 484 (1949).
- [121] B. Baudisch, *Time resolved broadband spectroscopy from UV to NIR: beneficial use of the coherent artifact and pyrene dynamics*, PhD thesis, Ludwig-Maximilians-Universität München (2018).
- [122] M. Kasha, *Characterization of electronic transitions in complex molecules*, *Discuss. Faraday Soc.* **9**, 14 (1950).
- [123] M. K. Roos, S. Reiter and R. de Vivie-Riedle, *Ultrafast relaxation from 1L_a to 1L_b in pyrene: a theoretical study*, *Chem. Phys.* (2018), DOI: 10.1016/j.chemphys.2018.08.002.
- [124] M. Kasha, H. R. Rawls and M. A. El-Bayoumi, *The exciton model in molecular spectroscopy*, *Pure Appl. Chem.* **11**, 371 (1965).
- [125] N. J. Hestand and F. C. Spano, *Expanded Theory of H- and J-Molecular Aggregates: The Effects of Vibronic Coupling and Intermolecular Charge Transfer*, *Chem. Rev.* **118**, 7069 (2018).
- [126] F. Würthner, T. E. Kaiser and C. R. Saha-Möller, *J-Aggregates: From Serendipitous Discovery to Supramolecular Engineering of Functional Dye Materials*, *Angew. Chem. Int. Ed.* **50**, 3376 (2011).
- [127] E. E. Jelley, *Spectral Absorption and Fluorescence of Dyes in the Molecular State*, *Nature* **138**, 1009 (1936).
- [128] E. E. Jelley, *Molecular, Nematic and Crystal States of I: I-Diethyl-Cyanine Chloride*, *Nature* **139**, 631 (1937).
- [129] F. Nicoli, M. K. Roos, E. A. Hemmig, M. D. Antonio, R. de Vivie-Riedle and T. Liedl, *Proximity-Induced H-Aggregation of Cyanine Dyes on DNA-Duplexes*, *J. Phys. Chem. A* **120**, 9941 (2016).
- [130] L. Wang, J. Xiang, H. Sun, Q. Yang, L. Yu, Q. Li, A. Guan and Y. Tang, *Controllable cy3-MTC-dye aggregates and its applications served as a chemosensor*, *Dyes Pigm.* **122**, 382 (2015).
- [131] J. Guthmüller, F. Zutterman and B. Champagne, *Prediction of Vibronic Coupling and Absorption Spectra of Dimers from Time-Dependent Density Functional Theory: The Case of a Stacked Streptocyanine*, *J. Chem. Theory Comput.* **4**, 2094 (2008).
- [132] J.-M. Tarascon and M. Armand, *Issues and challenges facing rechargeable lithium batteries*, *Nature* **414**, 359 (2001).
- [133] D. Deng, *Li-ion batteries: basics, progress, and challenges*, *Energy Sci. Eng.* **3**, 385 (2015).

- [134] G. E. Blomgren, *The Development and Future of Lithium Ion Batteries*, J. Electrochem. Soc. **164**, A5019 (2017).
- [135] G. Zubi, R. Dufo-López, M. Carvalho and G. Pasaoglu, *The lithium-ion battery: State of the art and future perspectives*, Renewable Sustainable Energy Rev. **89**, 292 (2018).
- [136] D. Andre, S.-J. Kim, P. Lamp, S. F. Lux, F. Maglia, O. Paschos and B. Stiaszny, *Future generations of cathode materials: an automotive industry perspective*, J. Mater. Chem. A **3**, 6709 (2015).
- [137] R. Jung, M. Metzger, F. Maglia, C. Stinner and H. A. Gasteiger, *Oxygen Release and Its Effect on the Cycling Stability of $\text{LiNi}_x\text{Mn}_y\text{Co}_z\text{O}_2$ (NMC) Cathode Materials for Li-Ion Batteries*, J. Electrochem. Soc. **164**, A1361 (2017).
- [138] J. Wandt, A. T. Freiberg, A. Ogorodnik and H. A. Gasteiger, *Singlet oxygen evolution from layered transition metal oxide cathode materials and its implications for lithium-ion batteries*, Mater. Today (2018), DOI: 10.1016/j.mattod.2018.03.037.
- [139] F. Sevin and M. L. McKee, *Reactions of 1,3-Cyclohexadiene with Singlet Oxygen. A Theoretical Study*, J. Am. Chem. Soc. **123**, 4591 (2001).
- [140] F. Maseras and K. Morokuma, *IMOMM: A new integrated ab initio + molecular mechanics geometry optimization scheme of equilibrium structures and transition states*, J. Comput. Chem. **16**, 1170 (1995).
- [141] S. Humbel, S. Sieber and K. Morokuma, *The IMOMO method: Integration of different levels of molecular orbital approximations for geometry optimization of large systems: Test for n-butane conformation and $\text{S}_{\text{N}}2$ reaction: $\text{RCl}+\text{Cl}^-$* , J. Chem. Phys. **105**, 1959 (1996).
- [142] T. Vreven, K. S. Byun, I. Komáromi, S. Dapprich, J. A. Montgomery, K. Morokuma and M. J. Frisch, *Combining Quantum Mechanics Methods with Molecular Mechanics Methods in ONIOM*, J. Chem. Theory Comput. **2**, 815 (2006).
- [143] T. Vreven and K. Morokuma, *Investigation of the $\text{S}_0 \rightarrow \text{S}_1$ excitation in bacteriorhodopsin with the ONIOM(MO:MM) hybrid method*, Theor. Chem. Acc. **109**, 125 (2003).
- [144] S. Roßbach and C. Ochsenfeld, *Influence of Coupling and Embedding Schemes on QM Size Convergence in QM/MM Approaches for the Example of a Proton Transfer in DNA*, J. Chem. Theory Comput. **13**, 1102 (2017).
- [145] H. P. Hratchian, P. V. Parandekar, K. Raghavachari, M. J. Frisch and T. Vreven, *QM:QM electronic embedding using Mulliken atomic charges: Energies and analytic gradients in an ONIOM framework*, J. Chem. Phys. **128**, 034107 (2008).
- [146] H. P. Hratchian, A. V. Krukau, P. V. Parandekar, M. J. Frisch and K. Raghavachari, *QM:QM embedding using electronic densities within an ONIOM framework: Energies and analytic gradients*, J. Chem. Phys. **135**, 014105 (2011).
- [147] F. Aquilante, L. D. Vico, N. Ferré, G. Ghigo, P.-A. Malmqvist, P. Neogrády, T. B. Pedersen, M. Pitonňák, M. Reiher, B. O. Roos, L. Serrano-Andrés, M. Urban, V. Veryazov and R. Lindh, *MOLCAS 7: The Next Generation*, J. Comput. Chem. **31**, 224 (2010).

- [148] M. J. Bearpark, M. A. Robb and H. B. Schlegel, *A direct method for the location of the lowest energy point on a potential surface crossing*, Chem. Phys. Lett. **223**, 269 (1994).
- [149] S. Ruiz-Barragan, K. Morokuma and L. Blancafort, *Conical Intersection Optimization Using Composed Steps Inside the ONIOM(QM:MM) Scheme: CASSCF:UFF Implementation with Microiterations*, J. Chem. Theory Comput. **11**, 1585 (2015).
- [150] L. González, D. Escudero and L. Serrano-Andrés, *Progress and Challenges in the Calculation of Electronic Excited States*, ChemPhysChem **13**, 28 (2012).
- [151] T. Vreven, L. M. Thompson, S. M. Larkin, I. Kirker and M. J. Bearpark, *Deconstructing the ONIOM Hessian: Investigating Method Combinations for Transition Structures*, J. Chem. Theory Comput. **8**, 4907 (2012).
- [152] G. Schaftenaar, E. Vlieg and G. Vriend, *Molden 2.0: quantum chemistry meets proteins*, J. Comput.-Aided Mol. Des. **31**, 789 (2017).
- [153] S. Oesterling, *Ab initio studies on photorelaxation: exploring, altering and crossing the excited state landscape*, PhD thesis, Ludwig-Maximilians-Universität München (2017).
- [154] M. Barbatti, G. Granucci, M. Ruckebauer, F. Plasser, R. Crespo-Otero, J. Pittner, M. Persico and H. Lischka, *NEWTONX, a package for Newtonian dynamics close to the crossing seam, version 1.4* (2014), www.newtonx.org.
- [155] M. Barbatti, M. Ruckebauer, F. Plasser, J. Pittner, G. Granucci, M. Persico and H. Lischka, *Newton-X: a surface-hopping program for nonadiabatic molecular dynamics*, WIREs Comput. Mol. Sci. **4**, 26 (2014).

Danksagung

Zu guter Letzt möchte ich noch denjenigen danken, die über die vergangenen Jahre hinweg in der einen oder anderen Weise zu dieser Doktorarbeit beigetragen haben.

Als erstes gilt mein Dank dabei meiner Doktormutter und Chefin Frau Prof. Regina de Vivie-Riedle für die Möglichkeit in diesem interessanten Fachgebiet zu promovieren. Die große Freiheit beim Forschen und das damit einhergehende Vertrauen in mich und meine Arbeit war dabei stets gepaart mit der Möglichkeit jederzeit Feedback und Expertise zu erhalten. Die übertragene Verantwortung auch für Lehre und administrative Tätigkeiten unterstreicht dieses Vertrauen und ließen mich als Person weiter reifen. Hierzu trugen auch die häufigen Gelegenheiten als Teil der wissenschaftlichen Community an Konferenzen teilzunehmen bei, wo ich auch meine Ergebnisse präsentieren konnte.

Auch bedanke ich mich bei allen experimentellen Kooperationspartnern, mit denen ich das Glück hatte in den vergangenen Jahren zusammen an spannenden Projekten zu arbeiten und teils gemeinsam zu veröffentlichen: Francesca Nicoli vom AK Liedl (LMU); Bastian Baudisch und Prof. Eberhard Riedle vom BMO; Anna Freiberg, Johannes Wandt und Prof. Hubert Gasteiger von der TUM.

Ein großer Dank geht auch an alle ehemaligen und momentanen Kollegen im Arbeitskreis: Artur, Thali, Patrick, Robert, Sven, Julius, Daniel, Flo, Thomas, Franziska, Martin und Sebastian. Die stets ausgezeichnete Arbeitsatmosphäre in der Gruppe – entspannt, aber gleichzeitig immer konstruktiv und fokussiert – hatte großen Anteil am Gelingen dieser Doktorarbeit. Besonders bedanke ich mich bei Thali, der in meinem F-Praktikum mein Interesse an der Femtochemie geweckt, dann meine Masterarbeit betreut und mich schließlich in den ersten Jahren als Doktorand begleitet hat. Außerdem danke ich allen Studenten, die ich im Rahmen ihrer Bachelor- oder Masterarbeit betreuen durfte: Alexey, Chaochen, Teresa, Sebastian und Franziska.

Nicht zu vergessen danke ich meinen Eltern, die mich immer gefördert und begleitet und mir das Studium ermöglicht haben, meinem Bruder Michi für die vielen Gedanken und Anregungen aus den langen Gesprächen in den vergangenen Jahren und meinen beiden Kommilitonen Thomas und Enrico für den Austausch beim freitäglichen Semesteressen und darüberhinaus.

Zum guten Schluss danke ich meiner Freundin Janina für ihre Liebe und Unterstützung.